1973

Dilatancy model for the failure of rocks

Kulbhushan Lal Logani
Iowa State University

Dilatancy model for the failure of rocks

by

Kulbhushan Lal Logani

A Dissertation Submitted to the
Graduate Faculty in Partial Fulfillment of
The Requirements for the Degree of
DOCTOR OF PHILOSOPHY

Department: Civil Engineering
Major: Soil Engineering

Approved:

Signature was redacted for privacy.

In Charge of Major Work

Signature was redacted for privacy.

For the Major Department

Signature was redacted for privacy.

For the Graduate College

Iowa State University
Ames, Iowa

1973

TABLE OF CONTENTS

	Page
INTRODUCTION	1
Statement of the Problem	1
BACKGROUND AND LITERATURE REVIEW	3
Dilatancy	3
Sliding Friction	9
Historical background	10
Modern theory of friction	13
Equivalent continuum contact area	13
Apparent contact area	14
True contact area	15
The Terzaghi theory of friction	16
The Bowden and Tabor adhesion theory of friction	18
Influence of surface film	23
Influence of removal of normal load	24
Influence of dust particles	24
Friction of Rock	25
Friction of a Dilatant Mass	29
Energy Theory of Dilatant Mass	31
Reynolds' energy concept	31
Taylor energy theory	31
Newland and Allely Theory	33
Rowe "Stress-Dilatancy" Theory	37
Horne confirmation	39
Tinoco and Handy Theory	41
MEASUREMENT OF COEFFICIENT OF SLIDING FRICTION	43
Principle	43
Specimen Preparation	46
Test Procedure	47
Test Results	47
Scanning Electronic Microscope Photographs	50
TEST APPARATUS, SAMPLE PREPARATION, AND TESTING TECHNIQUE	54
The Biaxial Test Apparatus	54

Page

Brief description 54
General features 54
Collapsible box 58
Lateral stress system 61
Calibration of Bellofram pressure units 63
Lateral deformation measurement system 65
Axial deformation system 67
Axial load measurement 69
Main frame 69

Material Tested 70
Sample Preparation 71
Testing Technique 72
Reproducibility 75

THEORETICAL INVESTIGATIONS 77

General Considerations 77
Forces Acting 77
Elastic Deformations 82
Stress Ratio $(\frac{\sigma_1}{\sigma_3})$ Formulation 89
General theory 89
Stress ratio at failure 92
Stress ratio in post-failure region 100
Volumetric Strain $(\frac{dv}{v_0})$ and Axial Strain (ε_1) Formulation 105
$(\frac{dv}{v_0})$-(ε_1) formulation 105
Effects of multiple failure planes and particle (rod) size 113

TESTING OF THEORY 121

Testing of the Predicted Maximum Stress Ratio $(\frac{\sigma_1}{\sigma_3})_{max}$ 121
Testing of the Predicted Stress Ratio $(\frac{\sigma_1}{\sigma_3})$ in the Post-Failure Region 124
Testing of the Predicted Volumetric Strain $(\frac{dv}{v_0})$ 163

CONCLUSIONS 202

SUGGESTION FOR FURTHER INVESTIGATIONS 206

BIBLIOGRAPHY 208

ACKNOWLEDGEMENTS 213

LIST OF TABLES

		Page
Table 1.	Variation of coefficient of sliding friction with normal load in the case of 1"-diameter rods	48
Table 2.	Variation of coefficient of sliding friction with normal load in the case of teflon rods	49
Table 3.	Maximum stress ratios for hexagonal array of cylinders (theoretical)	106
Table 4.	Maximum stress ratio (experimental)	122

LIST OF FIGURES

		Page
Figure 1.	Sliding type friction test apparatus; (a) section, (b) plan, (c) modeling two sliding rods	44
Figure 1.	(Continued) (d) variation of friction with load	51
Figure 1.	(Continued) (e) scanning electron micrograph – 300x natural size surface of the 1"-diameter rod	52
Figure 1.	(Continued) (f) scanning electron micrograph – 300x natural size surface of the 1/4"-diameter rod	53
Figure 2.	The biaxial test apparatus	55
Figure 3.	Collapsible box; (a) plan, (b) cross section	60
Figure 4.	Lateral stress system	62
Figure 5.	Lateral and axial deformation measurement and the axial load measurement system	64
Figure 6.	The biaxial test apparatus; (a) photographic set-up, (b) modified Ames dial	66
Figure 7.	Axial deformation system	68
Figure 8.	Mathematics of collapsible box	74
Figure 9.	Regular geometrical arrays; is the shape factor and λ is the distribution angle; (a) hexagonal array of oval shapes; (b) hexagonal array of circular shapes, $\lambda = 60°$, (c) cubic array of circular shapes, $\lambda = 45°$, (d) hexagonal array shown with forces	78
Figure 10.	An assemblage of rods subjected to biaxial stresses	81
Figure 11.	Elastic deformation; (a) two rods, (b) two rods deformed elastically under load F, (c) two rods deformed elastically under normal and tangential loads together	83
Figure 12.	Elastic deformations resolved into axial elastic strains (α is the distance of relative approach and δ is the lateral displacement)	85

		Page
Figure 13.	An assemblage of rods shown with possible directions of shear zone when subjected to biaxial stresses	90
Figure 14.	An array on an imminent shear zone	91b
Figure 15.	Forces acting on an array; (a) forces acting on moving wedge, (b) hexagonal array before failure and at $\frac{\sigma_1}{\sigma_3} = \cot^2\lambda$	93
Figure 16.	Mathematics of semirigid wedge	95
Figure 17a.	Hexagonal array at $\frac{\sigma_1}{\sigma_3} > \cot^2\lambda$	97b
Figure 17b.	Limiting equilibrium of contact $\acute{J}$ and $\acute{M}$ of rod P at failure	97b
Figure 18.	An array on a shear surface in post failure deformations	101b
Figure 19a.	Hexagonal array in post failure deformation	102b
Figure 19b.	Equilibrium of rod P in post failure deformation of the array	102b
Figure 20.	An assemblage showing the number of volume units (shown shaded) taking part in volume changes along shear plane	104
Figure 21.	Mathematics of the shear zone	107
Figure 22a.	Hexagonal array in pre-failure stage	109b
Figure 22b.	Hexagonal array in post-failure stage	109b
Figure 23.	ℓn (axial strain x 10^3) versus number of shear planes curve	118
Figure 24.	ℓn (axial strain x 417) versus number of shear planes curve	119
Figure 25.	Variation of maximum stress ratio with σ_3	123
Figure 26.	Theoretical stress ratio curves	125
Figure 27.	Stress ratio curves	131
Figure 28.	Stress ratio curves	132
Figure 29.	Stress ratio curves	133
Figure 30.	Stress ratio curves	134
Figure 31.	Stress ratio curves	135
Figure 32.	Stress ratio curves	136
Figure 33.	Stress ratio curves	137
Figure 34.	Stress ratio curves	138

		Page
Figure 35.	Stress ratio curves	139
Figure 36.	Stress ratio curves	140
Figure 37.	Stress ratio curves	141
Figure 38.	Stress ratio curves	142
Figure 39.	Stress ratio curves	143
Figure 40.	Stress ratio curves	144
Figure 41.	Stress ratio curves	145
Figure 42.	Stress ratio curves	146
Figure 43.	Stress ratio curves	147
Figure 44.	Stress ratio curves	148
Figure 45.	Stress ratio curves	149
Figure 46.	Stress ratio curves	150
Figure 47.	Stress ratio curves	151
Figure 48.	Stress ratio curves	152
Figure 49.	Stress ratio curves	153
Figure 50.	Stress ratio curves	154
Figure 51.	Stress ratio curves	155
Figure 52.	Stress ratio curves	156
Figure 53.	Stress ratio curves	157
Figure 54.	Stress ratio curves	158
Figure 55.	Stress ratio curves	159
Figure 56.	Stress ratio curves	160
Figure 57.	Axial strain to stress ratio curves; (a) failure mechanism 1, (b) failure mechanism 2, (c) two combinations of failure mechanisms 1 and 2	162
Figure 58.	Theoretical volumetric strain curve	164
Figure 59.	Volumetric strain curves	170
Figure 60.	Volumetric strain curves	171
Figure 61.	Volumetric strain curves	172
Figure 62.	Volumetric strain curves	173
Figure 63.	Volumetric strain curves	174
Figure 64.	Volumetric strain curves	175

		Page
Figure 65.	Volumetric strain curves	176
Figure 66.	Volumetric strain curves	177
Figure 67.	Volumetric strain curves	178
Figure 68.	Volumetric strain curves	179
Figure 69.	Volumetric strain curves	180
Figure 70.	Volumetric strain curves	181
Figure 71.	Volumetric strain curves	182
Figure 72.	Volumetric strain curves	183
Figure 73.	Volumetric strain curves	184
Figure 74.	Volumetric strain curves	185
Figure 75.	Volumetric strain curves	186
Figure 76.	Volumetric strain curves	187
Figure 77.	Volumetric strain curves	188
Figure 78.	Volumetric strain curves	189
Figure 79.	Volumetric strain curves	190
Figure 80.	Volumetric strain curves	191
Figure 81.	Volumetric strain curves	192
Figure 82.	Volumetric strain curves	193
Figure 83.	Volumetric strain curves	194
Figure 84.	Volumetric strain curves	195
Figure 85.	Volumetric strain curves	196
Figure 86.	Volumetric strain curves	197
Figure 87.	Volumetric strain curves	198
Figure 88.	Volumetric strain curves	199
Figure 89.	Single shear plane in the case of 1"-diameter rods	200
Figure 90.	Multiple shear planes in the case of 1/2"-diameter rods	201

INTRODUCTION

Statement of the Problem

The purpose of this research is to study and formulate a failure mechanism which could apply to movement of rock bodies along their joints and fracture planes. Rock bodies can acquire these features of layering, jointing and fracturing either as a part of their geological origin or from external causes such as stress release, earthquakes, blasting, or other engineering activities. Such features in rock bodies are centers of weakness and control strength.

Observed failures involving shear within rock or soil masses often occur in plane section, i.e. with a relatively constant cross section normal to the failure surface. Such a two-dimensional failure can be modelled by plane-strain shear tests, whereby the rock or soil material is confined to prevent strain in the third dimension. In the present study, such strain was prevented not by confinement but by the geometry of the individual particles, which are rods lying parallel to one another in a shear box.

This research, therefore, involves subjecting ideal assemblages of rods to a biaxial stress field, varying the principal stress ratio, and recording the stresses, strains, volume changes, and translocations and rotations of individual members of the assemblage. Simultaneously, a theory was developed to predict the behavior, such that the theory

could be tested and revised as necessary.

The biaxial testing method used has the following advantages over the tests of natural materials:

1. A continuous photographically recorded inventory of individual particle movements in relation to assemblage stress, strain and volume changes.
2. Ready prediction of an ideal behavior, such that departures from the ideal can be identified and related to causes.
3. Controlled test conditions which minimize the sampling variable by reusing the same sample.
4. Ability of testing different regular geometrical array, affording a precise variation of void ratio and packing density.
5. An accurate visualization of failure mechanism, in that failure by sliding and/or rotation can be differentiated.

BACKGROUND AND LITERATURE REVIEW

In order to formulate a failure theory for a granular mass subjected to a biaxial stress field, it is necessary to understand the past and present concepts of dilatancy and sliding friction.

Dilatancy

Dilatancy — "The property of granular masses of expanding in bulk with change of shape. It is due to the increase of space between the individually rigid particles as they change their relative positions" (Century Dictionary).

Dilatancy was first described and named by Professor Osborne Reynolds (1885), who showed that a dense sand mass expands upon shearing. He observed:

> . . . I would point out the existence of a singular fundamental property of such granular media which is not possessed by known fluids and solids. On perceiving some thing which resembles nothing within the limits of one's knowledge, a name is a matter of great difficulty. I have called this unique property of granular masses "dilatancy", because the property consists in a definite change of bulk, consequent on a definite change of shape or distortional strain, any disturbance whatever causing a change in volume and generally dilation.

Reynolds observed that with granular media, so long as the grains are held in mutual equilibrium by stresses transmitted through the mass, every change of relative position of the grains is attended by a consequent change in volume; and, if in any way the volume is fixed, then all change of shape is prevented. Professor Reynolds made one assumption,

that the position of any internal particle becomes fixed if the positions of surrounding particles are fixed. Without frictional bridging of particles over voids, this condition would always be fulfilled. It follows that no grain in the interior can change its position in the mass by passing between the contiguous (touching) grains without disturbing them; hence, whatever alteration the medium may undergo, the same particle will always be in the same neighborhood. If, then, such a medium is subjected to internal strain, the shape of the internal groups of particles will all be altered. The shape of each elementary group is determined by shape and arrangement of surrounding particles. Any distortion of the boundaries of such a medium will cause distortion of the arrangements of its particles, necessitating a change in volume and, hence, the mean density. If particles are rigid, the relations between distortion and dilatancy are independent of friction; that is to say, the same distortion of any bounding surface must mean the same internal distortion whatever the friction may be. The only possible effect of friction is to render the grains stable under circumstances in which they would not otherwise be stable.

Mead (1925), while applying Reynolds' theory of dilatancy to solid rocks, concluded that incoherent, granular masses such as sand, in a condition approaching maximum density packing (rhombic packing), are dilated by deformation; whereas, in a condition of open packing (cubic packing), they

deform without dilation. Prevention of free dilation by enclosing pressures induces failure by fracture or shear when the mass is deformed, and with development of joints and faults along thin zones of dilation. This manner of failure requires a minimum increase in volume and involves dilation only in the shear zone. When free dilation is not prevented, the granular mass deforms by flow. Such a deformation of closely packed grains involves the entire mass and causes a much greater volume increase than that required by failure along definite shear planes, and can be called plastic deformation or plastic flow.

Performing an experiment somewhat similar to Reynolds' experiments with a rubber balloon, sand and water, Mead (1925) observed that if the amount of fluid in the granular aggregate is only sufficient to fill the voids in the condition of maximum density packing, deformation of the mass requires an increase in volume, and the mass fails largely by fracture and not by plastic deformation. If the fluid available is slightly in excess of this amount, the aggregate is easily deformed plastically up to a point where the increased voids absorb the available fluid, at which point the mass becomes rigid. On the other hand, when the available fluid phase is sufficient to fill the voids with grains arranged in a cubic or minimum density packing, the mass may be deformed to any extent without an increase in volume, and failure may be due to plastic flow offering very little resistance to

deformation.

The mechanics of response to deformation of incoherent granular masses can be applied to solid rocks by conceiving of them as having a solid and, potentially, an ideally imcompressible fluid phase. The latter may cause the rock to yield to deformation by flowing or by fracture. In simplest terms, the rocks may be regarded as a granular aggregate, the hard grains the solid phase. To the extent that the rocks are porous, the pores represent the volume of fluid phase and the material that occupies the pores is the fluid phase. Alternately, the solid phase can be represented by harder, more resistant minerals of rock mass, whereas the potentially fluid phase can be represented by those constituents of rock which are relatively mobile, as evidenced by their rearrangement to schistose (foliated, i.e., capable of splitting up in thin irregular plates) structures through processes of crystallization and recrystallization. Thus, potential fluid phases occur under certain conditions of composition, pressure, temperature and rate of deformation.

Brown and Hawksley (1947), while experimenting with regular two-dimensional packings of equal spheres, observed a marked tendency for the spheres to move together in groups; thus, they found a third process (besides the appearance of slip lines and dilatant expansion) by which the tight regions in the array break down. They pointed out that relative movement between groups of tight packing leads to the loss of

the peripheral spheres by a sort of "abrasion" between the groups which gave loose irregular packing between the groups.

In effect, their observation showed that there is a tendency for local regions in packings to become or to remain tightly packed. In general, the tight regions did not dilate uniformly, but either failed locally in a line of slip or moved as a group. An initially uniform loose packing collapsed locally, while an initially tight packing failed irregularly along lines of slips, in either case giving a nonuniform distribution of voids. Groups of tight packing were not found to mesh with each other.

They concluded that in tight regular arrangements, dilatancy is a geometrical necessity if deformation is to occur; whereas, in irregular arrangements, dilatancy does occur, but the explanation lies in the "stability" of the packing. Moreover, since the groups of tight packing have been observed to move as a whole without dilation, or when they do dilate to fail along the line of slip (in preference to a uniform dilation), it would seem that these groups possess some rigidity. Thus an assemblage, regarded as an arrangement of fundamental units which are semirigid, may dilate through the interplay of these units. Since there can be an interchange of particles between adjacent units, such an interplay is more "flexible" than the interplay between individual particles.

Andrade and Fox (1949), while working with a two-dimensional regular (hexagonal) array of ebonite and polythene rods, pointed out that the dilation of a regular array is intimately connected with the mechanism of deformation. They detected two classes of dilational deformations, both of them consequences of slip on well-defined planes. In the first, the dilation was localized at the boundaries of regular areas of rods which preserved their original packing; in the second, it was more or less irregular throughout some of these areas. The first type is, in a sense, the more fundamental since the deformation necessarily involves slip which, in turn, involves the primary dilation. The occurrence of secondary dilation was ascribed to some extent, at least, to surface cohesion of the array. In the absence of secondary dilation, the primary dilation showed a fairly regular alternation corresponding to the slipping and healing of the array. The regularity of this alternation was probably disturbed by the secondary dilation since secondary dilation could not be expected to show any regular variations. Secondary dilation was also found to be dependent on internal friction – the smaller the internal friction, the smaller the role played by secondary dilation. The result was that greater friction gave dilation which was not as regular as it was in the case of less friction. More surfaces of misfit, some of which became healed in the progressive stages, were observed with greater friction. This fact could be held as the direct

consequence of secondary dilation and increased internal friction.

Apparently internal friction stabilizes the array against the onset of slip; but, when frictional forces are eventually overcome, the deformation becomes catastrophic with, consequentially, a greater tendency for the areas of rods to break up than when the deformation proceeds gradually, as in the case of low friction.

Hills (1963) notes that the relationship of dilatancy to the spacing of shear planes developed in a deformed rock may be very important. Since a considerable amount of work is done in developing a single shear plane under dilatant conditions, the principle of least work suggests that the number of planes will be small in coarse-grained materials; whereas, with a fine-grained aggregate, each shear plane involves less work and the effort may be expended with equal facility on a greater number of planes.

Sliding Friction

Friction is a physical phenomenon which appears to have been recognized since before the dawn of civilization. Primitive man made use of this universal attribute of matter in making fire. The Egyptians, the Greeks, and the Romans were fully aware of the fact that an effort is required to move an object over another object, including the earth's surface, and of the use of lubricants to reduce friction and wear.

In the examination of sliding friction, some historical background will be briefly examined. The modern concept of sliding friction will then be presented.

Historical background (reviewed in Bowden and Tabor, 1964)

Writers such as Aristotle, Pliny the Elder, and Vitruvius recognized the reality of friction, but it was not until the middle fifteenth century that Leonardo da Vinci (1452-1519) translated the phenomenon into scientific laws. Unfortunately, his work remained unnoticed in his notebook. It was in 1699 when a French architect, Guillaume Amontons (1663-1705), obviously unaware of Leonardo da Vinci's work, rediscovered the laws of friction and presented them to the French Academy in the form of a paper. His paper described the two main laws of friction, which are:

1. Friction force is proportional to the normal load. For most surfaces, it is one-third of the normal load.
2. Friction is independent of the size of the bodies.

Amontons and his French contemporaries and successors saw the cause of friction in surface roughnesses. He even discussed the role of surface asperities and suggested that they could act in two ways. He said, "Either they are rigid, in which case friction is certainly due to pulling the weight up the slopes, or they are deformable, in which case the asperities are pressed down by the moving body and a similar

force must be expended in doing this."

Leonhard Euler (1707-1773), a Swiss-born mathematician and physicist, presented two papers in 1748 to the Royal Academy of Science in Berlin in which he discussed the mechanism of friction in terms of surface roughness and suggested that surfaces are covered with a series of ratchet-like teeth at different slopes, and that the ratio of the force of friction and the normal force is equal to the tangent of the angle of steepest slope. He also, for the first time, pointed out the distinction between static and kinetic friction.

Charle Augustine Coulomb (1736-1806), a French scientist who was a civil engineer by training, reviewed Amonton's work in between his own earth pressure and electrical experiments and discoveries. He considered that friction could arise from lifting over asperities, bending of asperities, and breaking of asperities. He also considered the possibilities of cohesion, but rejected it as a cuase of friction because he thought the cohesion would increase proportionately with the number of regions of contact, i.e., gross contact area; whereas, friction was found to be independent of geometric area.

Jean Theophile Desaguliers (1683-1744), an English physicist, discovered adhesion between like solid bodies in 1724 and considered that a similar force might be involved in friction. He thus introduced a new element into the field

of theory of friction.

Samuel Vince (1749-1821), another English scientist, carried out experiments which supported the view that adhesion was an important part of friction. He stated that static friction is the sum of kinetic friction, which he called the true friction, and cohesion between surfaces.

The development of the science of surface chemistry during the nineteenth century caused doubts and reexamination of the so-called "roughness hypothesis" or the interlocking theory of friction, eventually leading Ewing (1892) and Sir William Hardy (1919, 1936) to revive the molecular adhesion theory of friction. This approach of friction, due to molecular attraction operating across an interface, was elaborated by Tomlinson (1929). As the "adhesion theory" required the frictional force to be proportional to the area of contact, it gained no recognition until the distinction was made between the real area and the apparent area of contact, on the basis of the works of Holm in 1938 using electrical contacts and of Bowden and Tabor in 1942 on frictional contact. As the real contact area was shown to be proportional to the load and independent of gross contact area, the adhesion hypothesis was able to establish itself. On the basis of his studies, Karl Terzaghi (1960, pp. 173-174) agreed intuitively with the adhesion hypothesis.

Modern friction research really started with the publication of the historic work of Beare and Bowden (1934),

followed by the classical works of Bowden and Leben (1939), and of Bowden and Bowden and Tabor (1939) on the friction of metals. These basic works dispelled the interlocking theory in favor of the adhesion theory. The observation of Beare and Bowden that the physical processes occurring during sliding are too complicated to yield to mathematical treatment is still true today.

Modern theory of friction

Before discussing the latest accepted theory of friction, it will be worthwhile to discuss what we mean by area of contact.

When two surfaces are brought together into contact with each other under a normal load, there develops an area of contact through which the normal load is transmitted from one surface to another. There are three descriptions for contact area, namely:

1. Equivalent continuum contact area,
2. Apparent contact area, and
3. Net contact area or true contact area.

Equivalent continuum contact area

Consider a small hypothetical element buried within a mass of soil (Lambe and Whitman, 1969, p. 97), with soil particles pushing against its horizontal and vertical faces. The soil particles generally exert a normal force and a shear force on the faces of the element. If each face of the

element is square, with dimension a on each side, then we can define the macroscopic stress acting on the face of the element as the ratio of force and total area a^2. The total area a^2 used for defining the macroscopic stresses can be called equivalent continuum contact area.

Apparent contact area

When two contacting surfaces are subjected to a normal load, then a region of contact is bounded by an ellipse (Hertz theory) having semiaxes a and b. The area of this elliptical surface is called an apparent contact area. The apparent contact area Aa, in other words, is nothing different than the elastic contact area which can be obtained from the elastic properties of the two contacting surfaces. The values of a and b are given by (Timoshenko, 1951, p. 379):

$$a = m \sqrt[3]{\frac{3\pi}{4} \frac{W(K_1 + K_2)}{(A+B)}}$$

$$b = n \sqrt[3]{\frac{3\pi}{4} \frac{W(K_1 + K_2)}{A+B}}$$

where W is the normal load, K_1, K_2 are the elastic constants, A and B are constants depending on the magnitudes of the principal curvatures R_1 and R_2 of the surfaces in contact and on the angle between the planes of the principal curvatures of the two surfaces; and m and n are coefficients depending on the ratio $\frac{B - A}{A + B}$.

$$\text{Apparent contact area} = \pi ab = K\, W^{2/3}$$

where

$$K = \pi mn \left[\frac{3\pi}{4} \frac{(K_1 + K_2)}{(A + B)}\right]^{2/3}$$

Terzaghi (1960) denotes this area as the area of gross contact surface.

True contact area

From the above formula for apparent contact area (Hertzian or elastic contact area), it can be seen that the apparent area depends to a large degree on the radii of curvature of the contacting surfaces and, furthermore, does not increase in direct proportion with load W, but with $W^{2/3}$. From very accurate experimental observations, it has been shown that the frictional resistance is caused by physicochemical interactions or bonds between surfaces in contact. The shear strength of such bonds for a given composition of contacting surfaces cannot possibly depend on any other factor than the area of the surfaces over which the molecular attraction is taking place. If the molecular interaction was active over the entire contact area (i.e., apparent contact area) computed by the Hertz formula, it would not be possible for the relationship between the load and friction to be independent of the radii of curvatures of the contacting surfaces, and the direct proportionality between these quantities could not be valid. Moreover, no matter how smooth the

surfaces may be, they must be considered rough in relation to the diameter of the sphere of influence of a molecule, and for the small pressures they will touch at only three points. (For stability, a surface must be supported at three points.) Hence, it is out of necessity that one must assume that within the apparent contact area there are located substantially smaller island areas of true contact. Hence, net or true contact area can be defined as that part of the apparent contact area through which the pressure is being transmitted from one surface to another, only from molecule to molecule; whereas, the spheres of influence of the molecules on both sides of the plane of separation must penetrate each other.

The Terzaghi theory of friction

On a submicroscopic scale, most surfaces — even carefully polished ones — are actually rough and contain projections of material above the average surface elevation. These projections are known as asperities. Two surfaces will be in apparent contact only where the projections touch one another. The actual contact area is a very small fraction of the apparent contact area.

Because contact occurs at discrete sites (island areas of true contact within the apparent contact area), the normal stresses across these contacts will be extremely high and, even under light loading, will reach the yield strength of the material at these sites. Thus, the actual area of

contact is the area where material has yielded and is given by

$$A_c = \frac{W}{y}$$

where W is the normal load and y is the yield strength of the softer surface. This shows that an increase in normal load between the two contacting surfaces must mean a proportional increase in the area of actual contact.

The extremely high contact stresses cause the two surfaces to adhere at the points of actual contact, i.e., two surfaces are joined by chemical bonds and shear strength is provided by adhesive strength of these points. The maximum possible shear force T_{max} is thus given by

$$T_{max} = s\ A_c$$

where s is the shear strength of adhered junctions which will be, in the absence of work hardening, the shear strength of the material of the softer surface. With work hardening, s will be more than the shear strength of material of the softer surface.

From the above equations and the empirical observation, the coefficient of friction f is equal to the ratio of tangential force to normal force, i.e.,

$$f = \frac{T_{max}}{W} = \frac{s}{y} .$$

The Bowden and Tabor adhesion theory of friction

We have seen in the earlier discussion that the apparent contact area A_a is proportional to $W^{2/3}$. If we define mean pressure p_m over the area of apparent contact as the ratio of normal load W to the area of apparent contact A_a, then it will be proportional to $W^{1/3}$. As the load W is increased, the mean pressure p_m increases, first within elastic limits so that the surfaces return to their original configuration on the removal of load between them, and then reaching such a value that at a critical point within the softer material the elastic limit is exceeded. This occurs at a region where the shear stresses are a maximum, which is given by Hertz' analysis to be at a depth of 0.5 times the sum of the semiaxes of the apparent contact area (elliptical). The elastic limit is just exceeded at this point when the mean pressure p_m is given by

$$p_m = cy$$

where y is the yield stress or elastic limit of the softer metal as found in pure tension and c is approximately equal to 1.1. If the load is increased further, the area of contact and the mean pressure p_m rise in such a manner that a region of plasticity grows rapidly, and a stage is soon reached at which the whole of the material around the region of contact is flowing plastically. At this stage, c in the above equation is approximately equal to 3. If the load is

increased still further, it is found that although the size of the deformed area increases, the above relation with $c \approx 3$ is still valid, provided (1) the deformed area is not too large compared with the size of the specimens, and (2) there is no work hardening. The mean pressure p_m, which we may call the "yield pressure", is almost independent of the size of asperities and of the size of indentation and, therefore, of the load.

In the case of a spherical asperity pressing on a flat plate, the load W_L which causes the initiation of a plastic region is given by

$$W_L = 13.1\, p_m^{\,3}\, r^2 \left(\frac{1}{E_1} + \frac{1}{E_2}\right)^2$$

where r is the radius of the sphere and E_1 and E_2 are elastic modulii for plate and sphere, respectively. The tip of a conical or pyramoidal shape can be considered a sphere of diminishing radii; so, from the above relation, it can be seen that a very small load can deform asperity beyond the elastic limit.

For metals which do not work-harden, the yield stress y is a constant; thus, p_m ($\approx 3y$) is a constant. Consequently, we may expect that in most practical cases for all types of shapes of surface irregularities, the true area of contact A_c over which plastic flow occurs will be very nearly directly proportional to load W and inversely proportional to the mean yield pressure $p_m \approx 3y$ of the

asperities, and is given by

$$A_c = \frac{W}{p_m} \approx \frac{W}{3y} .$$

The above analysis establishes that, on a macroscopic scale, elastic deformations are taking place and the area of apparent contact is increased with $W^{2/3}$; whereas, on a microscopic scale, plastic deformations are taking place on the tips of the asperities, and the area of true contact is increased with W, the normal load.

In summary, it can be said that the true contact area A_c is the sum of the flattened tips of the asperities or is the plastic contact area, while the apparent contact area A_a is the region covering the macroscopic indentation or is the elastic contact area. The ratio of the true to the apparent contact area is approximately equal to

$$\frac{A_c}{A_a} = \frac{\text{elastic limit } y}{\text{raised elastic limit due to work-hardening } y_h} .$$

This ratio is about 0.5, even in the case of highly work-hardened specimens. In other words, the plastic flow of the asperities provides the true area of contact which supports the load, and the stresses in the asperities are taken up by the elastic deformations on the apparent contact area of the underlying metal.

On the basis of experimental work, it has been observed that frictional effects are not confined to the surface of a solid, but cause distortion and deformation to a depth

beneath the surface. The physical processes that occur during sliding are too complex to yield easily to a simple mathematical treatment; but the experiments show that, under the intense pressure which acts at the summits of the surface irregularities, a localized adhesion and welding together of metal surfaces occurs. When sliding takes place, work is required to shear these welded junctions and also to plough out the metal. We may therefore express the frictional resistance as the sum of two terms, one of which represents the shearing and the other the ploughing process.

The shearing resistance τ_{max} is the force required to shear the junctions formed at the points of intimate contact between the two surfaces. This is given by

$$\tau_{max} = A_c \, s$$

where A_c is the true contact area $\frac{W}{cy}$ under normal load W, and s is the force per unit area which, acting in a direction tangential to the interface, is required to shear the junction.

The ploughing resistance P is the force required to displace the softer metal from the front of the harder sliding asperity. This is given by

$$P = A'p'$$

where A' is the area of cross section of the grooved track and p' is the mean pressure required to displace the metal

in the surface; p' may be expected of the same order as $p_m = cy$.

The total frictional force F is given by

$$F = \tau_{max} + P = A_c s + A'p'.$$

If the ploughing term is negligible, then

$$F = A_c s.$$

True contact area depends only on W and p_m, and is almost independent of the apparent contact area of the surfaces. This is equivalent to Amonton's first law.

$$F = \frac{W}{p_m} s$$

$$\frac{F}{W} = \frac{s}{p_m}$$

The coefficient of friction f equals $\frac{s}{p_m}$; hence, the coefficient of friction is virtually independent of the load W. This is equivalent to Amonton's second law.

$$f = \frac{\text{shearing strength of junction}}{\text{yield pressure of the softer material}}$$

As shearing usually occurs in the softer material, then

$$f = \frac{\text{shearing strength of the softer material}}{\text{yield pressure of the softer material}} .$$

Two conclusions can be arrived at from the above equation. The first is that the s and the p_m, being strength properties of the same material, vary together; and their

ratio is roughly the same for most diverse materials. The second conclusion is that temperature should affect s and p_m much the same, and should not have a marked effect on the coefficient of friction.

The examination of Terzaghi's theory of friction and Bowden and Tabor's adhesion theory of friction make it evident that both the theories are practically the same and originate from the adhesion concept of contacting surfaces. Terzaghi stated his hypothesis in 1925 in his pioneering book on soil mechanics entitled Erdbaumechanik, but his ideas on this subject were overlooked for many years. The hypothesis was independently stated and shown to describe the frictional behavior of a wide variety of materials by Bowden, Tabor and their colleagues late in the 1930's. This is now called the adhesion theory of friction and serves as the starting point for all friction studies.

Influence of surface film

Most surfaces under the normal laboratory conditions are covered with contaminating films and oxide layers and, during sliding, these oxides and surface films will be torn and some metallic contact will occur. The shear strengths of the metallic junction and that of the contaminating film are far different in magnitude. In addition, experiments show that the deliberate addition of a lubricant film reduces the intimacy of contact and the mean strength of

adhesion of the junction. Therefore, we should expect the adhesion and shear strength of contaminated surfaces to be less than that of pure surfaces.

Let ρ be the fraction of the area of contact over which metallic contact occurs, and let s_1, s_2 be the shear strengths of metallic and contaminated junctions. Then the force of friction F is equal to

$$F = A_c\rho s_1 + A_c(1-\rho)s_2$$
$$= A_c[\rho s_1 + (1-\rho)s_2]$$

Influence of removal of normal load

Terzaghi (1960) believes that when cohesion exceeds adhesion, even by a small amount, the joint between contacting surfaces will open up during unloading because of elastic stresses, and the true contact area will almost approach zero.

Bowden and Tabor (1954) agree to the fact that when the load is reduced there is a relaxation of elastic stresses in the contacting surfaces, and they separate according to the laws of elastic deformation. In the case of harder metals and contaminated surfaces, these deformations are sufficient to break junctions, thus decreasing the area of contact.

Influence of dust particles

Metal surfaces are generally rough on an atomic scale. When they are placed together, they first make contact at the

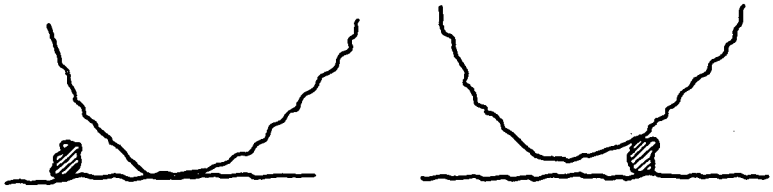

tips of the most prominent projections. With metal exposed to the atmosphere, one type of projection that may be important is dust particles. The dust particle does not shield an area of surface equal only to its own cross-sectional area. Its region of influence is much larger for geometric reasons (see the above figure), since if it supports the edge of the conical tip it will still prevent contact.

Friction of Rock

Frictional effects are of importance in rock mechanics mainly in two connections: first, on a very small scale, between the surfaces of minute Griffith cracks (minute internal and surface flaws, stress concentration at their ends cause failure); and second, on a large scale, between the surfaces of joints or fracture planes. In the latter case, the surfaces in question may be new surfaces or joints on which no sliding has occurred, or they may be old surfaces or faults on which considerable sliding has already taken place.

The adhesion theory of friction has proven experimentally satisfactory for metals; but it is of doubtful validity

for rocks and minerals due to the fact that minerals tend to fail by brittle fracture rather than by plastic flow, and the cold welding hypothesis for metal may not be true for minerals. However, the concept of contact at a limited number of asperities should be true.

Byerlee (1967), using a truncated cone as a model asperity and with the assumption that it fails by tensile fracture, came to the conclusion that Amonton's law holds for a single asperity with a small coefficient of friction (0.1); but higher coefficients of friction may be attributed to the interlocking of asperities.

Apart from the above microscopic effects, the extended surfaces which occur in practical rock mechanics are probably very irregular; and the effects of ploughing and irregular sliding should not be ruled out.

Murrell (1965) found that a simple law, as given below, gave a better fit to his experimental results over a wide range of σ.

$$\tau = \mu_o \sigma^{m_o}$$

where μ_o and m_o are constants, σ is the normal stress across the surfaces in contact, and τ is the shear stress across them necessary to initiate sliding.

Jaeger (1959) found a very good agreement of his experimental results, particularly at low stresses, with the linear

law

$$\tau = s_o + \mu\sigma$$

where s_o and μ are constants.

Bowden (1954) and his coworker made some experiments on minerals. In the case of rock salt, it appeared that there was considerable fragmentation of the surface, both on a crystalline and on a microcrystalline scale. For diamond on diamond, it was found that the frictional force is proportional to $W^{2/3}$, suggesting that only elastic deformation is involved.

Bowden and Tabor (1954, 1964) report very large effects due to surface contamination: for example, for freshly cleaved mica, the coefficient of friction is of the order 1; for a surface which has become contaminated by exposure, the coefficient of friction falls to 0.3; while for a surface which has been outgassed in a vacuum, it may rise as high as 35. These results suggest that the coefficient of friction may be very high in newly opened Griffith cracks.

Horn and Deere (1962) and Penman (1953), while using small contacts of single mineral, demonstrated an important effect of wetting the surfaces; in some cases, for example quartz, the coefficient of friction is raised, while in others, e.g. biotite, it is lowered.

Byerlee (1967), by using larger specimens (2 cm^2 area) of various minerals sliding on sapphire, found an increase of coefficient of friction from 0.1 to 0.4 with increasing

roughness of the sapphire surface.

Patton (1966), Ripley and Lee (1961), and Coulson (1970) studied the macro-irregularities in more detail and came to the conclusion that

$$\tau = \sigma \tan(\theta+\phi)$$

where θ is the inclination of the slope in the direction of τ.

Drennon and Handy (1972), in their investigation of stick-slip of lightly loaded limestone at various conditions of loading, concluded that smooth slip at room temperature does involve asperity-to-asperity bonding, but through a film of adsorbed water having an activation energy as -5 to -10 Kcal/mole for liquid water. Above 100°C, the activation energy sharply increased, indicative of more direct bonding, and the stick-slip became the dominant mode of deformation, with the development of asperity fracture debris. Higher normal loads also favored stick-slip at room temperature, apparently through perforation of the adsorbed water layer. The introduction of debris reduced this tendency, indicating that debris increased the true contact area and again allowed sliding on the adsorbed water film. However, debris, either added or generated as a result of asperity fracturing during slip, increased the coefficient of friction, indicating that the larger true contact areas — even with lowering bond energy due to adsorbed water — had a greater resistance to shear

than did the accumulated smaller contact areas which perforated the adsorbed water films. If their interpretation is correct, this effect should diminish at higher loads as the area of direct contact increases.

Friction of a Dilatant Mass

The internal friction of a soil or of any dilatant mass, thus, is considered to be comprised of two components: sliding friction, and dilatancy or "interlocking". Interlocking has also been recognized by later workers in metals. At the present stage of knowledge, it can be said that Reynolds' dilatancy theory superimposed on the adhesion theory of friction can roughly formulate the friction theory of dilatant masses. If F_d is the force of friction due to dilatancy (see the following page) and F_a is that due to adhesion, then F, the force of friction of the dilatant mass, is given by

$$\begin{aligned} F &= F_d + F_a \\ &= W \tan\phi + K W \\ &= W(K + \tan\phi) \\ \frac{F}{W} &= (K + \tan\phi) \end{aligned}$$

where $\frac{F}{W}$ can be called the coefficient of friction of dilatant masses, K is a constant reflective of adhesion friction, and ϕ is the angle of sliding friction.

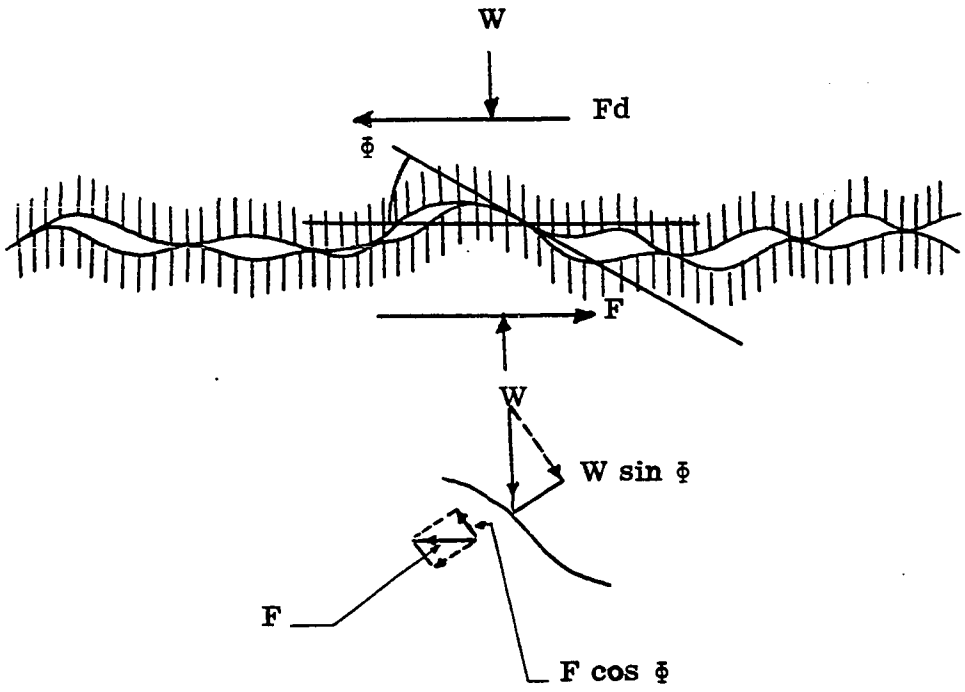

$$Fd \cos \Phi = W \sin \Phi$$

$$Fd = W \frac{\sin \Phi}{\cos \Phi} = W \tan \Phi$$

Dilatancy Theory (Top)

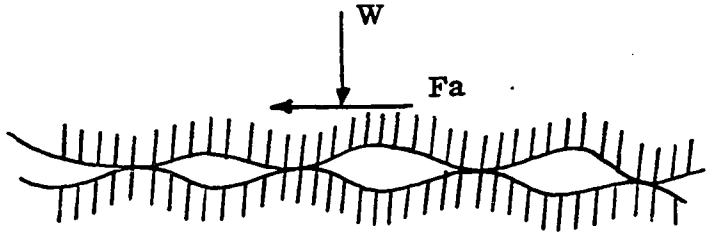

Actual contact area, $Ac = K_1 W$

Adhesion friction, $Fa = K_2 Ac = KW$

Adhesion Theory of friction (bottom)

Energy Theory of Dilatant Mass

Reynolds' energy concept

Taylor (1948) is usually credited with being the first to attempt separation of two components of friction of dilatant masses by evaluating the work done by dilatant expansion in direct shear against the normal pressure; but it seems that Reynolds (1885) had a similar energy concept in mind and which he applied to granular masses, only with the difference that he neglected friction. He said,

> If the particles were rigid the medium would be absolutely without resilience and hence the only energy of which it would be susceptible would be kinetic energy, so that, supposing the motion slow, the work done upon any group in distorting it would be zero. Thus, supposing contraction in one direction and expansion at right angles, then if px be the stress in the direction of contraction, and py, pz the stress at right angles, a being contraction, b and c expansion,
>
> $$px\ a + py\ b + pz\ c = 0$$
>
> or supposing $b = c$, $py = pz$
>
> $$px\ a + py(a+c) = 0$$
>
> with friction the relation will be different; the friction always opposes strain, i.e. tends to give stability.

Taylor energy theory

Let σ_n be the normal stress, τ the shear stress, τ_d that portion of shearing stress which acts to supply the energy of expansion or shear stress necessary to cause the sample to dilate against the normal stress, δ_Δ the incremental displacement in direct shear test in the direction of

shearing force, and δ_v the incremental volume per unit area which is incremental displacement in the direction of the normal stress. Then

Work done against normal stress

= Work done by τ_d in moving through δ_Δ

$$\sigma_n \, \delta_v = \tau_d \, \delta_\Delta$$

$$\frac{\tau_d}{\sigma_n} = \frac{\delta_v}{\delta_\Delta}$$

shearing strength contribution by friction = $\tau - \tau_d$

$$\frac{\tau - \tau_d}{\sigma_n} = \frac{\tau}{\sigma_n} - \frac{\tau_d}{\sigma_n} = \tan(\text{angle of internal friction})$$

$$= \tan \phi_r$$

$$\frac{\tau}{\sigma_n} = \tan \phi_r + \frac{\tau_d}{\sigma_n}$$

$$\tan \phi_{max} = \tan \phi_r + \frac{\delta_v}{\sigma_\Delta}$$

where ϕ_{max} is the angle of friction of the granular mass and ϕ_r is the internal coefficient of friction.

The above energy equation was later adapted to the triaxial test by Skempton and Bishop (1950).

Let σ_1, σ_2, σ_3 and $d\varepsilon_1$, $d\varepsilon_2$, $d\varepsilon_3$ be major, intermediate and minor principal stresses and corresponding incremental strains, respectively; dW_f, the incremental work done by friction and cohesion; dv, the incremental volume change per unit volume. As $\sigma_2 = \sigma_3$ in the triaxial test, then

Work done during a small increment of strain $d\varepsilon_1$ at failure

= work done against friction and cohesion

+ work done against σ_3 by dilating sample

or

$$\sigma_1 \, d\varepsilon_1 = dW_f + \sigma_3 (d\varepsilon_2 + d\varepsilon_3).$$

But

$$dv = d\varepsilon_1 + d\varepsilon_2 + d\varepsilon_3 .$$

Here, $d\varepsilon_2$ and $d\varepsilon_3$ are extension strain increments and $d\varepsilon_1$ is the compression strain increment. Therefore,

$$d\varepsilon_2 + d\varepsilon_2 = dv + d\varepsilon_1$$

$$\sigma_1 \, d\varepsilon_1 = dW_f + \sigma_3 (dv + d\varepsilon_1)$$

$$d\varepsilon_1 (\sigma_1 - \sigma_3) = dW_f + \sigma_3 \, dv$$

$$(\sigma_1 - \sigma_3) = \frac{dW_f}{d\varepsilon_1} + \sigma_3 \frac{dv}{d\varepsilon_1}$$

The portion of the strength which can be associated with volume change is, therefore, equal to $\sigma_3 \frac{dv}{d\varepsilon_1}$. Bishop further developed the above equation in the form

$$\tan^2(45 + \tfrac{1}{2} \phi_r) = \left(\frac{\sigma_1}{\sigma_3}\right)_r = \left(\frac{\sigma_1}{\sigma_3}\right)_{max} - \sigma_3 \frac{dv}{d\varepsilon_1}$$

where ϕ_r and $\left(\frac{\sigma_1}{\sigma_3}\right)_r$ are residual angle and stress ratio, respectively.

Newland and Allely Theory

Newland and Allely (1957) considered that the direction of sliding of one particle relative to another is, in

general, inclined at an angle to the direction of the applied shear stress. By resolving forces and displacements of particles parallel and perpendicular to their sliding surfaces, they arrived at the following expression for the direct shear test.

$$\frac{\tau_{max}}{\sigma_n} = \tan(\phi_f + \theta)$$

$$\left(\frac{\delta_v}{\delta_\Delta}\right)_{max} = \tan\theta$$

$$\frac{\tau'_R}{\sigma_n} = \tan\phi_f$$

where θ is the angle of sliding surface with the direction of shear stress; ϕ_f is the angle of internal friction, which accounts for the influence of not only the coefficient of sliding friction, but also of the mode of failure; τ'_R is the stress required to overcome frictional force, assuming sliding planes are parallel to the direction of the shear stress; σ_n is the normal stress; and $\frac{\delta_v}{\delta_\Delta}$ is the rate of volume expansion.

They suggested that using experimental values of $\frac{\tau_{max}}{\sigma_n}$ and $\left(\frac{\delta_v}{\delta_\Delta}\right)_{max}$ in the above equations, τ'_R can be obtained. τ'_R, in turn, can be compared to experimental residual stress τ_R.

Newland and Allely extended their analysis to the triaxial test and obtained the following expressions:

$$\frac{\sigma_{1_{max}}}{\sigma_3} = \tan^2(45 + \frac{\phi f}{2} + \frac{\theta}{2})$$

$$\frac{\delta\nu}{\delta v} = \frac{\tan\alpha - \tan(\alpha - \theta)}{\tan(\alpha-\theta)}$$

or

$$\tan\theta = \frac{\frac{\sigma_{1_{max}}}{\sigma_3}\ (\frac{\delta\nu}{\delta v})_{max}}{\{1 + \frac{\sigma_{1_{max}}}{\sigma_3} + (\frac{\delta\nu}{\delta v})_{max}\}}$$

$$\frac{\sigma'_R}{\sigma_3} = \tan^2(45 + \frac{\phi f}{2})$$

where σ_3 is the chamber pressure, $\sigma_{1_{max}}$ is the maximum (or peak) axial stress, and σ'_R is that part of $\sigma_{1_{max}}$ required to mobilize the frictional resistance assuming $\theta = 0$. Again, the experimental value of $\frac{\sigma_{1_{max}}}{\sigma_3}$ and $(\frac{\delta\nu}{\delta v})_{max}$ will give θ, ϕ_f and σ'_R which, in turn, can be compared to its corresponding experimental values.

Newland and Allely compared their equation with that of Taylor and Bishop, and considered that the difference between the energy approach method and their method lies in the tacit assumption that the work done in overcoming δWf is the same at both the peak and the residual states; whereas, according to their theory, the shear stress has a component normal to the plane of sliding which contributes to frictional strength but which decreases in magnitude as expansion occurs. In other words, the work done in overcoming frictional forces is

greater at the point of maximum shear stress than at residual stress state.

Caquot (1934) derived the following expression relating angle of friction at constant volume ϕ_{cv} and true angle of friction ϕ_u between mineral surfaces:

$$\tan\phi_{cv} = \frac{1}{2}\pi \tan\phi_u$$

Bishop (1954) also developed an approximate solution in the form

$$\sin\phi_{cv} = \frac{15 \tan\phi_u}{10 + 3 \tan\phi_u}$$

While the precise validity of these equations is doubtful, the experimental values fit the above equations closely.

Rennie (1959) studied the least stress ratio which will cause failure in a close-packed face-centered packing and obtained the approximate solution

$$\frac{\sigma_1}{\sigma_3} = 2 + 2\sqrt{6}\ u + (\text{higher terms in } u)$$

Thurston and Deresiewicz (1959) also considered a face-centered array of equal spheres with $\sigma_2 = \sigma_3$ and arrived at the following expression:

$$\frac{\sigma_1}{\sigma_3} = \frac{\sqrt{6} + 8u}{\sqrt{6} + 4u}$$

where u is a coefficient of friction.

Rowe "Stress-Dilatancy" Theory

Rowe considered, experimentally and theoretically, the behavior of assemblies of cohesionless, uniform rods in a parallel stack and spherical particles of uniform size, arranged initially in regular arrays. The assemblies of particles are subjected to axially symmetrical state of stress. From his analysis based on a consideration of the forces between particles, he arrived at the following findings for regular packing.

1. Whatever the geometrical arrangement of solids, the stress ratio at the peak strength and during subsequent states of deformation follows the law

$$\frac{\sigma_1}{\sigma_3} = \tan\alpha \tan(\phi_u + \beta).$$

2. The energy ratio $\dot{E}$ for a fixed orientation of particle movement is given by the expression

$$\dot{E} = \frac{\tan(\phi_u + \beta)}{\tan\beta} = \frac{\sigma_1}{\sigma_3 (1 + \frac{\dot{dv}}{v\dot{\varepsilon}_1})}$$

3. Slip occurs well past the peak stress ratio at failure, thus establishing that the slip plane is not the cause but the result of failure.

In the above findings, α is the angle which the imaginary plane of particle interlocking makes with the direction of the minor principal stress, β is the angle of deviation

of the tangent at the contact point from the direction of major principal stress, and ϕ_u is the angle of sliding friction.

Rowe extended his analysis to a random mass of irregular particles by suggesting that the form of law which applies to any individual packing may be expected to apply to mixture of packings. He observed that the angle α, characteristic of the particular packing arrangement, disappeared in the expression for $\dot{E}$; thus, he concluded that the energy equation applies to random assemblages of particles, as well as to regular arrays. Since in random, the values of β vary initially throughout the mass, the angle of sliding must also be determined. He then shows that there exists a critical angle of β [namely, $\beta = (\frac{1}{4}\pi - \frac{1}{2}\phi_u)$] which makes $\dot{E}$ a minimum, and transforms the energy ratio equation into

$$\dot{E} = \tan^2(\frac{\pi}{4} + \frac{1}{2}\phi_u) = \frac{\sigma_1}{\sigma_3\,(1 + \frac{\dot{dv}}{v_{\dot{\varepsilon}_1}})}$$

Departure from the stress dilatancy behavior given by the energy ratio equation is explained by Rowe in terms of a process he refers to as rearranging. In a loose sand, and in an initially dense sand when it reaches a point near the maximum stress ratio $\frac{\sigma_1}{\sigma_3}$, the length of the individual slide paths of one particle over another becomes appreciable with respect to the dimensions of the particles; hence, according to Rowe, sliding is no longer restricted to a value of β

which gives the minimum rate of expenditure of energy in internal friction. The effective value of ϕ_u then becomes ϕ_f, where $\phi_f > \phi_u$.

At the ultimate state of deformation when the sample reaches the stage at zero rate of volume change, the effective value of ϕ_u at this ultimate constant volume condition, denoted by ϕ_{cv}, is obtained from the equation $\frac{\sigma_1}{\sigma_3} = \tan^2(\frac{1}{4}\pi + \frac{1}{2}\phi_{cv})$, by using the observed stress ratio.

Rowe (1963) applied the stress dilatancy theory to the stability of earth masses behind retaining walls, in slopes, and in foundations.

The stress dilatancy theory of granular masses postulated by Rowe was discussed by Scott et al. (1964), Gibson and Morgenstern (Trollope et al., 1963), Scott (1963), and Trollope et al. (1963). Their main criticism was directed towards:

1. the assumed mechanism of deformation,
2. the assumed absence of rolling,
3. the assumption that the energy ratio $\dot{E}$ is minimum in a random assembly, and
4. the significance of the α-plane.

Horne confirmation

A more general derivation was presented by Horne (1965) who did not restrict his analysis to ideal packing. He obtained exactly similar results to that of Rowe and, thus,

substantiated his theory. Horne built up his analysis on the basis of the following hypotheses:

1. The assembly consists of rotund, rigid, cohesionless particles with a constant coefficient of sliding friction. Elastic and plastic deformation, crushing, and cracking are all ignored.
2. Deformation occurs as a result of relative motion between groups of particles. Motion is not facilitated by the presence of individual particles acting as rollers between groups.

Horne obtained the expression for the energy ratio $\dot{E}$ by writing a virtual work equation for the input $\sigma_1\dot{\varepsilon}_1$. Then he minimized this ratio to obtain a value of $\beta_c = 45 - \frac{1}{2}\phi_u$ which then led to

$$\dot{E} = \frac{\sigma_1\dot{\varepsilon}_1}{\sigma_2\dot{\varepsilon}_2 + \sigma_3\dot{\varepsilon}_3} = \tan^2(45 + \frac{1}{2}\phi_u)$$

For the triaxial compression test with $\sigma_2 = \sigma_3$ and $\dot{\varepsilon}_2 = \dot{\varepsilon}_3$, this reduces to Rowe's equation. Horne thus established the limitation of the stress dilatancy theory and concluded that the equation of energy ratio $\dot{E}$ that provides a relationship between work quantities $\sigma_1\dot{\varepsilon}_1$, $\sigma_2\dot{\varepsilon}_2$ and $\sigma_3\dot{\varepsilon}_3$ does not provide a relationship between stress and strain rates separately. He also concluded that the relationship may not apply to a highly compacted assembly with a high degree of interlocking.

Tinoco and Handy Theory

Tinoco and Handy (1967) considered a random particle assemblage and the possibilities for either sliding or rolling. They demonstrated that sliding occurs at contacts where the angle of inclination β is maximized, whereupon

$$\frac{\sigma_1}{\sigma_3} = \frac{1 + \sin\phi_s}{1 - \sin\phi_s} = \tan^2(45 + \frac{\phi_s}{2})$$

which is identical to the empirical Mohr-Coulomb theory. Next, considering the work of volume change, they derived an equation for principal stresses due to friction. In simplified form,

$$\frac{\sigma_1}{\sigma_3} = (1 + \frac{\delta v}{\delta \varepsilon_1}) = \Omega_{TC} + [\frac{\sigma_1}{\sigma_3} + (1 + \frac{\delta v}{\delta \varepsilon_1})]\sin\phi_s$$

where ϕ_s is the angle of sliding friction, $\frac{\delta v}{\delta \varepsilon_1}$ is the unit volume change per unit axial strain, and Ω_{TC} is a dimensionless constant.

For the triaxial compression test, they arrived at the expression

$$\Omega_{TC} = [(\frac{\sigma_1}{\sigma_3} - 1)(1 - \sin\phi_s)]\frac{\delta \varepsilon_{1D}}{\delta \varepsilon_1}$$

where $\frac{\delta \varepsilon_{1D}}{\delta \varepsilon_1}$ is the axial unit strain contributing to volume change. The equation was tested by plotting $\frac{\sigma_1}{\sigma_3} + (1 + \frac{\delta v}{\delta \varepsilon_1})$ versus $\frac{\sigma_1}{\sigma_3} + (1 + \frac{\delta v}{\delta \varepsilon_1})$ which should give a straight line of slope $\arctan \sin\phi$ and an intercept of Ω. All the graphs showed linear portions with slopes consistent with

mineralogical composition, suggesting establishment of an equilibrium interlocking parameter Ω prior to dilation. After dilatant expansion, a new line is sometimes established at a lower Ω but still with the same slope, further supporting that this gives an independent measurement of sliding friction. From the plots it becomes evident that if the coefficient of sliding friction is constant, then the interlocking function Ω first increases with increasing strain, indicating compaction, and then decreases upon dilation and failure.

MEASUREMENT OF COEFFICIENT OF SLIDING FRICTION

Since modern friction theory applied to granular systems separates dilatancy and sliding friction components, an independent investigation was made to evaluate sliding friction between individual rods used in the experiments. The friction test apparatus and method finally used are those of Shyam Bahadur (1970). A brief description follows; for a more complete description, see Shyam Bahadur (1970).

Principle

The principle involved in the design of the friction apparatus was to achieve a sliding motion between two specimens at different speeds, and to measure the friction force developed between the sliding surfaces. The machine has a disc rotated by a reduction system of gearing from a reversible drive motor. A flat friction specimen is attached by screws to the top of this disc. The other specimen, which is in the shape of an indentor, is secured in a head at the end of the cantilever beam.

The indentor is loaded through an L beam (Fig. 1) by means of a loading string and pulley. When the indentor is loaded, it presses on the flat specimen and the force of friction causes the cantilever to deflect laterally. The displacement (in terms of thickness of air gap) of the cantilever beam is measured by a sensing element and, by means of a previous calibration, the frictional force is recorded.

Figure 1. Sliding type friction test apparatus; (a) section, (b) plan, (c) modeling two sliding rods

1. Indentor
2. Cantilever beam or horizontal leg of L beam
3. Sensing device
4. Loading string
5. Pulley
6. Dead load
7. Aluminum holding disc
8. Flat specimen
9. Revolving disc
10. Reduction gears
11. 1/3 h.p. motor
12. Air gap
13. Vertical leg of L beam
14. Bearing fixed to the main frame
15. Arrow showing direction of motion of revolving disc
16. A parallel bar to hold the transducer
17. Horizontal member
18. Indentor head

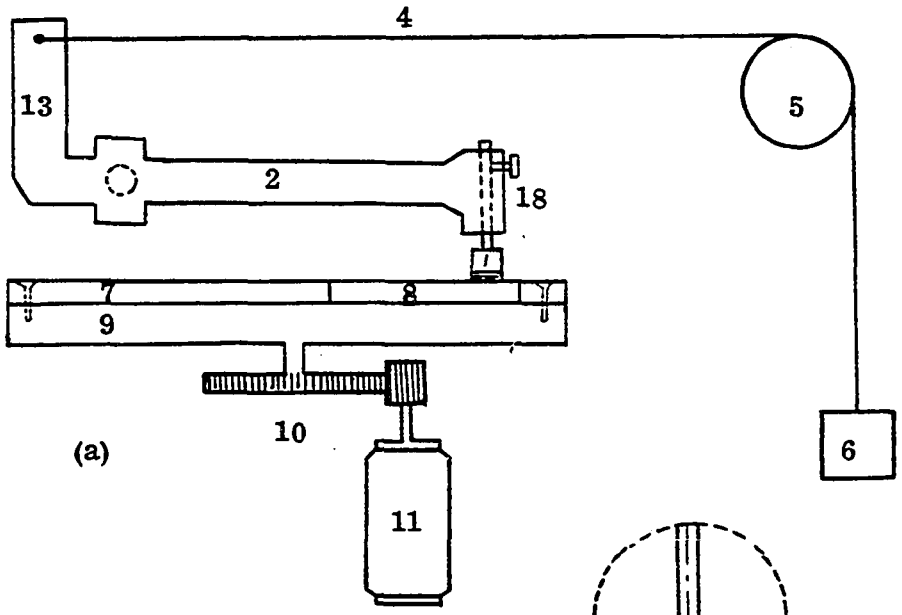

(a)

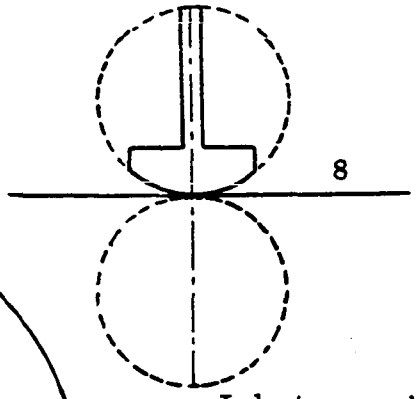

Indentor as viewed from right.

(c)

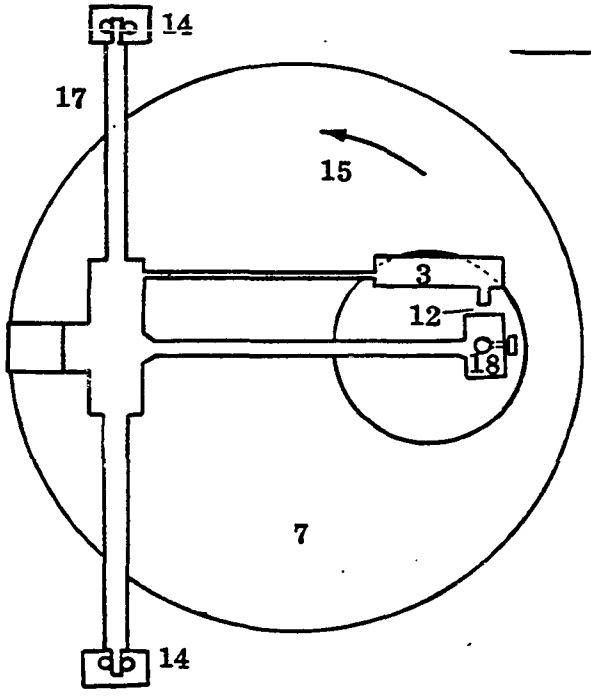

(b)

The flat specimen can be rotated at any desired speed. Arrangement is also provided to measure friction on various tracks on the flat specimen.

The lever arm of this loading system is designed such that a suspended load of 200 gm. can load the specimen with 875 gm. The L-beam is machined from a single steel block and the horizontal leg is slender enough for appreciable deflection in the horizontal plane, but is relatively stiff in the vertical plane. The L-beam is supported by a horizontal axle which allows rotation in a vertical plane. A parallel bar carrying an induction transducer on one end is fixed rigidly to the horizontal axle at the other end and creates an air gap in the indentor head. The cantilever is calibrated in such a way that the frictional force is read directly from the change in resistance of the air gap.

Specimen Preparation

As our rods have a maximum diameter of 1", a flat specimen in the shape of a disc of 2-7/8" diameter and 1/8" thickness could not be obtained. To overcome this difficulty, a disc of 1" diameter and 1/8" thickness was cut out of a 1" diameter rod. This 1" diameter disc was pressed 1/4" away from the edge into a 2-7/8" diameter and 1/8" thick aluminum disc. The surface of the assembly of the aluminum disc and steel disc was machine polished. The indentor was cut from a 1" diameter rod into a shape of a T, in such a way that the

outer face of the horizontal leg of the T has the radius of curvature of the original cylindrical surface, which is 1/2" in the case of the 1" diameter rods.

Test Procedure

The flat specimen and the indentor were cleaned with methyl alcohol and were kept in a desiccator. After drying, the flat specimen is mounted on the revolving disc with screws in such a way that the 1" diameter steel disc pressed into the larger aluminum disc was very nearly under the indentor head. The indentor was held to the head in such a manner that it can model the sliding between two parallel rods. Care was taken to switch on all the electrical and electronic devices at least half an hour before the start of the test to stabilize the working of all the components. The test was started by turning the revolving disc at the desired speed of 0.001" per minute, the force of friction being observed at regular intervals. Two calibration readings were taken for each test — one before and the other after the test. After observing the force of friction for a few times with a particular normal load, the normal load was changed quite a number of times during the same test to enable plotting a graph of the coefficient of friction versus normal load.

Test Results

Table 1 gives the experimental values of the frictional force F_r in gms. and the coefficient of friction f for

Table 1. Variation of coefficient of sliding friction with normal load in the case of 1"-diameter rods

Normal load, W (gms)	Friction force, Fr (gms)	Coefficient of friction, f
283.7	54.990	.1938
	51.324	.1809
371.6	71.487	.1924
	76.986	.2072
459.5	91.650	.1995
574.4	106.314	.1942
	109.980	.2009
635.3	114.563	.1803
723.2	128.310	.1774
	131.976	.1825
811.1	146.640	.1808
	164.970	.2034
899.0	174.135	.1937
	183.300	.2034

Table 2. Variation of coefficient of sliding friction with normal load in the case of teflon rods

Normal load, W (gms)	Friction force, Fr (gms)	Coefficient of friction, f
1758	1.0	0.0153
	1.1	0.0168
3330	1.9	0.0156
	2.0	0.0164
	1.9	0.0160
4901	2.0	0.0112
	2.2	0.0123
	2.1	0.0117

various normal loads W in gms. A curve of coefficient of friction versus normal load in Kg is given in Fig. 1d. An examination of the curve indiates that the sliding coefficient friction is about equal to 0.2 for 1"-diameter steel rods.

Table 2 gives similar experimental values for teflon. An examination of Table 2 indicates that the coefficient of friction for teflon is approximately one-tenth of that of steel and lies between 0.01 and 0.02.

Scanning Electronic Microscope Photographs

S.E.M. photographs (magnification = 300x) for the surfaces of 1/4" and 1"-diameter rods are shown in Figures 1e and 1f. An examination of the photographs shows that even on a macroscopic scale, the surfaces are rough from point to point.

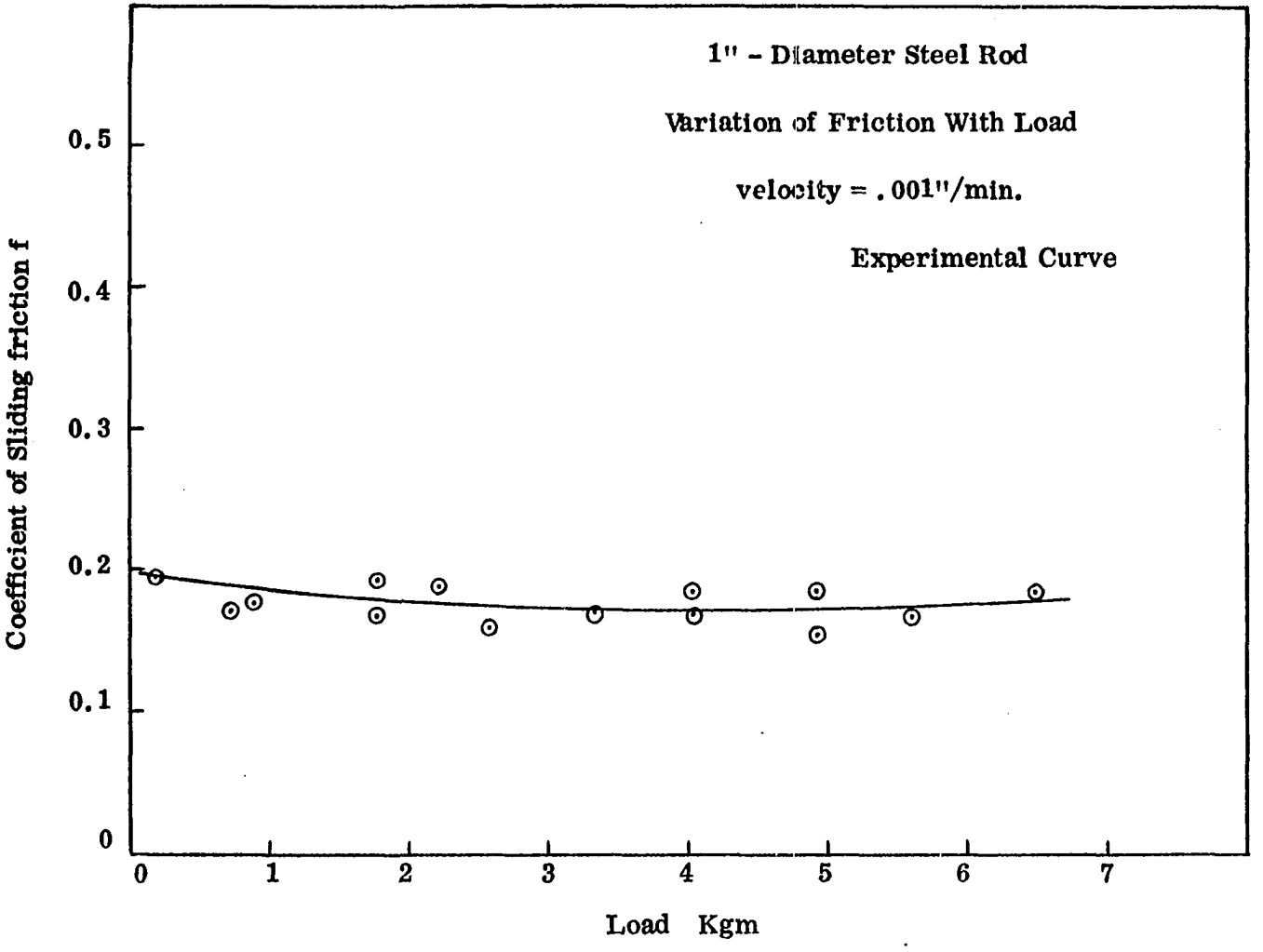

Figure 1 (Continued) (d) variation of friction with load

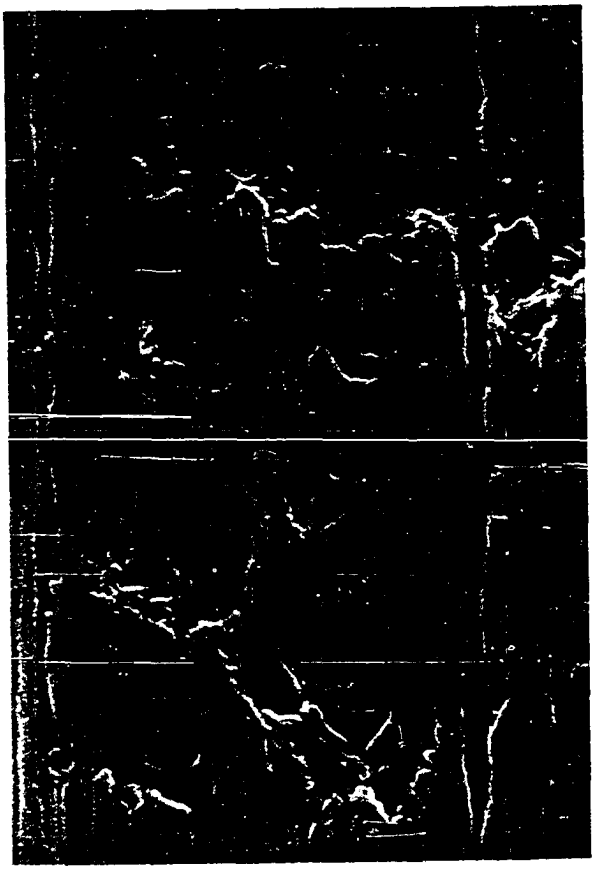

Figure 1 (Continued) (e) scanning electron micrograph — 300x natural size surface of the 1"-diameter rod

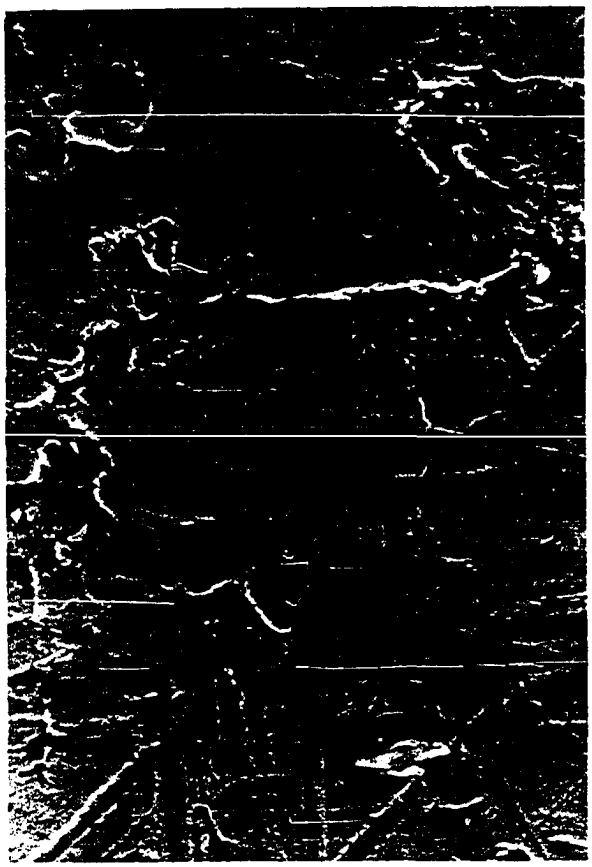

Figure 1 (Continued) (f) scanning electron micrograph — 300x natural size surface of the 1/4"-diameter rod

TEST APPARATUS, SAMPLE PREPARATION, AND TESTING TECHNIQUE

The Biaxial Test Apparatus

Brief description

Briefly, the biaxial load test apparatus which formed the core of the experimental program consists of a horizontal load frame with an included horizontal removable teflon-lined test bed to contain an assemblage of vertical rods. Controllable confining stresses are introduced along the sides of the bed by aluminum plates and pressure cylinders. An axial strain is applied at one end of the test bed by a screw and jack arrangement powered by a 1/6 h.p. motor, the axial force being monitored with a Dillon load cell (Fig. 2). Axial and lateral deformations are measured with 0.001" mechanical dial gages (known as Ames dials), a 35mm camera being used to simultaneously record the dial readings and positions of the test rods after every 0.005" axial strain in the beginning, and 0.010 and 0.020" in the later stages of each experiment. The axial deformation rate is kept constant at 0.00465" per minute with a $\pm$2.5% variation. This gives a strain rate of 0.001% per second with, of course, a $\pm$2.5% variation.

General features

The biaxial test apparatus is a complex set up, consisting of four major systems described later. The basic concept involved in the design of this machine was to deform to

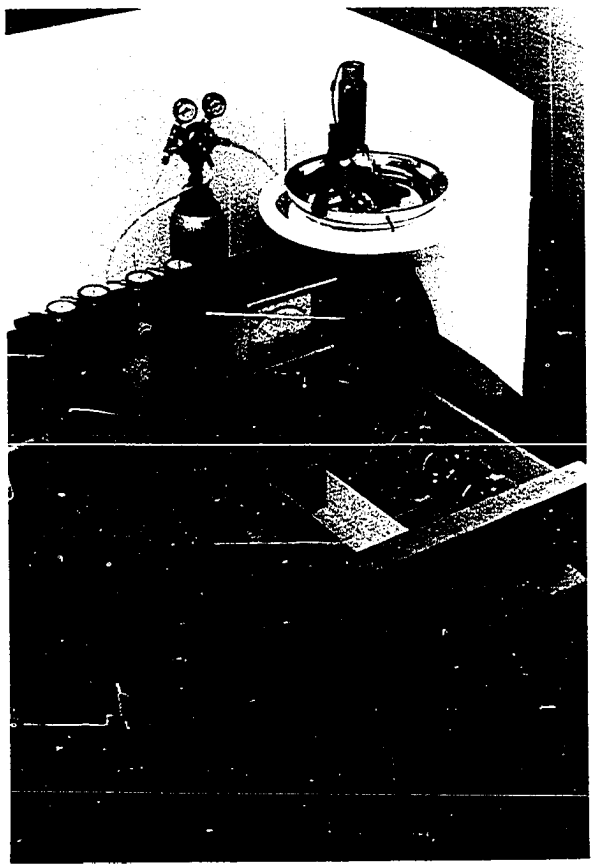

Figure 2. The biaxial test apparatus

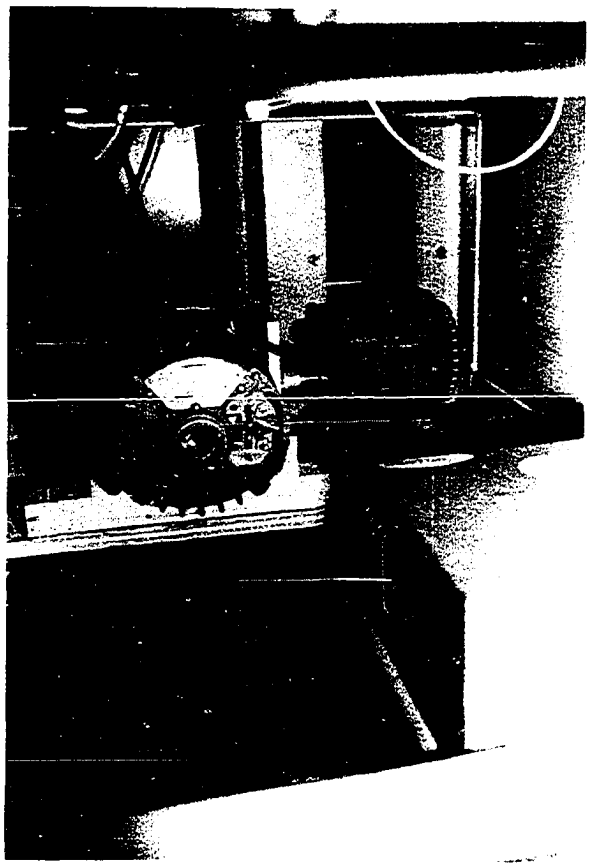

Figure 2 (Continued)

failure an assemblage of rods under constant lateral pressure (σ_3), and to measure the volume changes and axial (σ_1-axis) loads. Axial load is the measurement of resistance offered by the assemblage to the axial (σ_1-axis) deformations. The machine has a collapsible box (Fig. 3) which is 15" long, 5" wide, and 4" high, with an open top and a false bottom. The width of the box can be varied to a reasonable extent so as to accommodate assemblages of rods of different diameters. The rods are made to stand on their ends in a fixed geometrical arrangement. This has been done so as not to introduce a gravity effect (due to self loads of the rods) in the axial direction. Constant lateral stress (σ_3) is applied through a system of pistons with "Bellofram rolling diaphragms" which work with negligible friction under fluid pressure. The axial deformation is applied with a jack driven by a 1/6 h.p. motor through a speed reduction system (Fig. 7). When an axial deformation is applied, the axial and lateral dimensions of the assemblage change. The axial deformation is measured by an Ames dial fixed to the jack. The lateral deformation is measured with a set of four Ames dials mounted on the open face of the collapsible box (Fig. 5). These dials and the plan deformation of the geometry of the rods are photographed at regular time intervals by a camera mounted to look down on the top of the collapsible box (Fig. 6a). Volume changes are calculated from a mathematical formulation using readings of all the Ames dials. The axial

deformation is applied at a constant rate throughout the duration of the experiment. Axial deformations and axial loads are observed manually with the help of an axial Ames dial and a Dillon load cell mounted directly onto the face of the jack. The experiment is performed at room temperature and humidity.

Provision was made to mount seven, instead of four, Ames dials to measure lateral deformations of the collapsible box, with six instead of three side platens on each side of the collapsible box. Provision was also made to work with the box under constant volume. Neither of these features was used in the experiments; in fact, as will be shown, the constant volume arrangement would cause the box to "lock", prohibiting gross axial deformations by preventing dilatant expansion of the assemblage.

Collapsible box

The collapsible box (Fig. 3) consists of three aluminum 5"x4"x1/2" rectangular plates on each side of the box and a bottom plate of teflon 16"x8"x1/4" supported by a plate of steel 16"x8"x1/16". The steel plate rests on a layer of steel ball bearings held separated by an aluminum spacer. These, in turn, rest on an adjustable horizontal rest plate supported by the main frame. With this arrangement, the bottom of the box has three degrees of freedom of motion, namely, axial, lateral and vertical, and may be accurately levelled. Each side plate of the box is connected to four

Figure 3. Collapsible box; (a) plan, (b) cross section

1. Side plates or platens
2. Teflon side plates
3. Swivel joints or ball and socket
4. Fixed plate
5. Movable plate connected to load cell through ball and socket
6. Dillon load cell
7. Pressure unit
8. Steel rods
9. Bottom teflon plate
10. A bottom supporting steel plate
11. Aluminum spacer
12. Horizontal rest plate fixed to the main frame
13. Steel shots
14. Piston rod
15. Piston
16. Bellofram
17. Ball and socket

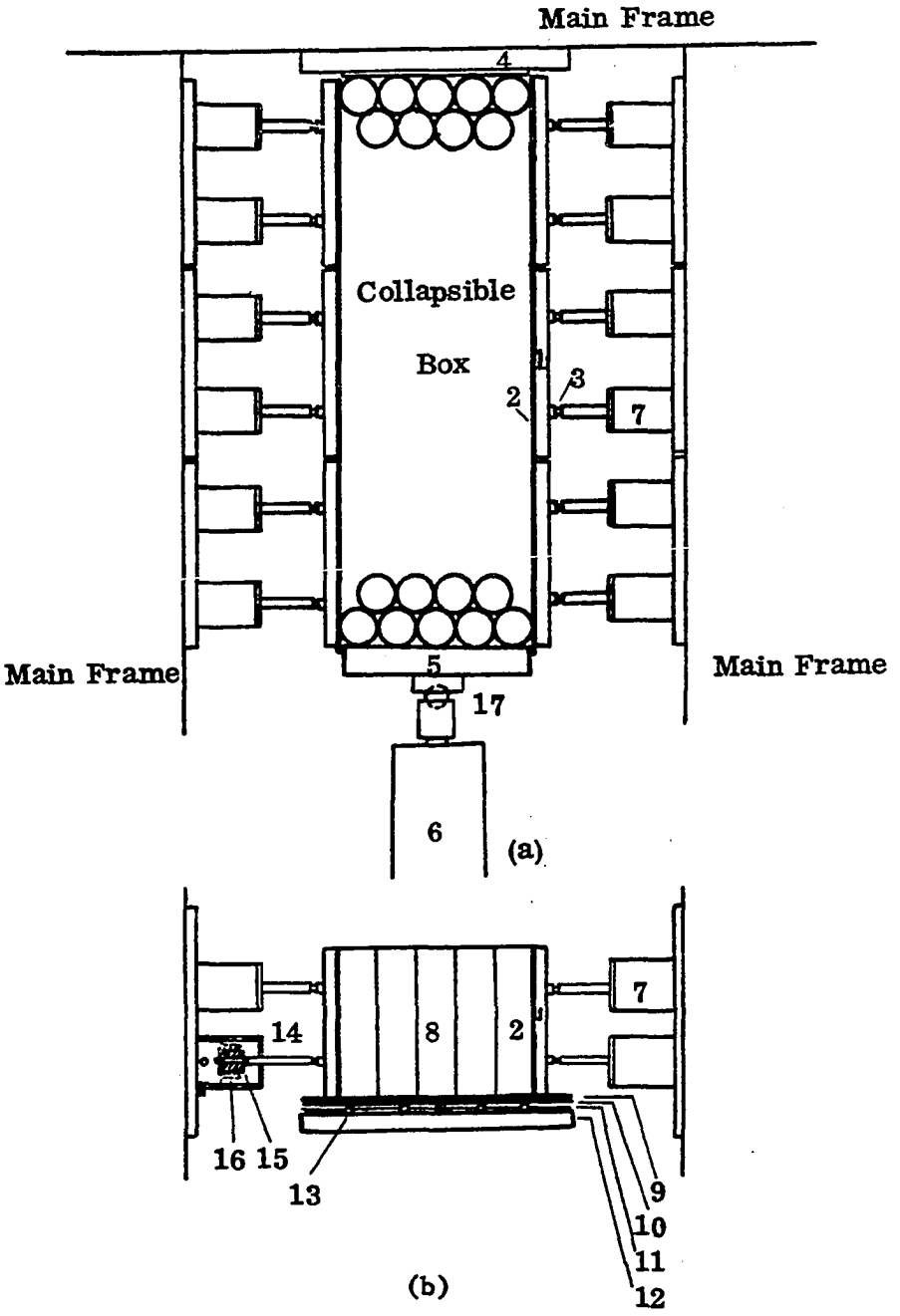

Figure 3. Collapsible box; (a) plan, (b) cross section

pressure units through ball-and-socket joints at the ends of the piston rods to facilitate free rotation of the plate in two directions. One end of the box consists of a 5"x4"x1" steel plate rigidly connected to the main frame, and the other consists of a similar steel plate which is connected to the load cell by a ball-and-socket arrangement.

Lateral stress system

Constant lateral stress is applied through a system of twelve pressure units, four for each plate, on each side of the collapsible box (Fig. 4). Each pressure unit consists of a pressure cylinder and a piston fitted with a "Bellofram rolling diaphragm", used because it is capable of:

1. providing a leak-proof device to convert gas or fluid pressure into a linear stroke,
2. tolerating minor accentricities and cocking of the piston rod and cylinder without affecting the operation of the unit,
3. providing a long stroke within a relatively confined area,
4. responding to small pressure variations because of very low friction and hysteresis, and
5. providing a working pressure area which is constant (within 1%) through its entire range.

All the pressure units on both sides of the collapsible box are connected to the same pressure source. For a low lateral

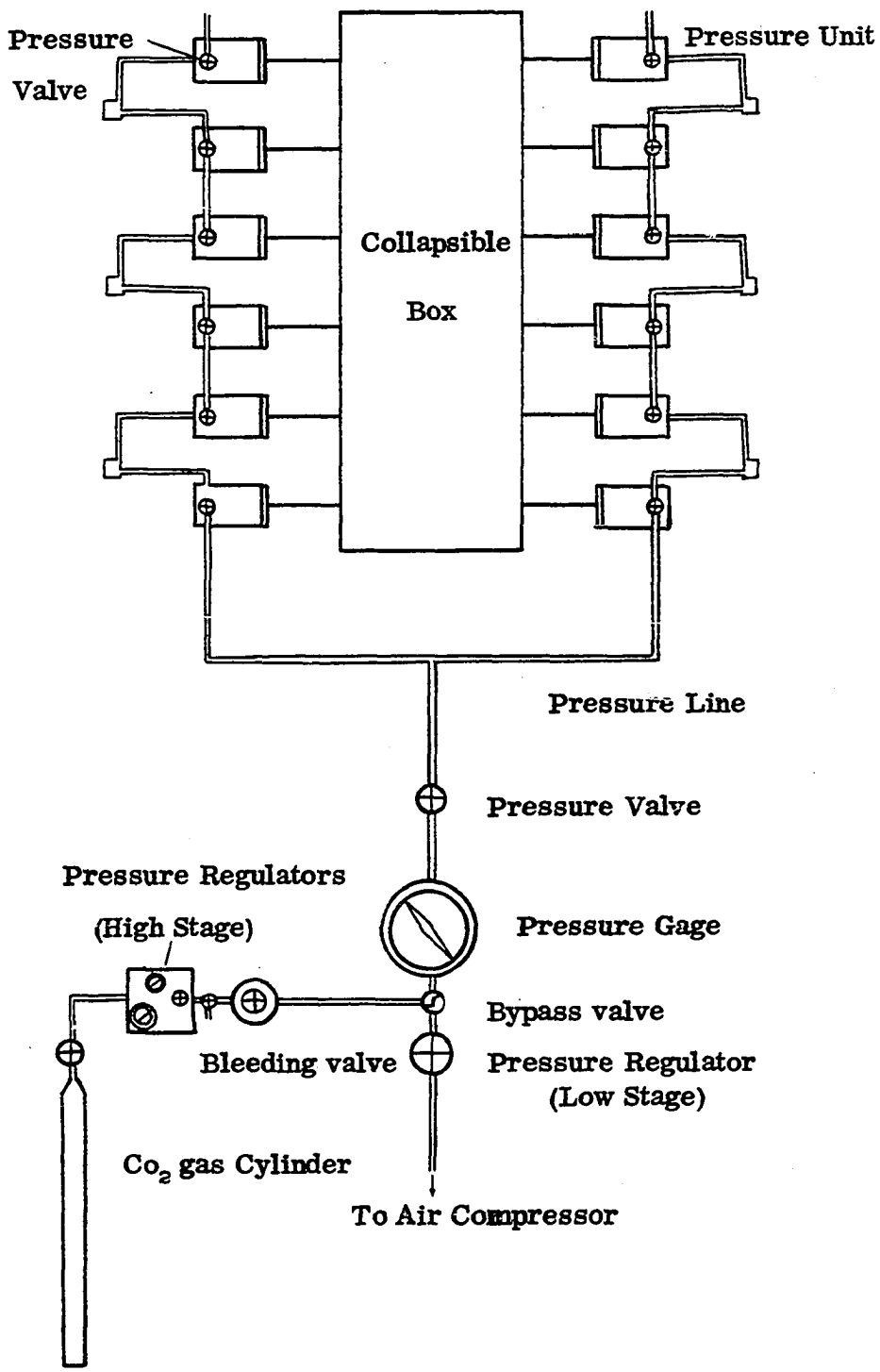

Figure 4. Lateral stress system

pressure, up to 115 psi gage or 30 psi lateral pressure on the assemblage, compressed air is used; whereas, for higher pressures, liquid carbon dioxide (CO_2) is used. Liquid CO_2 is capable of providing a constant pressure of up to 900 psi at room temperature. A maximum gage pressure of 200 psi was used in the present experimentation, dictated by the capacity of Bellofram rolling diaphragms. It has been possible to keep the pressure variations to a maximum of $\pm 1\%$ by the use of precision pressure regulators with operating ranges selected for the different lateral pressures used.

Calibration of Bellofram pressure units

Pressure units were calibrated in sets of two. Each set was subjected to gage pressures from 0 to 280 psi increasing at an interval of 20 psi, and from 280 psi to 0 psi decreasing at intervals of 50 or 20 psi. A previously calibrated proving ring was used to establish the relation between gage pressure and force. The proving ring was calibrated by use of a direct load, varying from 0 to 900 lbs — increasing and decreasing at equal intervals of 100 lbs, on a calibrated platform scale. Calibration of the pressure units was repeated five times for each set to obtain average values. The lateral stress σ_3 and gage pressure was related through the relation

$$\sigma_3 = 0.2552 \text{ (gage pressure)} + 0.7188$$

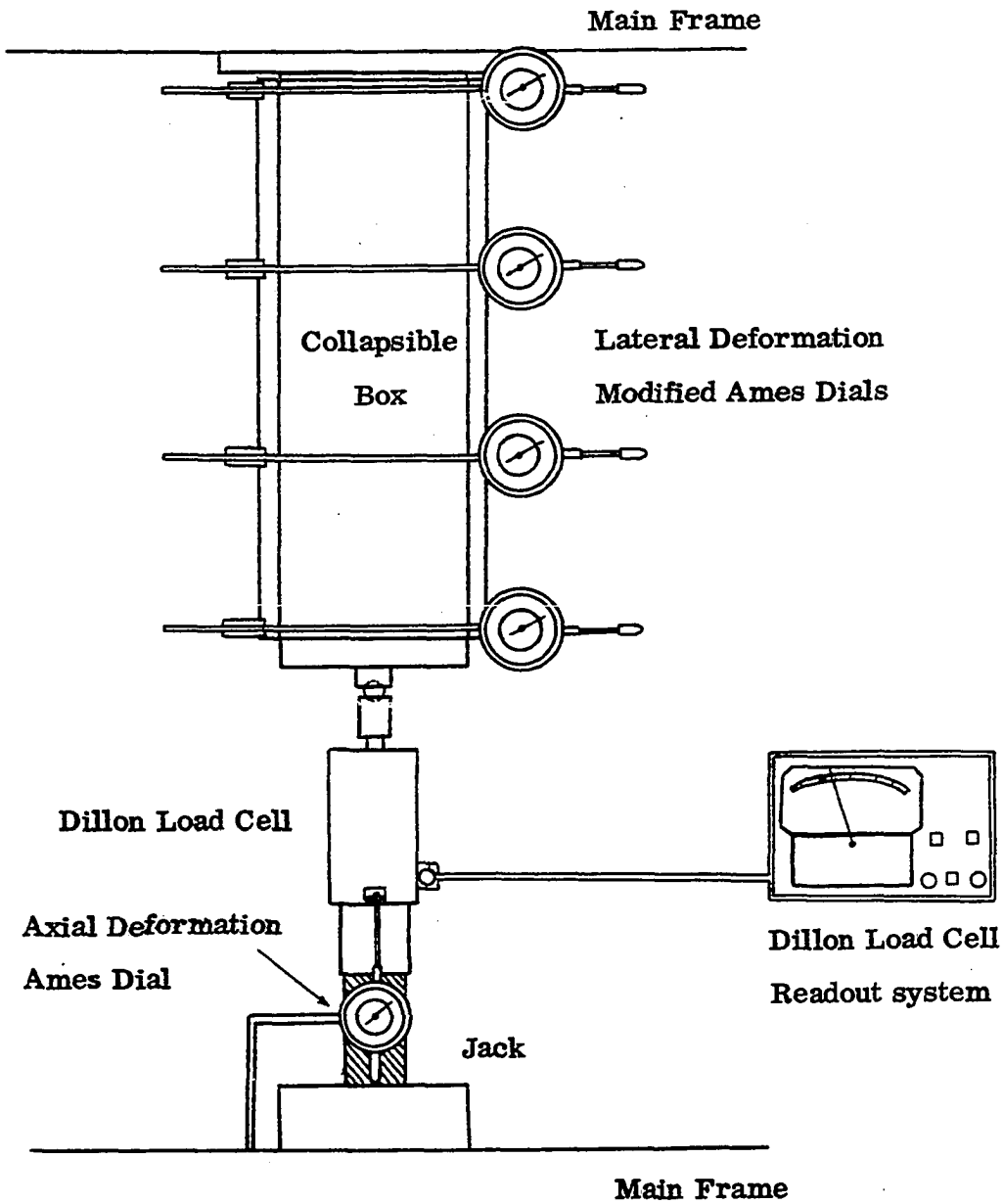

Figure 5. Lateral and axial deformation measurement and the axial load measurement system

or

$$\text{gage pressure} = 3.9185\ \sigma_3 - 2.817.$$

Lateral deformation measurement system

Lateral deformations are measured at four points — two at the ends and two in between along the length of the collapsible box. Ames dials capable of reading to 0.001" with a total range of 1" were used to measure separation of points on two opposite sides of the collapsible box. The dial stems were extended by brass rods of 9" length (Fig. 6b) and 1/8" diameter threaded at both ends. Coupling to the box was by two steel stops, one fixed to the bottom of the dial and the other to the brass rod. The latter stop can be fixed at any position of the rod along its length, thus giving a capability to measure across the collapsible box with variable initial width.

In order to read all four Ames dials simultaneously, along with axial deformations and loads, a photographic arrangement was made at the top of the collapsible box. The arrangement consists of two concentric neon light tubes with a 35mm Kodak f2.8/50mm camera at their center. The camera is capable of rotation in a vertical plane. The assembly of light and the camera (Fig. 6a) is mounted on a horizontal leg and can slide to any position along the leg. The horizontal leg can revolve around a column which, in turn, is fixed to the main frame. The horizontal leg also can revolve

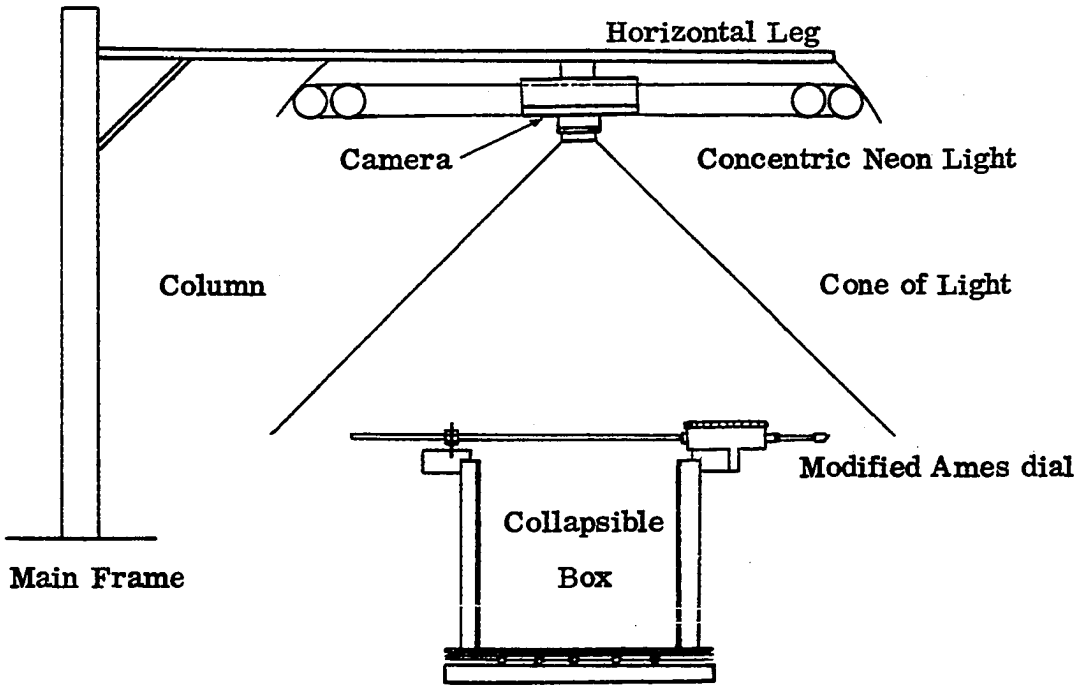

(a)

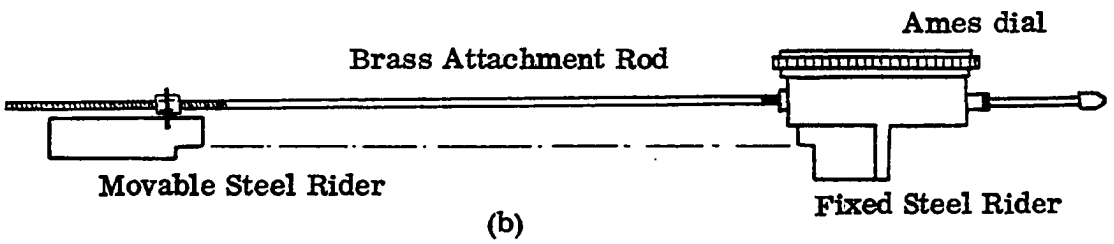

(b)

Figure 6. The biaxial test apparatus; (a) photographic set-up, (b) modified Ames dial

in a horizontal plane and can move up and down against the column. With this arrangement, the camera can be easily focused and the light intensity can be adjusted for good photography. Photographs are made at regular time intervals, allowing all the Ames dials to be recorded, while the plan deformation of the assemblage is photographed, enabling location of the plane or zone of failure and its inclination. This also facilitates the study of translational and rotational movements of each individual rod, made possible by marking lines on the exposed rod ends prior to starting each experiment.

Axial deformation system

The axial deformation system (Fig. 7) consists of a Norton-Duff ten-ton jack driven by an electric motor of 1/6 h.p. through a complex speed reduction arrangement. Application of the axial load is thus strain-controlled.

The electric motor is fitted with a precision motor speed control which is theoretically capable of regulating the speed in 100 steps. The speed reduction system consists of two Boston reducers, five sprockets of 30, 30, 15, 9 and 112 teeth, and a worm gear jack. The Boston gears reduce the speed by 2,000 times, and the sprockets can further effect a reduction of 12 times. Thus, the whole speed reduction system, including the worm gear jack, is capable of providing an axial deformation range of 0 to 2.5 thousandths of

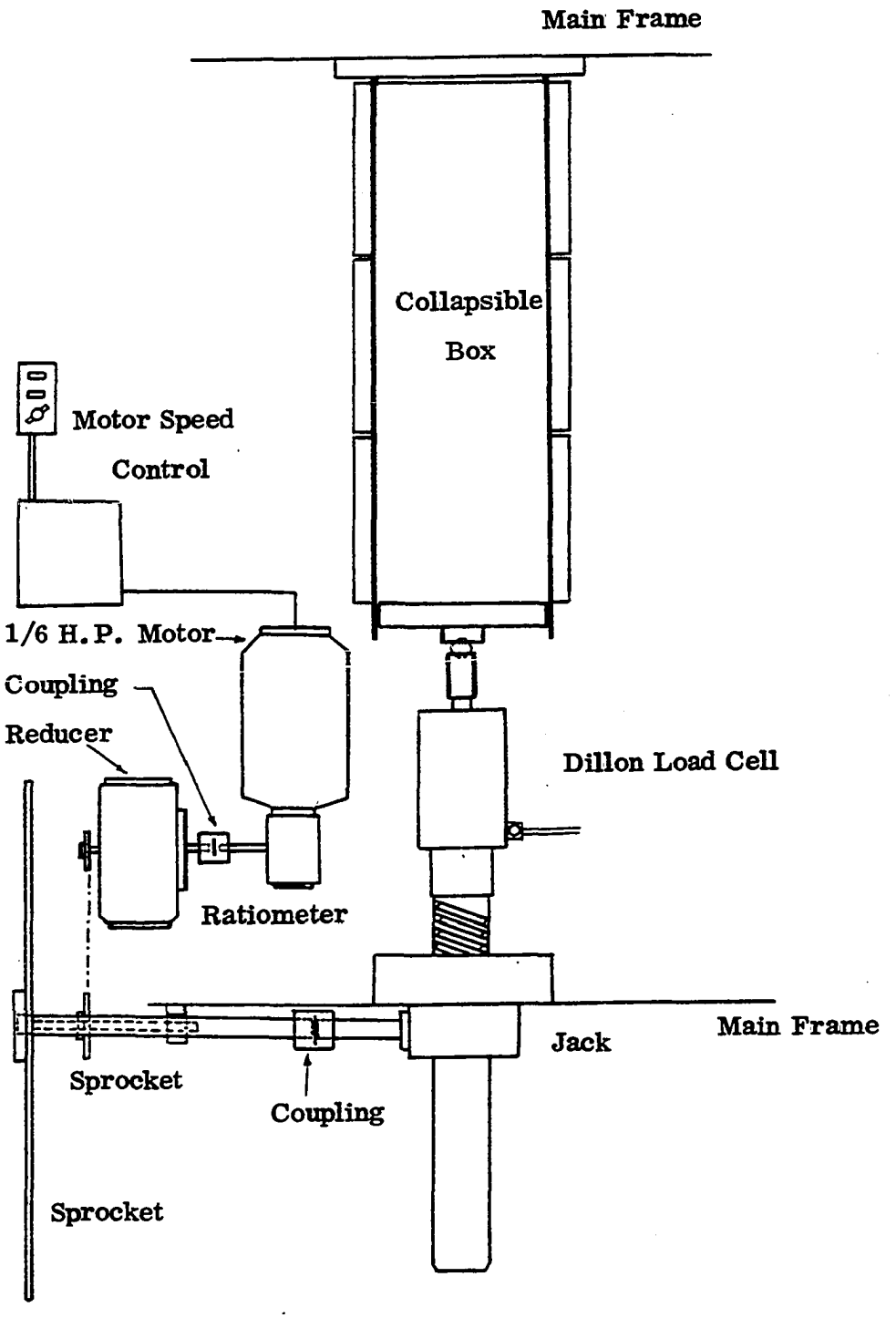

Figure 7. Axial deformation system

an inch per minute. An Ames dial is connected to the worm shaft of the jack such that it directly measures the axial deformations in thousandths of an inch.

Axial load measurement

For measurement of axial load, a Dillon load cell (Fig. 5) with its readout system is used. The load cell is of a 10,000-lb. capacity and is mounted on the end of the worm shaft of the ten-ton jack. The other end of the load cell is connected to the collapsible box through a ball and socket arrangement. The Dillon readout system is in two stages, namely 0 to 5,000 lbs. and 5,000 to 10,000 lbs., which gives better precision in reading the axial load.

Main frame

The main frame (Fig. 2) was designed as a rigid closed box section for an axial load of 15,000 lbs. and a lateral load of 5,000 lbs. The maximum deflection in the box section was kept equal to one thousandth of an inch under the above load system. In practice, the maximum axial load used is less than 4,000 lbs., which gives a calculated maximum structural axial deformation equal to one-quarter of a thousandth of an inch, compared to a total axial deformation of 1/2" in the assemblage. The box section was rigidly welded to a four-legged skeleton supported on rollers, which gives further rigidity to the box section.

Material Tested

The granular assemblage is modeled by cylindrical rods of different diameters, materials and shapes. Two different materials, namely steel and teflon, were available in geometrical shapes of cylinders and square bars. The following five sizes of steel rods of circular cross section were experimented with:

1" diameter cold rolled steel rods
3/4" diameter cold rolled steel rods
1/2" diameter cold rolled steel rods
1/4" diameter steel welding rods
1/8" diameter steel welding rods
3/4" diameter teflon rods

All the sizes, except the 1/8"-diameter welding rods, were machine cut and lightly polished on a lathe with a fine emery cloth. The rods then were covered by a thin layer of light machine oil to prevent rusting. The lengths of the rods were accurately cut so as to give a reasonably smooth surface while standing with their axes vertical. The 1/8" steel welding rods were saw-cut, so the length could not be controlled as precisely, with the result that a smooth planar surface was not attained when they were made to stand with their axes vertical in the collapsible box.

Sample Preparation

Before testing, the rods were washed with acetone to remove any loose material and lubricant from the surface, and were then cleaned with a clean dry cloth. A second acetone bath was given to the rods before they were used for experimentation.

Countless possibilities existed for an initial arrangement of regular and random rod assemblages. To simulate a densest packing, a rhombic geometrical array was used in all tests, the long axis of the rhombus coinciding with the major principal stress direction (σ_1). Care was taken in arranging the rods in a regular geometrical array with its center line coincident with the line of application of the load, a string line being used for this purpose. In a rhombic array, the rods in alternate rows number r and r-1, and it was always seen that the first and the last rows of the assemblage had the same number (i.e., r) of rods so as to insure a symmetrical assemblage. Before application of axial strain, the assemblage was subjected to the required predetermined constant lateral stress (σ_3) and the loaded end platen moved axially with the help of the disengaged jack, so that contact with the load corresponding to $\sigma_1 = \sigma_3$ was shown by the Dillon load readout system. At this point, the axial deformation dial was set to zero. Lines making an angle of 60° with the σ_3 direction were then drawn with a felt-tipped pen through the centers of the exposed rod ends. These lines

helped in establishing movements of the rods during deformation. After the linear grid was marked with black ink, the four lateral deformation modified Ames dials were fitted on to rest (Fig. 5) on the top of the side platens. The first lateral deformation dial was placed on the center line of the cylinders in the first row from the load side, and the last dial was placed on the center line of the last row; whereas, the second and third dials were exactly 5" apart on the edges of the central side platens. The camera was adjusted and focussed in such a manner that the lateral deformation dials could be read comfortably, along with a reasonably sharp picture of the deformation pattern. Special care was taken in aperture and shutter adjustment for the sake of neat photography.

Testing Technique

Five values of constant lateral stresses, namely 10, 20, 30, 40 and 50 psi, were used for the experiments. After all preparations are completed and the axial deformation dial is set for an initial zero deformation reading, a constant axial strain at the nominal rate of 0.001% per second is applied. Photographs are taken at the interval of 0.005" of axial deformation during the initial stage; then this interval is increased to 0.01" and finally to 0.02". Total time for which the axial deformation is applied to assemblage, along with the total axial deformation itself, is noted to find the

true axial strain rate. After the assemblage has been subjected to a required axial deformation, the experiment is stopped and the film is processed. Processed film is projected through an enlarger to read the lateral deformation dials and observe the movement of individual rod and failure planes. Dial readings are converted to volume change by the formulations given below (refer to Figs. 8 and 10):

Effective width of the assemblage

= distance between the centers of the first and last rods in the first row

$= 2(r - 1)d \sin\lambda$

Effective length of the assemblage

= distance between the center lines of the first and the last rows

$= (n - 1)d \sin(90 - \lambda)$

$$\text{Axial strain } (\varepsilon_1) = \frac{E}{(n-1)d \sin(90-\lambda)}$$

$$\text{Initial volume } (v_0) = 2(r-1)n-1)d^2L \sin(90-\lambda)\sin\lambda$$

$$\text{Change in volume } (dv) = \left[\frac{A+B}{2}a + \frac{B+C}{2}b + \frac{C+D}{2}e - 2(r-1)dE \sin\lambda\right]L$$

$$\text{Volumetric strain } \left(\frac{dv}{v_0}\right) = \frac{1}{2(r-1)(n-1)d^2\sin(90-\lambda)\sin\lambda}\left[\frac{A+B}{2}a+\frac{B+C}{2}b+\frac{C+D}{2}e-2(r-1)dE \sin\lambda\right]$$

$$\text{Axial stress } (\sigma_1) = \frac{G}{2(r-1)d \sin\lambda L}$$

where $\lambda = 30$ in the present experimentation

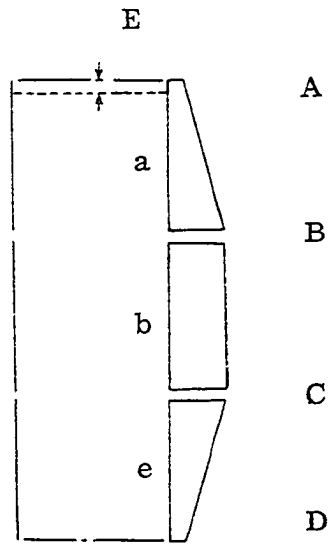

A. Reading of first (from load side) lateral deformation dial

B. Reading of second (from load side) lateral deformation dial

C. Reading of third (from load side) lateral deformation dial

D. Reading of fourth (from load side) lateral deformation dial

E. Reading of the axial deformation dial

a. Distance between first and second dials

b. Distance between second and third dials

e. Distance between third and fourth dials

r. Number of rods in the first cross row (from load side)

d. Diameter of rods

L. Length of rods

G. Dillon load cell readout reading

λ. Distribution angle

Figure 8. Mathematics of collapsible box

Reproducibility

The rate of application of axial strain and axial load was reproducible with a high degree of accuracy, and the use of a two-stage pressure regular made it possible to attain an almost constant lateral pressure. The reproducibility of the regular geometrical array with its center line coincident with the line of application of load was somewhat less precise, in spite of the extreme care taken in arranging the rods. In addition, there was unavoidable variation in the surface finish of the rods.

Another important factor which may affect reproducibility is the initial zero setting of the axial deformation dial. It was observed that after application of constant stress, the axial deformation dial could not be uniquely set for load, corresponding to $\sigma_1 = \sigma_3$ on the Dillon load cell readout system. For example, after setting the axial dial at zero with the readout load corresponding to $\sigma_1 = \sigma_3$, if the assemblage was subjected to some axial load and left for some time, then after bringing the axial load to its original value, the axial deformation dial could not come to the initial zero setting. This effect was particularly pronounced in smaller diameter rods. Some of the possible reasons, in the case of the smaller diameter assemblage, can be: (1) it is extremely difficult, if not impossible, to align the center line of the assemblage along the σ_1-axis; and (2) the smaller diameter rods, being relatively more

slender than the larger diameter rods, can bend more easily along their length, thus rendering the perfect fit of the assemblage impossible.

This could be a reason for a floating $(\frac{\sigma_1}{\sigma_3})_{max}$ with respect to axial strain, or a shifting $\frac{dv}{v_0}$ versus ε_1 curve along the direction of the axial strain on plots. These effects were apparent from repeated tests. Flotation of the $(\frac{\sigma_1}{\sigma_3})_{max}$ point and the $\frac{dv}{v_0}$ versus ε_1 curves with different lateral stresses can also be due to different initial elastic deformations, since increasing lateral stresses will induce greater initial elastic deformations.

THEORETICAL INVESTIGATIONS

General Considerations

When an assemblage of rods is subjected to a stress field, then the forces between the cylinders are at first indeterminate because each cylinder is in contact with six neighboring cylinders. Any small change in the geometry of its boundary, e.g. a change in the shape of the surrounding frame which is brought about by moving the load side platen, results in a geometrical change of pattern which always includes a series of gaps or slack contacts (this follows from Osborne Reynolds' theory of dilatancy). A very small change of shape in the boundary is sufficient to produce this effect; it needs to be only of the same order of magnitude as the elastic strain in the cylinders. The gaps are definite limits to the lines of action of the forces. Thus, creation of two gaps around a cylinder will reduce the neighboring contacts from six to four, which will make the forces between the cylinders determinate. Since dilatancy may be looked upon as a cause of gaps and also of slack contacts (no visible gaps), its intimate connection with the pressure distribution is apparent.

Forces Acting

Let us consider an assemblage of cylinders having a distribution angle equal to λ (angle for some skew arrangement such that $\lambda = 30°$ gives us a hexagonal array and $\lambda = 45°$

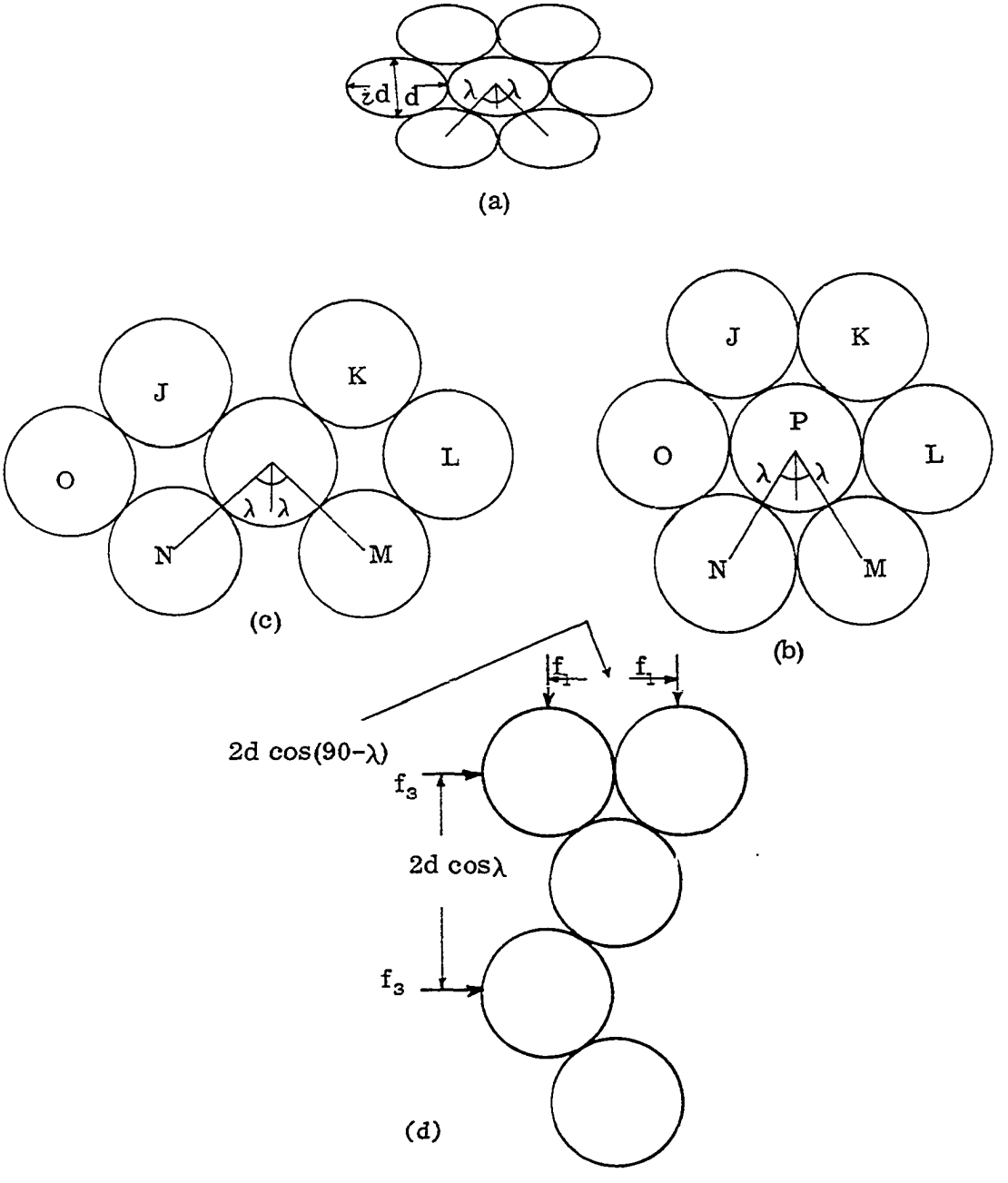

Figure 9. Regular geometrical arrays; ι is the shape factor and λ is the distribution angle; (a) hexagonal array of oval shapes, (b) hexagonal array of circular shapes, λ = 30°, (c) cubic array of circular shapes, λ = 45°, (d) hexagonal array shown with forces

gives us a cubic array, shape factor $\iota = 1$). When it is subjected to a biaxial stress field, a sort of mass transmission of forces takes place in the axial and lateral directions. If cylinder K (Fig. 10) in an upper layer is supported by two cylinders P and L in the lower layer, cylinder K tends to push cylinders P and L apart, tending to break the contact between them. Now consider a λ-array (distribution angle = λ) of cylinders in which cylinder P is surrounded by six cylinders, L, M, N, O, J and K (Fig. 10). This is the geometric arrangement which gives the minimum void ratio when $\lambda = 30°$. In the axial direction, rods J and K are supported by rods O and P, and P and L, respectively. Similarly, rod P is axially supported by rods N and M. In the lateral direction, rod O is supported by rods J and N, and rod P by K and M, assuming no contacts between O and P, and P and L. This gives rise to the mass transmission of forces from cylinder to cylinder. If f_1 is the axial force on one cylinder and f_3 is the lateral force, then

$$f_1 = 2d\ \sigma_1\ \cos(90 - \lambda) \tag{1}$$

$$f_3 = 2d\ \sigma_3\ \cos\lambda \tag{2}$$

where d is the diameter of cylinders, σ_1 and σ_3 are axial and lateral stresses on a gross area basis, respectively, and λ is the distribution angle.

Figure 10. An assemblage of rods subjected to biaxial stresses

r = Number of rods in first cross row (from load cell side)

n = Number of cross rows of rods in the box

L = Length of rod

d = Diameter of rod

σ_1 = Axial stress

σ_3 = Lateral stress

f_1 = Force acting on one rod in axial direction = $2d\ \sigma_1\ \sin\lambda$

f_2 = Force acting on one rod in lateral direction = $2d\ \sigma_3\ \cos\lambda$

F = Normal force acting on one rod

T = Tangential force acting on one rod

Length of assemblage = $(n-1)d\ \cos\lambda$

Width of assemblage = $2(r-1)d\ \sin\lambda$

Original volume $V_o = (n-1)(r-1)d^2L\ \sin 2\lambda$

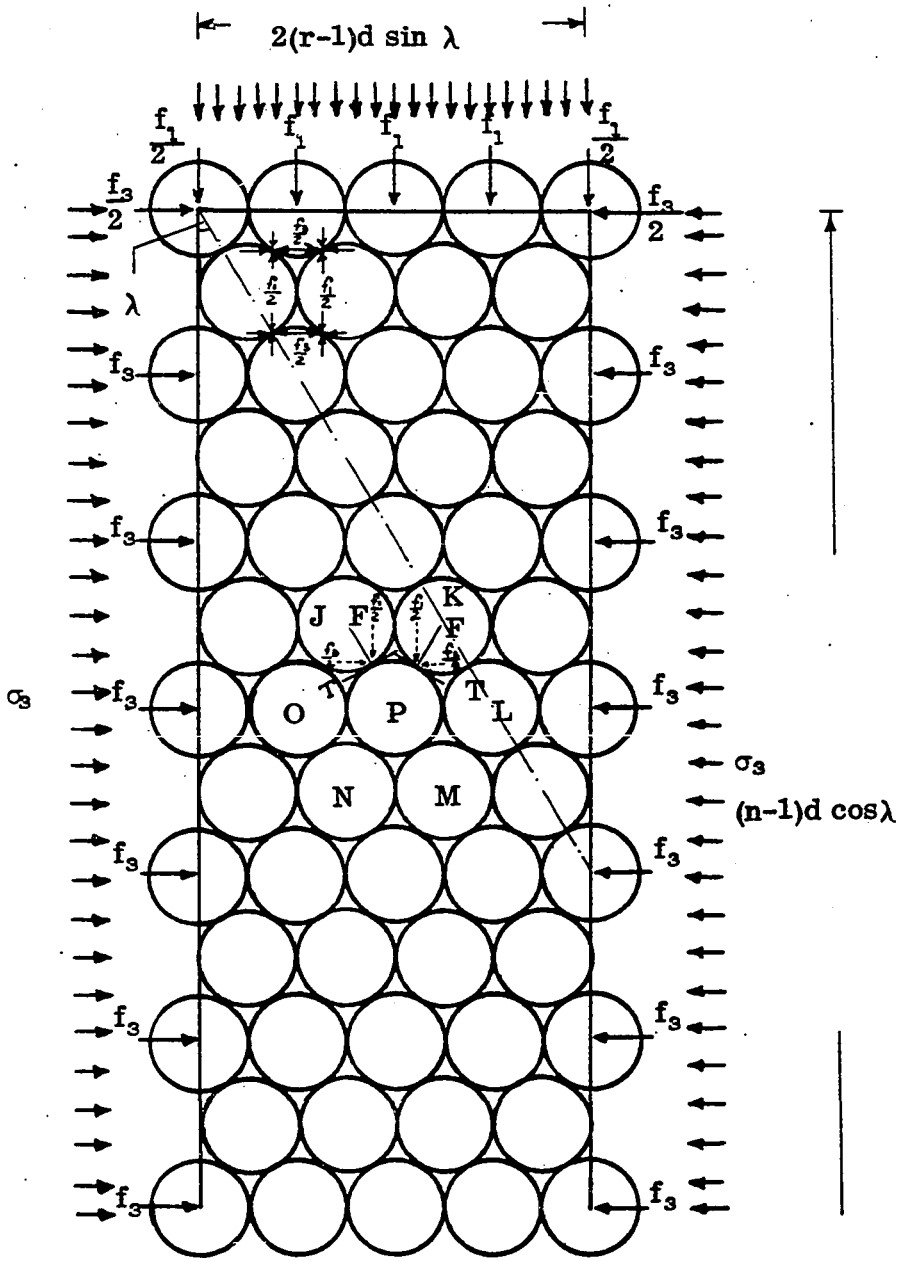
2(r-1)d sin λ
λ
J
F
K
F
O
P
T
T
L
N
M
σ3
(n-1)d cosλ

Next, consider a cylinder P of the array and resolve the axial and lateral forces $\frac{f_1}{2}$ and $\frac{f_3}{2}$ to give a normal force F acting along the $(90 - \lambda)$-direction from the σ_3-axis, and a tangential force T at a right angle to the $(90 - \lambda)$-direction. Then

$$F = \frac{f_1}{2} \cos\lambda + \frac{f_3}{2} \sin\lambda.$$

Substituting the values of f_1 and f_3 from Eqs. (1) and (2), respectively, then

$$\begin{aligned} F &= d\sigma_1 \cos(90-\lambda)\cos\lambda + d\sigma_3 \cos\lambda \sin\lambda \\ &= d \cos\lambda \sin\lambda (\sigma_1 + \sigma_3) \\ &= d \frac{\sin 2\lambda}{2} (\sigma_1 + \sigma_3) \end{aligned} \tag{3}$$

$$\begin{aligned} T &= \frac{f_1}{2} \sin\lambda - \frac{f_3}{2} \cos\lambda \\ &= d\sigma_1 \cos(90-\lambda)\sin\lambda - d\sigma_3 \cos\lambda\cos\lambda \\ &= d\sigma_1 \sin^2\lambda - d\sigma_3 \cos^2\lambda \\ &= d(\sigma_1 \sin^2\lambda - \sigma_3 \cos^2\lambda) \end{aligned} \tag{4}$$

Elastic Deformations

Now let us consider cylinders P and J of the array and rotate the center line JP in a clockwise direction through angle λ. The pair after rotation, as shown in Fig. 11, is being acted on by a normal force F and a

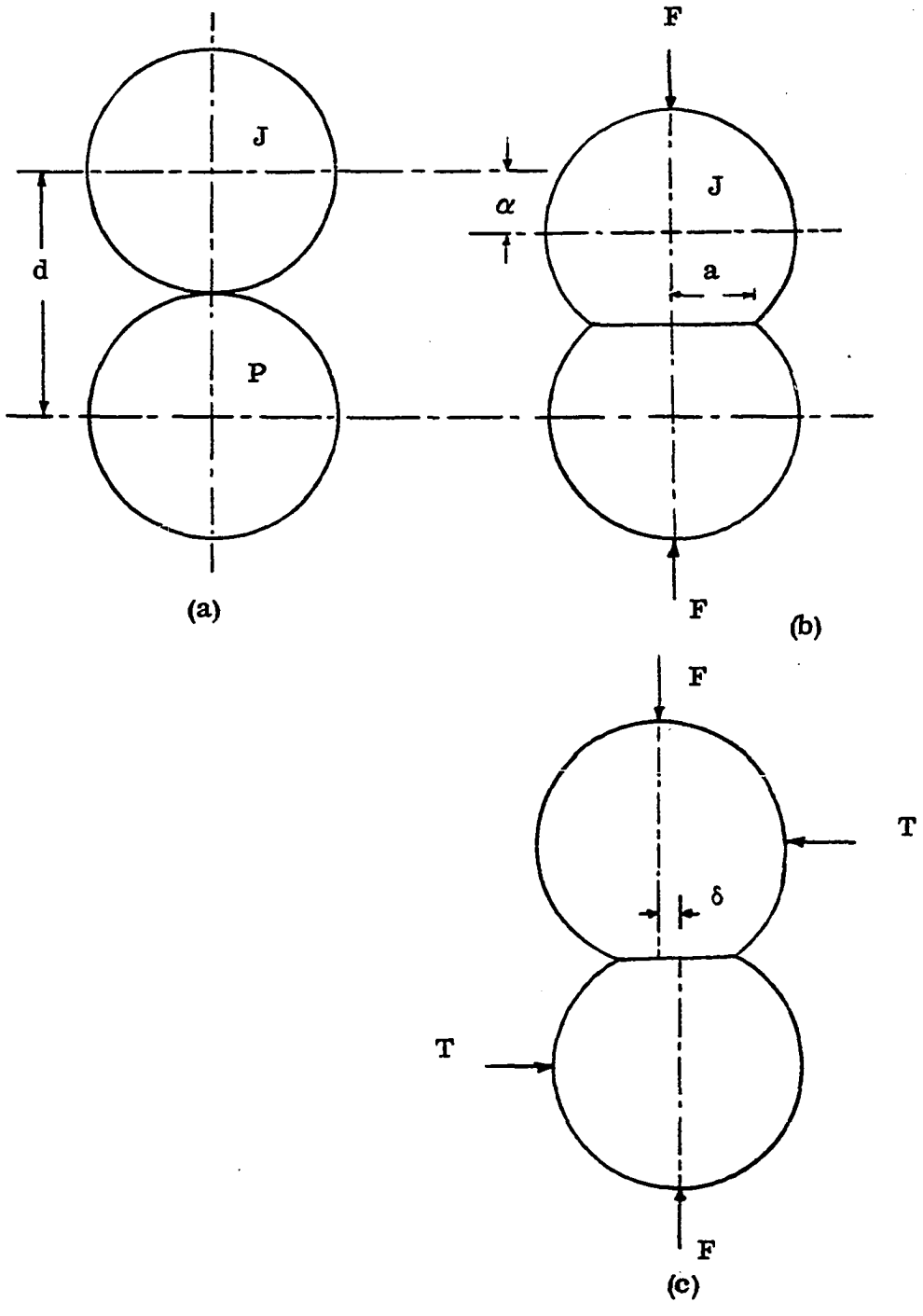

Figure 11. Elastic deformation; (a) two rods, (b) two rods deformed elastically under load F, (c) two rods deformed elastically under normal and tangential loads together

tangential force T at their contact. These contact forces give rise to elastic deformations in the normal and tangential directions at the line (actually area) of contact. The normal elastic deformation of the contact surfaces brings the centers of cylinders J and P closer to each other by a distance known as the distance of relative approach, and is here denoted by α. The tangential elastic deformation displaces cylinders J and P laterally by a distance δ, known as the displacement of distant points with respect to uniform displacement of the adhered portion. These normal and tangential displacements are taking place along the direction making an angle $(90-\lambda)$ with the σ_3 direction. The displacements, when properly resolved in the axial and lateral directions, will give elastic axial and lateral strains on cylinder P.

Similarly, the elastic axial and lateral strains of cylinder P can be obtained from its contact with cylinder K. Considering both pairs of cylinders — P and J, and P and K — (Figs. 10 and 12), then

$$\alpha = \text{distance of relative approach}$$

$$\delta = \text{lateral displacement}$$

$$\text{angle iac} = (90-\lambda) \text{ and angle tac} = \lambda$$

From Fig. 12, it can be seen that irrespective of the magnitude of σ_1 and σ_3, the axial components of α from pairs

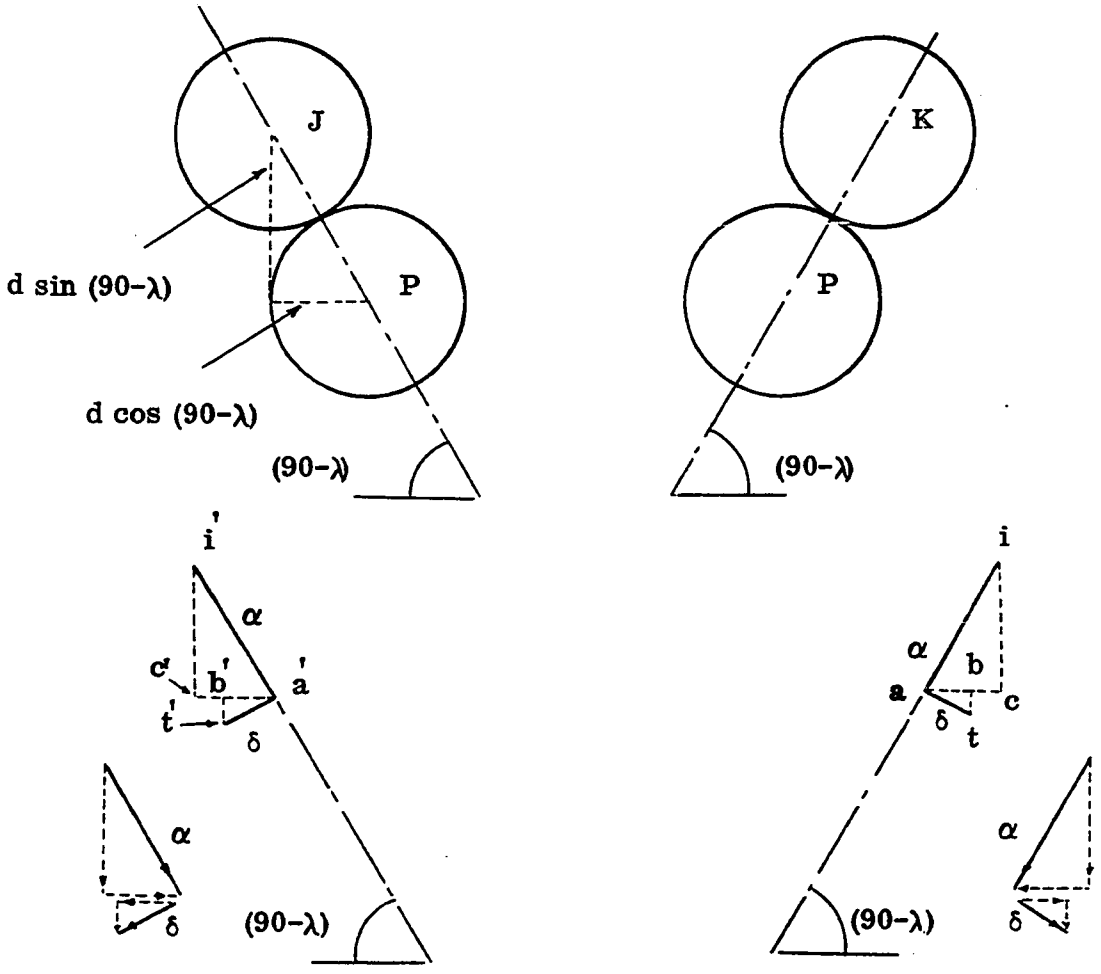

Figure 12. Elastic deformations resolved into axial elastic strains (α is the distance of relative approach and δ is the lateral displacement)

P and J, and K and P are positive and give axial compressive strains; whereas, lateral components of α from both pairs are opposite and cancel each other. Also, the axial components of δ from both pairs are positive and give rise to axial compressive strain, whereas their lateral components also cancel each other.

From the above, it is evident that contact elastic deformations from an axial compressive stress give only axial compressive strain which results in a decrease in volume of assemblage. Such a volume decrease was measured in the initial stages of the experimental $\frac{dv}{v_0}$ versus ε_1 curves.

Let ε_{1e} be the elastic axial compressive strain. $d\cos\lambda$ and $d\sin\lambda$ are the axial and lateral components, respectively, of distance d between the centers of two cylinders. Then ε_{1e} will be equal to the sum of the axial components of α and δ from both the pairs divided by $d\cos\lambda$.

$$\varepsilon_{1e} = \frac{2(\alpha\cos\lambda + \delta\sin\lambda)}{d\cos\lambda}$$

$$= \frac{2}{d}(\alpha + \delta\tan\lambda) \qquad (5)$$

But

$$(\delta v)_e = \varepsilon_{1e} + \varepsilon_{2e} + \varepsilon_{3e}$$

where $(\delta v)_e$ is the elastic volume change per unit length of the cylinders, and ε_{1e}, ε_{2e} and ε_{3e} are the axial, intermediate and lateral strains. Since we are dealing with

plane strain, the intermediate strain is zero and we have already shown that lateral strain ε_{3e} is also zero. Therefore

$$(\delta v)_e = \varepsilon_{1e} = \frac{2}{d}(\alpha + \delta\tan\lambda). \qquad (6)$$

We may note that $(\delta v)_e$ is the elastic volume change due to two contacts at any cylinder, say P. With two contacts broken, each cylinder is touching four neighboring cylinders and has four contact points. Hence, the total elastic volume change per unit length of cylinders $(dv)_e$ corresponding to one cylinder will be twice $(\delta v)_e$; thus

$$(dv)_e = 2(\delta v)_e = \frac{4}{d}(\alpha + \delta\tan\lambda). \qquad (7)$$

The total number of cylinders in the assemblage is $(n-1)(r-1)$, where n is the number of cross rows and r is the number of cylinders in the first cross row. Therefore, total elastic volume change per unit length of cylinders, $(dv)_e$ is given by

$$(dv)_e = (n-1)(r-1)\,\frac{4}{d}\,(\alpha + \delta\tan\lambda). \qquad (8)$$

The original length and width of the assemblage (Fig. 10) are given by $(n-1)d\cos\lambda$ and $2(r-1)d\sin\lambda$, respectively. Therefore, the original volume, per unit length of cylinders, of the assemblage, v_0, is given by

$$v_0 = (n-1)(r-1)d^2\sin 2\lambda \qquad (9)$$

$$\therefore \quad \frac{(dv)_e}{v_0} = \frac{4(\alpha + \delta\tan\lambda)}{d^3 \sin 2\lambda} \tag{10}$$

where $\frac{(dv)_e}{v_0}$ is the elastic volumetric strain of the assemblage.

Analytical solutions for δ and α for cylindrical rods, to the best knowledge of the author, are not available. As previously shown,

$$F = d \frac{\sin 2\lambda}{2} (\sigma_1 + \sigma_3) \tag{3}$$

$$T = d(\sigma_1 \sin^2\lambda - \sigma_3 \cos^2\lambda) \tag{4}$$

By definition within the elastic region, $\frac{\sigma_1}{\sigma_3}$ varies linearly with ε_1; this also is seen in the experiments. If σ_3 is kept constant throughout the experiment,

$$\sigma_1 \propto \varepsilon_1$$

$$\sigma_1 = E_s \varepsilon_1 \tag{11}$$

where E_s is a constant and can be called an elasticity modulus of the assemblage.

From the above, it can be seen that for a particular diameter d and distribution angle λ of the assemblage,

$$F = \text{some constant} \times \varepsilon_1$$

$$T = \text{another constant} \times \varepsilon_1$$

Thus, once a relation is found between α, δ, F and T from

the theory of elasticity, one could easily find a relation between $\frac{(dv)_e}{v_0}$ and axial strain ε_1.

Stress Ratio $(\frac{\sigma_1}{\sigma_3})$ Formulation

General theory

With increasing stress ratio, the contact forces F and T increase in magnitude, and give rise to high contact surface tractions. The area of contact surface being so small, the surface traction may exceed the yield point of the material and cause cold welding of the contact surfaces. The strength of these contact junctions may be different due to different surface properties, which results in stronger junctions at some points than at others. The tendency for slipping to occur through the weakest junctions reorientates the assemblage into rigid body groups. Thus, a transformation from mass transmission of forces, from cylinder to cylinder, to transmission of forces from one rigid group to another, takes place. The latter takes place through the particles (cylinders) on the contacting surfaces of two groups.

For the purpose of theoretical analysis, these groups are assumed to be like a rigid wedge, ABC in Fig. 13. Once the wedge action develops, the forces acting on wedge ABC as a whole will be transmitted to the other wedge FGH through particles (cylinders) lying on the contacting surface AB. As will be shown in the theoretical analysis [Eq. (16)], at

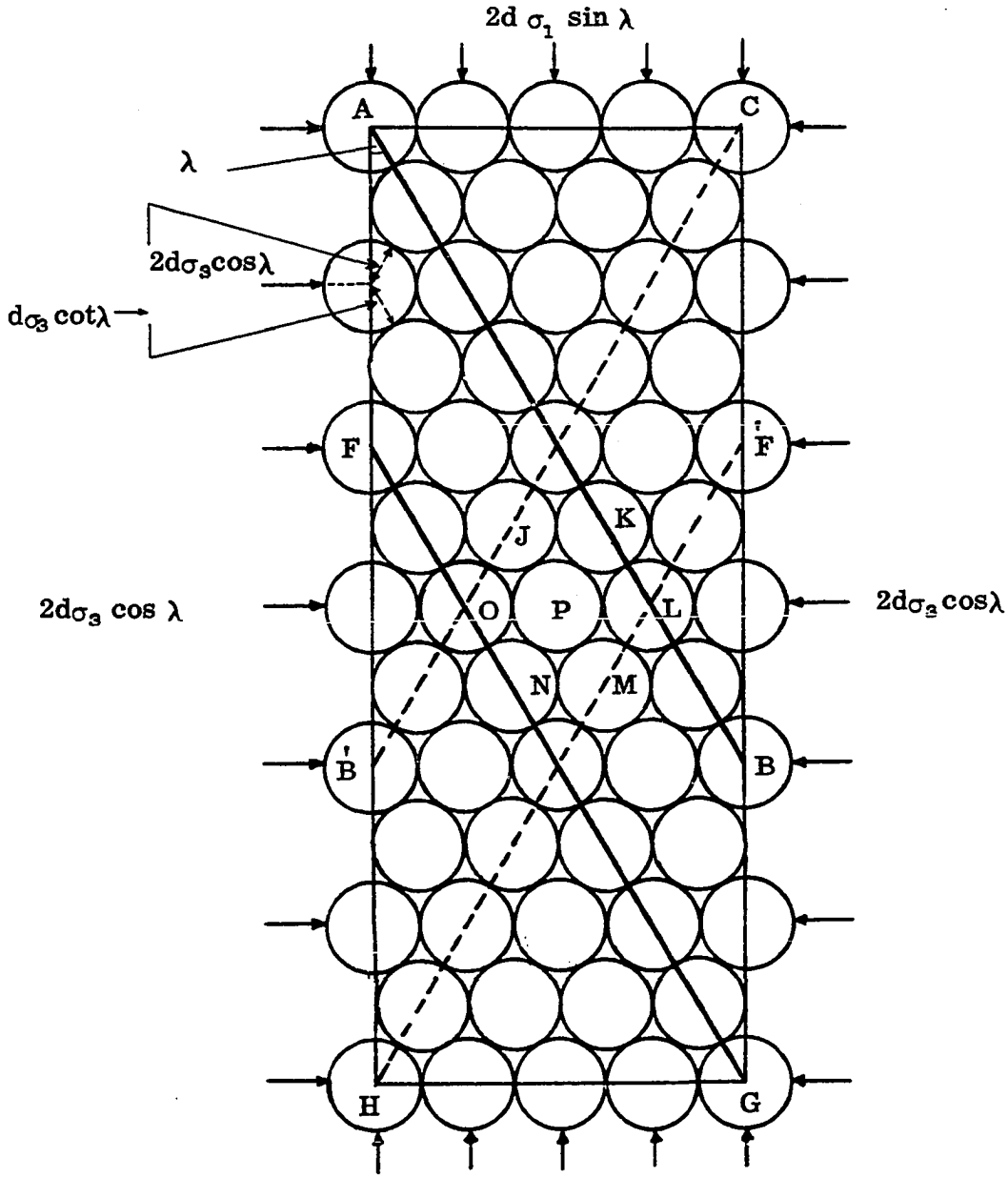

Figure 13. An assemblage of rods shown with possible directions of shear zone when subjected to biaxial stresses

Figure 14. An array on an imminent shear zone

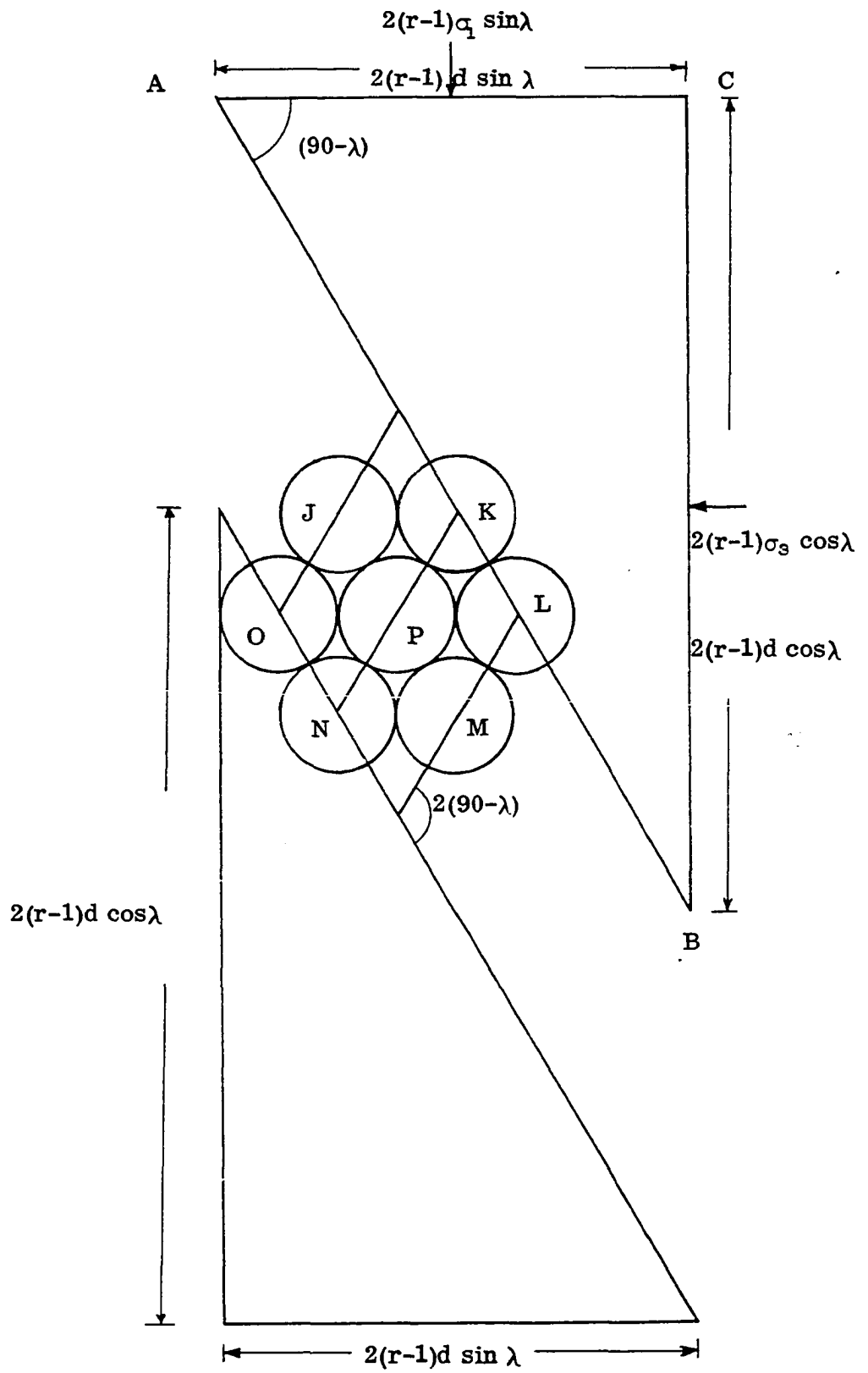
2(r-1)σ1 sinλ
2(r-1)d sin λ
A
C
(90-λ)
J
K
L
O
P
N
M
2(r-1)σs cosλ
2(r-1)d cosλ
2(90-λ)
2(r-1)d cosλ
B
2(r-1)d sin λ

a stress ratio $(\frac{\sigma_1}{\sigma_3})$ of $\cot^2\lambda$ (λ is the distribution angle of the assemblage), the force from one rigid group is transmitted to the other group along the center line of the contacting cylinders, and no tangential components are brought into effect. But, as soon as the stress ratio exceeds $\cot^2\lambda$, the transmitting forces no longer remain along the center line of cylinders, which brings into play the tangential component at the contact points. Stability then depends on limiting equilibrium at two contacting points out of four, and sliding takes place at the two points of limiting equilibrium while the other two contacting points just rotate. Failure takes place in one layer of particles (cylinders), subtending an approximate angle of $(90-\lambda)$ with a σ_3-direction, acting as rollers between the two rigid groups.

Stress ratio at failure

From Fig. 13, it can be seen that the sides of the wedge ABC are given by

$$AC = 2(r-1)d \sin\lambda$$
$$BC = 2(r-1)d \cos\lambda$$
$$AB = 2(r-1)d$$

Then $2(r-1)d \cos\lambda\sigma_3$ and $2(r-1)d \sin\lambda\sigma_1$ are the lateral and axial forces, respectively, acting on the wedge ABC. If R is their resultant force, then from Fig. 15(a)

$$R = 2(r-1)d \sqrt{\sigma_1^2\sin^2\lambda + \sigma_3^2\cos^2\lambda} \qquad (12)$$

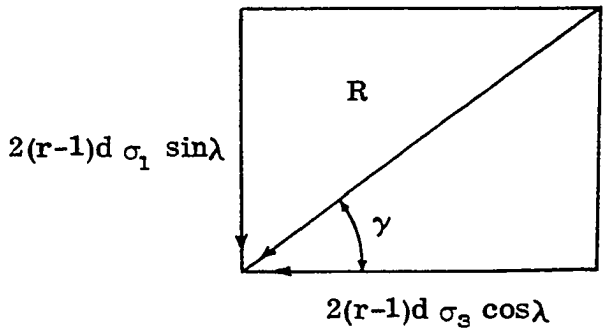

(a)

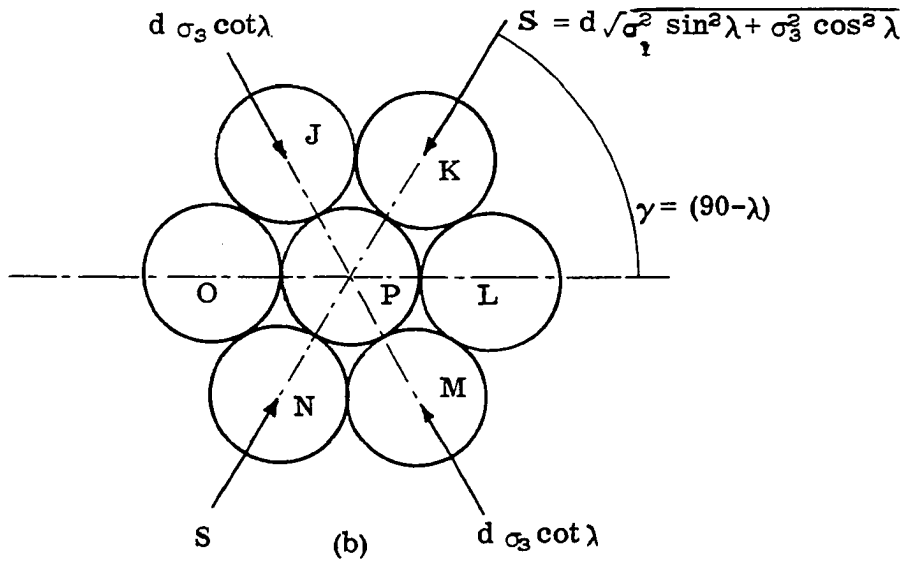

Figure 15. Forces acting on an array; (a) forces acting on moving wedge, (b) hexagonal array before failure and at $\frac{\sigma_1}{\sigma_3} = \cot^2\lambda$

and

$$\tan\gamma = \frac{2(r-1)d\ \sin\lambda\ \sigma_1}{2(r-1)d\ \cos\lambda\ \sigma_3}$$

$$= \frac{\sigma_1}{\sigma_3}\tan\lambda \qquad (13)$$

where γ is the angle that the resultant force R subtends with the σ_3-direction. If we assume the resultant force R is being transmitted equally through all the cylinders along side AB of the wedge ABC to the wedge FGH (Fig. 13), then S, the force transmitted through one cylinder, will be given by

$$S = \frac{R}{2(r-1)}$$

$$= \frac{2(r-1)d\sqrt{\sigma_1^2\sin^2\lambda + \sigma_3^2\cos^2\lambda}}{2(r-1)}$$

$$= d\sqrt{\sigma_1^2\sin^2\lambda + \sigma_3^2\cos^2\lambda} \qquad (14)$$

in which S makes an angle γ with the σ_3-direction.

As σ_1 increases from its initial value, γ increases along with it (Eq. 13) and reaches a point when its value is given by $(90-\lambda)$. At this point, σ_1 is given by

$$\tan\gamma = \frac{\sigma_1}{\sigma_3}\tan\lambda = \tan(90-\lambda) \qquad (15)$$

$$\sigma_1 = \sigma_3\cot^2\lambda \qquad (16)$$

At this value of σ_1, the force S is being transmitted along the center line of the contacting cylinders; in other words, it is acting normal to the cylinders and no

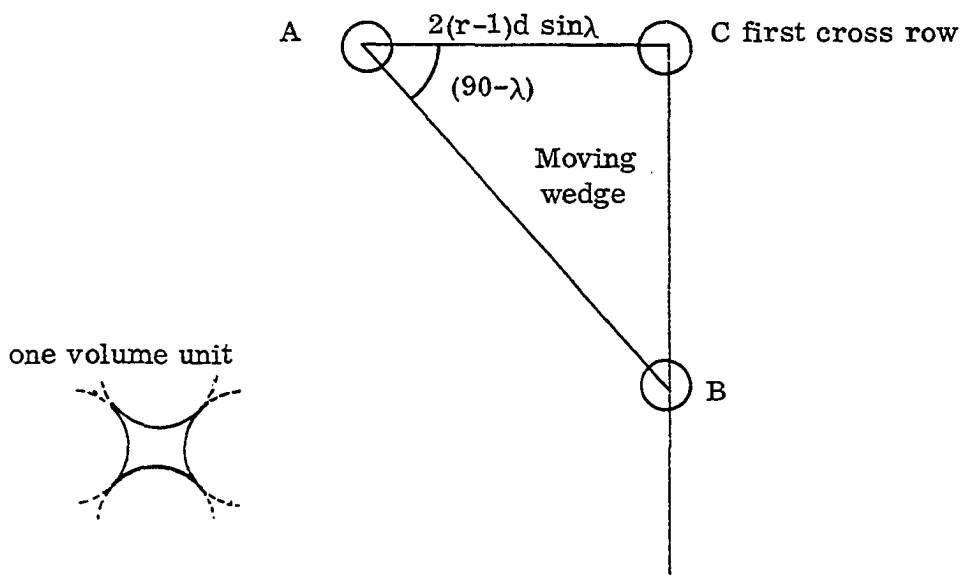

ABC moves as a rigid wedge

d = Diameter of rods

r = Number of rods in the first cross row

λ = distribution angle

$\frac{AC}{AB} = Cos(90-\lambda) = \sin\lambda$

$AB = AC/\sin\lambda = 2(r-1)d\,\frac{\sin\lambda}{\sin\lambda} = 2(r-1)d$

$BC = AB\cos\lambda\ 2(r-1)d\cos\lambda$

Number of rods along $AB = \frac{2(r-1)d}{d} = 2(r-1)$

Number of volume units taking part in volume change along AB = 2 x 2(r-1)

Figure 16. Mathematics of semirigid wedge

tangential force is brought into effect. When γ exceeds $(90-\lambda)$ or σ_1 exceeds $\sigma_3 \cot^2\lambda$, then S no longer acts along the center line of cylinders, and a tangential force component must exist at the point of contact.

Let us consider an array containing cylinder P on the surface of the imminent failure plane (Fig. 14). At a stress ratio $(\frac{\sigma_1}{\sigma_3})$ of $\cot^2\lambda$, all the forces are being transmitted along the center line of cylinders; i.e., S is acting at $(90-\lambda)$ to the σ_3-direction. The forces acting on the cylinder P [Fig. 15(a)]

$$\text{Along JP} = d \cot\lambda \, \sigma_3 \tag{17}$$

$$\text{Along KP} = d\sqrt{\sigma_1^2 \sin^2\lambda + \sigma_3^2 \cos^2\lambda} \tag{14}$$

At stress ratio $\frac{\sigma_1}{\sigma_3} = \cot^2\lambda$, this becomes

$$= d\sqrt{(\sigma_3 \cot^2\lambda)^2 \sin^2\lambda + \sigma_3^2 \cos^2\lambda}$$

$$= d \cot\lambda \, \sigma_3 \tag{18}$$

Thus, at a stress ratio of $\cot^2\lambda$, the forces acting on cylinder P along JP and KP direction are equal, so failure can take place along any direction KP or JP, depending upon unknown conditions at that instant. As soon as the stress ratio exceeds $\cot^2\lambda$, S no longer acts along KP; i.e., $\gamma > (90-\lambda)$, but makes an angle of $(\gamma+\lambda-90)$ [Fig. 17(a)] with KP, whereas the other force $d \cot\lambda \, \sigma_3$ is still acting along JP. S can now be resolved into a normal force along the

Figure 17a. Hexagonal array at $\frac{\sigma_1}{\sigma_3} > \cot^2\lambda$

Figure 17b. Limiting equilibrium of contact $\acute{J}$ and $\acute{M}$ of rod P at failure

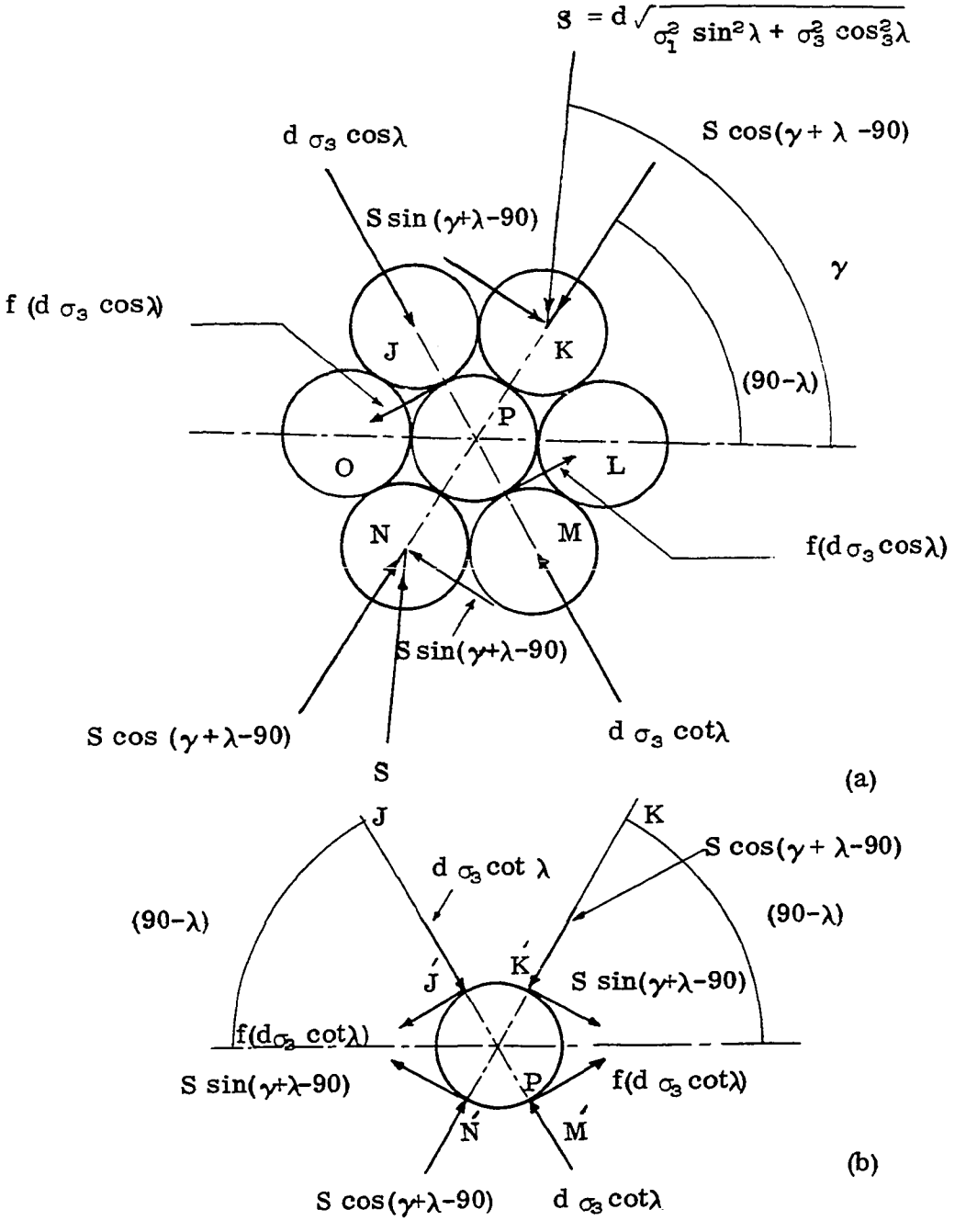
S = d √(σ1² sin²λ + σ3² cos²λ)
d σ3 cosλ
S cos(γ + λ -90)
S sin (γ+λ-90)
γ
f (d σ3 cosλ)
J
K
(90-λ)
P
O
L
N
M
f(d σ3 cosλ)
S sin(γ+λ-90)
S cos (γ+λ-90)
d σ3 cotλ
S
(a)
J
K
S cos(γ + λ-90)
d σ3 cot λ
(90-λ)
(90-λ)
J'
K'
S sin(γ+λ-90)
f(dσ3 cotλ)
S sin(γ+λ-90)
P
f(d σ3 cotλ)
N'
M'
S cos(γ+λ-90)
d σ3 cotλ
(b)

direction of PK and a tangential component at a right angle to PK [Fig. 17(a)]

$$\text{normal component of } S \text{ along PK} = S\cos(\gamma+\lambda-90) \tag{19}$$

$$\text{tangential component of } S \text{ at right angle to PK} = S\sin(\gamma+\lambda-90) \tag{20}$$

After the stress ratio exceeds $\cot^2\lambda$, which it does before 0.1% to 0.2% of the axial strain (experimental observation), the force component along PK goes on increasing along with the stress ratio, but the force along JP stays constant; hence, with an increasing stress ratio, the tangential stresses at contact point J' will reach the limiting case before those at contact point K'. This induces sliding at J' and M' and simple rotation at K' and N'; in other words, failure takes place by rotation and sliding of cylinder P.

Let us next examine the limiting equilibrium of cylinder P [Fig. 17(b)].

$$\text{The limiting tangential force at contact J' and M'} = f(d\cot\lambda\ \sigma_3) \tag{21}$$

where f is the coefficient of sliding friction. The force at J' and M' induces a counterclockwise couple, and that at K' and N' (Eq. 19) induces a clockwise couple. For equilibrium, these couples must balance (motion being very,

very slow):

couple due to limiting forces at J' and M'

$$= f(d \cot\lambda\ \sigma_3)d \tag{22}$$

couple due to forces at K' and N'

$$= S \sin(\gamma+\lambda-90)d \tag{23}$$

where d is the diameter of rods. Therefore, for equilibrium

$$f(d \cot\lambda\ \sigma_3)d = S \sin(\gamma+\lambda-90)d.$$

Substituting for S from Eq. 14,

$$f \cot\lambda\ \sigma_3 d^2 = d^2 \sin(\gamma+\lambda-90)\sqrt{\sigma_1^2\sin^2\lambda + \sigma_3^2\cos^2\lambda}$$

$$f \cot\lambda = \sqrt{\left(\frac{\sigma_1}{\sigma_3}\right)^2\sin^2\lambda + \cos^2\lambda}\ \sin(\gamma+\lambda-90)$$

$$f \frac{\cos\lambda}{\sin\lambda} = \sqrt{\left(\frac{\sigma_1}{\sigma_3}\right)^2\tan^2\lambda + 1}\ \cos\lambda(-1)\cos(\gamma+\lambda)$$

or

$$\sqrt{\left(\frac{\sigma_1}{\sigma_3}\right)^2\tan^2\lambda + 1} = -\frac{f}{\sin\lambda\ \cos(\gamma+\lambda)}$$

Since

$$\tan\gamma = \frac{\sigma_1}{\sigma_3}\tan\lambda \tag{15}$$

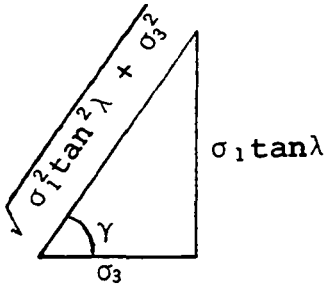

$$\sin\gamma = \frac{\sigma_1\tan\lambda}{\sqrt{\sigma_1^2\tan^2\lambda + \sigma_3^2}} \tag{24}$$

$$\cos\gamma = \frac{\sigma_3}{\sqrt{\sigma_1^2\tan^2\lambda + \sigma_3^2}} \tag{25}$$

$$\therefore \quad \sqrt{\left(\frac{\sigma_1}{\sigma_3}\right)^2 \tan^2\lambda + 1} = \frac{f}{\sin\lambda(\sin\gamma \sin\lambda - \cos\gamma \cos\lambda)}$$

$$= \frac{f\sqrt{\sigma_1^2 \tan^2\lambda + \sigma_3^2}}{\sin\lambda(\sigma_1 \tan\lambda \sin\lambda - \sigma_3 \cos\lambda)}$$

$$\frac{1}{\sigma_3} = \frac{f}{(\sigma_1 \sin^3\lambda/\cos\lambda - \sigma_3 \cos\lambda \sin\lambda)}$$

$$(\sigma_1 \sin^3\lambda - \sigma_3 \cos^2\lambda \sin\lambda) = f\ \sigma_3 \cos\lambda$$

$$\sigma_1 \sin^3\lambda = f\ \sigma_3 \cos\lambda + \sigma_3 \cos^2\lambda \sin\lambda$$

$$\frac{\sigma_1}{\sigma_3} = (f + \sin\lambda \cos\lambda)\ \frac{\cos\lambda}{\sin^3\lambda} \qquad (26)$$

which is the stress ratio at failure.

Stress ratio in post-failure region

Next let the cylindrical array of Figure 14 be deformed to an extent represented by an angle ω [Figs. 18 and 19a] so that S makes an angle $(\gamma + \lambda + \omega - 90)$ with the center line of the same cylinders after failure. The force $(d \cot\lambda\ \sigma_3)$ will still be acting along the center lines of cylinders J, P and M. We may again resolve the force S along and at a right angle to the center line NPK, and consider the equilibrium of cylinder P. Tangential forces at J' and M' are still present and give rise to a counter-clockwise couple. Induced tangential forces at K' and N' give rise to another couple which is clockwise and should

Figure 18. An array on a shear surface in post failure deformations

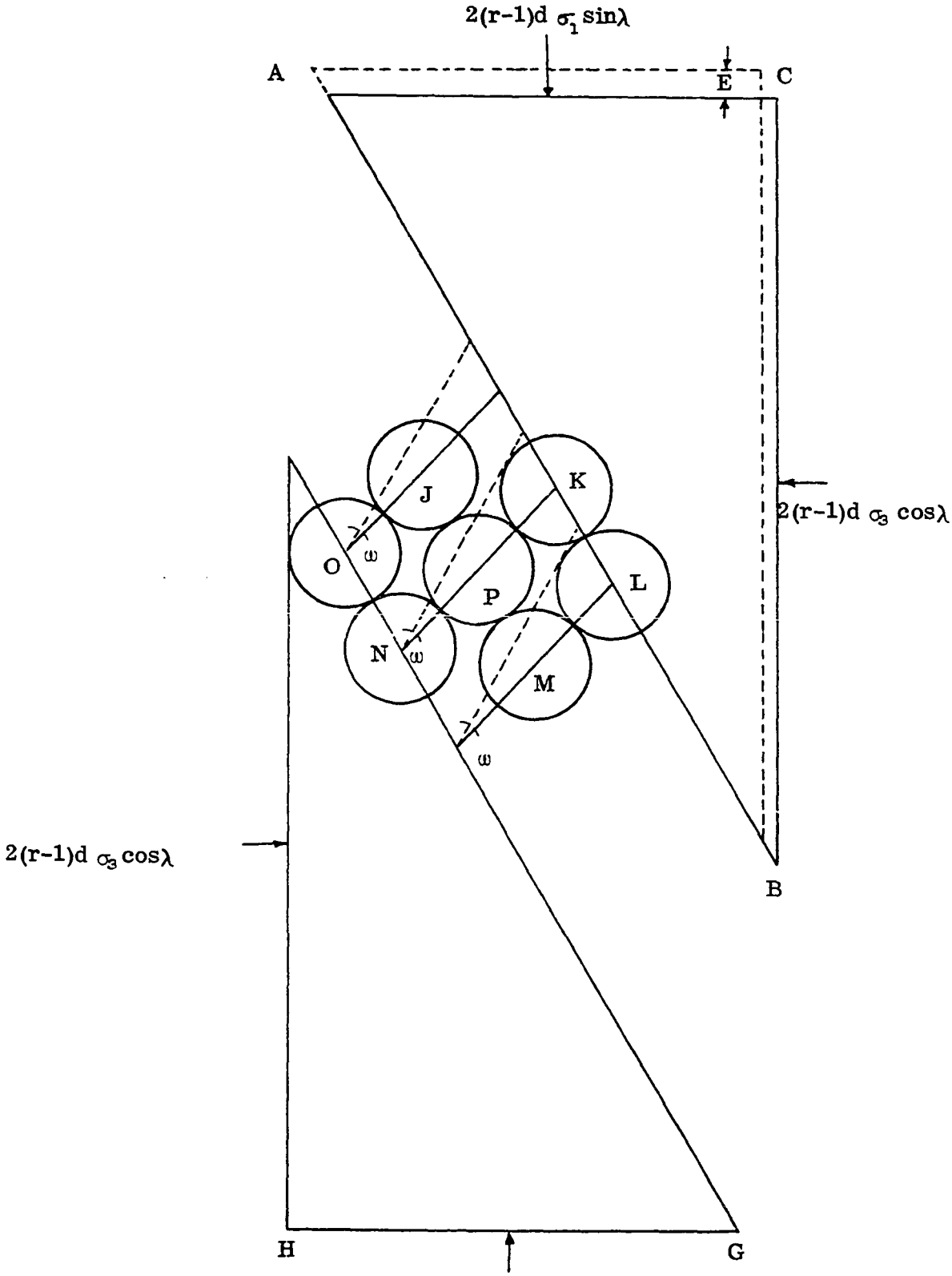
2(r-1)d σ1 sinλ
A
E
C
J
K
O
P
L
N
M
ω
2(r-1)d σ3 cosλ
2(r-1)d σ3 cosλ
B
H
G

Figure 19a. Hexagonal array in post failure deformation

Figure 19b. Equilibrium of rod P in post failure deformation of the array

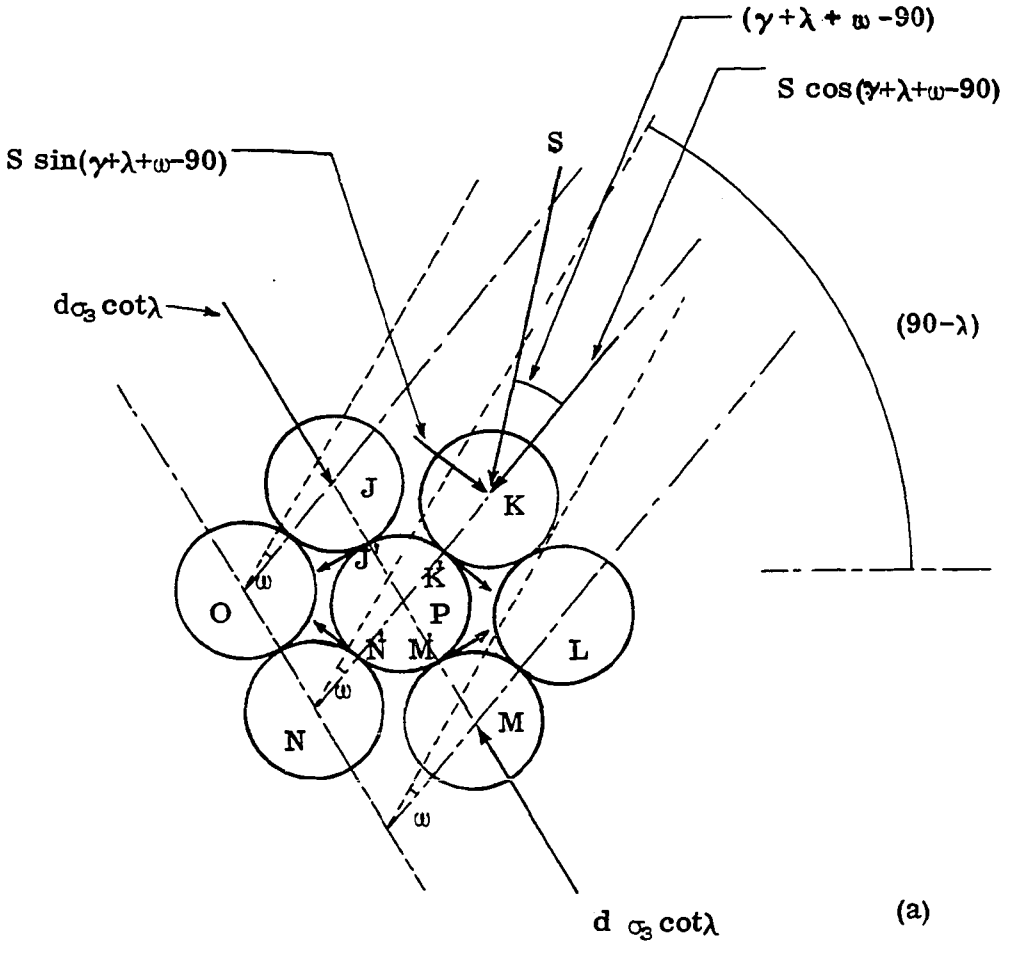
(γ+λ+ω-90)
S cos(γ+λ+ω-90)
S sin(γ+λ+ω-90)
S
dσ3 cotλ
(90-λ)
J
K
J'
K'
O
P
N'
M'
L
N
M
ω
d σ3 cotλ

(a)

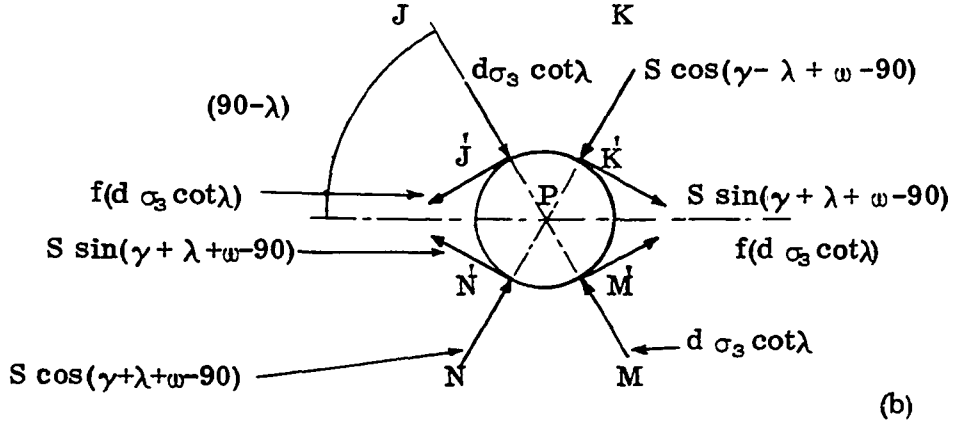
J
K
dσ3 cotλ
S cos(γ- λ + ω -90)
(90-λ)
J'
K'
f(d σ3 cotλ)
P
S sin(γ + λ + ω-90)
S sin(γ + λ +ω-90)
f(d σ3 cotλ)
N'
M'
d σ3 cotλ
S cos(γ+λ+ω-90)
N
M

(b)

balance the first couple for equilibrium:

$$\text{counterclockwise couple} = f(d \cot\lambda\ \sigma_3)d \tag{27}$$

$$\text{clockwise couple} = S \sin(\gamma + \lambda + \omega - 90)d \tag{28}$$

where d is the dialeter of the cylinders. For equilibrium

$$f\ d^2\cot\lambda\ \sigma_3 = S \sin(\gamma + \lambda + \omega - 90)d.$$

Substituting for S from Eq. 14,

$$f\ d^2\cot\lambda\ \sigma_3 = d^2\sqrt{\sigma_1^2\sin^2\lambda + \sigma_3^2\cos^2\lambda}\ \sin[\gamma - (90-\lambda-\omega)]$$

$$f\ \cot\lambda\ \sigma_3 = \sqrt{\sigma_1^2\sin^2\lambda + \sigma_3^2\cos^2\lambda}\ [\sin\gamma\ \cos(90-\lambda-\omega) - \cos\gamma\ \sin(90-\lambda-\omega)]$$

$\sin\gamma$ and $\cos\gamma$ are given by Eqs. 24 and 25. Substituting,

$$f\ \cot\lambda\ \sigma_3 = \frac{\sqrt{\sigma_1^2\sin\lambda + \sigma_3^2\cos^2\lambda}}{\sqrt{\sigma_1^2\tan^2\lambda + \sigma_3^2}}\ [\sigma_1\tan\lambda\ \cos(90-\lambda-\omega) - \sigma_3\sin(90-\lambda-\omega)]$$

$$= \cos\lambda[\sigma_1\tan\lambda\ \cos(90-\lambda-\omega) - \sigma_3\sin(90-\lambda-\omega)]$$

$$f\ \sigma_3 = \sin\lambda[\sigma_1\tan\lambda\ \cos(90-\lambda-\omega) - \sigma_3\sin(90-\lambda-\omega)]$$

$$\sigma_1\sin\lambda\ \tan\lambda\ \cos(90-\lambda-\omega) = \sigma_3[f + \sin\lambda\ \sin(90-\lambda-\omega)]$$

$$\frac{\sigma_1}{\sigma_3} = \cot\lambda\left[\frac{f}{\sin\lambda\ \cos(90-\lambda-\omega)} + \tan(90-\lambda-\omega)\right]$$

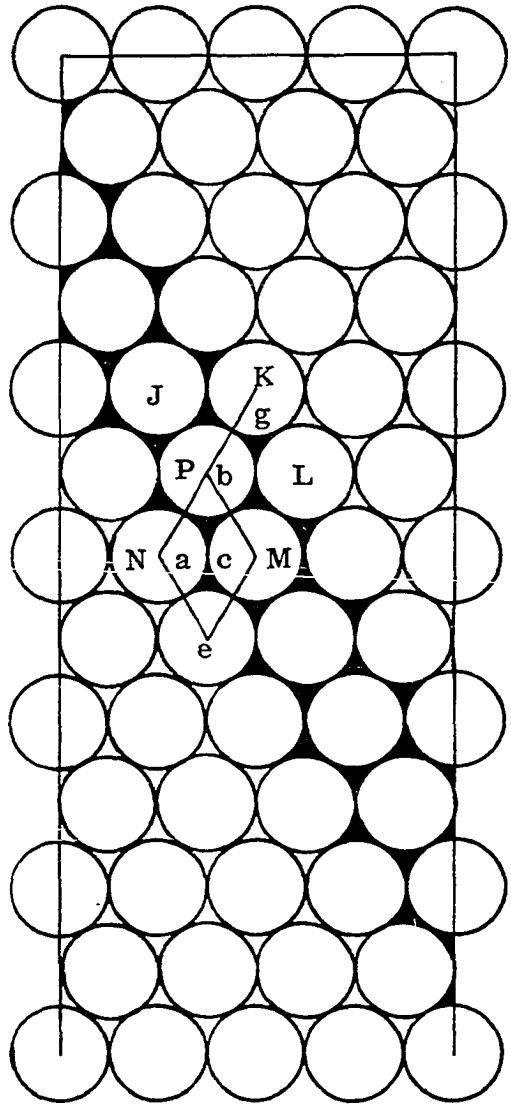

Figure 20. An assemblage showing the number of volume units (shown shaded) taking part in volume changes along shear plane

$$\frac{\sigma_1}{\sigma_3} = \cot\lambda\left[\frac{f}{\sin\lambda\ \sin(\lambda+\omega)} + \cot(\lambda+\omega)\right] \qquad (29)$$

Thus, the stress ratio should change according to the above relation with increasing deformation after initial failure. The relation between ω and the axial unit strain ε_1 may be shown to be

$$\omega = \text{arc tan}\left[\frac{d}{E\ \sin\lambda} - \cot 2\lambda\right]^{-1} \qquad (39a)$$

where

$$E = (n-1)d\ \varepsilon_1\ \cos\lambda \qquad (42)$$

Example solutions of Eq. 29 for a hexagonal array of cylinders, i.e., for $\lambda = 30°$, are given in Table 3. For a maximum stress ratio, $\omega = 0$ and Eq. 29 reduces to Eq. 26.

Volumetric Strain $(\frac{dv}{v_0})$ and Axial Strain (ε_1) Formulation

$(\frac{dv}{v_0})$-(ε_1) formulation

Let us assume that the upper wedge ABC [Figs. 21a,b] moves as a rigid body, which it actually does not do in that the first and second Ames dials do not record the same readings. If E is the axial deformation applied to the assemblage and λ is the distribution angle, then

$$\frac{E}{gf} = \sin(90 - \lambda)$$

or

$$gf = \frac{E}{\sin(90 - \lambda)} \qquad (30)$$

Table 3. Maximum stress ratios for hexagonal array of cylinders (theoretical)

Coefficient of sliding friction, f	Maximum stress ratio, $(\frac{\sigma_1}{\sigma_3})$
0.00	3.00
0.01	3.07
0.05	3.35
0.10	3.69
0.12	3.83
0.14	3.97
0.16	4.11
0.18	4.24
0.20	4.39
0.22	4.52
0.24	4.66
0.26	4.80
0.28	4.94
0.30	5.08

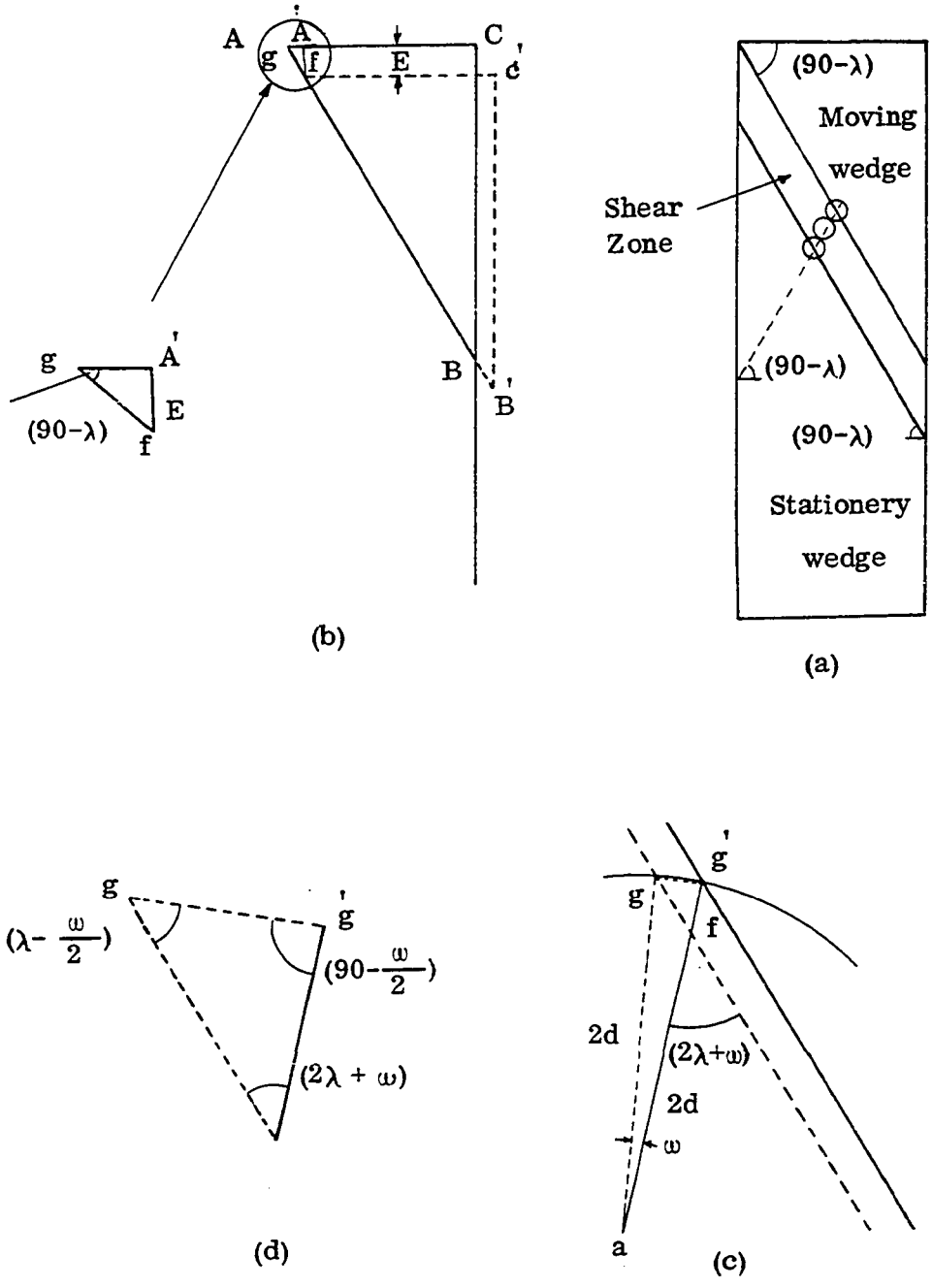

Figure 21. Mathematics of the shear zone

Again, let us consider an array containing rod P [Fig. 22a] surrounded by rods J, K, L, M, N and O. Before failure, a line passing through the centers of rods N, P and K is represented by line abg; but, after the failure, the same line is shifted to the position ab'g' [Fig. 22b]. The angle of shift from its original position is ω. During the process of shifting, the cylinders N, P and K have two components of motion. Such a motion, in the case of cylinder K, is represented by components gf and fg' [Fig. 22b]. Such a motion has been made possible, for example, in the case of cylinder P, sliding on its contacts with cylinders J and M, and rotating on its contacts with cylinders K and N. This deformation of the array results in its increase of volume, because parallelogram abce deforms to a larger area ab'c'e [Fig. 22b].

$$\text{Area abce} = 2\,\Delta\,\text{ace}$$

$$= 2\left[\frac{1}{2}\,d^2\sin 2\lambda\right]$$

$$= d^2\sin 2\lambda$$

$$\text{Area occupied by 4 sectors included in area abce} = \frac{\pi d^2}{4}$$

Area occupied by voids in area abce

$$= \text{Area abce} - \text{Area of 4 sectors}$$

$$= d^2\sin 2\lambda - \frac{\pi d^2}{4}$$

$$= d^2\left(\sin 2\lambda - \frac{\pi}{4}\right) \qquad (31)$$

Figure 22a. Hexagonal array in prefailure stage

Figure 22b. Hexagonal array in post-failure stage

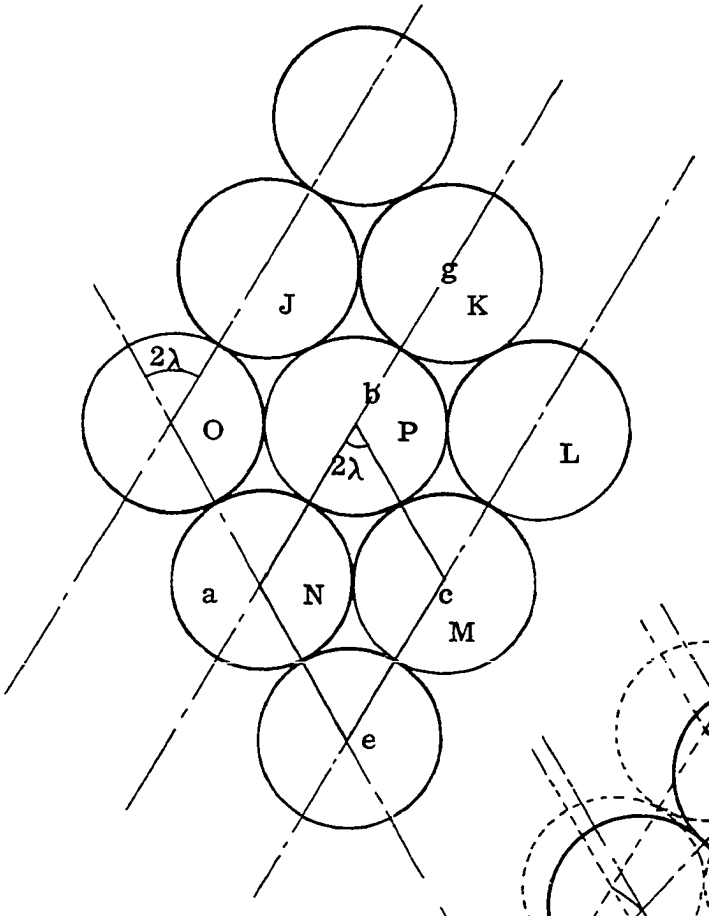

(a)

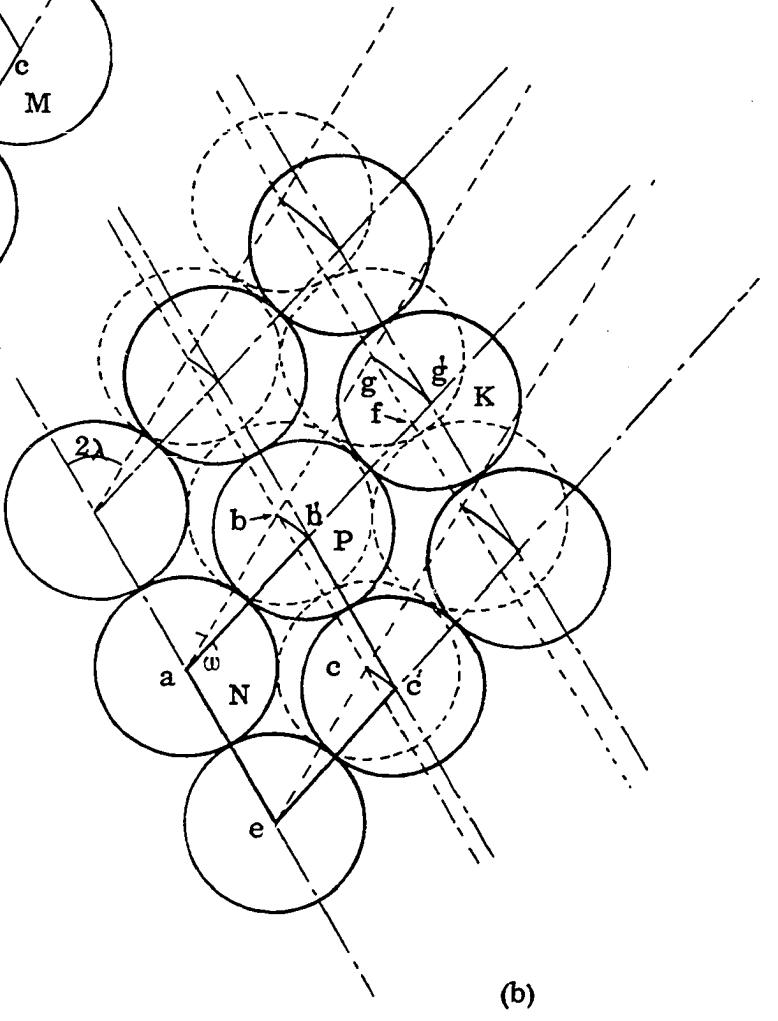

(b)

$$\text{Area } ab'c'e = 2[\tfrac{1}{2} d^2 \sin(2\lambda + \omega)]$$

$$= d^2 \sin(2\lambda + \omega)$$

Area of 4 sectors included in area $ab'c'e = \frac{\pi d^2}{4}$

Area occupied by voids in area $ab'c'e$

$$= d^2 \sin(2\lambda + \omega) - \frac{\pi d^2}{4}$$

$$= d^2[\sin(2\lambda + \omega) - \tfrac{\pi}{4}] \qquad (32)$$

Subtracting Eq. 30 from Eq. 31,

$$\text{Change in area of voids} = d^2[\sin(2\lambda+\omega) - \sin 2\lambda]$$

From Fig. 16,

Number of volume changing units $= 4(r - 1)$

Total change in area of voids

$$= 4(r-1)d^2[\sin(2\lambda+\omega) - \sin 2\lambda]$$

Total volume change (dv)

$$= 4(r-1)d^2[\sin(2\lambda+\omega) - \sin 2\lambda] \times \text{length of rod} \qquad (33)$$

From Fig. 10,

Original volume $v_0 = (n-1)(r-1)d^2 \sin 2\lambda \times$ length of rod (34)

Dividing Eq. 32 by Eq. 33,

$$\frac{dv}{v_0} = \frac{4[\sin(2\lambda+\omega) - \sin 2\lambda]}{(n-1)\sin 2\lambda} \tag{35}$$

where $(n-1)$ is a function of length of assemblage (depth of sample), diameter of cylinders, and distribution angle. From Fig. 10,

$$\text{Length of assemblage} = (n-1)d\cos\lambda$$

$$(n-1) = \frac{\text{length of assemblage}}{d\cos\lambda} \tag{36}$$

Substituting $(n-1)$ in Eq. 34,

$$\frac{dv}{v_0} = \frac{2d[\sin(2\lambda+\omega) - \sin 2\lambda]}{(\text{length of assemblage})\sin\lambda}$$

Denoting length of assemblage by L_0, we get

$$\frac{dv}{v_0} = \left(\frac{2d}{L_0}\right)\frac{\sin(2\lambda+\omega) - \sin 2\lambda}{\sin\lambda} \tag{37}$$

We can see from Eqs. 34 and 36 that the $\frac{dv}{v_0}$ equation contains the angle of shift ω. So we will proceed now to express ω in terms of axial deformation E.

Referring to Figs. 21c,d, from $\Delta agg'$

$$gg' = 2(2d\sin\tfrac{\omega}{2}) = 4d\sin\tfrac{\omega}{2} \tag{38}$$

From $\Delta gg'f$,

$$\frac{gf}{\sin(90-\frac{\omega}{2})} = \frac{gg'}{\sin(2\lambda+\omega)} \qquad \text{(Law of Sines)}$$

$$gg' = \frac{gf\sin(2\lambda+\omega)}{\sin(90-\frac{\omega}{2})}$$

Substituting gf from Eq. 30,

$$gg' = \frac{E \sin(2\lambda + \omega)}{\sin(90 - \lambda)\sin(90 - \frac{\omega}{2})}$$

Substituting gg' from Eq. 38,

$$4d \sin\frac{\omega}{2} = \frac{E \sin(2\lambda + \omega)}{\cos\lambda \cos\frac{\omega}{2}}$$

$$4d \sin\frac{\omega}{2} \cos\frac{\omega}{2} \cos\lambda = E \sin(2\lambda + \omega)$$

$$2d \sin\omega \cos\lambda = E \sin(2\lambda + \omega)$$

$$2d = \frac{\sin(2\lambda + \omega)}{\sin\omega \cos\lambda} E$$

$$\frac{2d}{E} = \frac{\sin2\lambda \cos\omega + \cos2\lambda \sin\omega}{\sin\omega \cos\lambda}$$

$$= \frac{\sin2\lambda}{\cos\lambda} \cot\omega + \frac{\cos2\lambda}{\cos\lambda}$$

$$\cot\omega = \frac{\cos\lambda}{\sin2\lambda} \left(\frac{2d}{E} - \frac{\cos2\lambda}{\cos\lambda}\right)$$

$$= \frac{1}{2\sin\lambda} \left(\frac{2d}{E} - \frac{\cos2\lambda}{\cos\lambda}\right)$$

$$= \left[\frac{d}{E \sin\lambda} - \cot2\lambda\right]$$

$$\tan\omega = \left[\frac{d}{E \sin\lambda} - \cot2\lambda\right]^{-1} \qquad (39)$$

$$\omega = \text{arc tan}\left[\frac{d}{E \sin\lambda} - \cot2\lambda\right]^{-1} \qquad (39a)$$

Substituting the value of ω from Eq. 39a in Eq. 35 or

in Eq. 37,

$$\frac{dv}{v_0} = \frac{4}{(n-1)\sin 2\lambda} \left\{\sin\left(2\lambda + \arctan\left[\frac{d}{E\sin\lambda} - \cot 2\lambda\right]^{-1}\right) - \sin 2\lambda\right\}$$

$$\frac{dv}{v_0} = \frac{4}{n-1} \left\{\frac{1}{\sin 2\lambda} \sin\left(2\lambda + \arctan\left[\frac{d}{E\sin\lambda} - \cot 2\lambda\right]^{-1}\right) - 1\right\} \qquad (40)$$

or

$$\frac{dv}{v_0} = \frac{2d}{L_0 \sin\lambda} \left\{\sin\left(2\lambda + \arctan\left[\frac{d}{E\sin\lambda} - \cot 2\lambda\right]^{-1}\right) - \sin 2\lambda\right\} \qquad (41)$$

If ε_1 is the axial strain, then it is given by

$$\varepsilon_1 = \frac{E}{\text{length of sample}}$$

Substituting the length of sample = $(n-1)d\cos\lambda$ from Fig. 10,

$$\varepsilon_1 = \frac{E}{(n-1)d\cos\lambda}$$

$$E = (n-1)d\,\varepsilon_1\cos\lambda \qquad (42)$$

Substituting the value of E from Eq. 42 into Eq. 40, we get $\frac{dv}{v_0}$ in terms of axial strain ε_1, distribution angle λ, and number of rows of rods in the assemblage n.

$$\frac{dv}{v_0} = \frac{4}{n-1}\left\{\frac{1}{\sin 2\lambda} \sin\left(2\lambda + \arctan\left[\frac{2}{(n-1)\varepsilon_1 \sin 2\lambda} - \cot 2\lambda\right]^{-1}\right) - 1\right\} \qquad (43)$$

Effects of multiple failure planes and particle (rod) size

It has been shown that the coefficient of friction on the surfaces of the particles (rods) is not constant, but is randomly distributed both in space and, as slipping occurs,

in time. Therefore, the resolved total friction will be different on the different possible failure planes, failure following a plane with the lowest resolved Σf. As slipping occurs on a failure plane, which may be called the active shear plane, the coefficient of friction on that plane will change; whereas, the coefficient of friction on other possible shear planes will remain constant due to absence of movement along them. Simultaneously increasing ω, the value of axial stress σ_1 decreases [Eq. 29]. Thus, in the process of slipping along the active shear plane, if the resolved friction along it $\Sigma f_{(active)}$ momentarily exceeds some other coefficient of friction Σf on another possible failure plane, then the slip will shift to the plane with the lower friction, where the process will repeat. However, a reduction of axial stress σ_1 has already occurred, due to slipping on the first plane, and cannot be undone, due to increased angle ω in Eq. 29; therefore, the test proceeds from the lower σ_1. As the axial strain progresses and axial stress σ_1 reduces considerably, then variation in $\Sigma f_{(active)}$ will not be sufficient to trigger slipping on fresh planes, and slipping will continue on the same plane. Hence, with increasing axial strain, the process of shifting to new failure planes slows down and ultimately stops.

Statistically, the resolved summation of friction Σf on various possible failure planes tends to be more uniform in the case of smaller particles (or smaller diameter rods)

than in the case of larger particles, because the smaller particles give more contacts per shear plane, giving more uniform averages and totals. This amounts to saying that the resolved friction Σf on all the possible failure planes, in the case of the smaller particles, is nearly the same; hence, more shear planes are simultaneously available for slip to take place than in the case of larger particles.

The relationship of dilatancy to the spacing of shear planes can also be explained by the principle of least work, in the following way. A considerable amount of work is done in developing a single shear plane under dilatant conditions, but proportionately less overall volumetric deformation is required in the smaller diameters for forming new groups or for regrouping. At the maximum stress ratio $(\frac{\sigma_1}{\sigma_3})_{max}$, which is fairly constant for all the rods, the principle of least work should give a smaller number of shear planes with the larger diameters; whereas, with smaller diameters, each shear plane involves less work and the same effort may be expended with equal facility on a greater number of shear planes.

The above arguments were confirmed by experimental observations, from which the following postulates are made:

1. The rate of change of the number of failure planes is inversely proportional to axial strain. This implies that the width of the failure zone increases sharply at first, and then slows down with

increasing axial strain.

2. For the same strain, the smaller the diameter of the rods, the larger is the number of failure planes.

If in the first postulate dL is the change of number of failure planes, L is the number of failure plane at any instant, $d\varepsilon_1$ is the axial strain. Then the first postulate may be expressed as an equation:

$$\frac{dL}{d\varepsilon_1} = \frac{1}{c}\,\frac{1}{\varepsilon_1} \tag{44}$$

where $\frac{dL}{d\varepsilon_1}$ is the slope of the tangent to L versus ε_1 curves and c is a constant. Rearranging and integrating Eq. 44,

$$c\,dL = \frac{d\varepsilon_1}{\varepsilon_1}$$

$$cL = \ell n\varepsilon_1 + \ell n\, k$$

$$= \ell n\varepsilon_1 k$$

$$L = \frac{1}{c}\,\ell n\varepsilon_1 k \tag{45}$$

where k is a constant of integration, or

$$\varepsilon_1 = \frac{1}{k}\,e^{cL} \tag{46}$$

Constants c and k can be found from experimental boundary conditions. A verification of the form of Eq. 46 will be shown by a linear relationship between L and $\ell n\varepsilon_1$. Such a

graph is plotted for d=1" cylinders in Fig. 23. From this, k may be evaluated as shown in Fig. 24, and Eq. 45 becomes

$$L = \ell n\ 417\ \varepsilon_1 \tag{47}$$

where ε_1 is the unit strain x 10^{-3}.

To express postulate 2 in a mathematical form, a general tabulation of the number of failure planes against axial strains was made for all the experiments. On the examination of this data, the following generalization was made:

On the average, if one failure plane is taking part in 1"-diameter assemblage, then $\frac{1}{0.9}$, $\frac{1}{0.7}$ and $\frac{1}{0.5}$ failure planes will take part in 1/2", 1/4" and 1/8"-diameter assemblage, respectively. Therefore, if L is the number of failure planes and d (in inches) is the diameter of the particles (rods), the above generalization can be expressed as:

$$L = (d)^{-0.33} \tag{48}$$

Combining Eqs. 47 and 48, we obtain

$$L = \frac{\ell n\ 417\ \varepsilon_1}{(d)^{0.33}} \tag{49}$$

To incorporate the requirement of postulates 1 and 2, the final relation for volumetric strain is obtained by multiplying Eqs. 43 and 49:

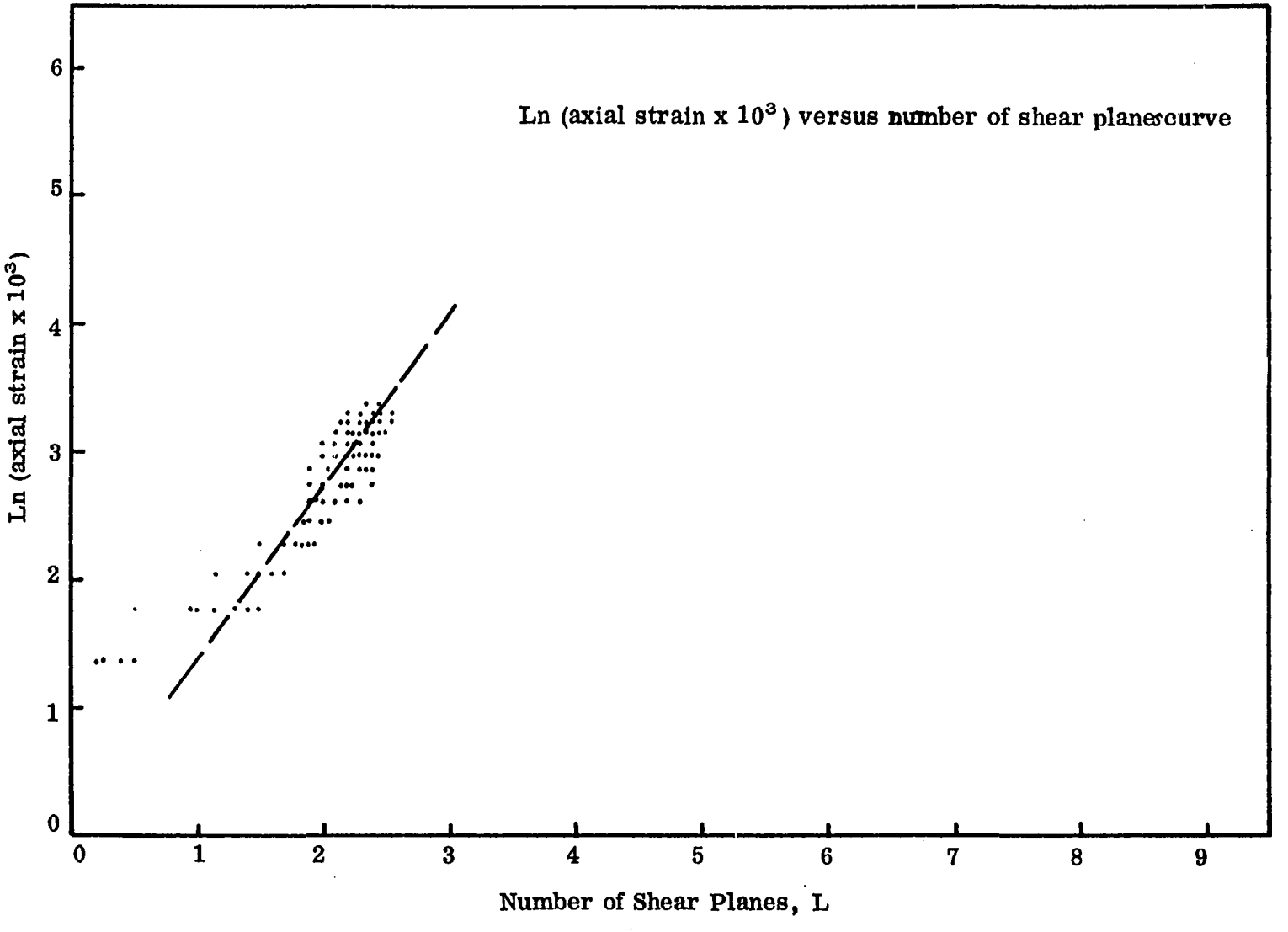

Figure 23. ℓn (axial strain x 10^3) versus number of shear planes curve

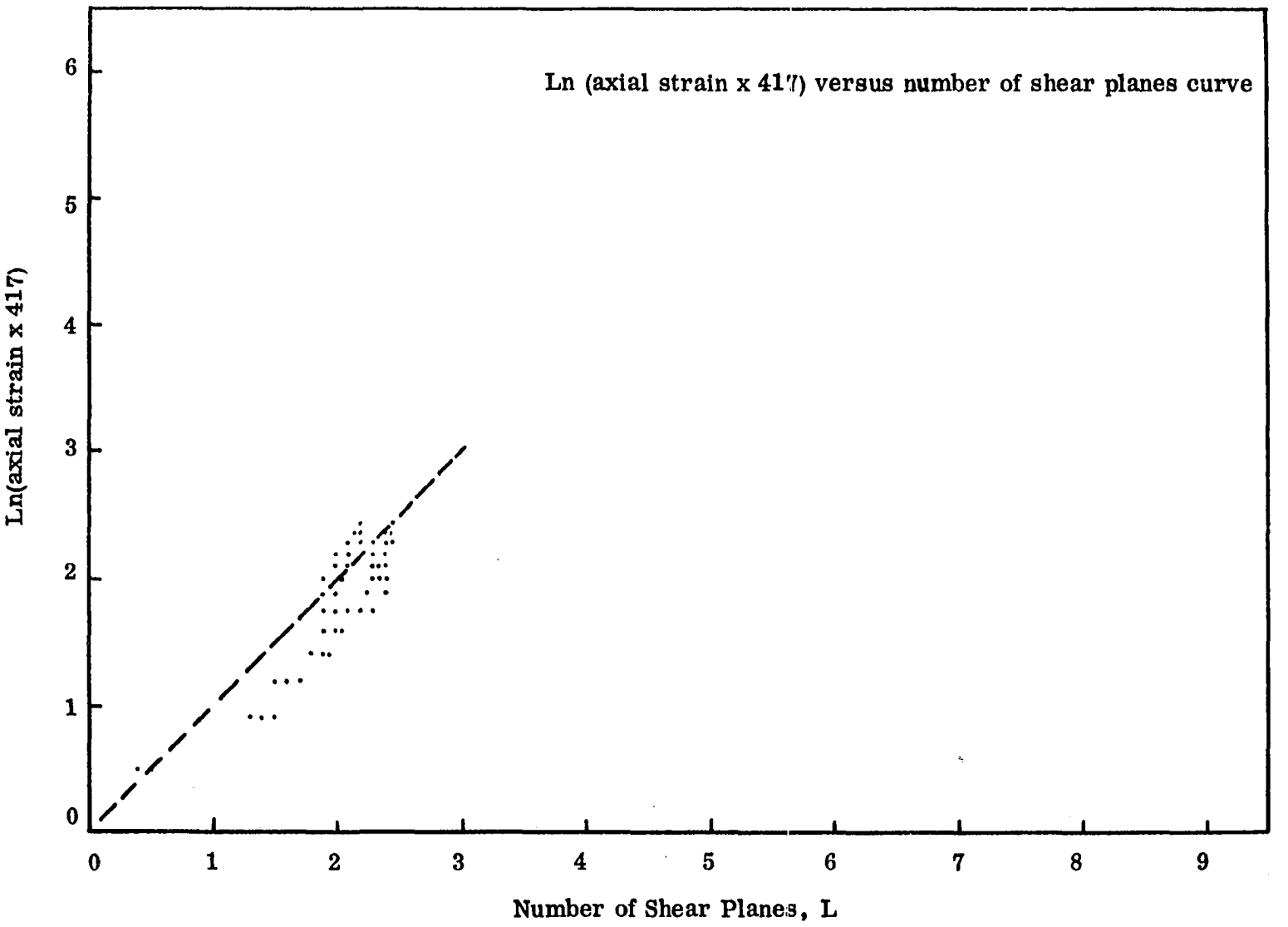

Figure 24. ℓn (axial strain x 417) versus number of shear planes curve

$$\frac{dv}{v_0} = \frac{\ell n\ 417\ \varepsilon_1}{(d)^{.33}}\left\{\frac{1}{\sin 2\lambda}\ \sin\left(2\lambda + \arctan\left[\frac{2}{(n-1)\varepsilon_1 \sin 2\lambda} - \cot 2\lambda\right]^{-1}\right) - 1\right\} \tag{50}$$

which should hold outside of the region of elastic deformation. Elastic deformations have been observed to be confined to the initial region of 0-0.2% axial strain.

TESTING OF THEORY

Testing of the Predicted Maximum Stress Ratio $(\frac{\sigma_1}{\sigma_3})_{max}$

To test Eq. 29, which expresses a relation between stress ratio $(\frac{\sigma_1}{\sigma_3})$ and axial strain (ε_1), the equation is reduced for maximum stress ratio $(\frac{\sigma_1}{\sigma_3})_{max}$ by substituting $\omega = 0$. The reduced equation becomes the same as Eq. 26. By substituting various values of coefficient of friction in Eq. 26, the corresponding predicted maximum stress ratios $(\frac{\sigma_1}{\sigma_3})_{max}$ were found and tabulated against the coefficient of friction in Table 3.

The experimental maximum stress ratios $(\frac{\sigma_1}{\sigma_3})$ are also tabulated against corresponding lateral stresses (σ_3) in Table 4 for all sizes of rods tested. To examine the effect of lateral stress (σ_3) on the maximum stress ratio, graphs of $(\frac{\sigma_1}{\sigma_3})_{max}$ versus lateral stress (σ_3) are plotted. A very slight and linear trend of increasing $(\frac{\sigma_1}{\sigma_3})_{max}$ with increasing lateral stress (σ_3) has been observed. This trend is particularly conspicuous in the case of 1"-diameter and 1/8"-diameter rods; but, in the case of other sizes of rods, this trend is very slight (Fig. 25).

The coefficient of friction was evaluated experimentally for the 1"-diameter rods, and plotted versus normal load in Fig. 1d. Data with the 1/8"-diameter rods are less reliable, due to the presence of teflon side plates in early tests.

Table 4. Maximum stress ratio (experimental)

Serial number	Material	Diameter of rods (inch)	σ_3 (psi)	$(\frac{\sigma_1}{\sigma_3})_{max}$
1	Cold rolled	1	10	4.13
2	steel		20	4.62
3			30	4.40
4			40	4.53
5			50	4.72
6		3/4	10	4.20
7			20	4.00
8			30	4.27
9			40	4.28
10			50	4.28
11		1/2	10	3.60
12			20	3.90
13			30	3.93
14			40	3.95
15			50	4.00
16		1/4	10	3.80
17			20	3.60
18			30	3.93
19			40	4.08
20			50	4.00
21		1/8	10	3.6
22			20	3.7
23			30	3.9
24			40	4.1
25			50	4.0
26	Teflon	3/4	10	3.1
27			20	3.18
28			30	3.21
29			40	3.24
30			50	3.36

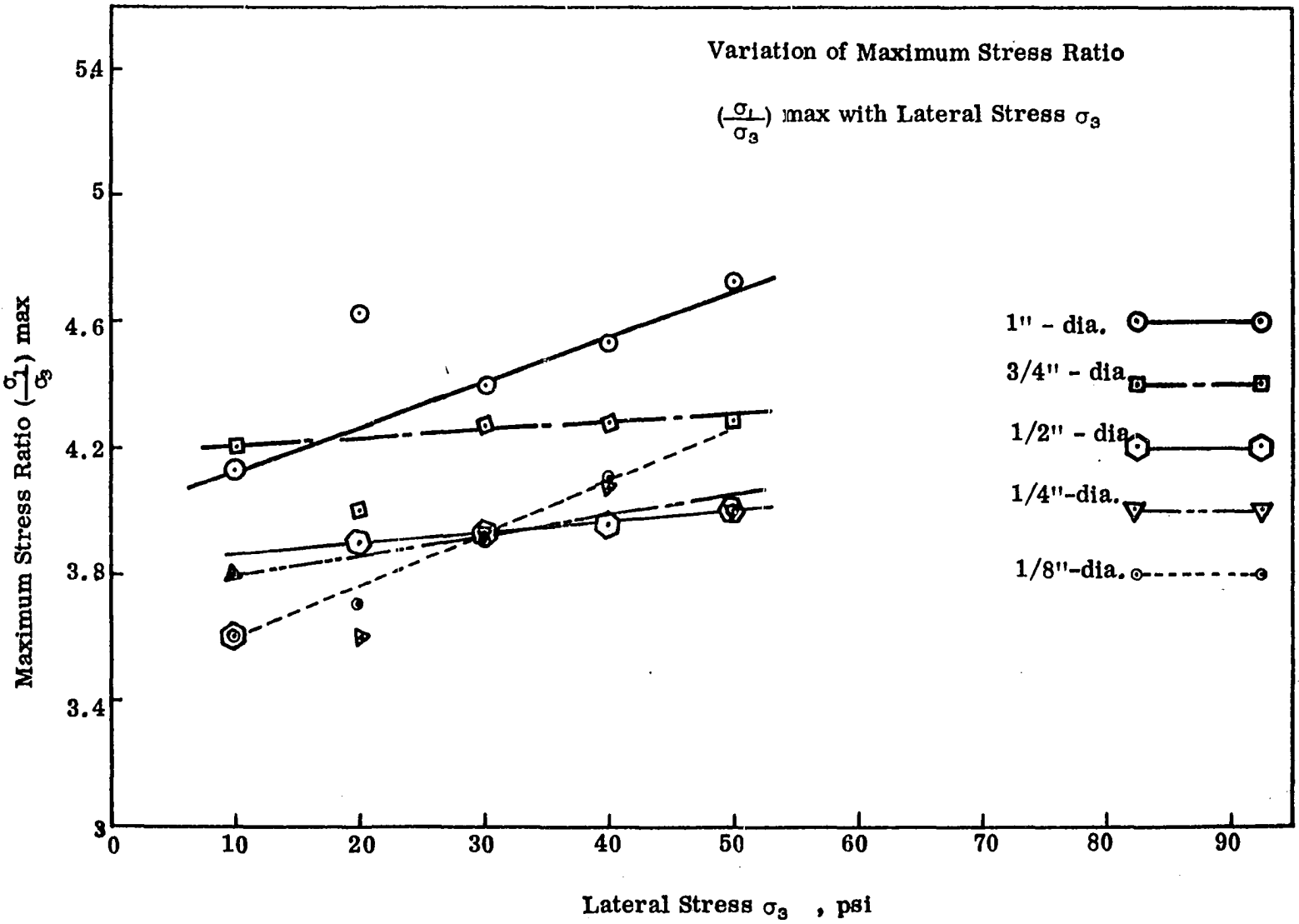

Figure 25. Variation of maximum stress ratio with σ_3

As can be seen from the experimental coefficient of friction graph, the 1"-diameter rods have a coefficient of friction of 0.2. Table 3 gives a value of 4.4 for the theoretical maximum stress ratio $(\frac{\sigma_1}{\sigma_3})_{max}$ corresponding to coefficient of friction 0.2; this value compares well with the experimental $(\frac{\sigma_1}{\sigma_3})_{max}$ data in Table 4 for 1"-diameter rods. This agreement is particularly satisfying when it is realized that the coefficient of friction changes at almost every point on the surface of the same rod.

Testing of the Predicted Stress Ratio $(\frac{\sigma_1}{\sigma_3})$ in the Post-Failure Region

To test Eq. 29 in the post-failure region, curves of the theoretical stress ratio $(\frac{\sigma_1}{\sigma_3})$ against axial strain (ε_1) have been drawn for various levels of coefficient of friction. For drawing the above curves, the axial strain at the maximum stress ratio $(\frac{\sigma_1}{\sigma_3})_{max}$ was assumed to be zero, because we are assuming that dilatancy begins after the maximum stress ratio is reached. It can be seen from Eq. 29 that, for a given distribution factor λ and coefficient of friction f, $(\frac{\sigma_1}{\sigma_3})$ varies with ω, ω representing the dilatancy of granular mass [Fig. 22b]. Refer to Fig. 2b.

The above theoretical curves are superimposed on experimental stress ratio curves in Figs. 27-56. This superimposition has been done in such a way that the point on the theoretical stress ratio $(\frac{\sigma_1}{\sigma_3})$ curve corresponding to $\omega = 0$ or, in other words, the point of maximum stress ratio $(\frac{\sigma_1}{\sigma_3})_{max}$,

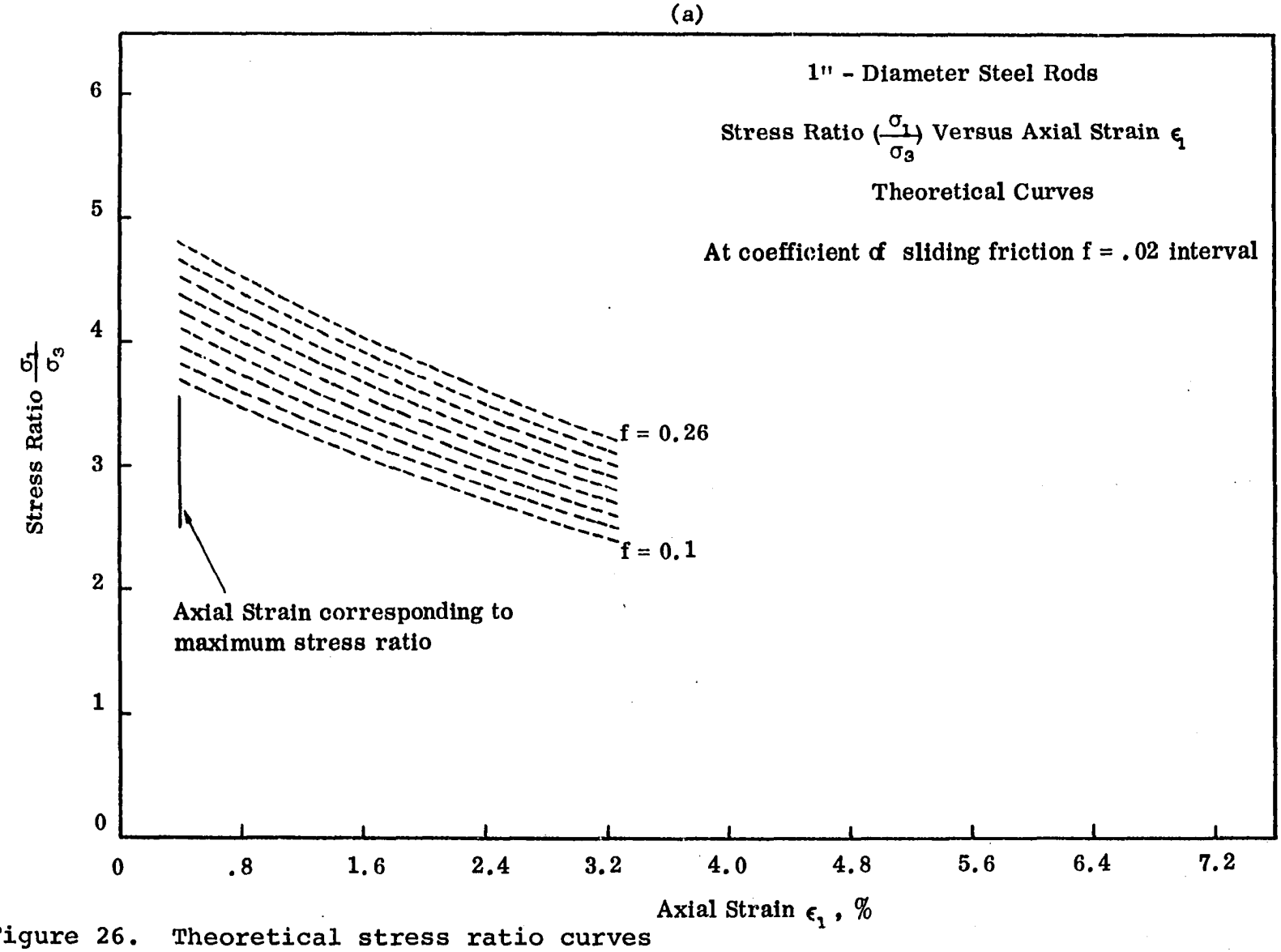

Figure 26. Theoretical stress ratio curves

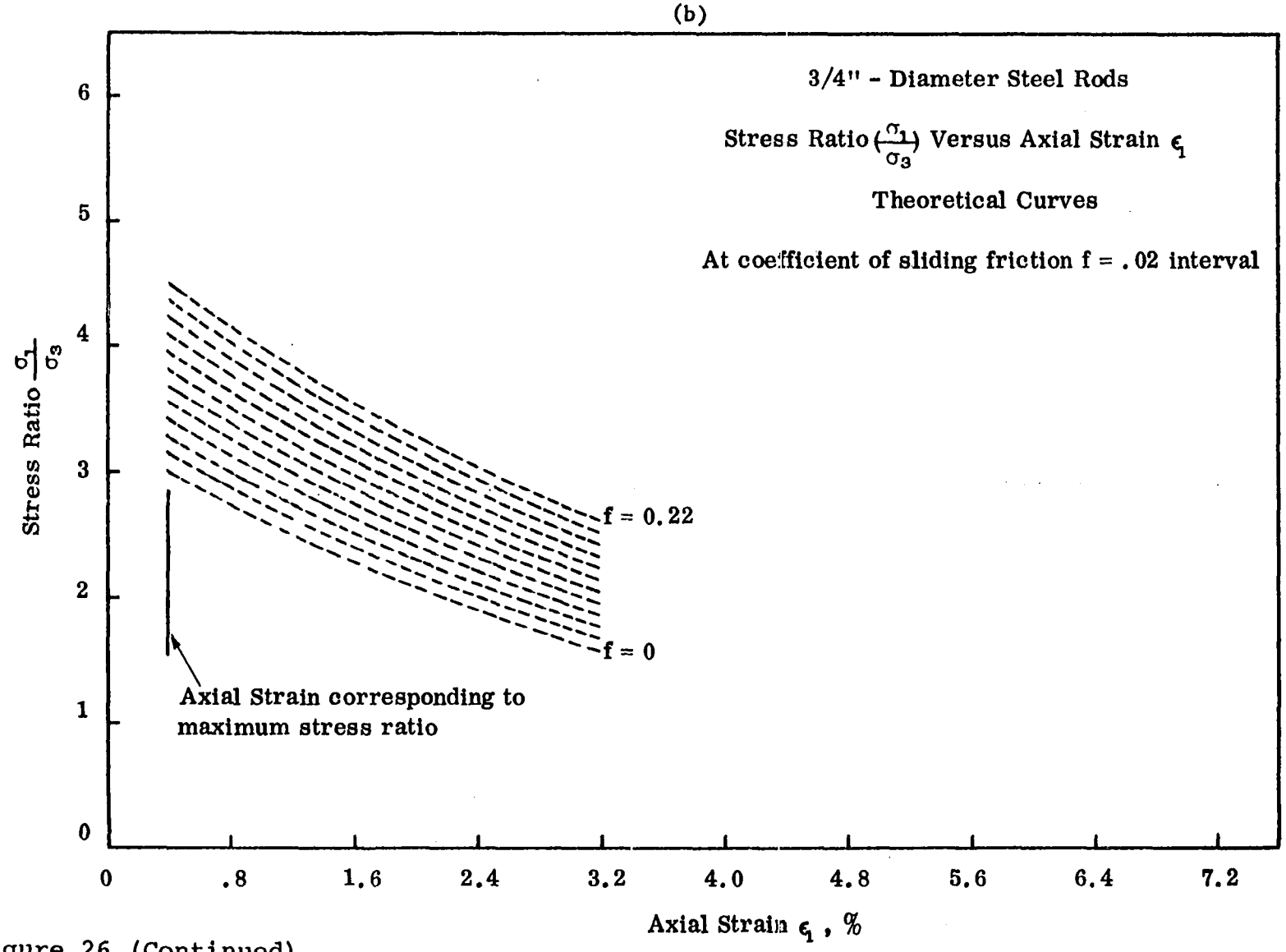

Figure 26 (Continued)

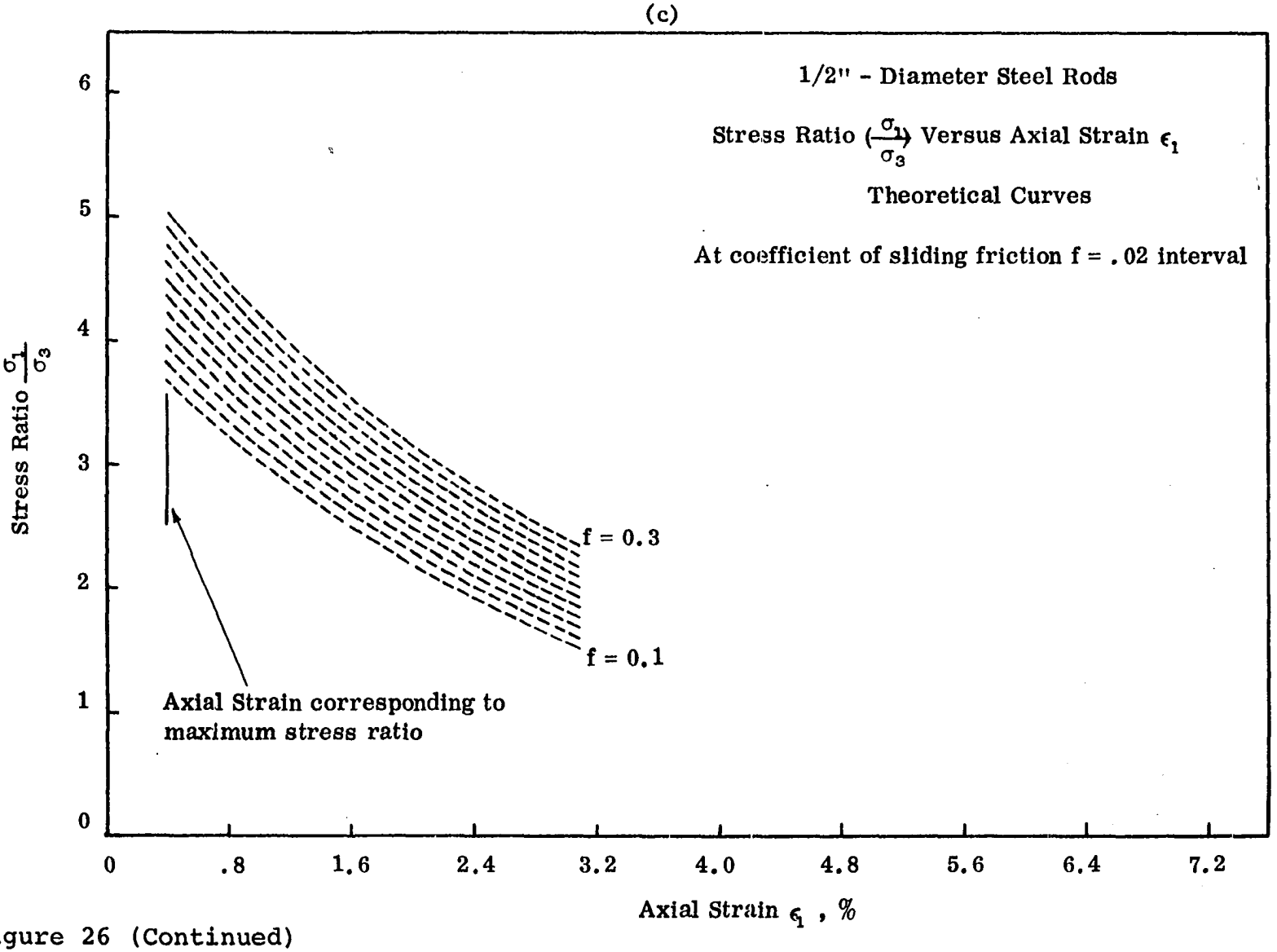

Figure 26 (Continued)

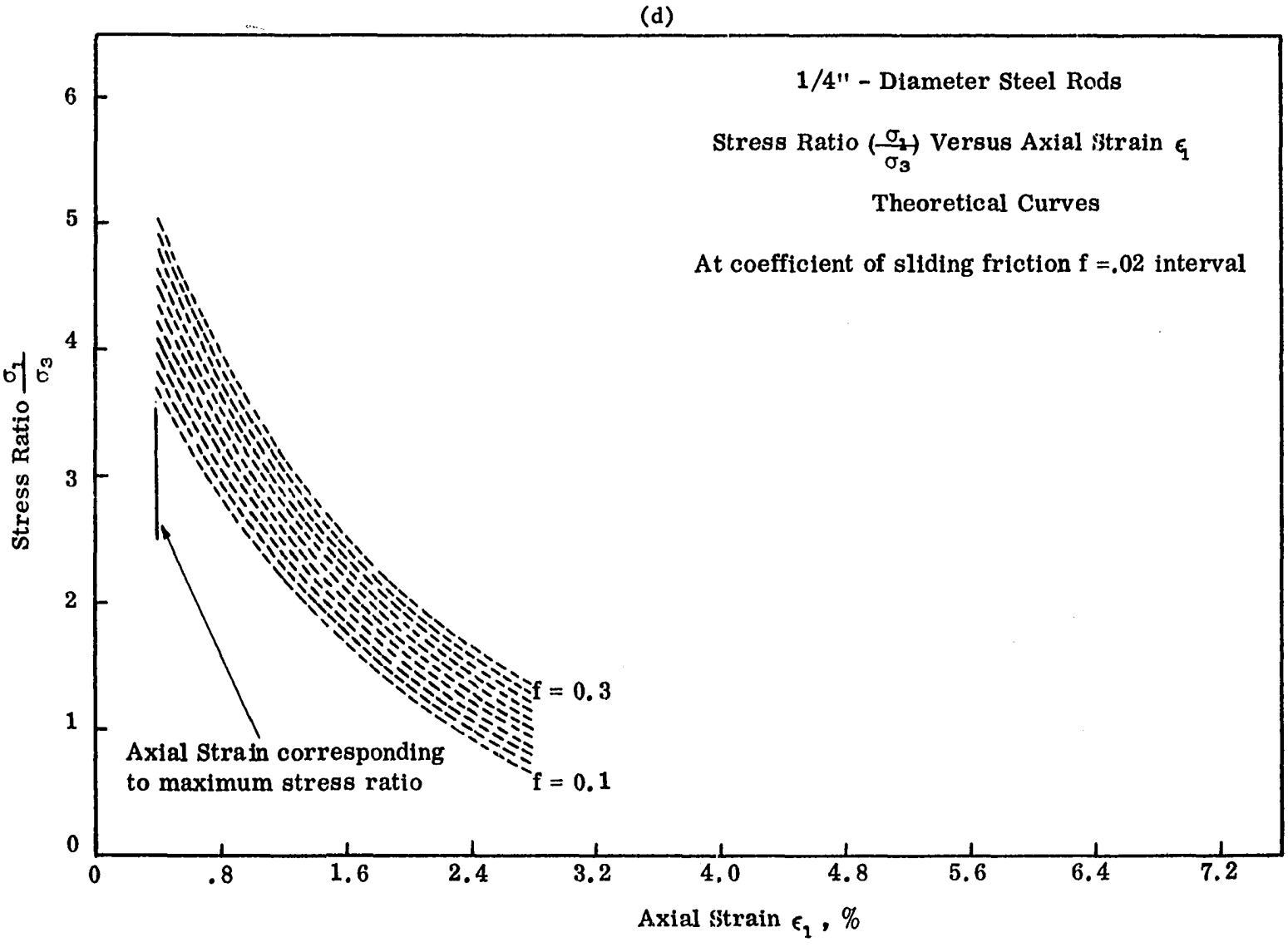

Figure 26 (Continued)

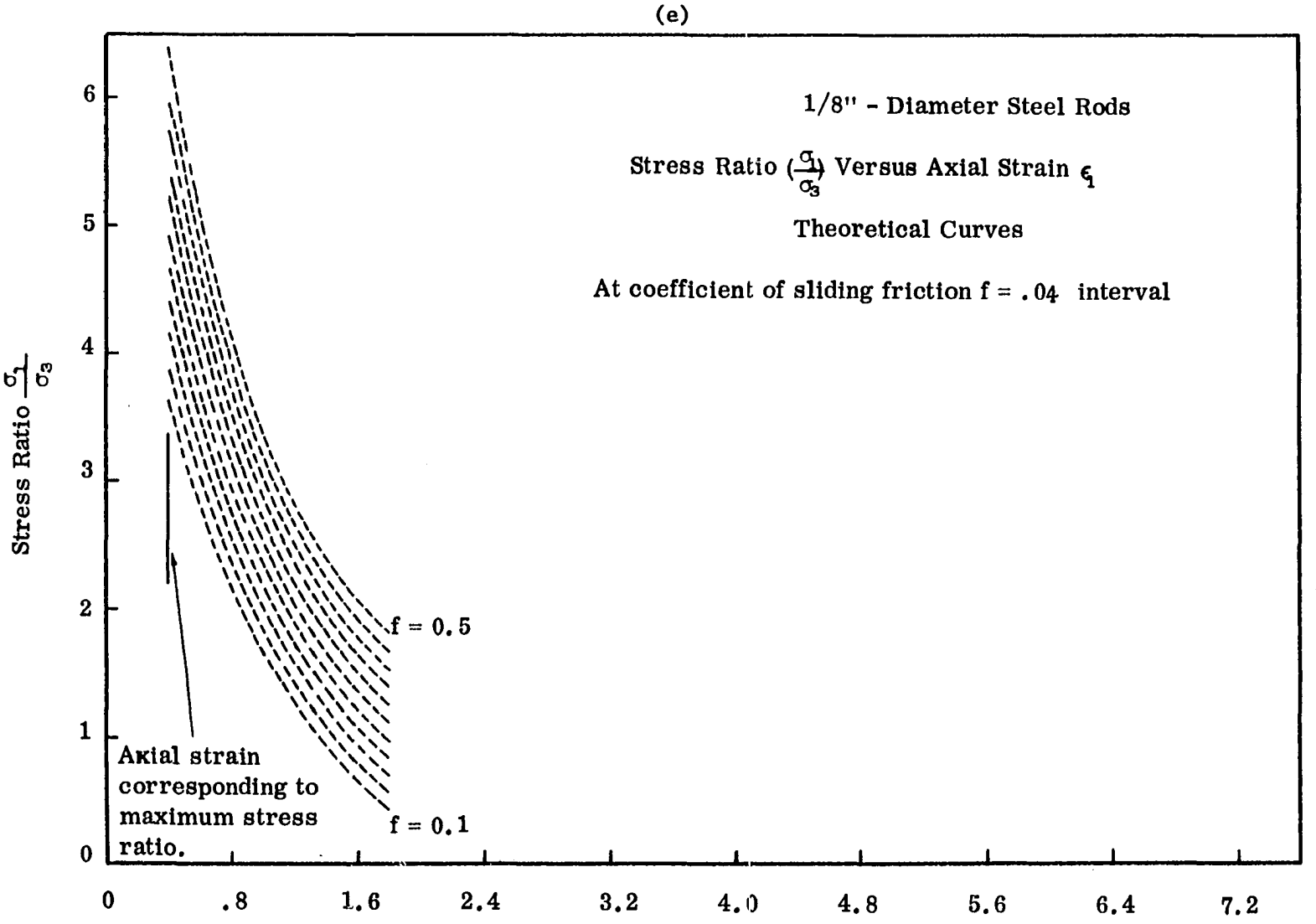

Figure 26 (Continued)

coincided with the point of maximum stress ratio $(\frac{\sigma_1}{\sigma_3})_{max}$ on the experimental stress ratio $(\frac{\sigma_1}{\sigma_3})$ versus the axial strain (ε_1) curve. The theoretical formulation for the stress ratio $(\frac{\sigma_1}{\sigma_3})$ does not take into account the arrested slip, which means that slip is assumed to be taking place only on a definite shear plane. The theoretical and experimental stress ratio curves are in good agreement in the case of larger diameter rods, i.e., 1" and 3/4".

From examination of the experimental versus theoretical curves, failure may be hypothesized to take place in the following manners:

1. Shear slip between the semirigid groups may confine itself to one plane throughout the post-maximum stress ratio $(\frac{\sigma_1}{\sigma_3})_{max}$ dilation. In this case, if the coefficient of sliding friction stays practically constant on the surfaces of the particles (rods), which means surfaces are macroscopically uniform, the experimental stress ratio $(\frac{\sigma_1}{\sigma_3})$ curve should coincide with one of the theoretical stress ratio $(\frac{\sigma_1}{\sigma_3})$ curves, depending upon the particular value of the coefficient of friction. If the coefficient of friction is changing chaotically from point to point on the surfaces of particles to such an extent that even a reasonable statistically constant value of coefficient of friction is unobtainable, then even if the slip is

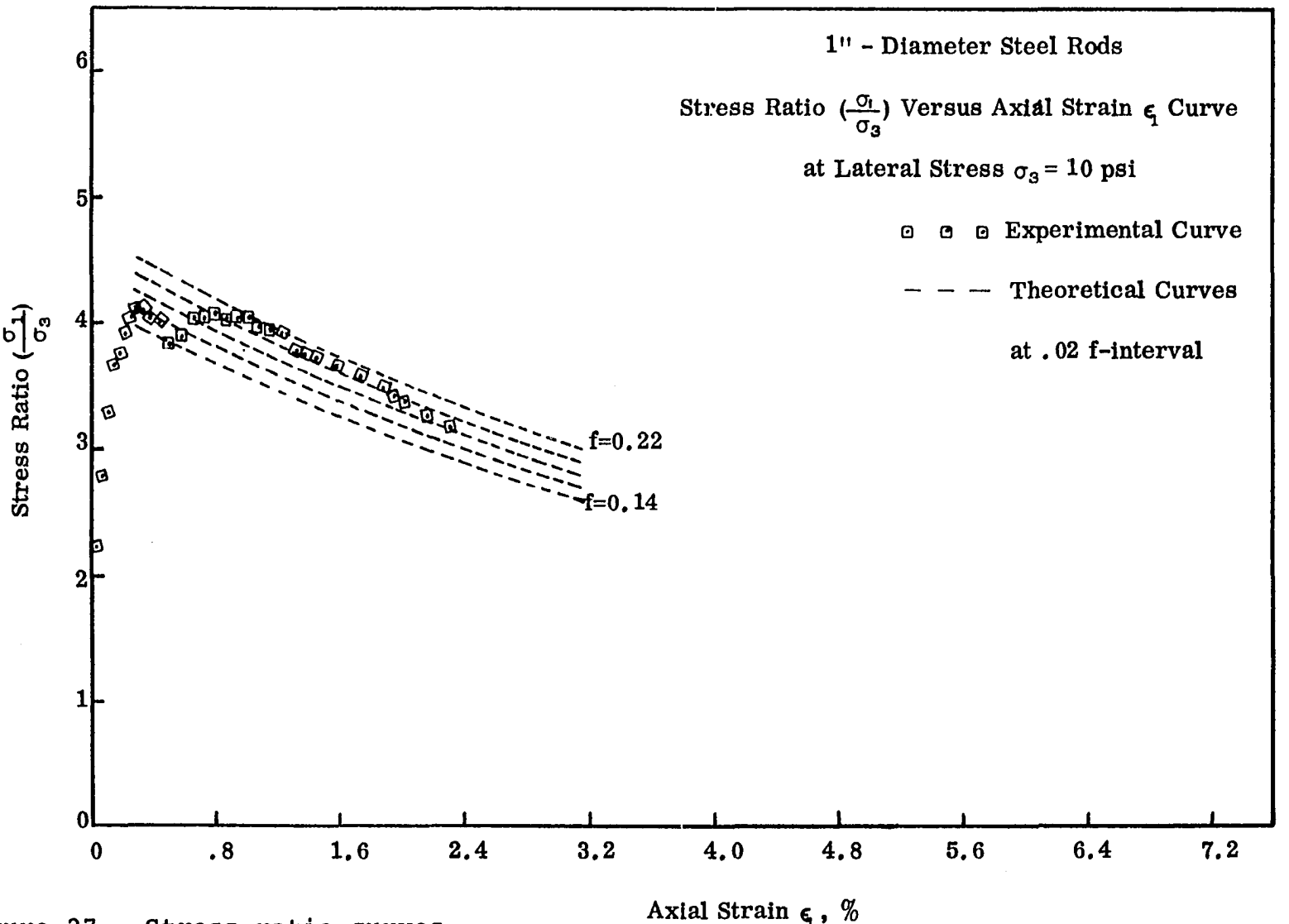

Figure 27. Stress ratio curves

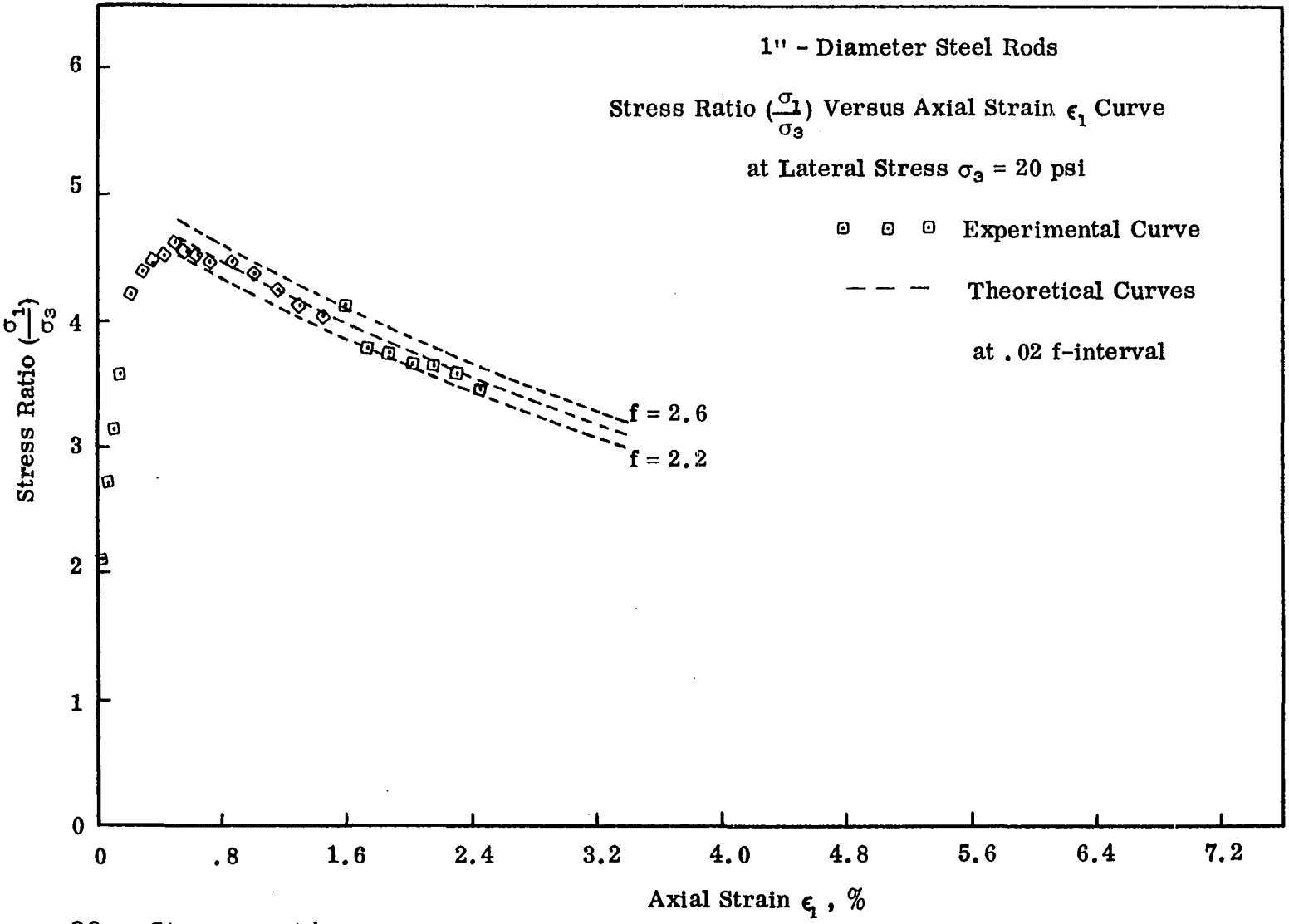

Figure 28. Stress ratio curves

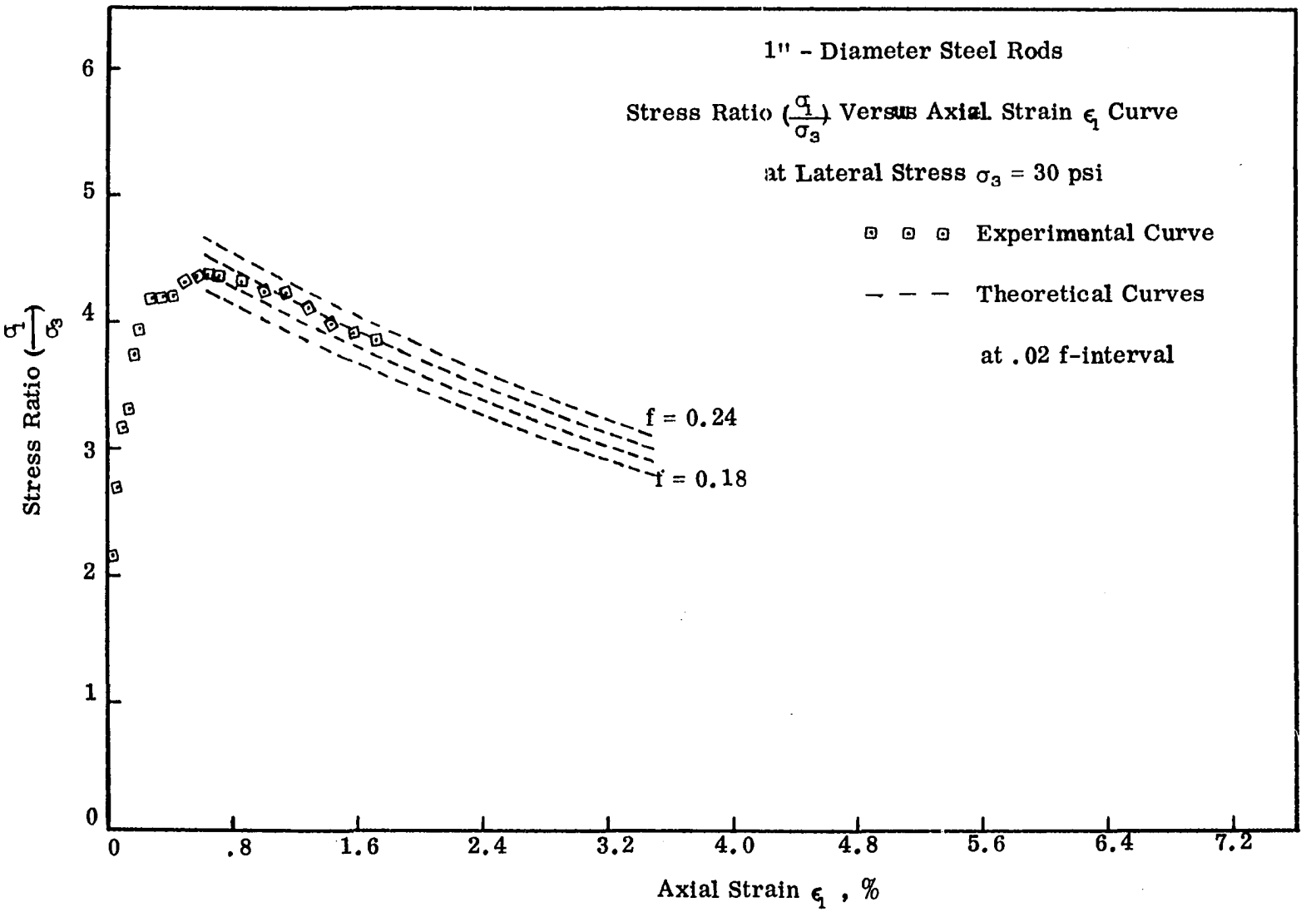

Figure 29. Stress ratio curves

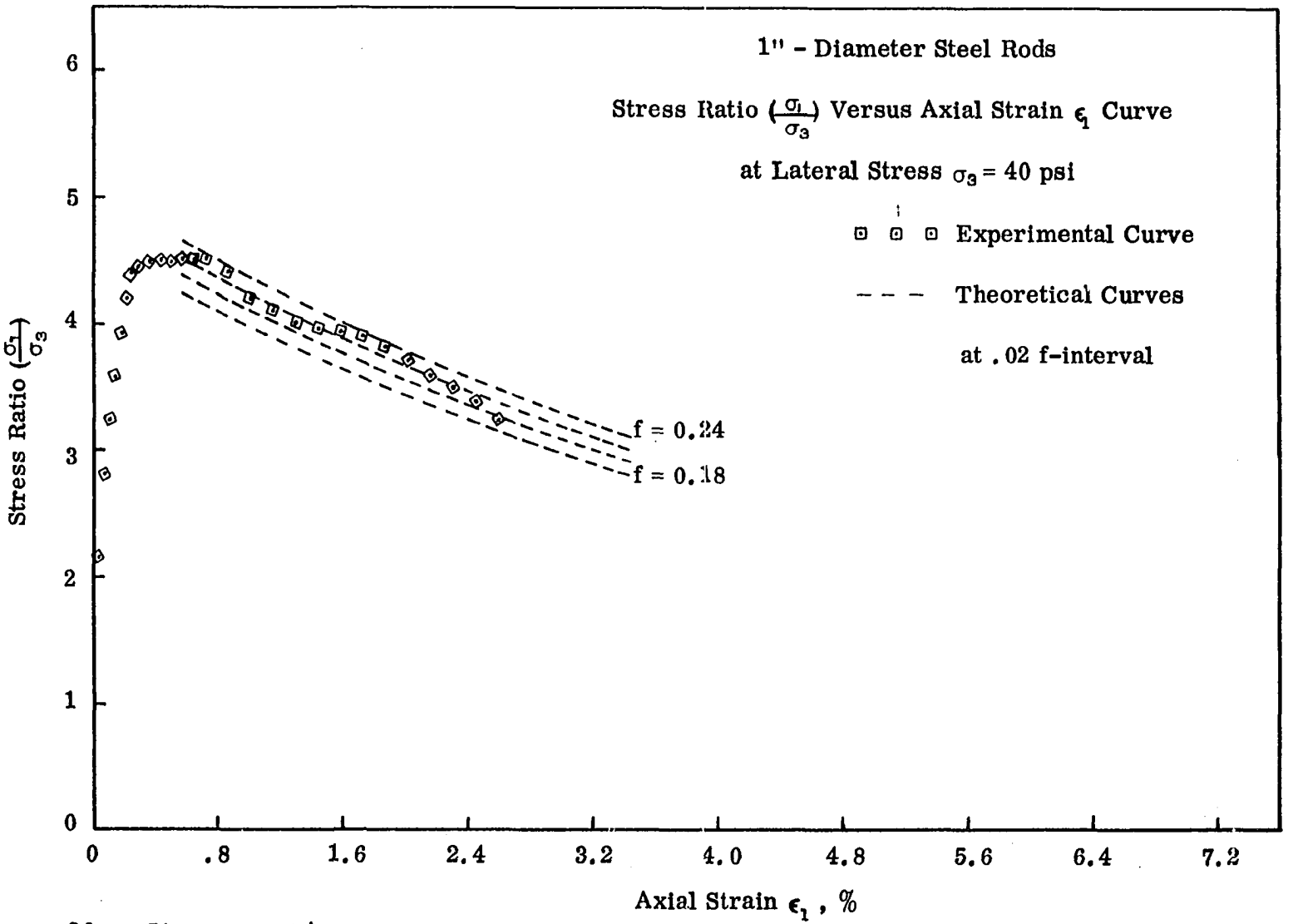

Figure 30. Stress ratio curves

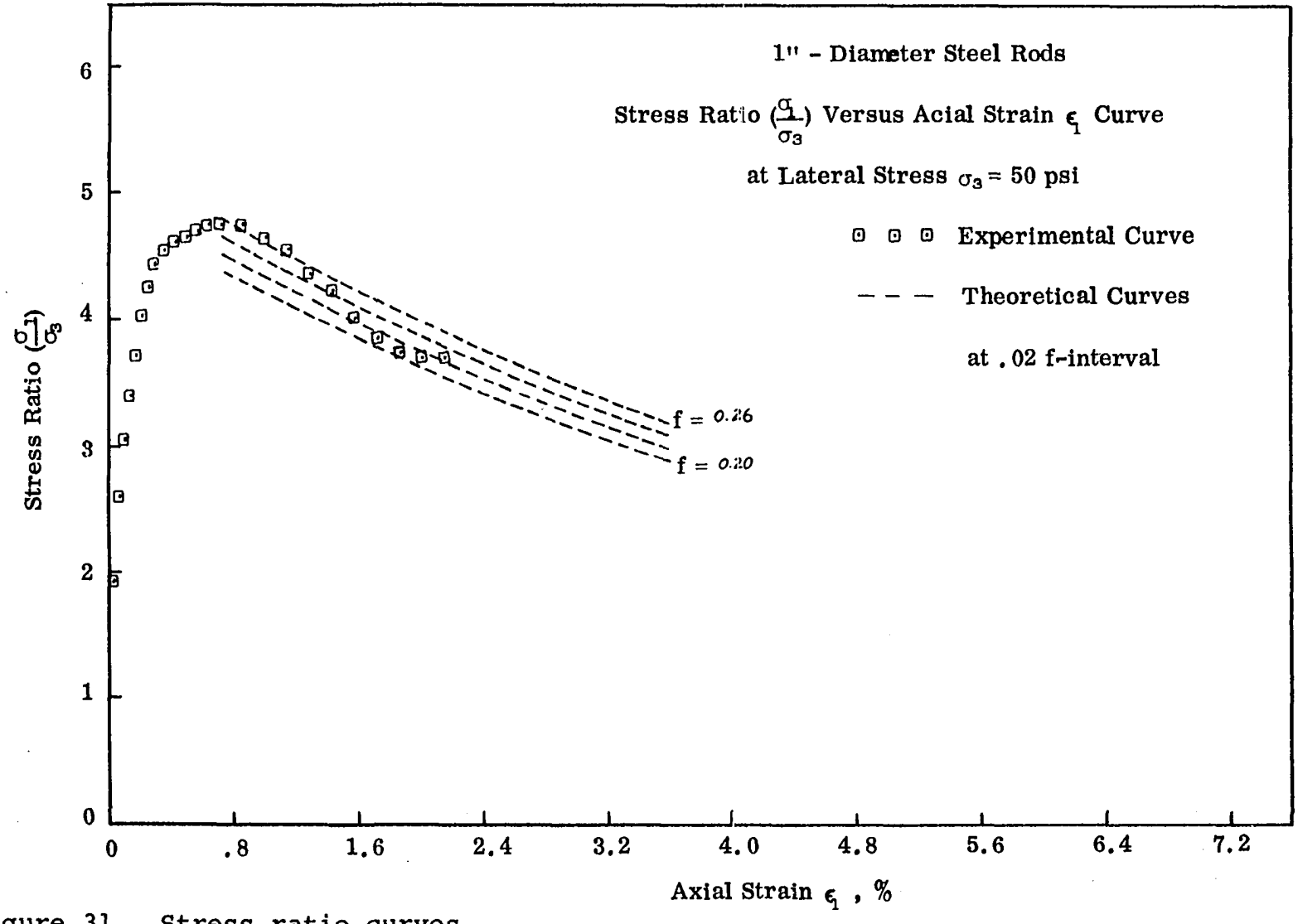

Figure 31. Stress ratio curves

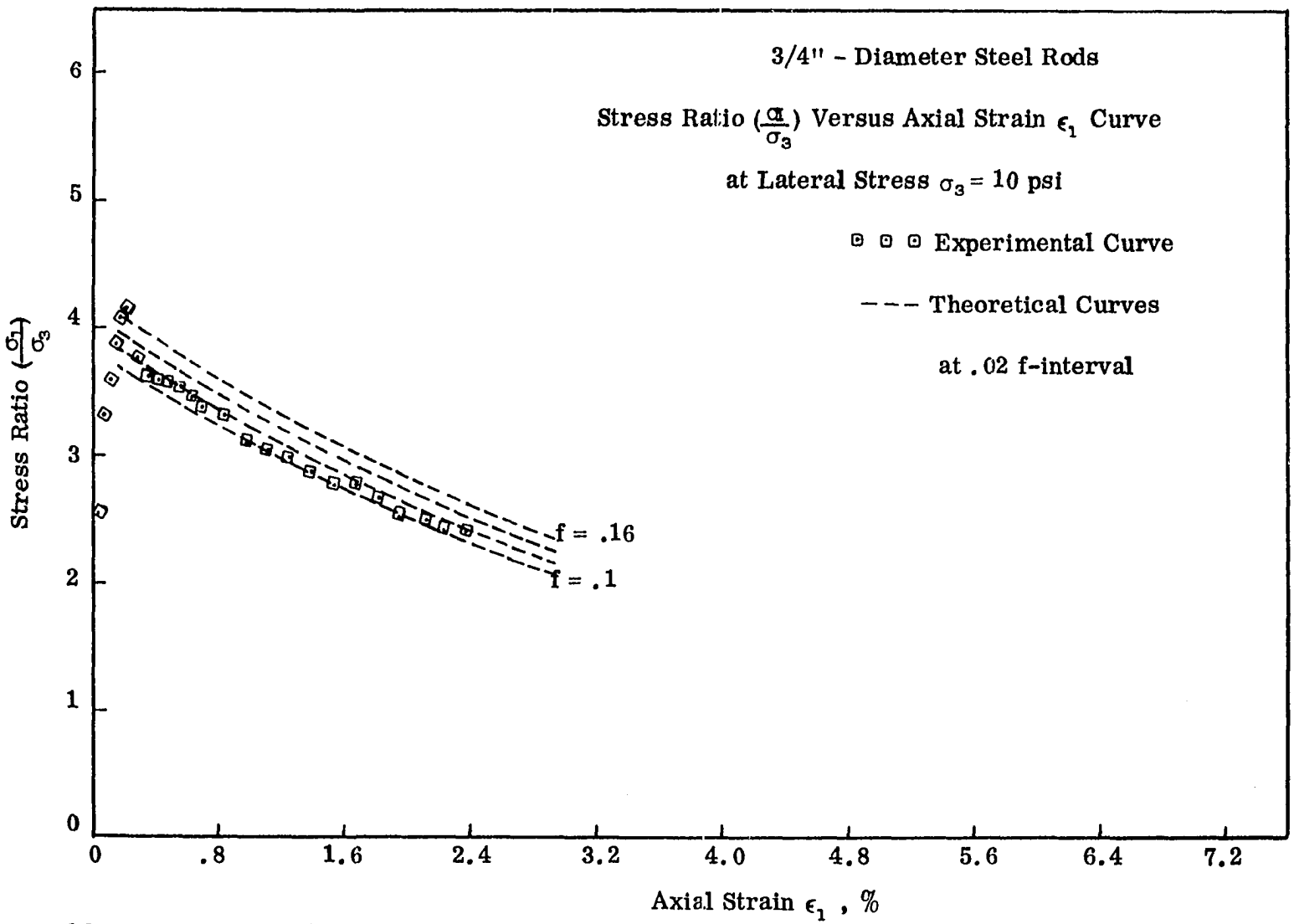

Figure 32. Stress ratio curves

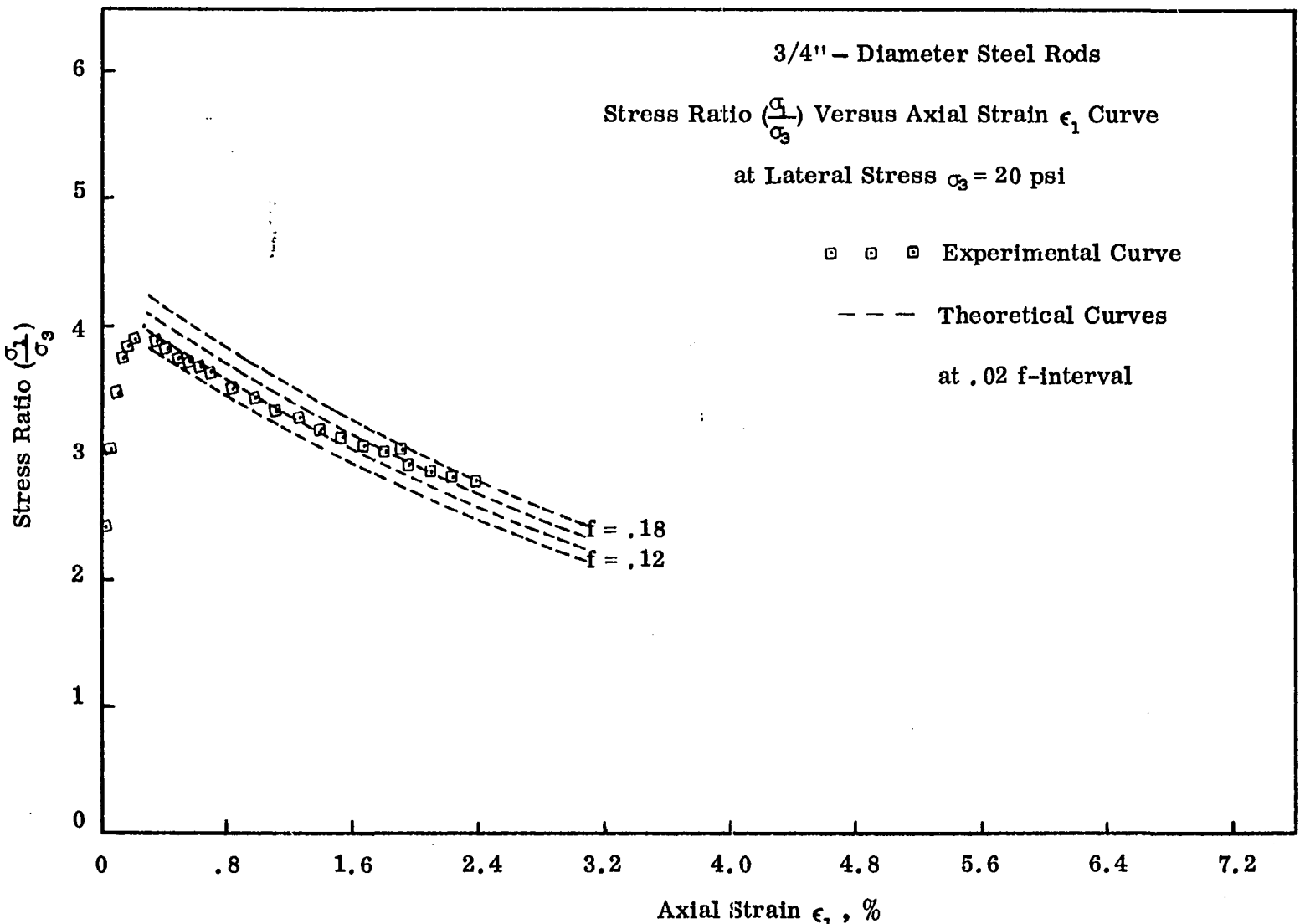

Figure 33. Stress ratio curves

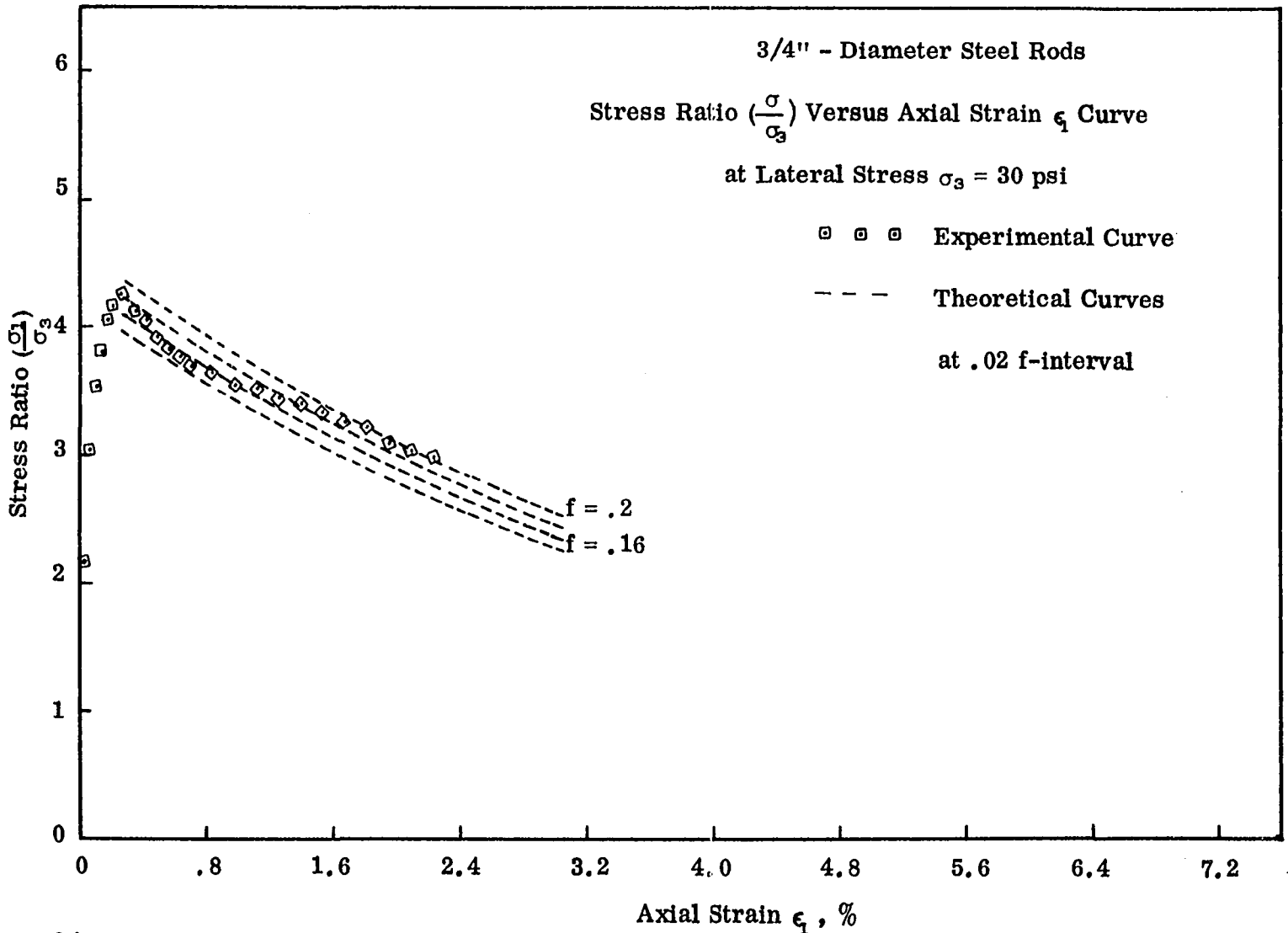

Figure 34. Stress ratio curves

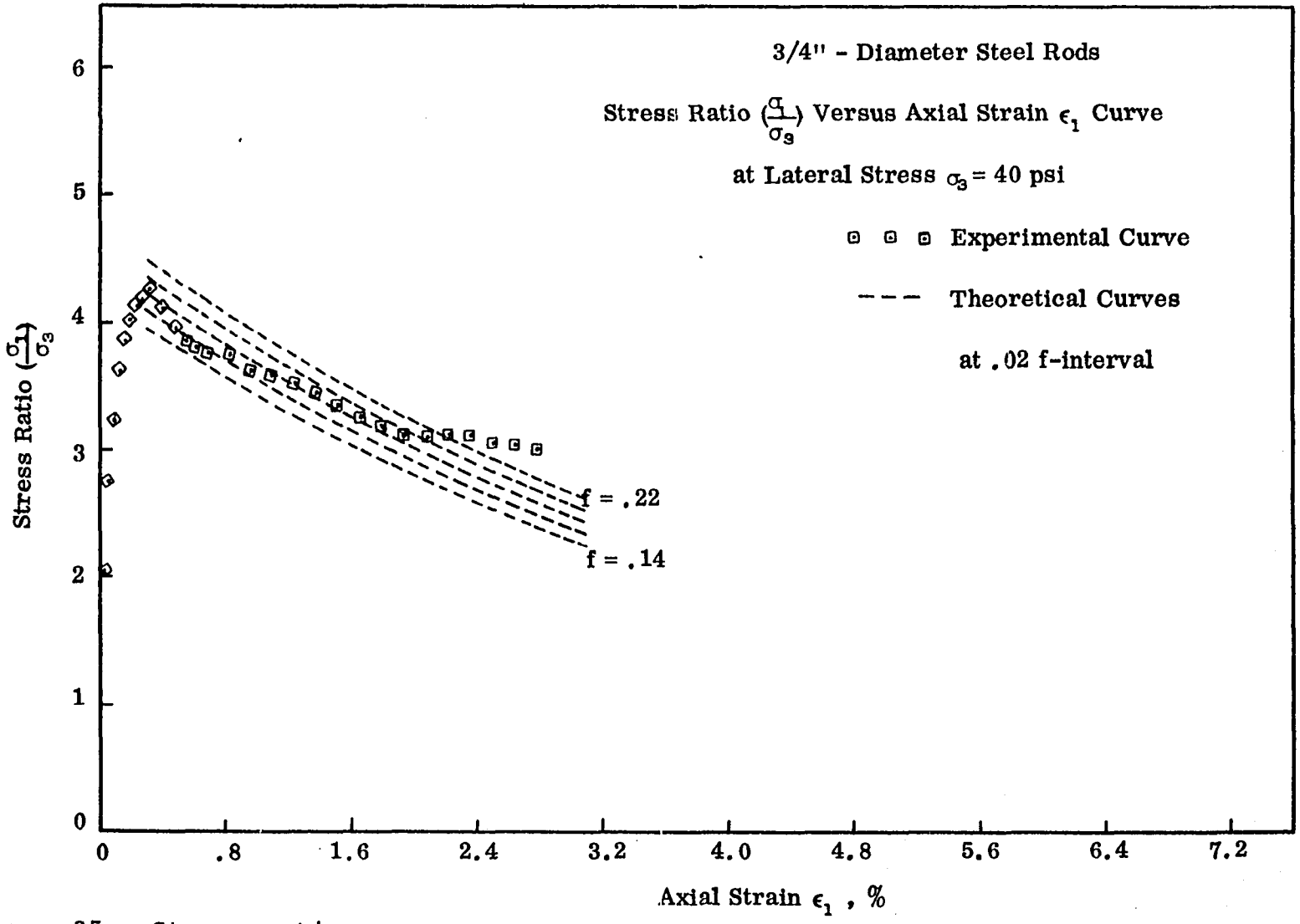

Figure 35. Stress ratio curves

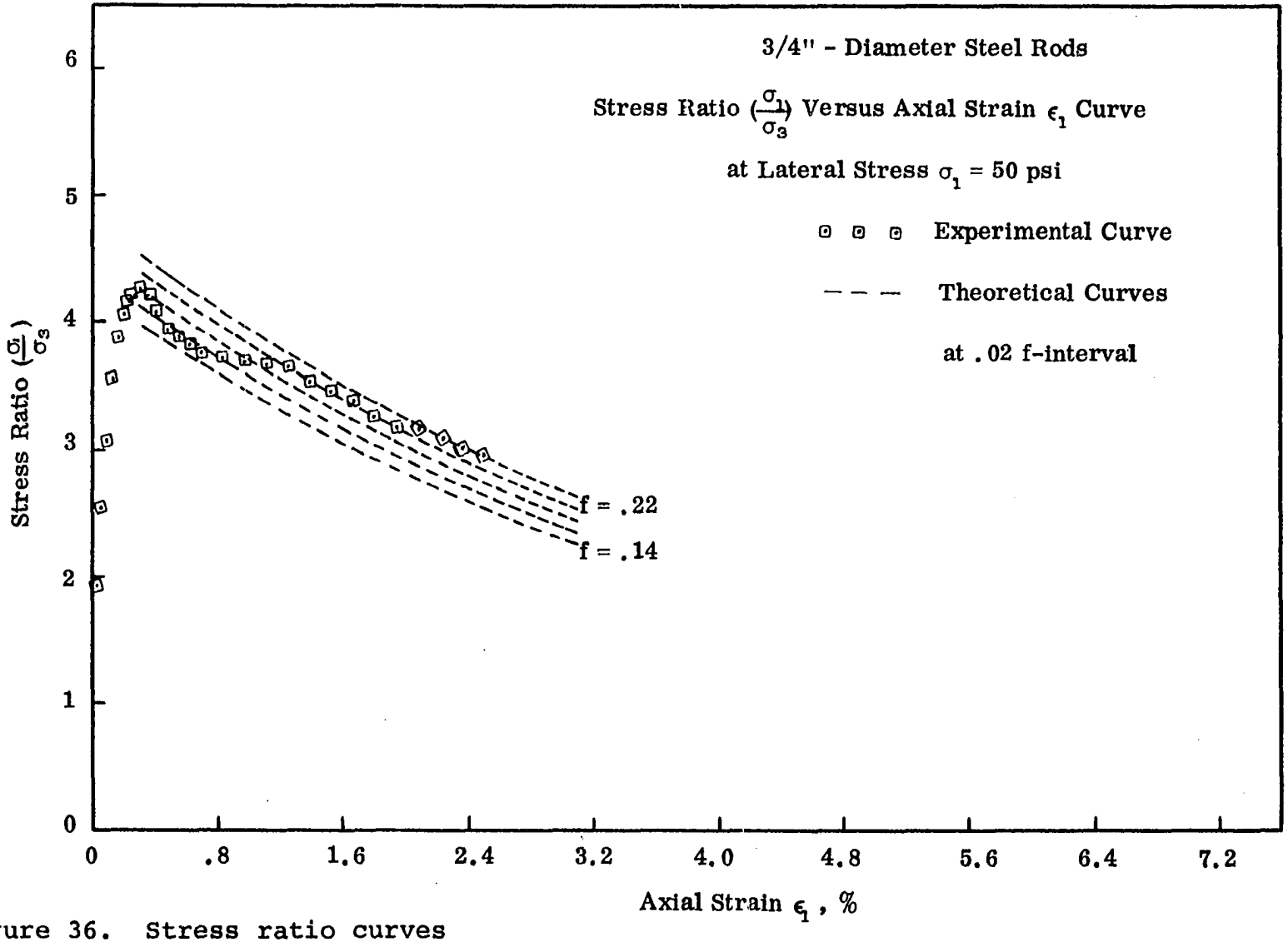

Figure 36. Stress ratio curves

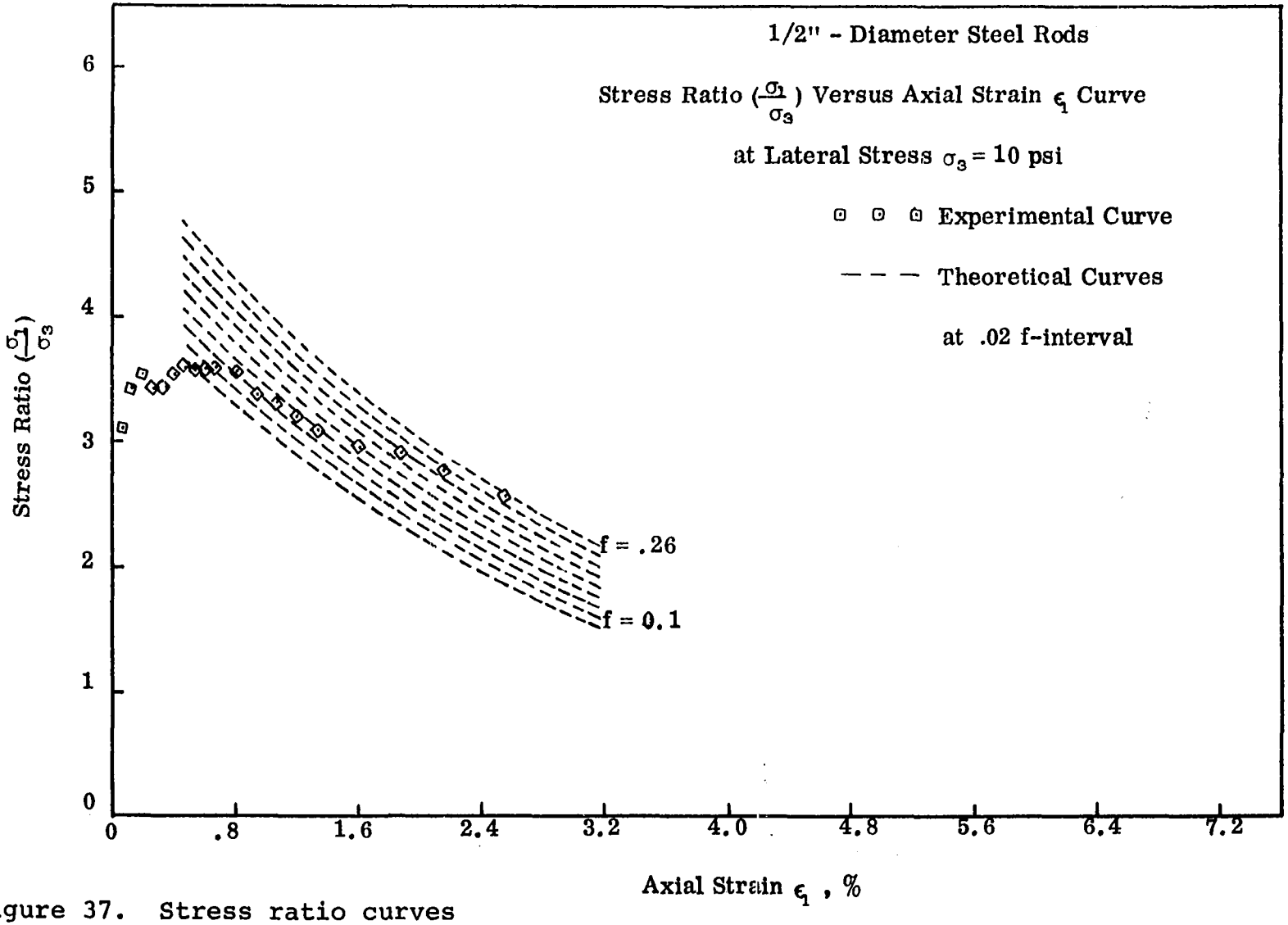

Figure 37. Stress ratio curves

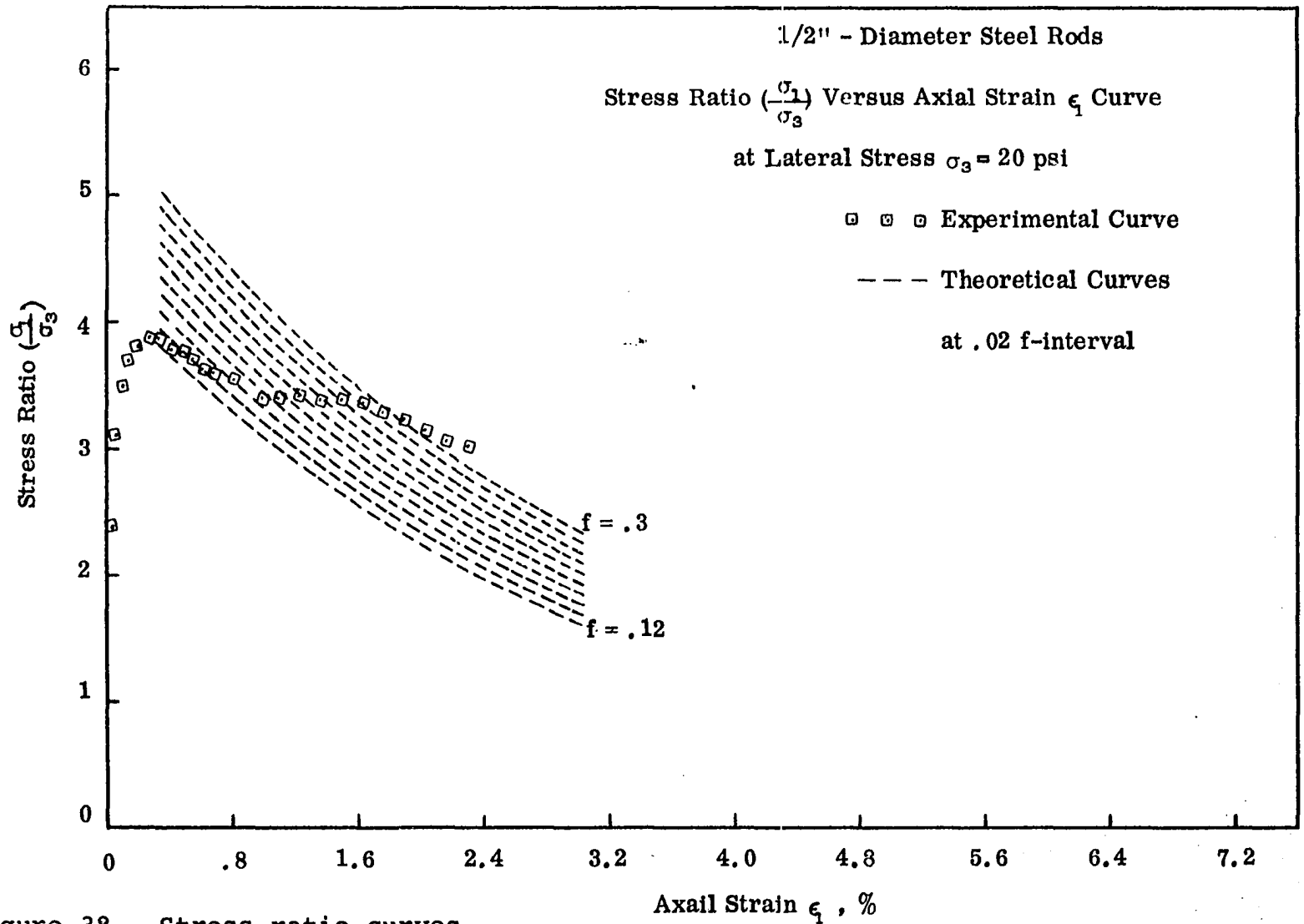

Figure 38. Stress ratio curves

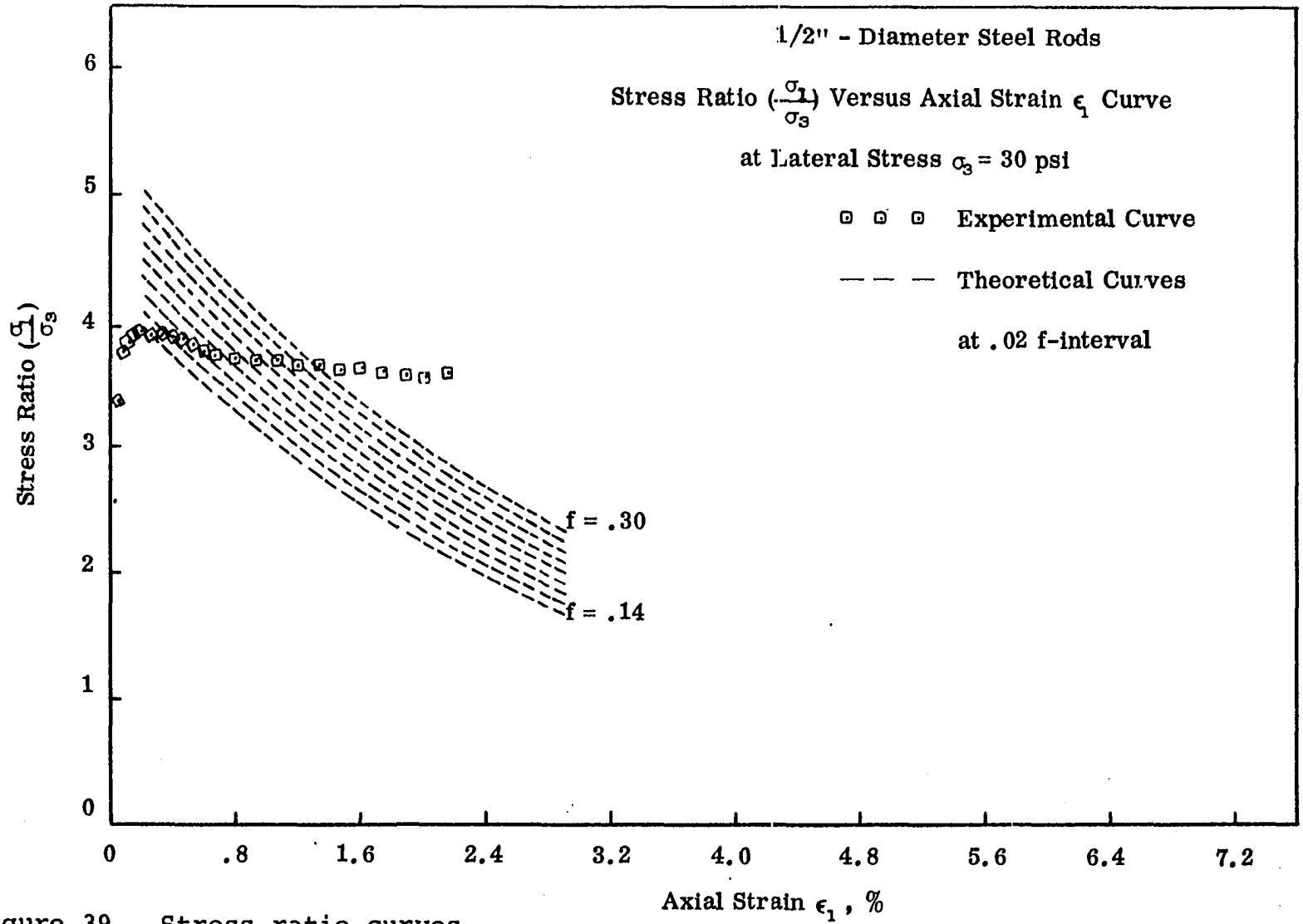

Figure 39. Stress ratio curves

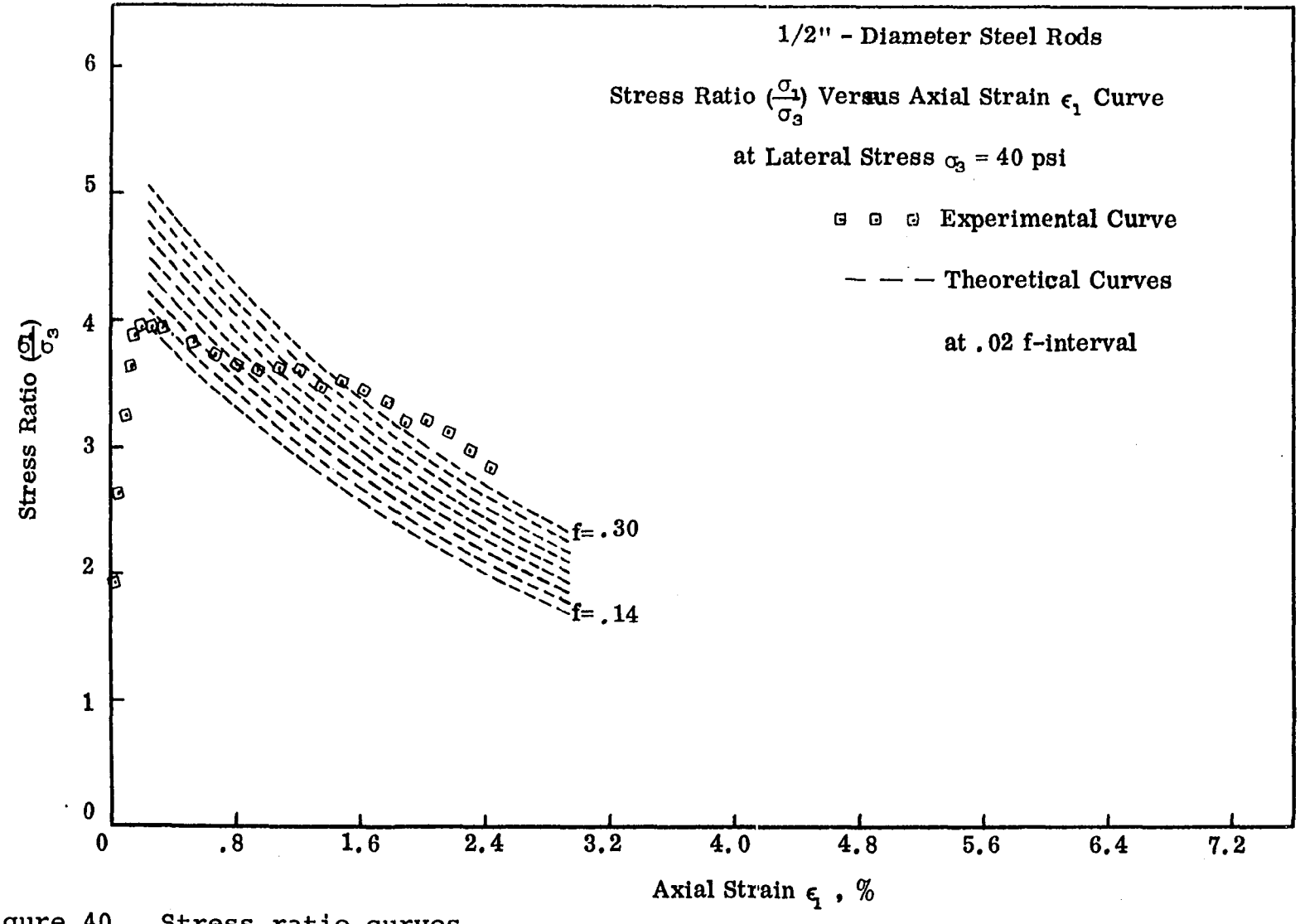

Figure 40. Stress ratio curves

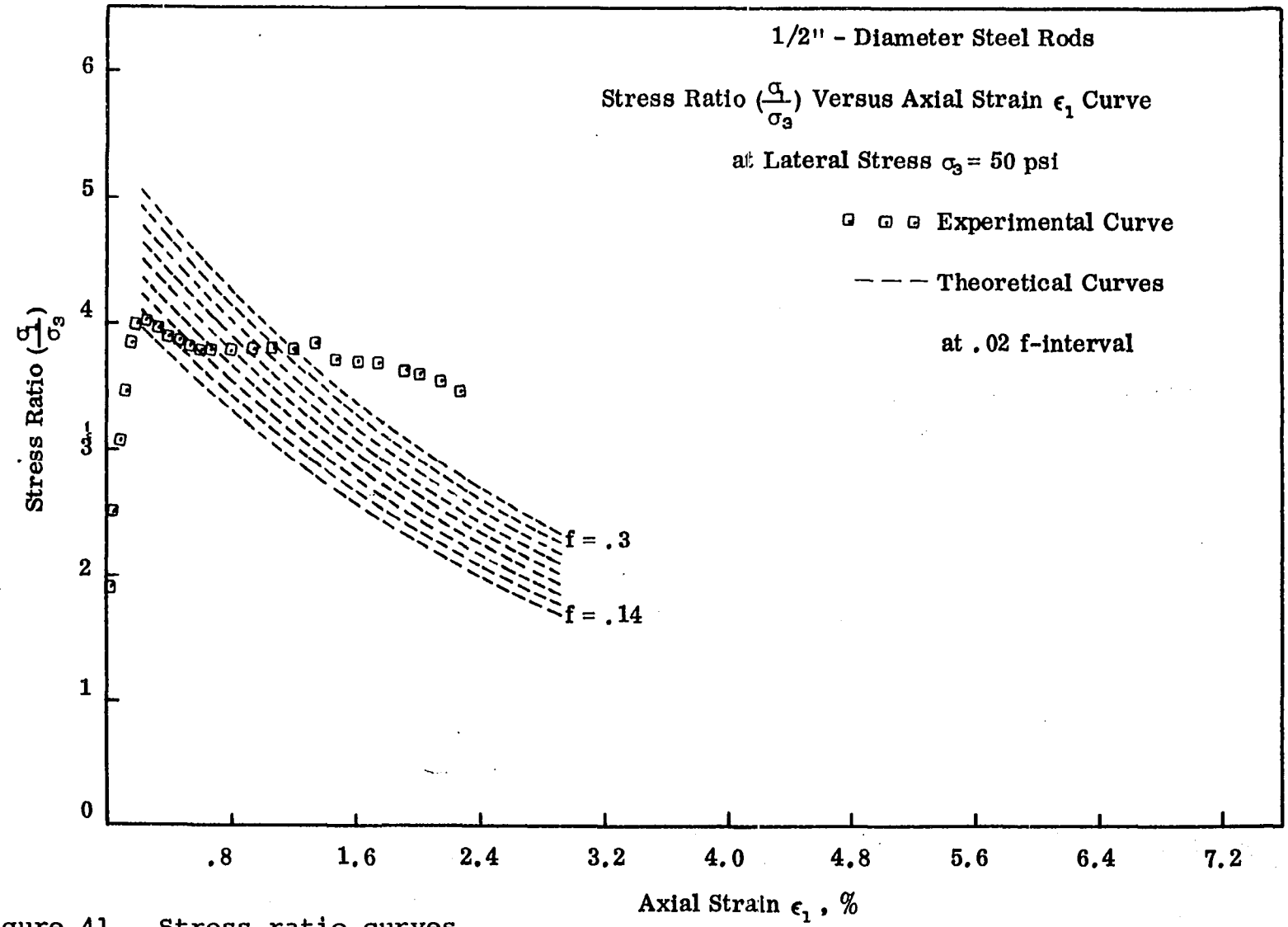

Figure 41. Stress ratio curves

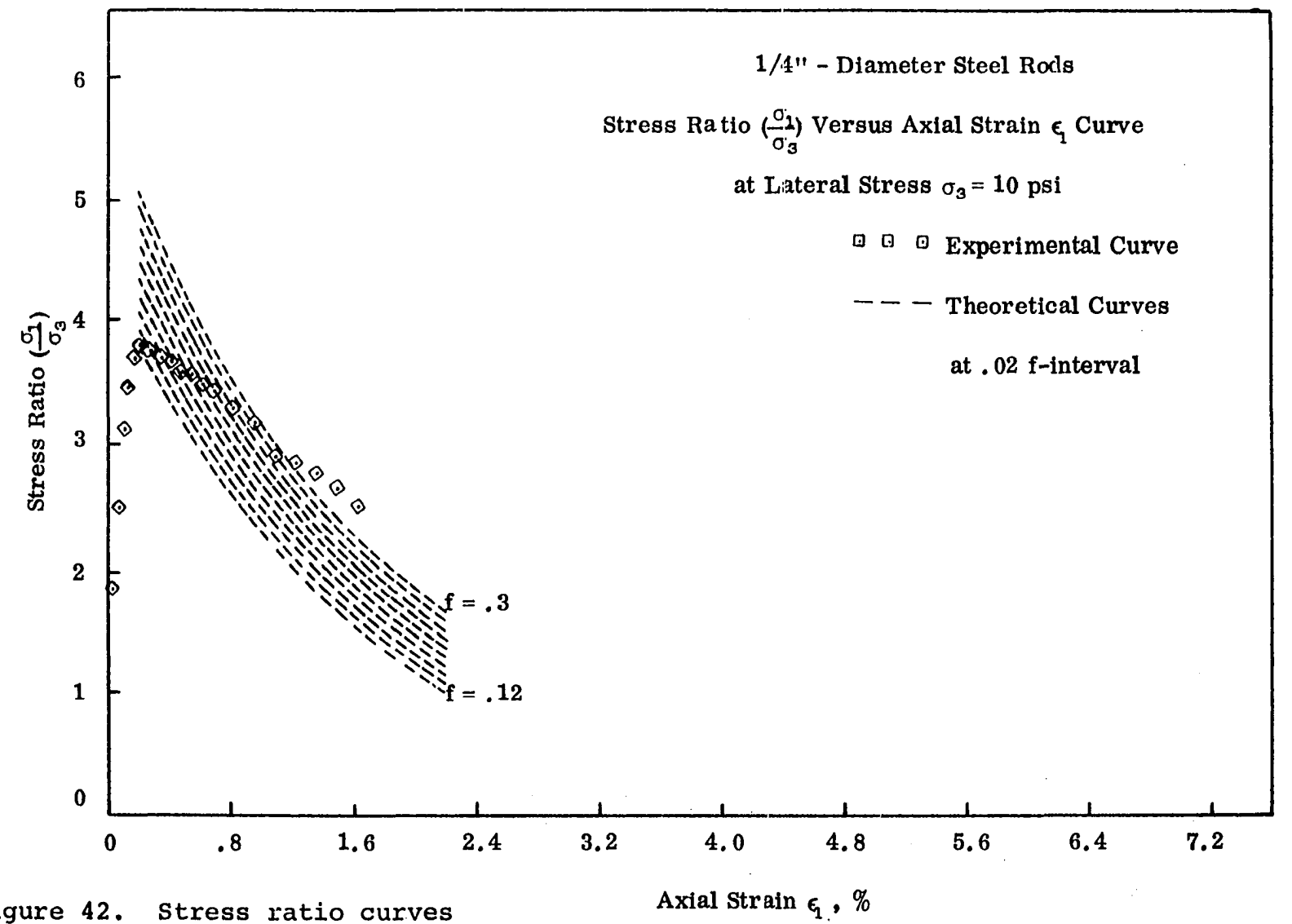

Figure 42. Stress ratio curves

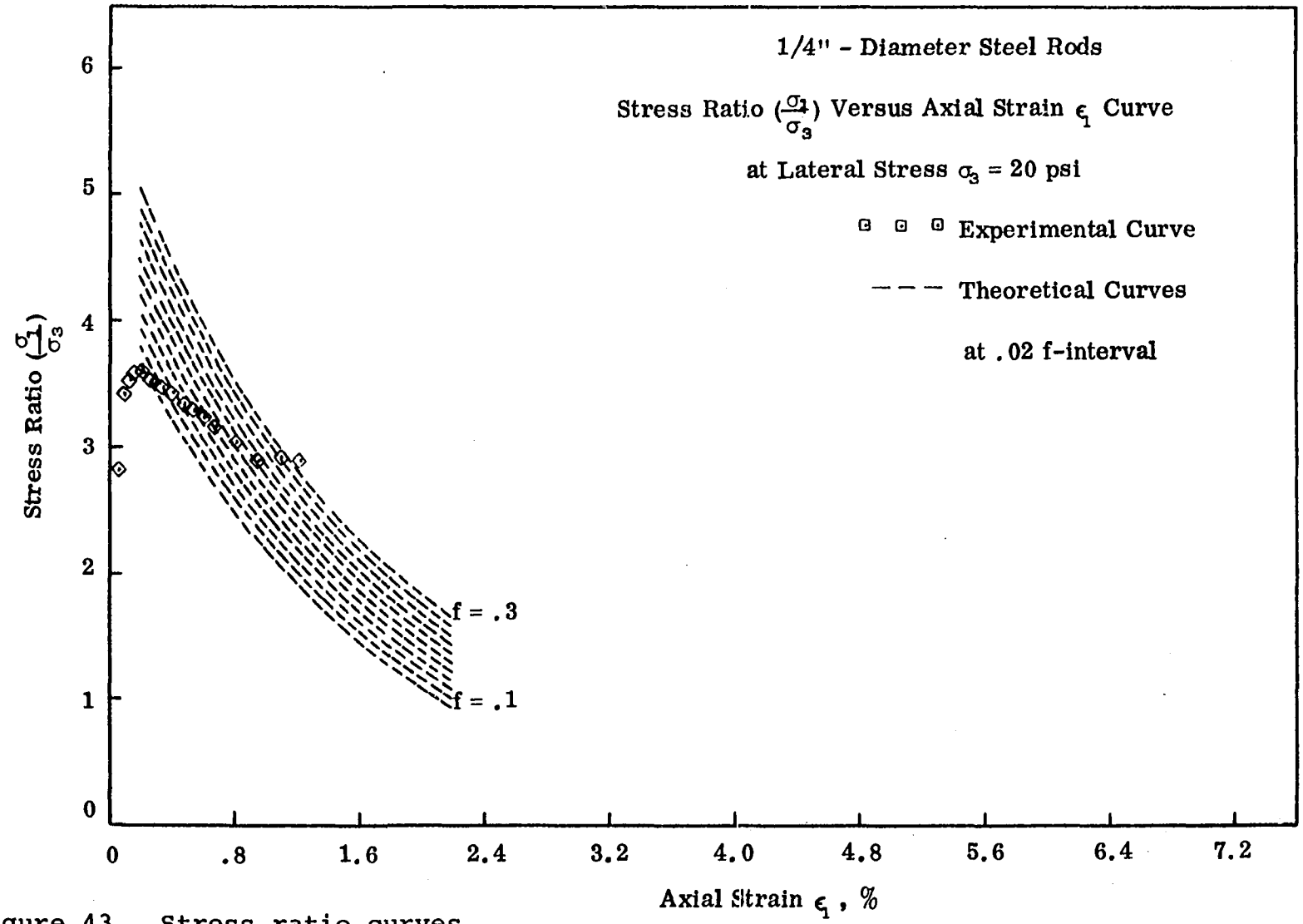

Figure 43. Stress ratio curves

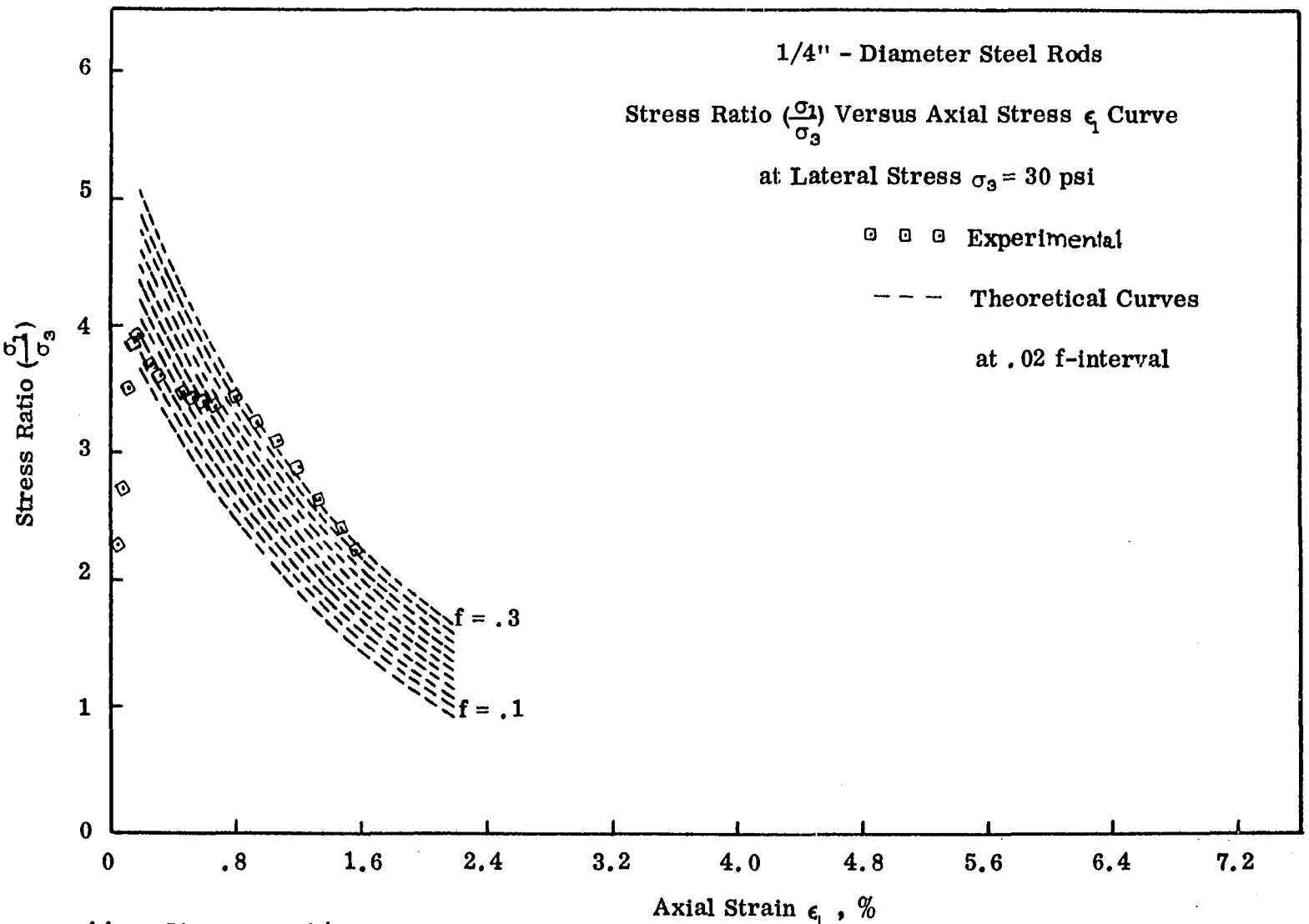

Figure 44. Stress ratio curves

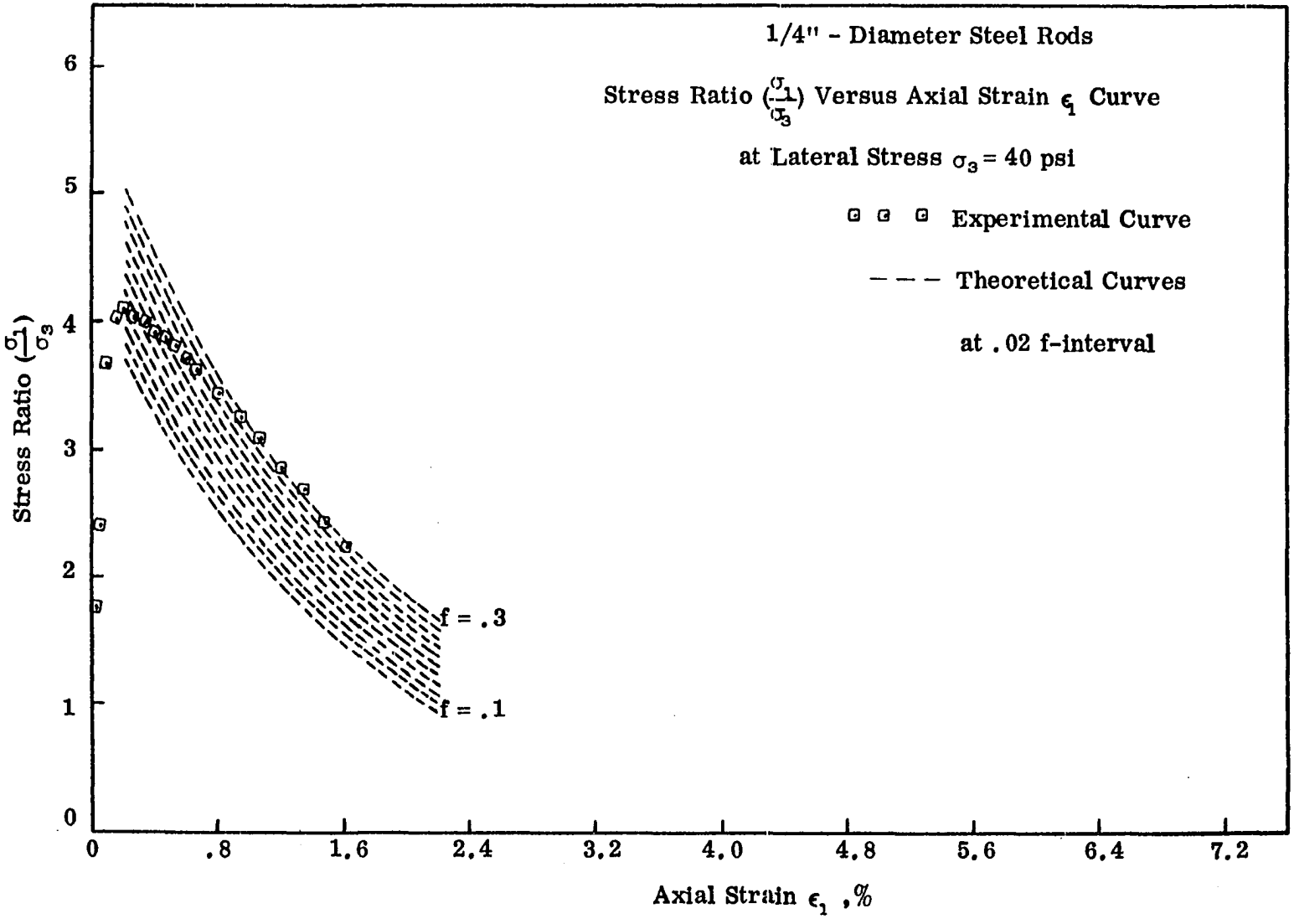

Figure 45. Stress ratio curves

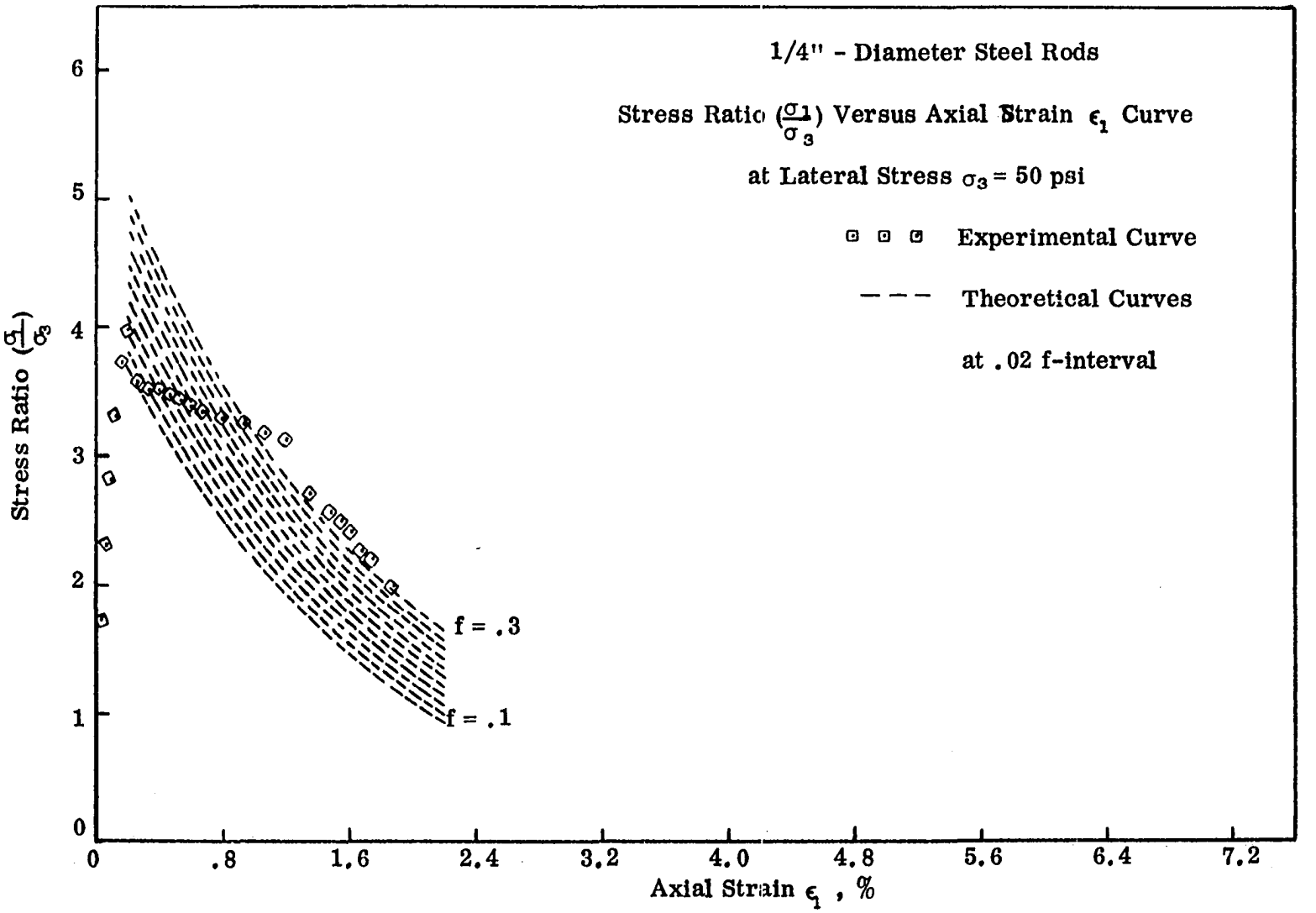

Figure 46. Stress ratio curves

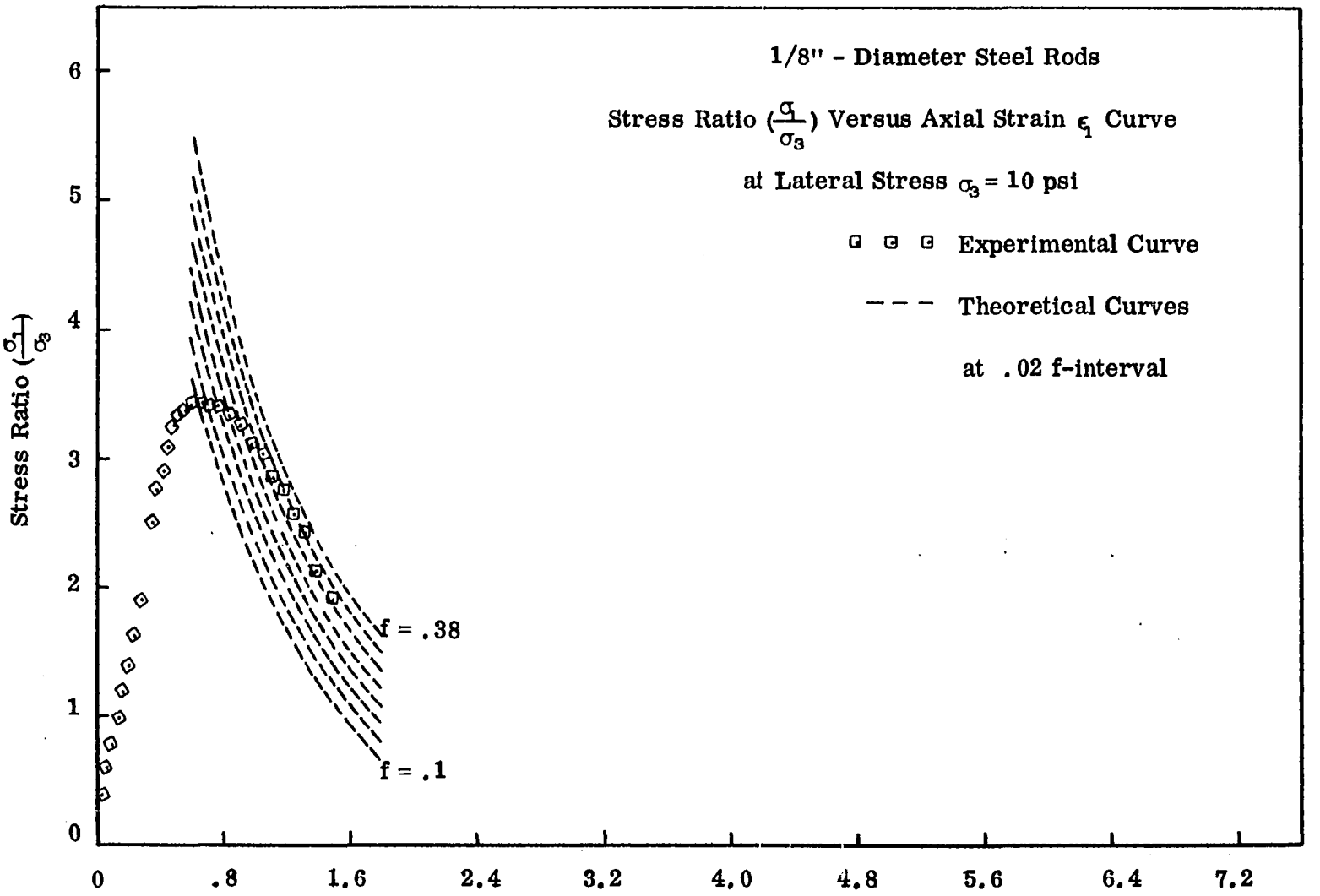

Figure 47. Stress ratio curves

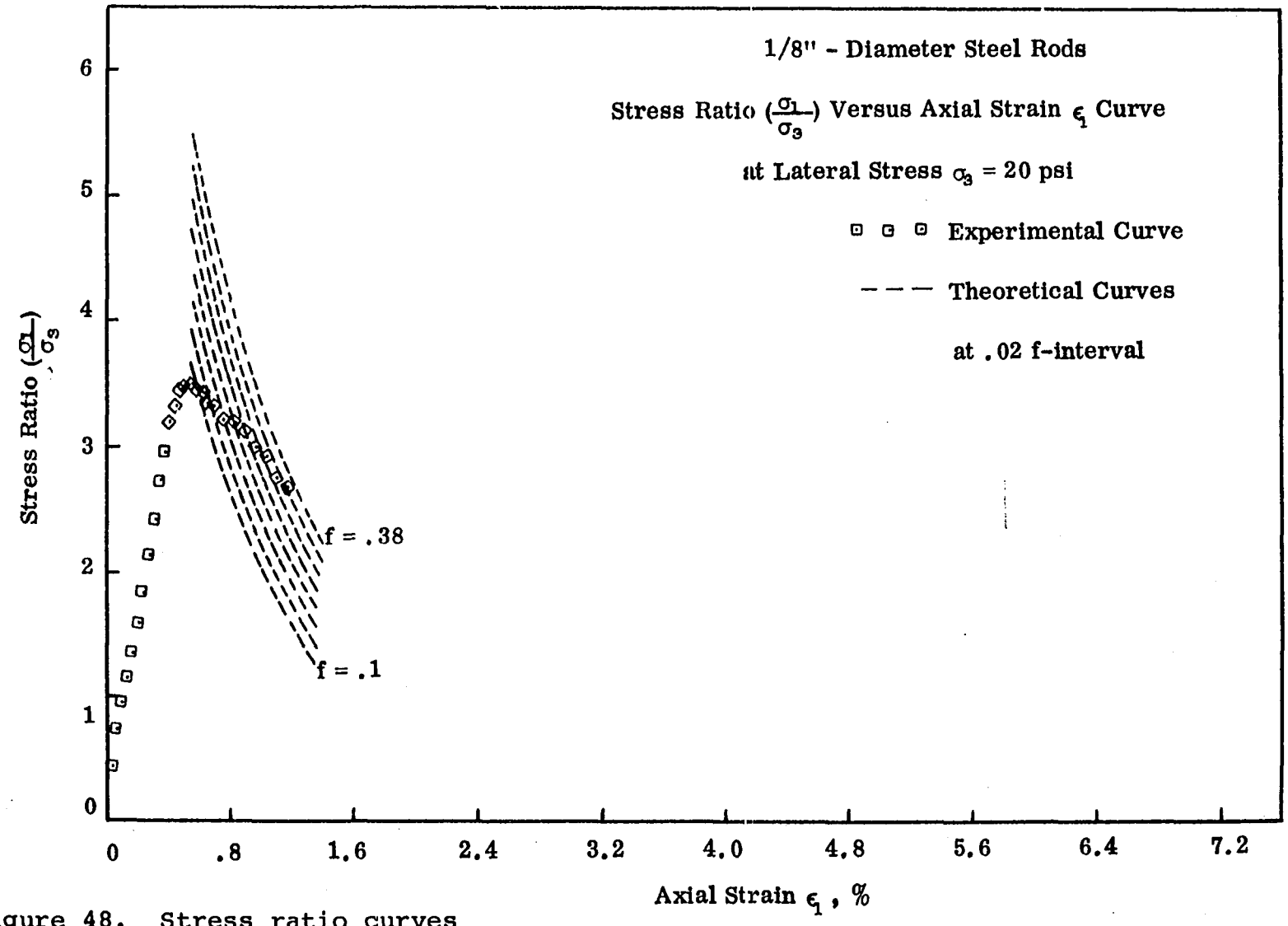

Figure 48. Stress ratio curves

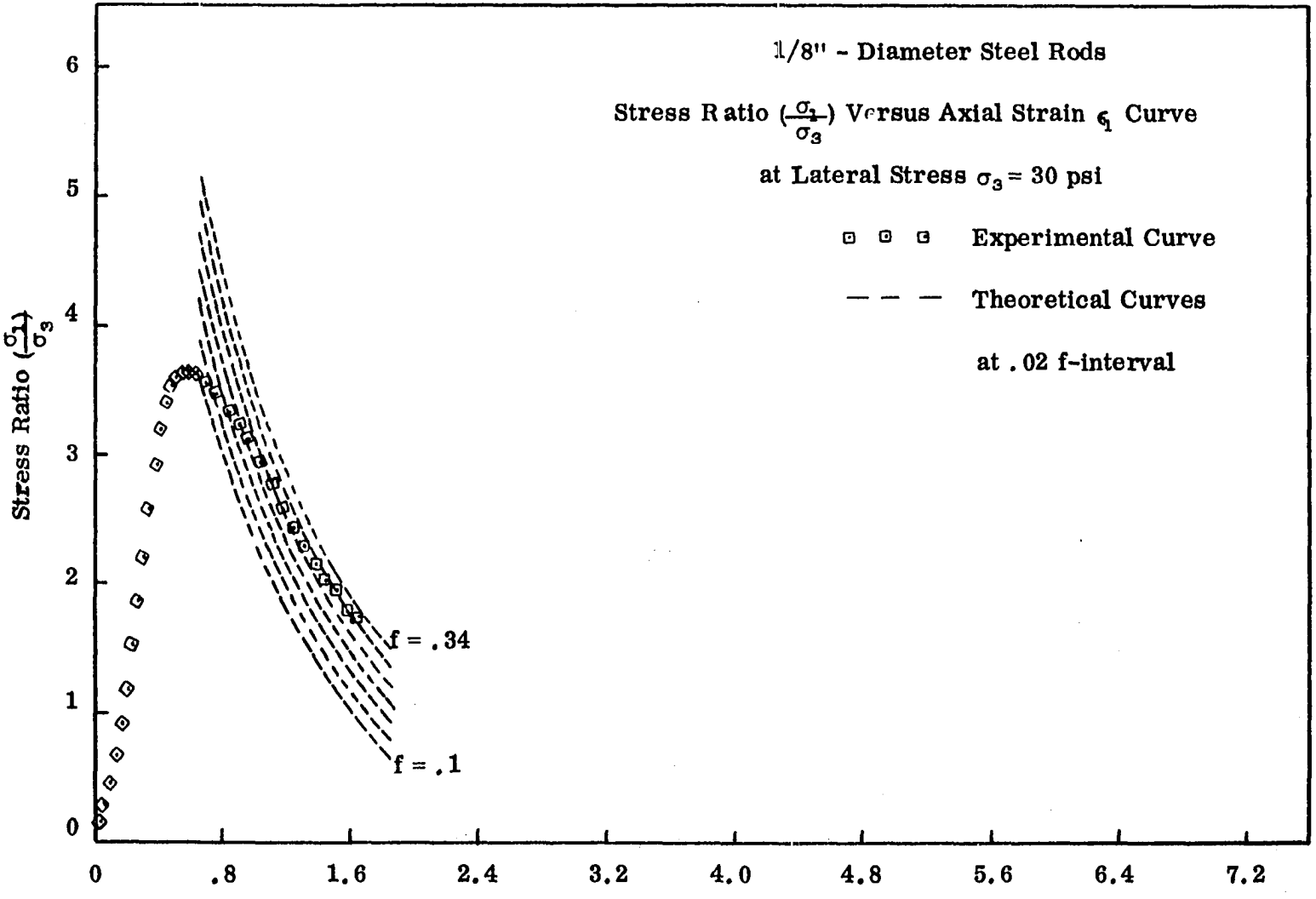

Figure 49. Stress ratio curves

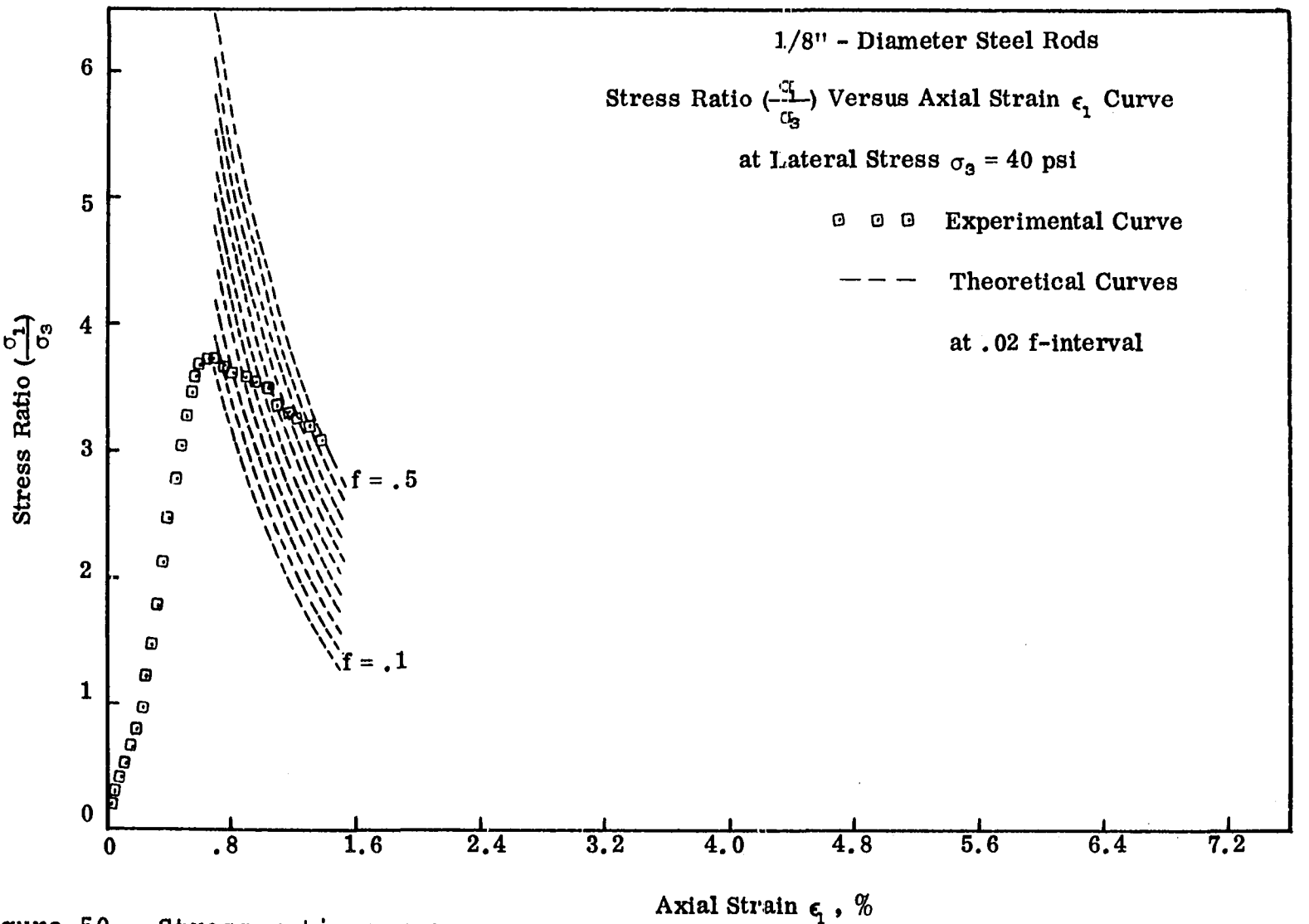

Figure 50. Stress ratio curves

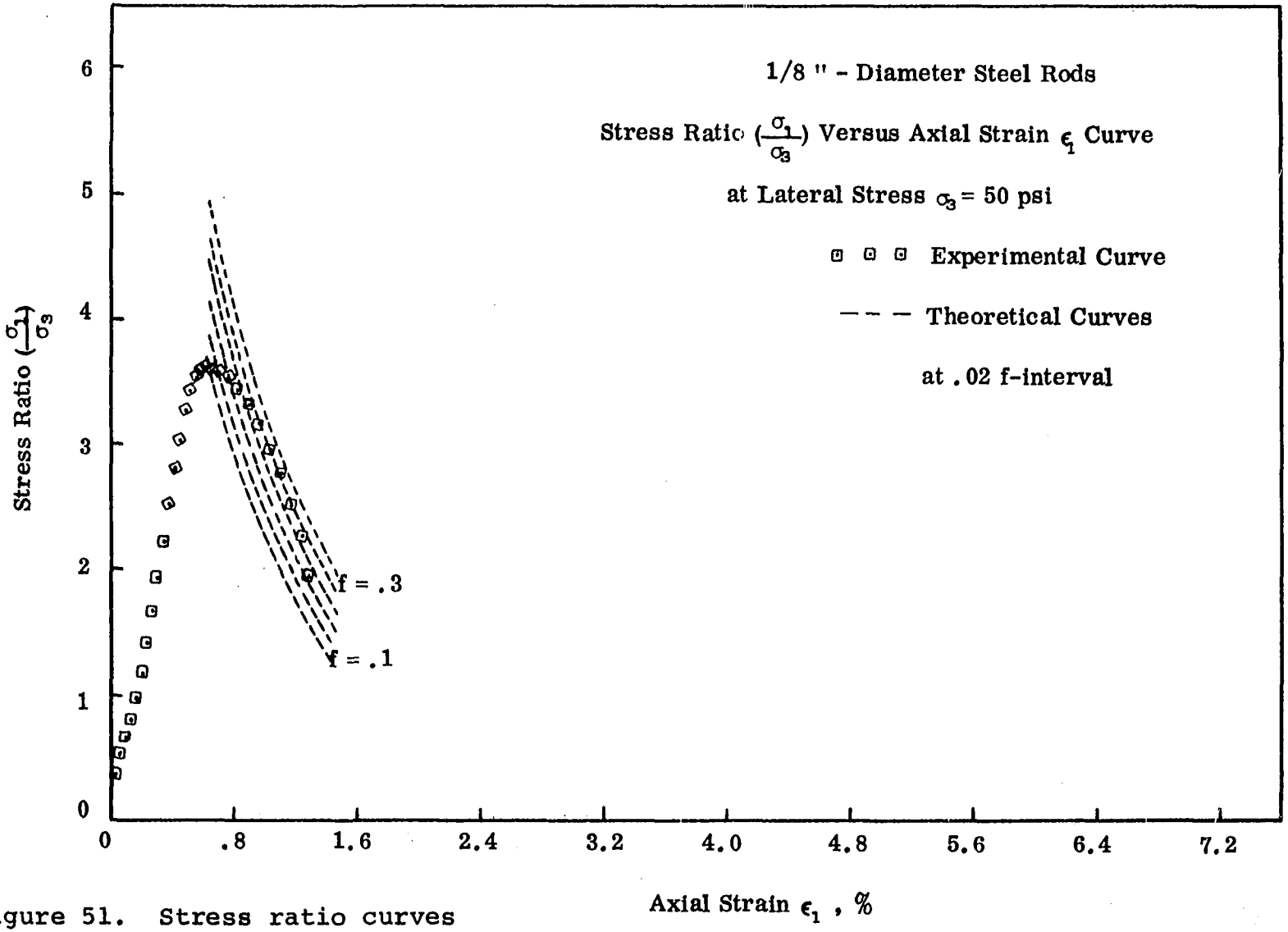

Figure 51. Stress ratio curves

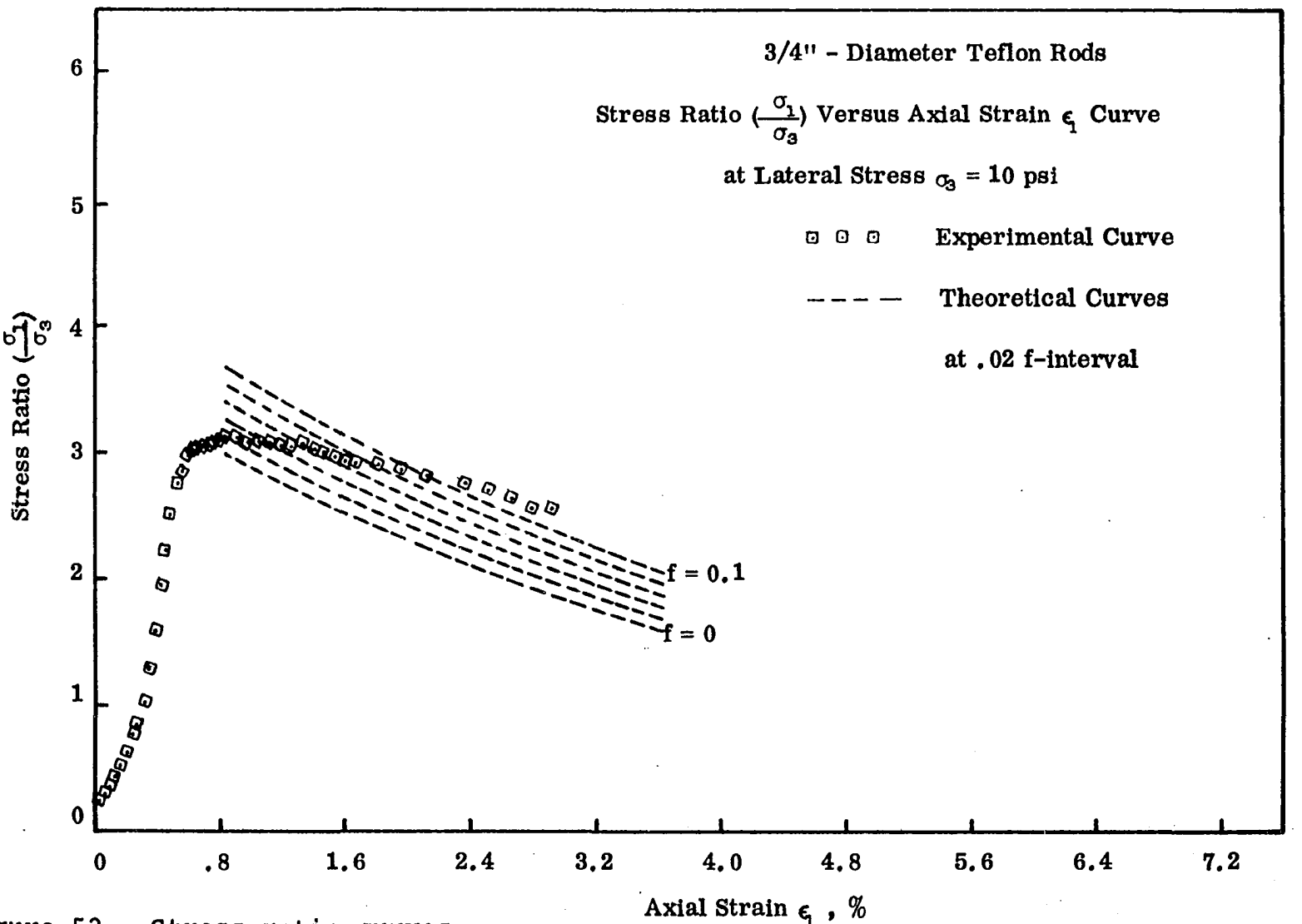

Figure 52. Stress ratio curves

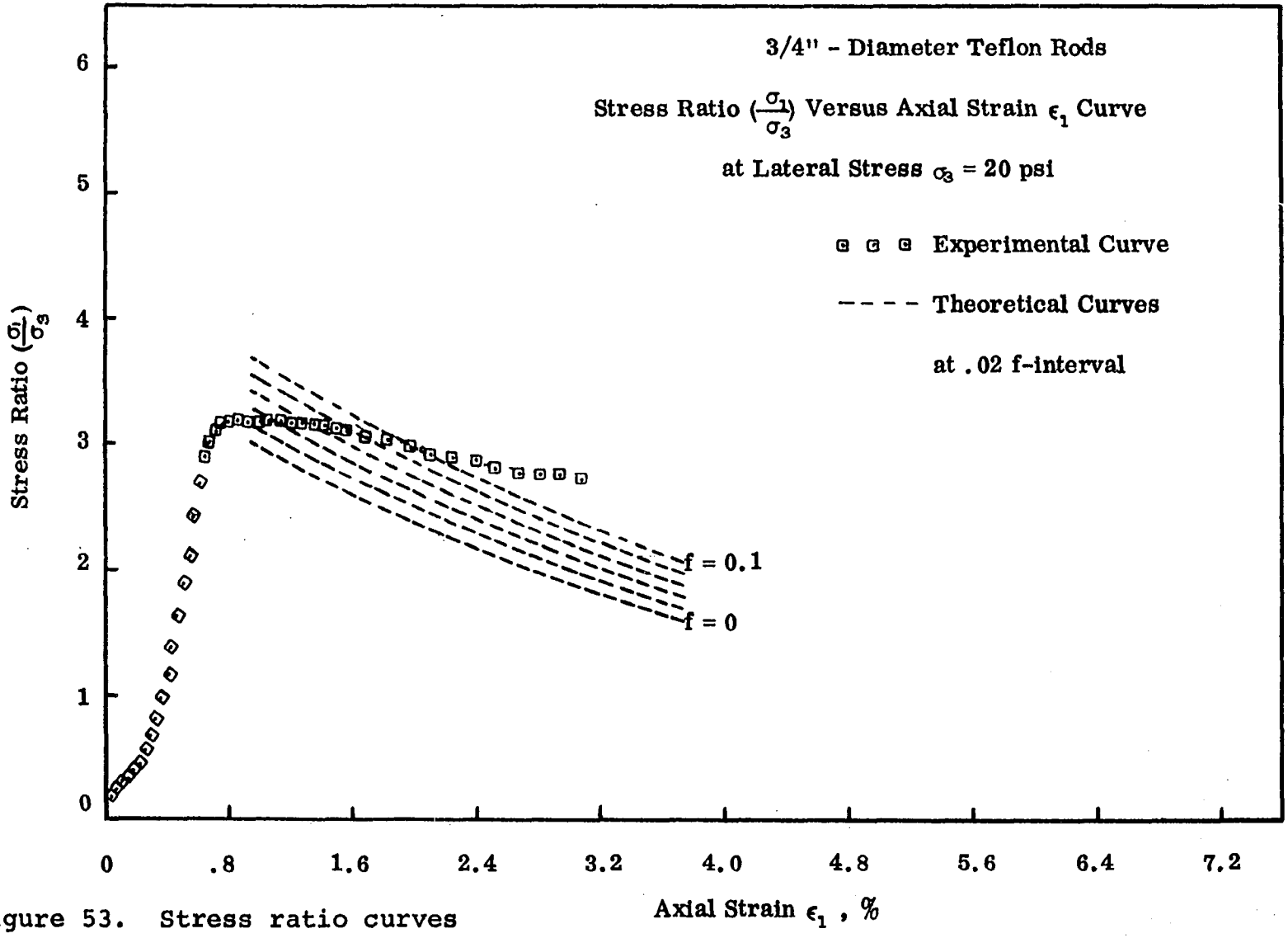

Figure 53. Stress ratio curves

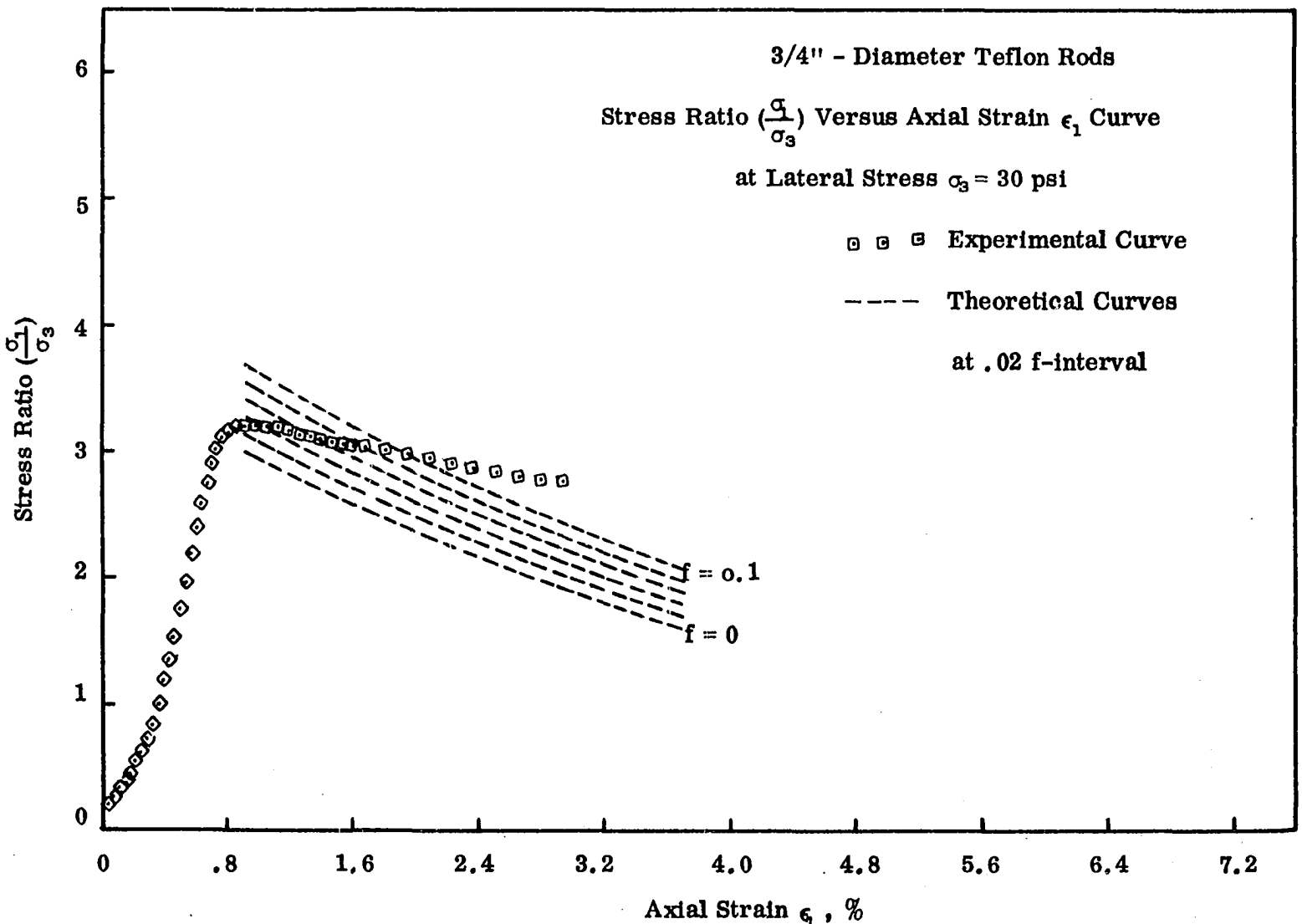

Figure 54. Stress ratio curves

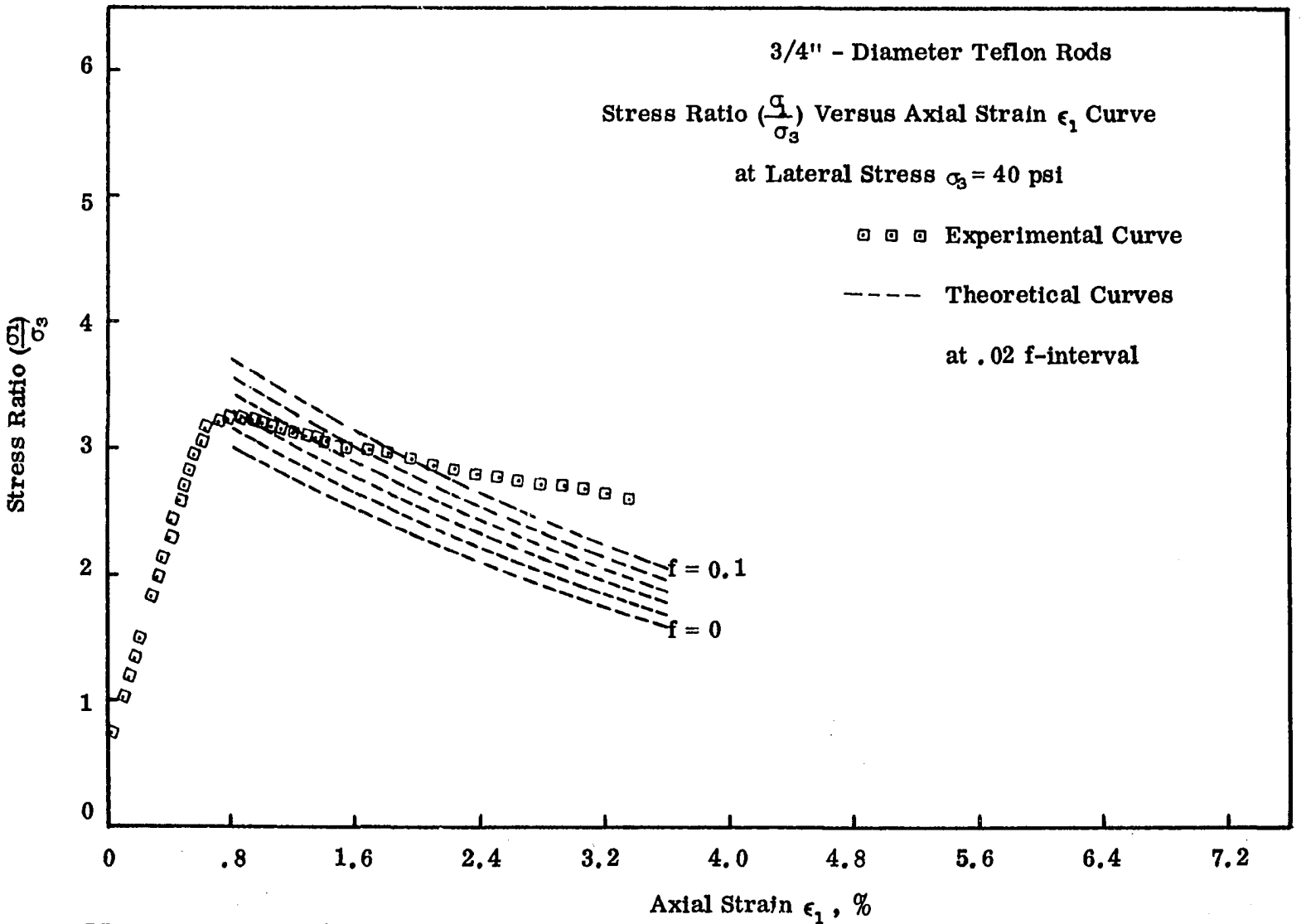

Figure 55. Stress ratio curves

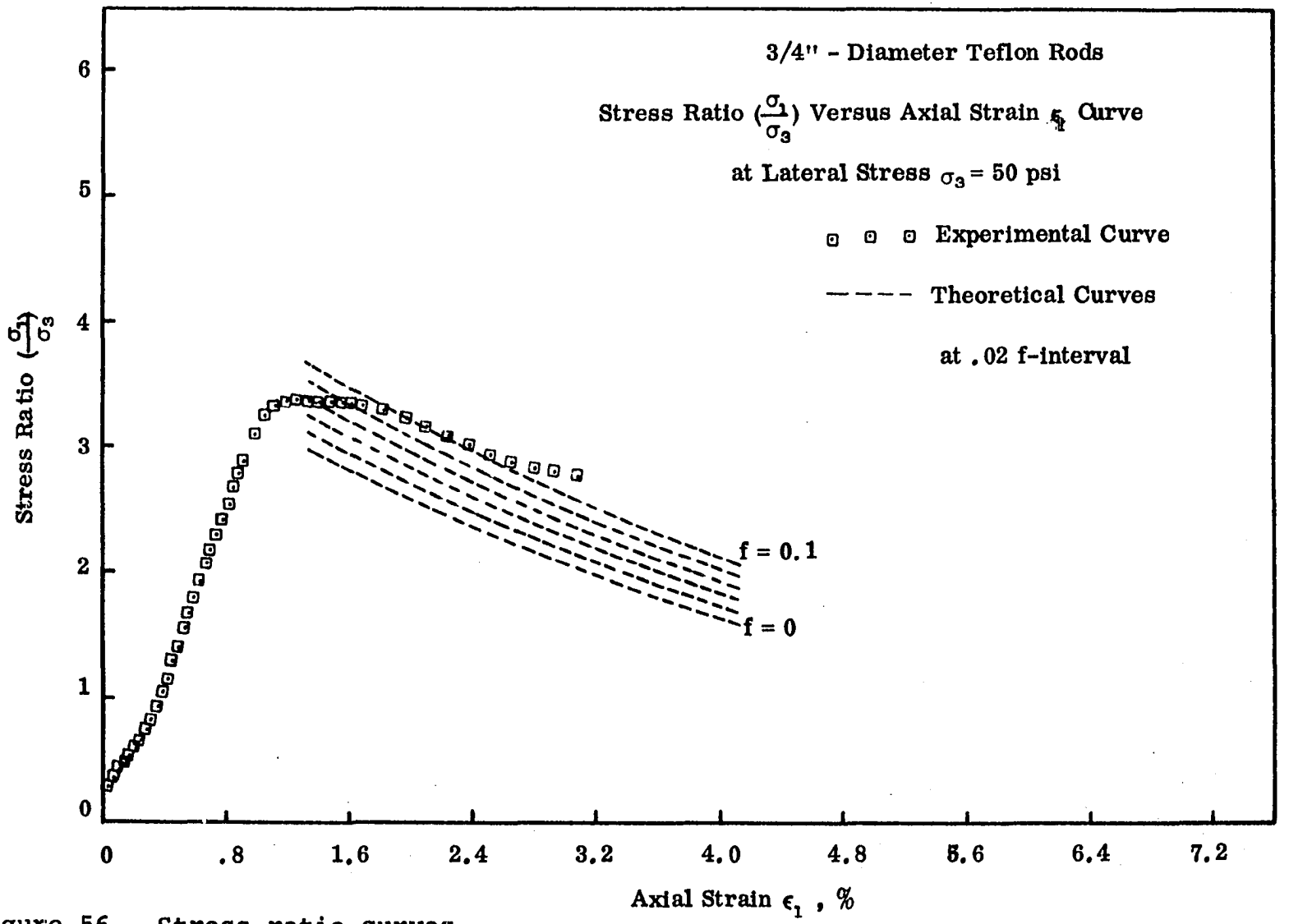

Figure 56. Stress ratio curves

confined to one plane, the stress ratio $(\frac{\sigma_1}{\sigma_3})$ will jump up and down on various theoretical friction level curves.

2. Shear slip transfers from plane to plane throughout the post-maximum stress ratio $(\frac{\sigma_1}{\sigma_3})_{max}$ dilation. That is, slip takes place on one shear plane, becomes arrested, and shifts to another, and so on. If the coefficient of friction is still considered constant, the experimental stress ratio curve, instead of following one theoretical f-level curve, will stay more or less parallel to the axial strain axis. This can be explained by considering that, with each shear plane abandonment and formation of a new plane, the theoretical stress ratio curve starts anew, i.e., is shifted to the right along the axis of axial strain. Thus, the failure point will move parallel to the axial strain axis (Fig. 57b). In the soil mechanics literature, such a stage in the stress ratio versus axial strain curve is called a residual stage or constant volume stage; whereas, in the above statement, the coefficient of friction stays constant while the volume may go on increasing. If the coefficient of friction does not remain constant, the point P (Fig. 57b) will not move parallel to the axial strain axis, but will shift (up or) down to various f-level

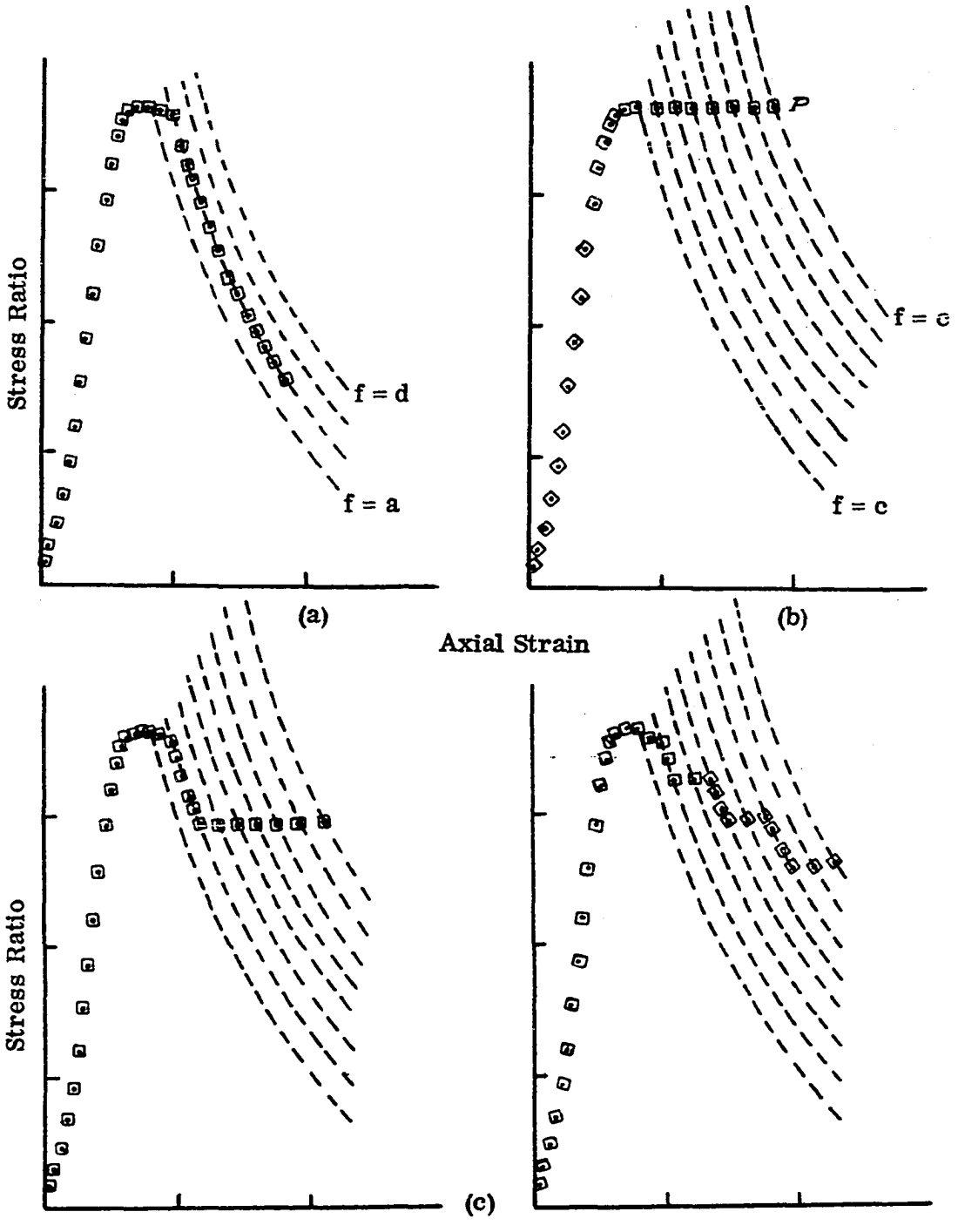

Figure 57. Axial strain to stress ratio curves; (a) failure mechanism 1, (b) failure mechanism 2, (c) two combinations of failure mechanisms 1 and 2

curves at each particular axial strain. Moreover, the curvature of each theoretical stress ratio $(\frac{\sigma_1}{\sigma_3})$ curve is changing with changing f-levels; this fact will also contribute in not letting the point P move parallel to the axial strain axis. Thus, changing coefficients of friction from point to point during sliding will cause the stress curve to move at some angle to the axial strain axis.

3. A third alternative can be a combination of the above two shear slip mechanisms. Various combinations, obtained by altering the duration of the shear slip on a particular plane and by altering placement of the two mechanisms with respect to the axial strain axis and also by changing their order along the axial strain axis, are shown in Fig. 57.

Testing of the Predicted Volumetric Strain $(\frac{dv}{v_0})$

To test Eq. 50, which expresses the relation between volumetric strain $(\frac{dv}{v_0})$ and axial strain ε_1, theoretical curves are superimposed on experimental volumetric strain $(\frac{dv}{v_0})$ versus axial strain ε_1 curves. This superimposition should be done such that the point of zero volumetric strain $(\frac{dv}{v_0})$ on the theoretical curve coincides with the point on the experimental curve where elastic volumetric strain becomes complete. This point is uncertain and, at the

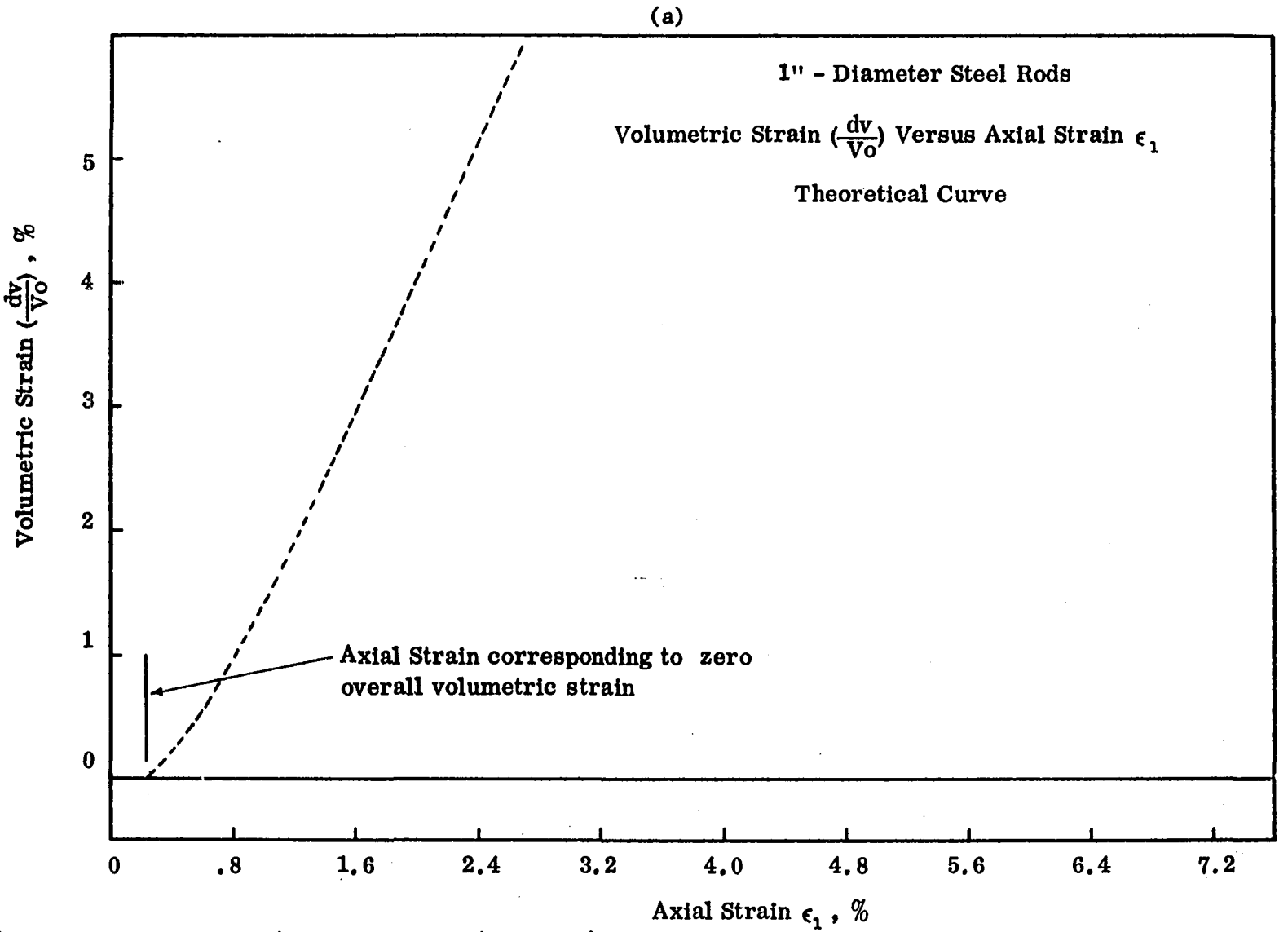

Figure 58. Theoretical volumetric strain curve

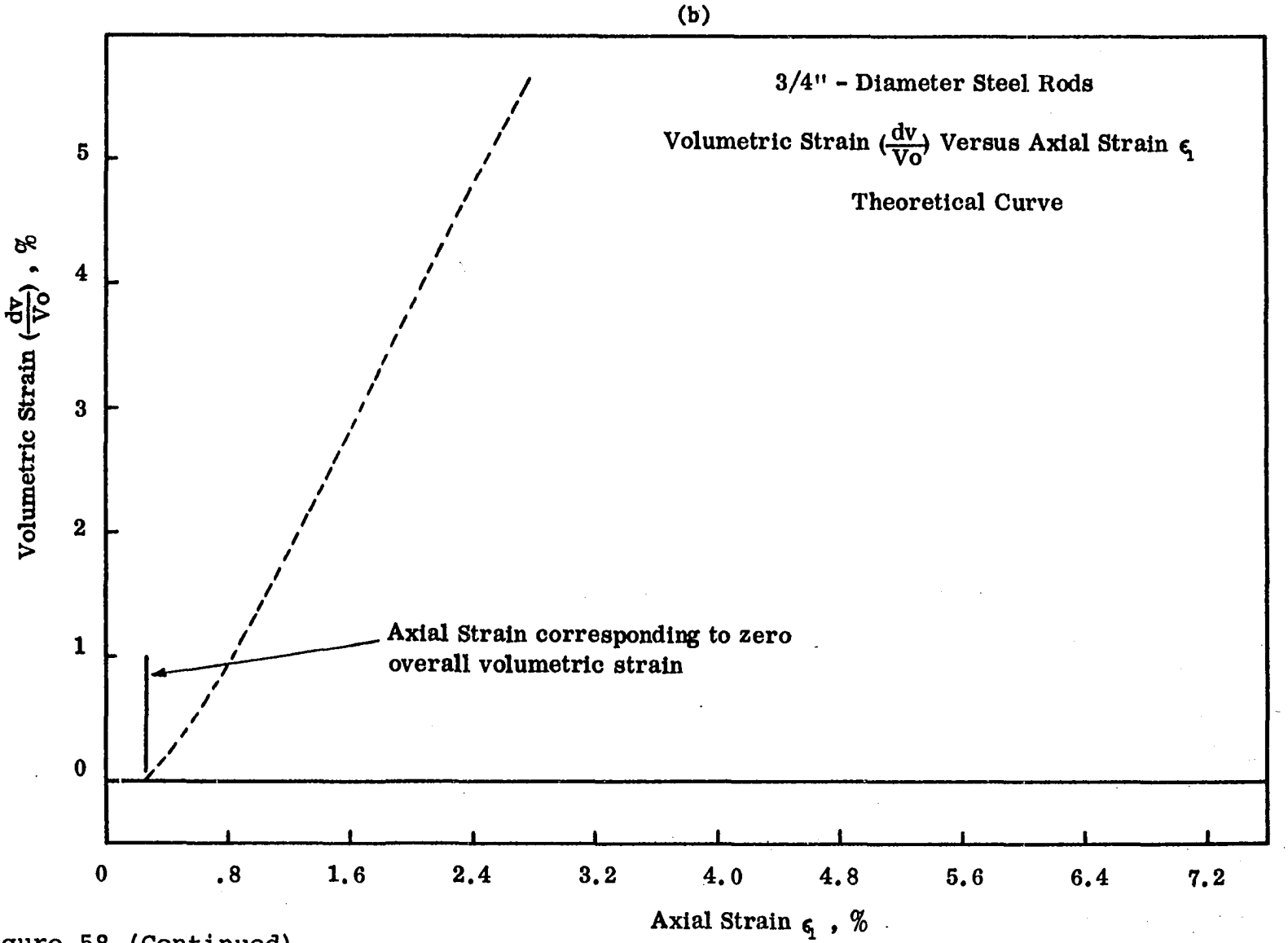

Figure 58 (Continued)

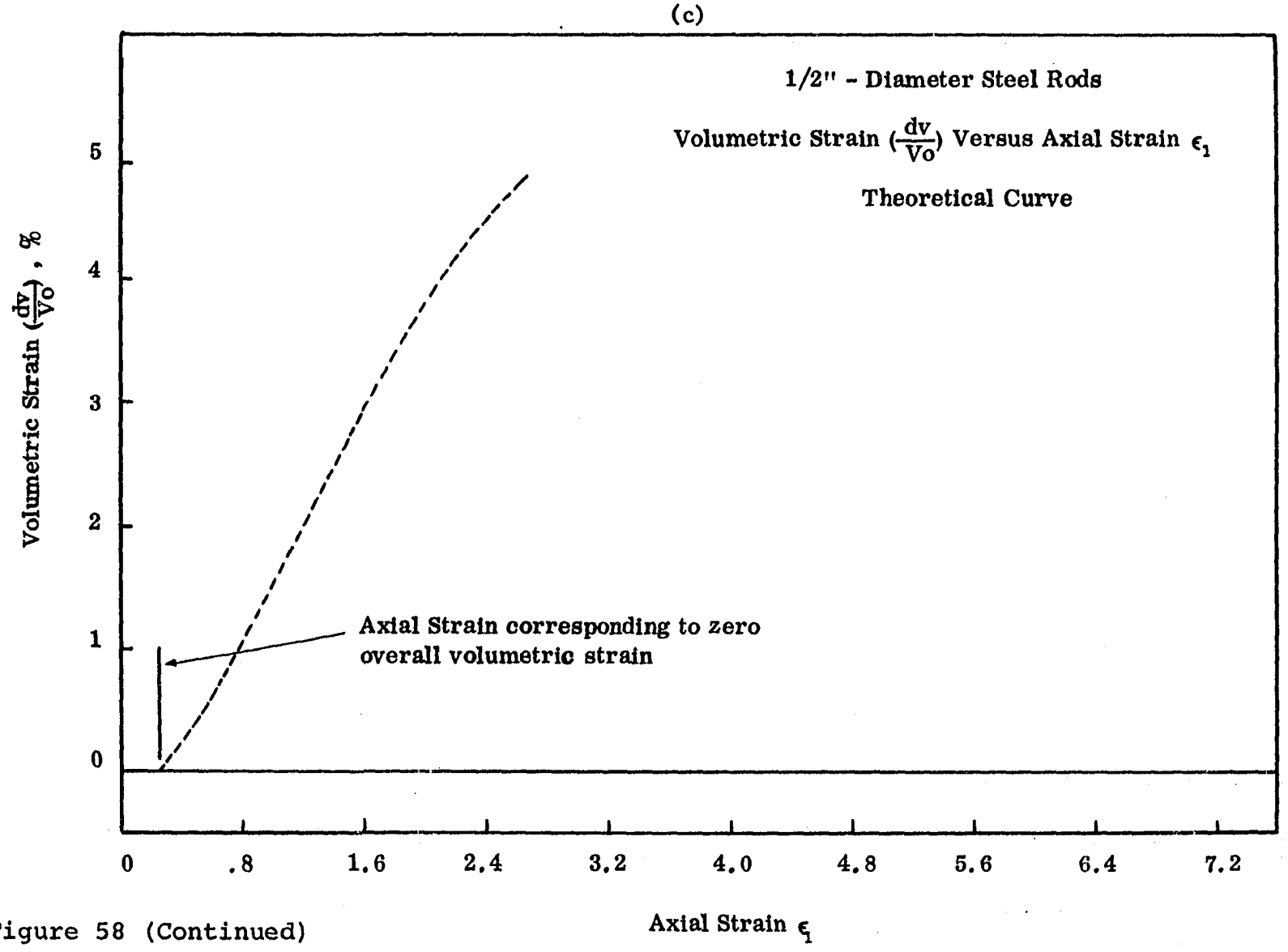

Figure 58 (Continued)

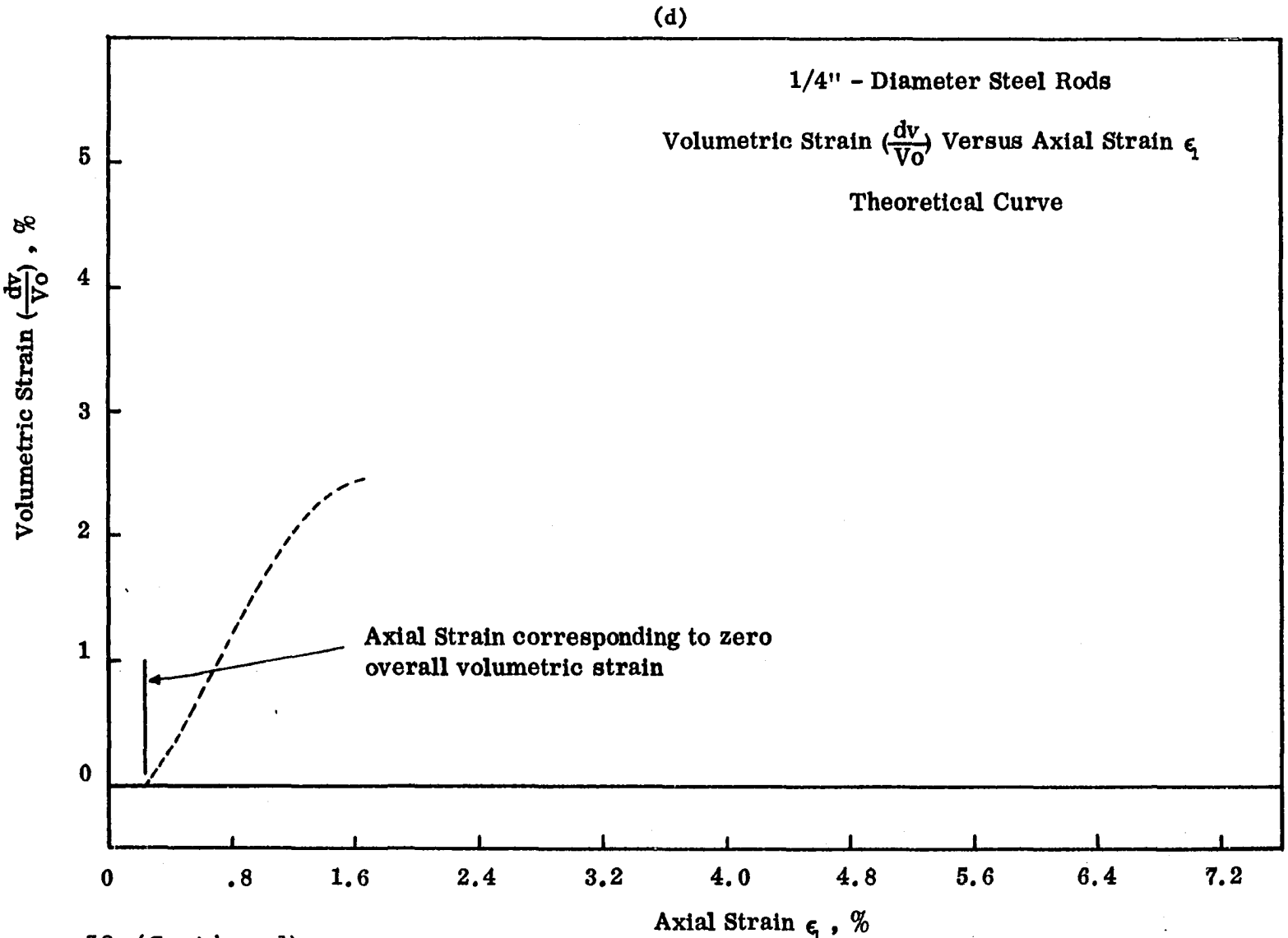

Figure 58 (Continued)

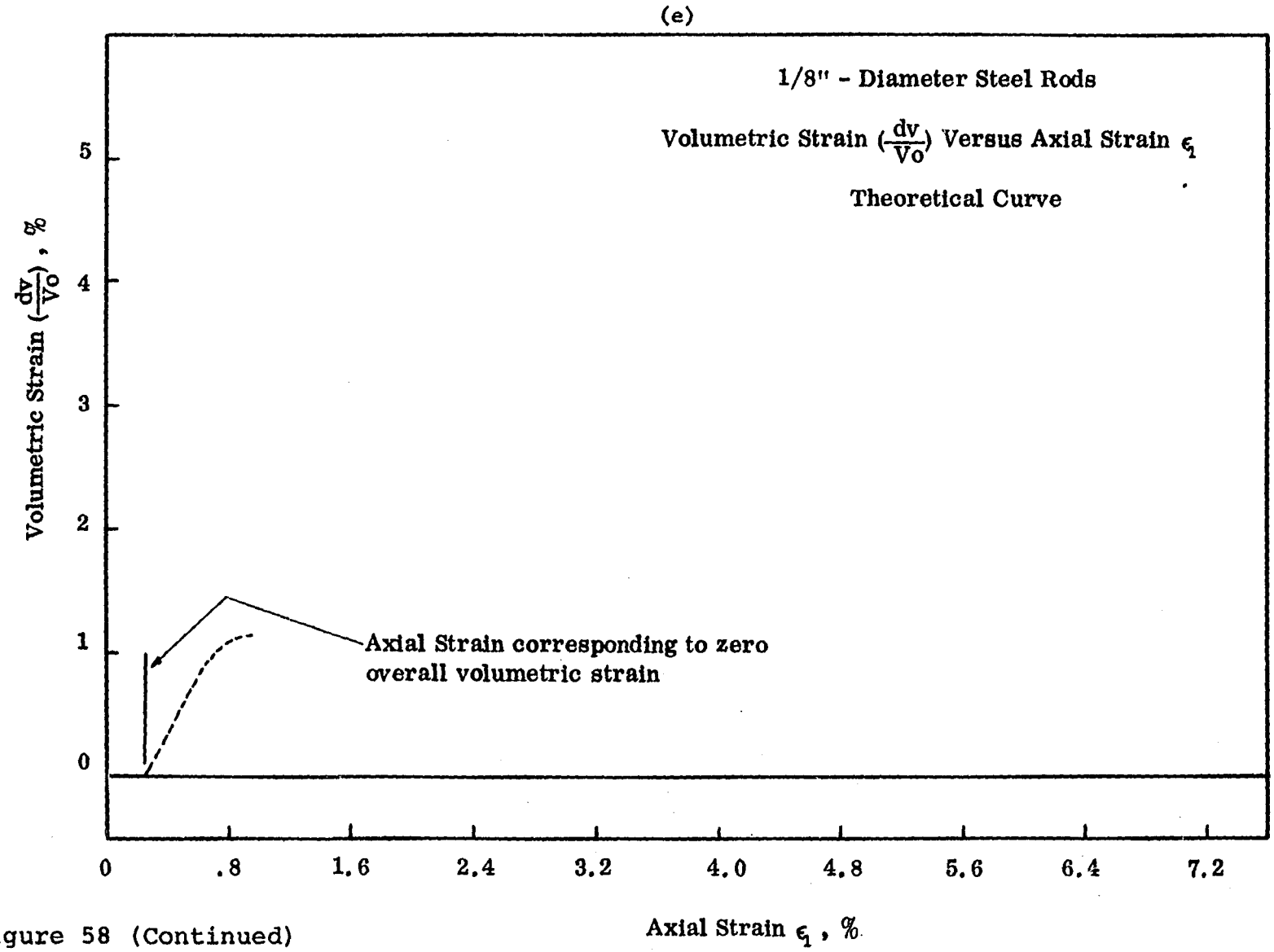

Figure 58 (Continued)

present stage of knowledge, it is difficult if not impossible to ascertain its coordinates with respect to axial deformation or axial strain. For the sake of simplicity, it is assumed that this point corresponds to the point of minimum volumetric strain. The difficulty is all the more problematic when one considers that elastic and dilational deformations probably overlap.

Inspite of the simplifying assumptions, it can be seen from the superimposed curves that there is fairly good agreement between the theoretical and the experimental data. A slight deviation from the theoretical curves has been observed in the intermediate stage of axial strain in that the experimental volumetric strain exceeds the theoretical value corresponding to a particular axial strain. Deviation from the theoretical volumetric strain $(\frac{dv}{v_0})$ versus axial strain ε_1 curve also becomes significant at very large axial strains because of more chaotic and less predictable movements of the particles at larged induced deformations.

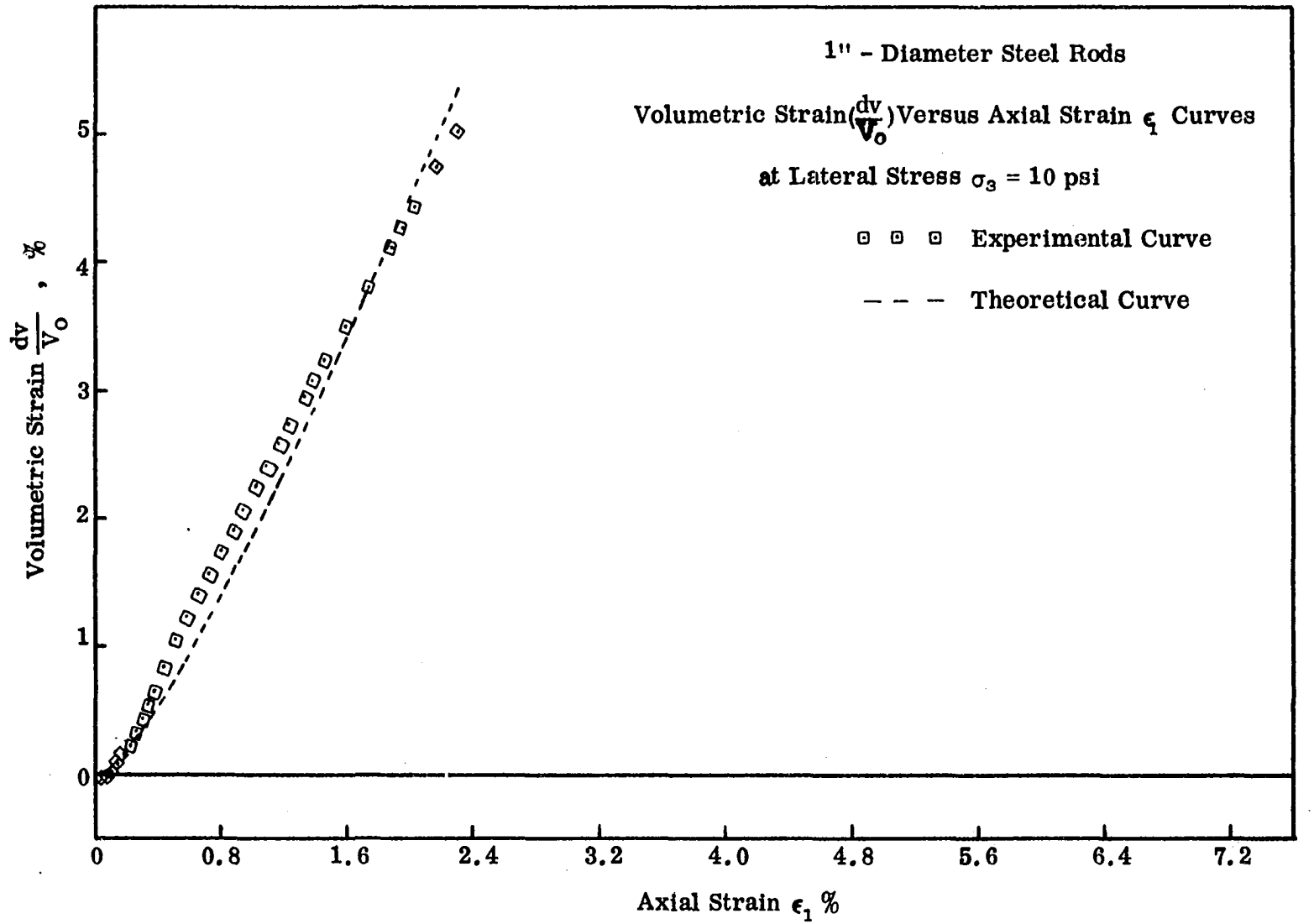

Figure 59. Volumetric strain curves

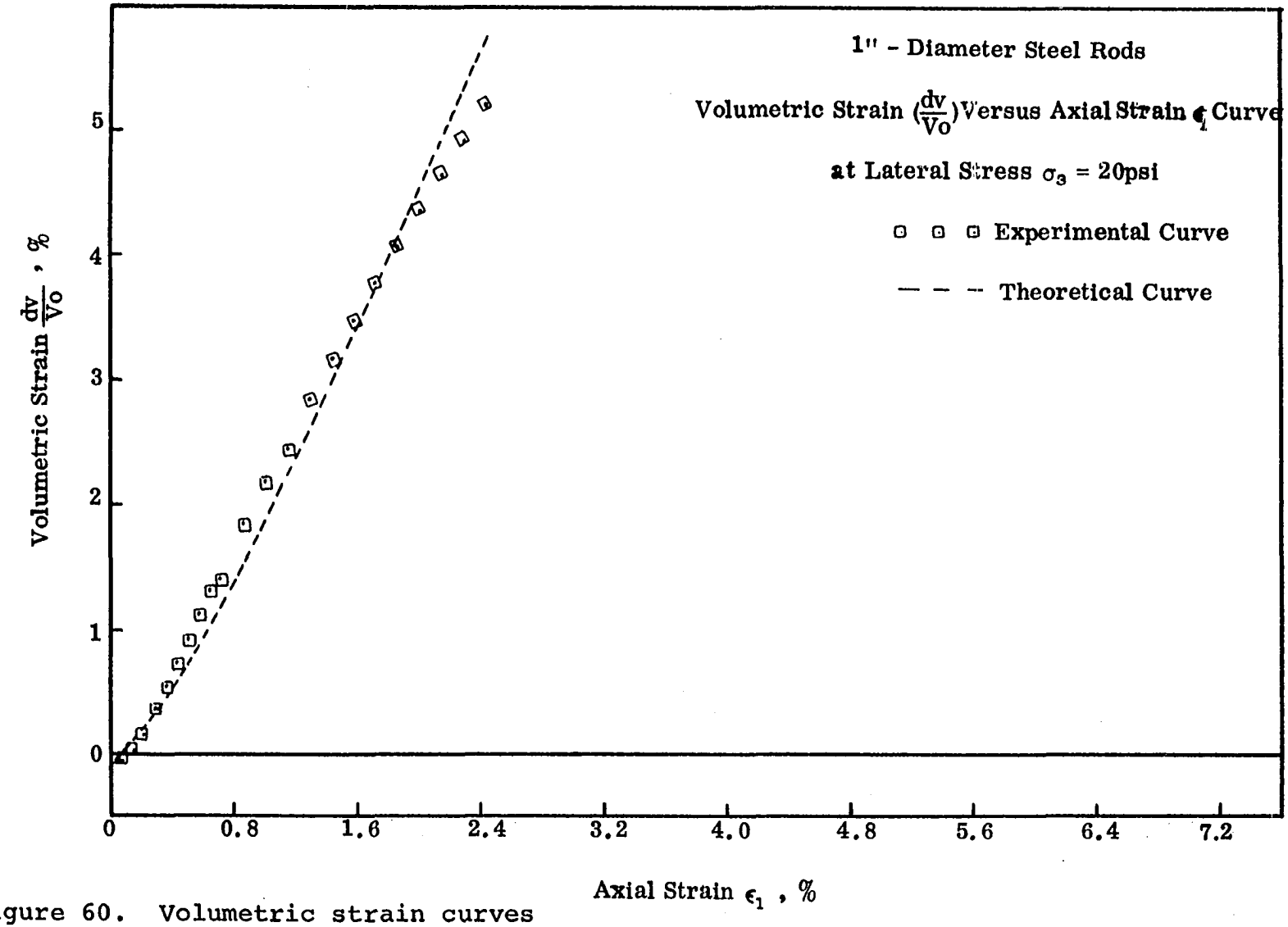

Figure 60. Volumetric strain curves

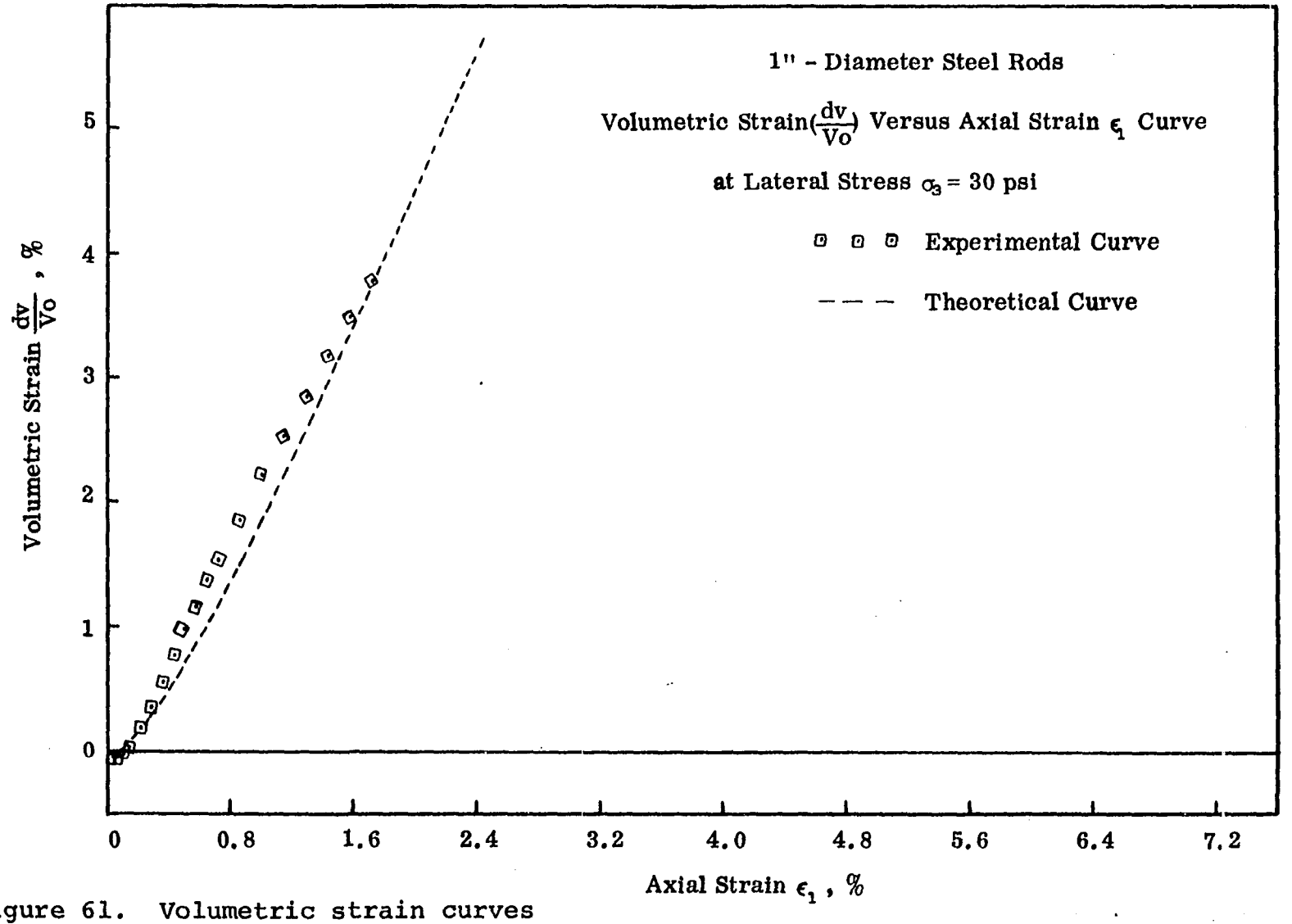

Figure 61. Volumetric strain curves

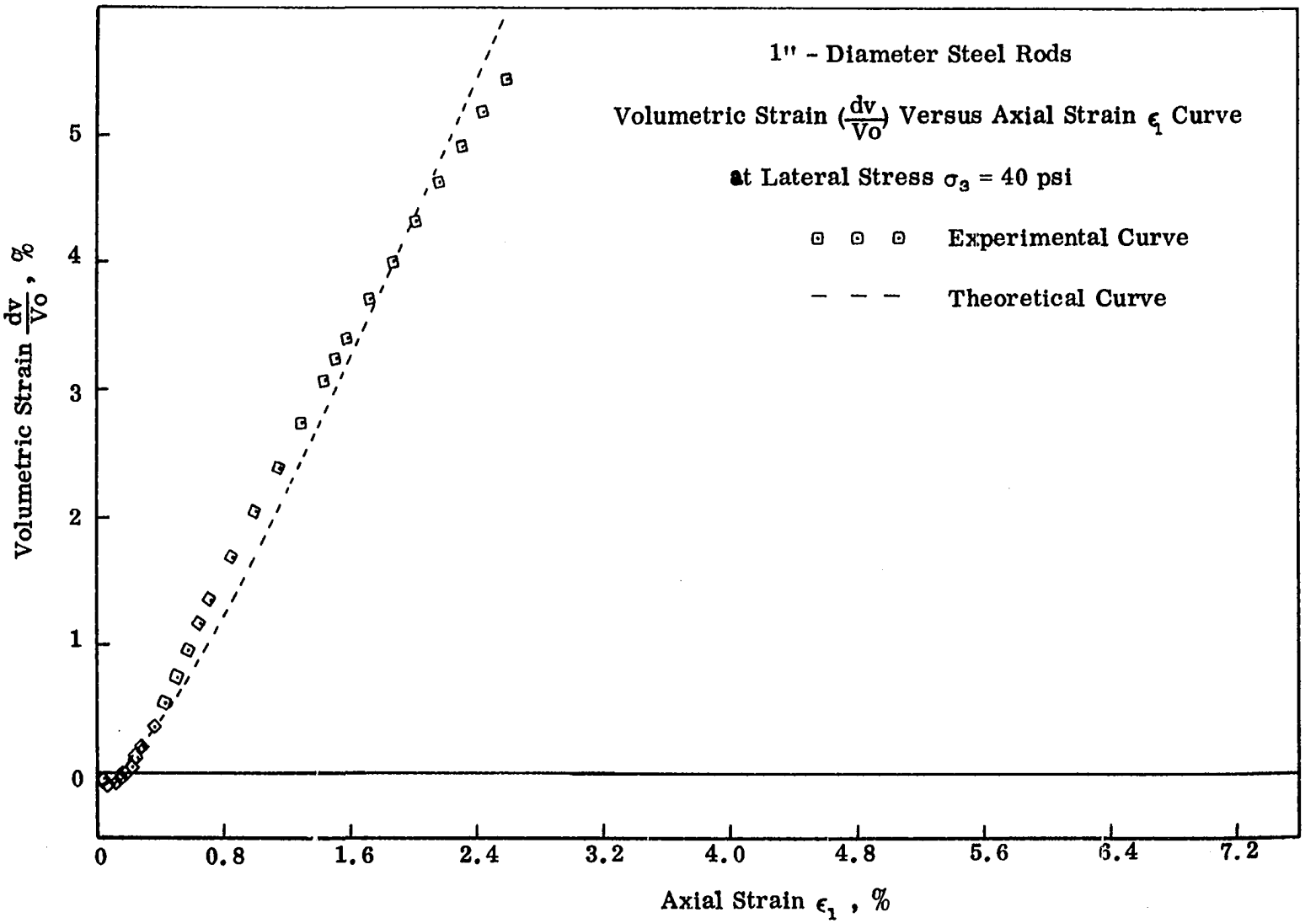

Figure 62. Volumetric strain curves

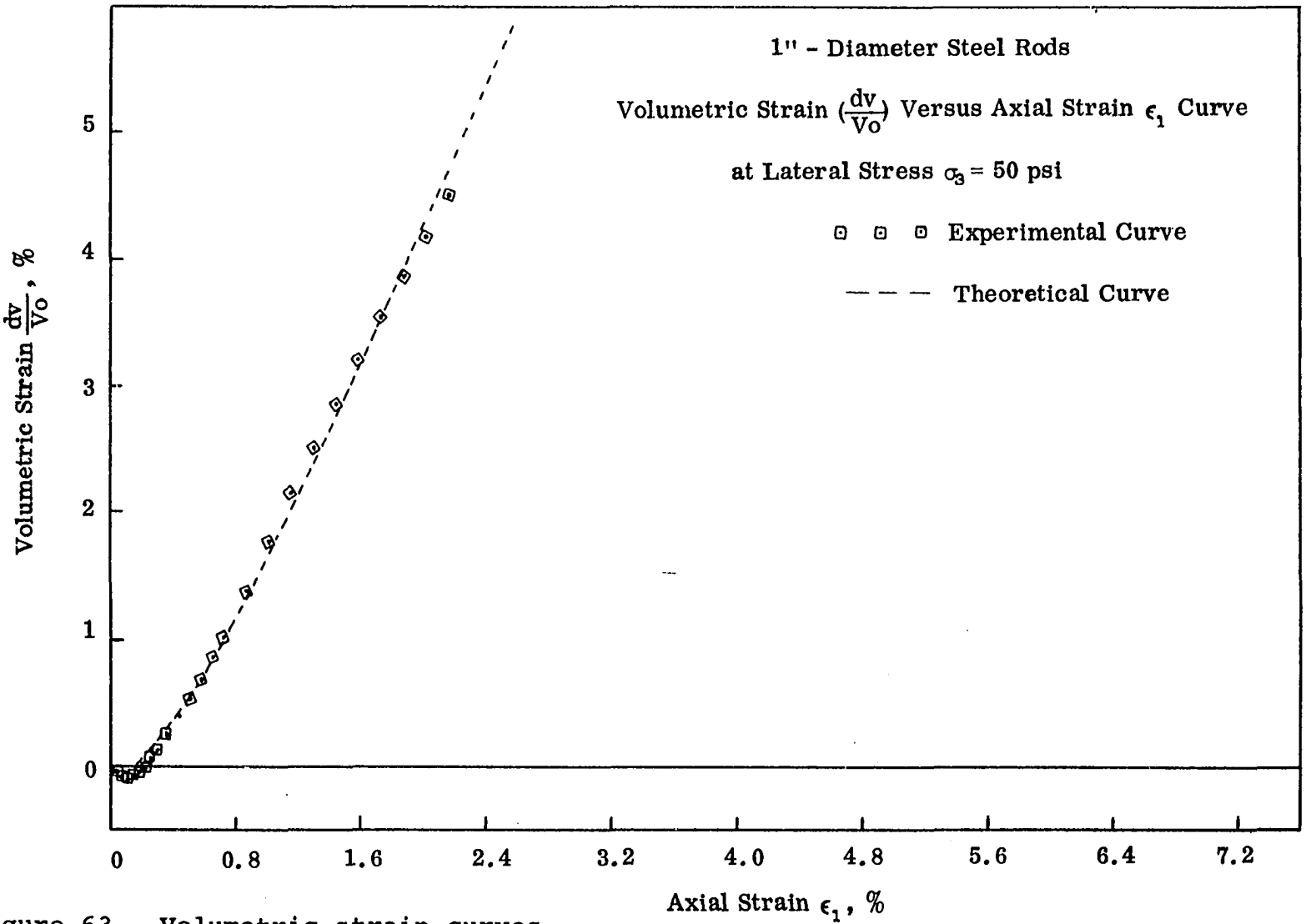

Figure 63. Volumetric strain curves

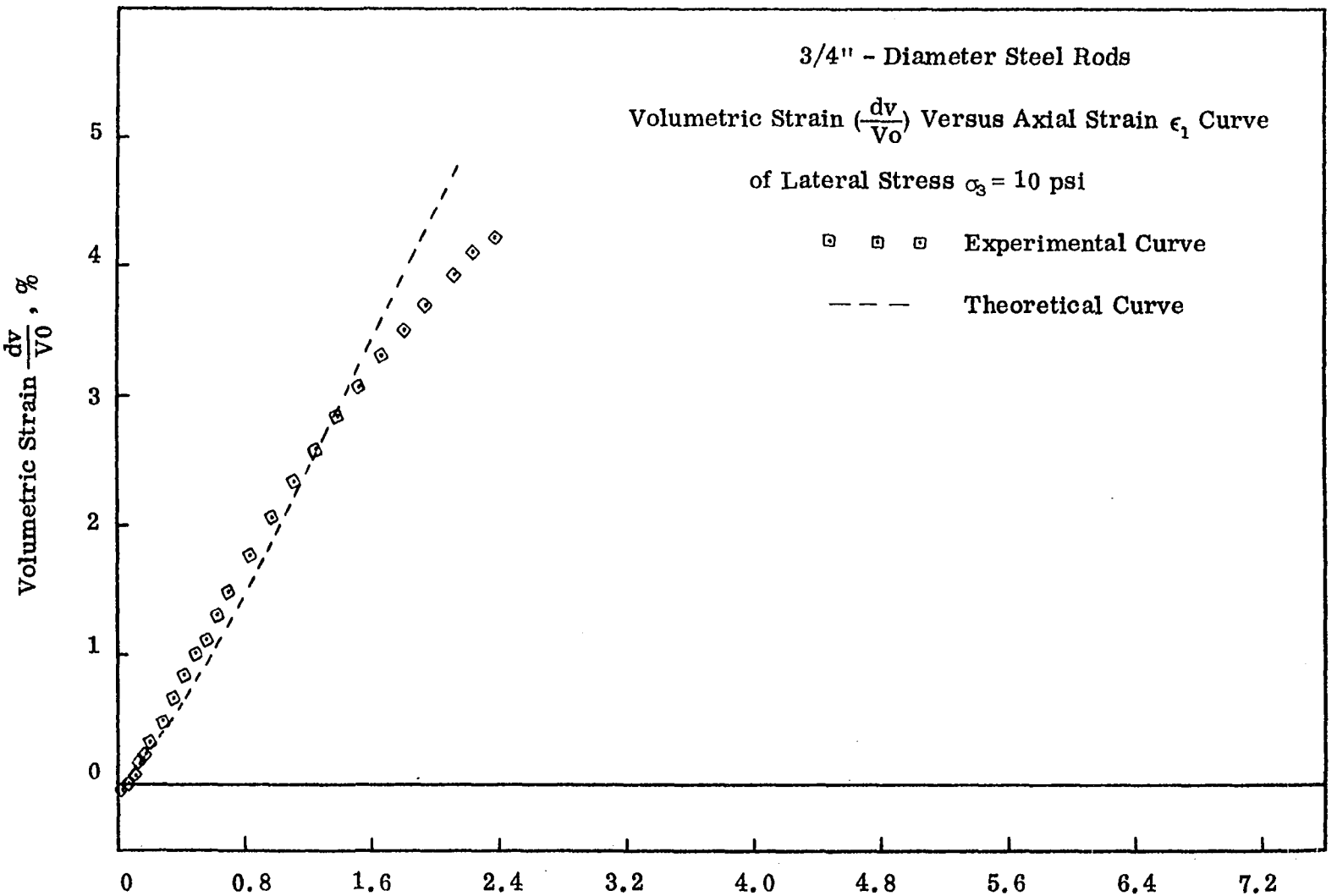

Figure 64. Volumetric strain curves

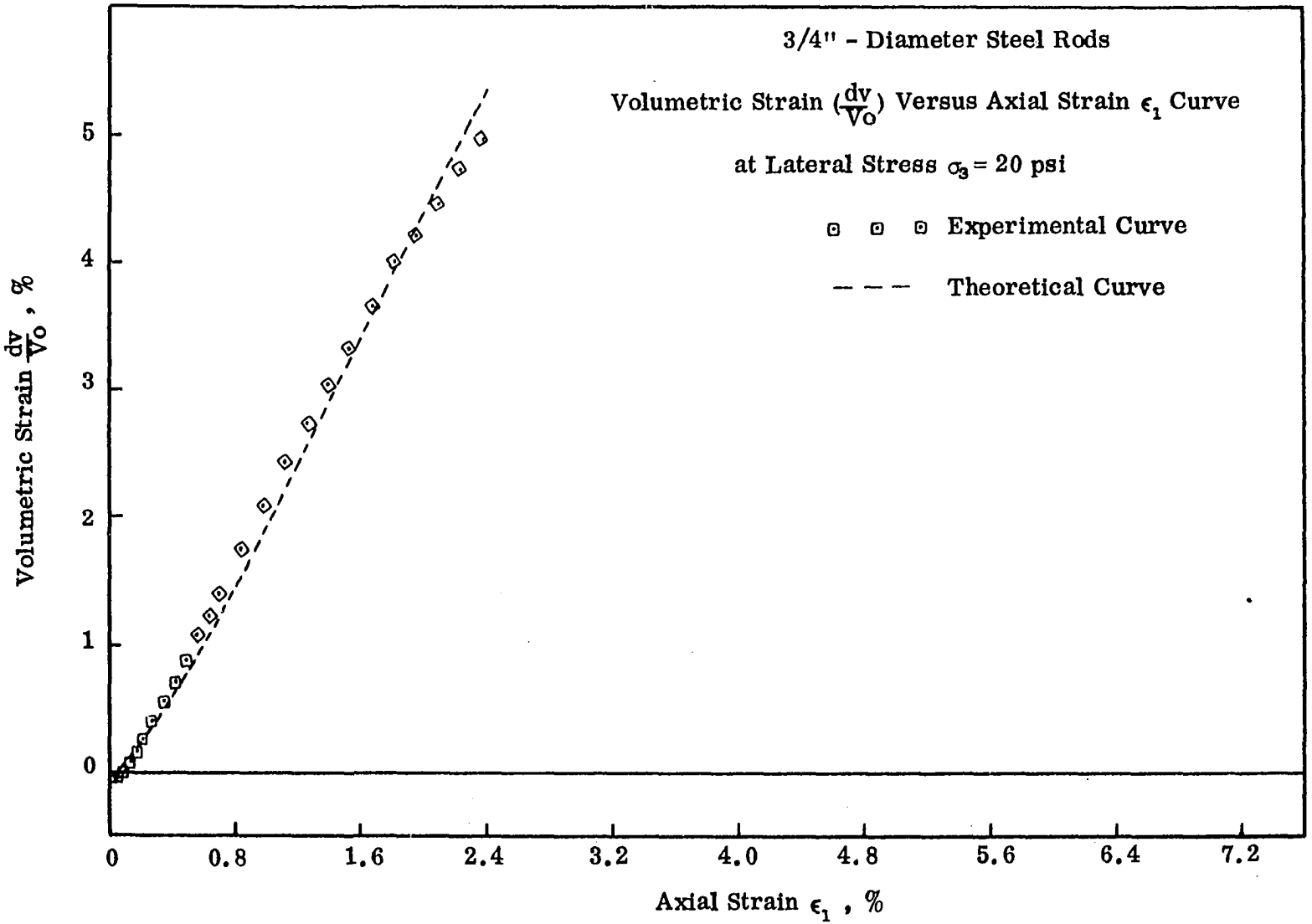

Figure 65. Volumetric strain curves

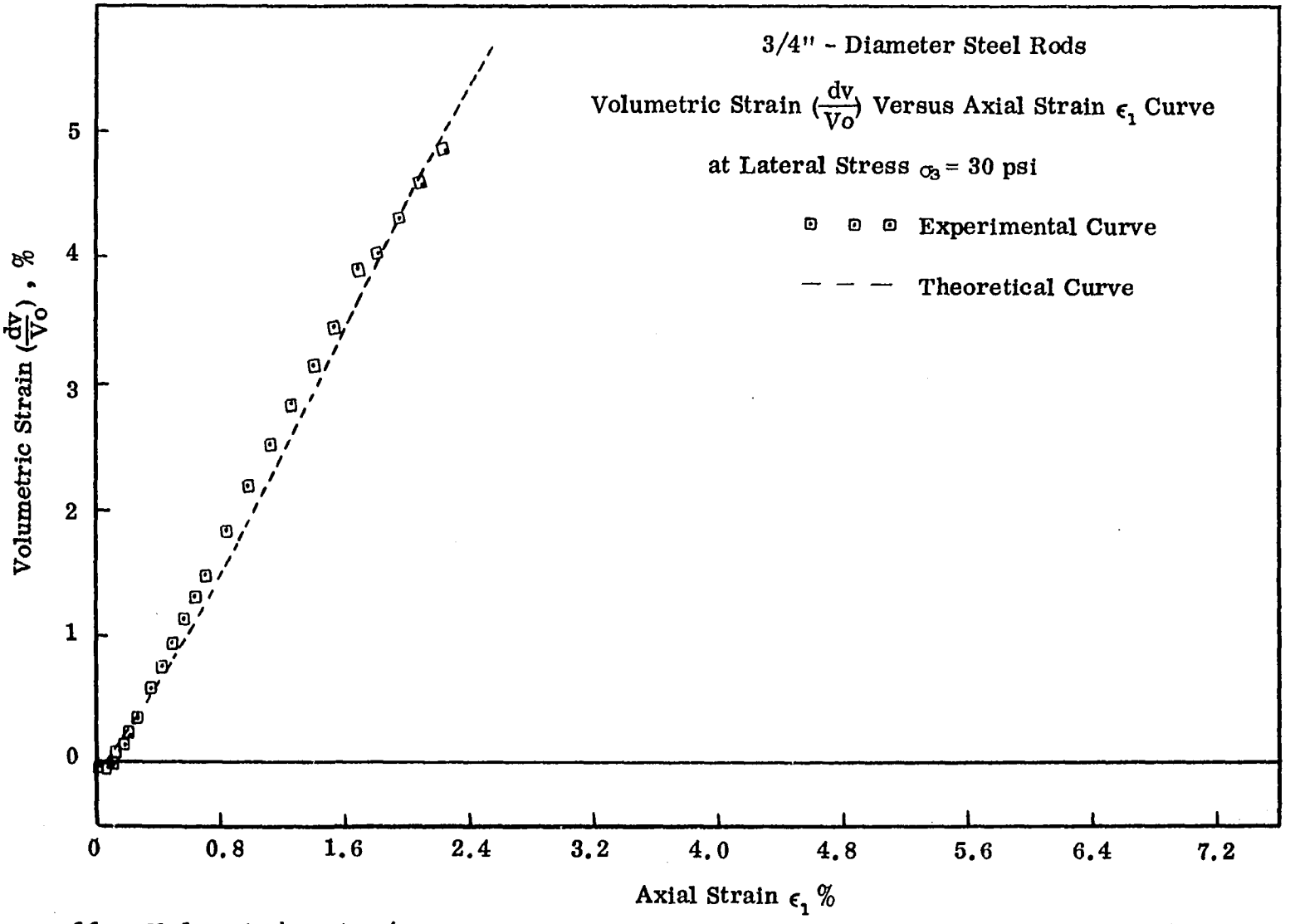

Figure 66. Volumetric strain curves

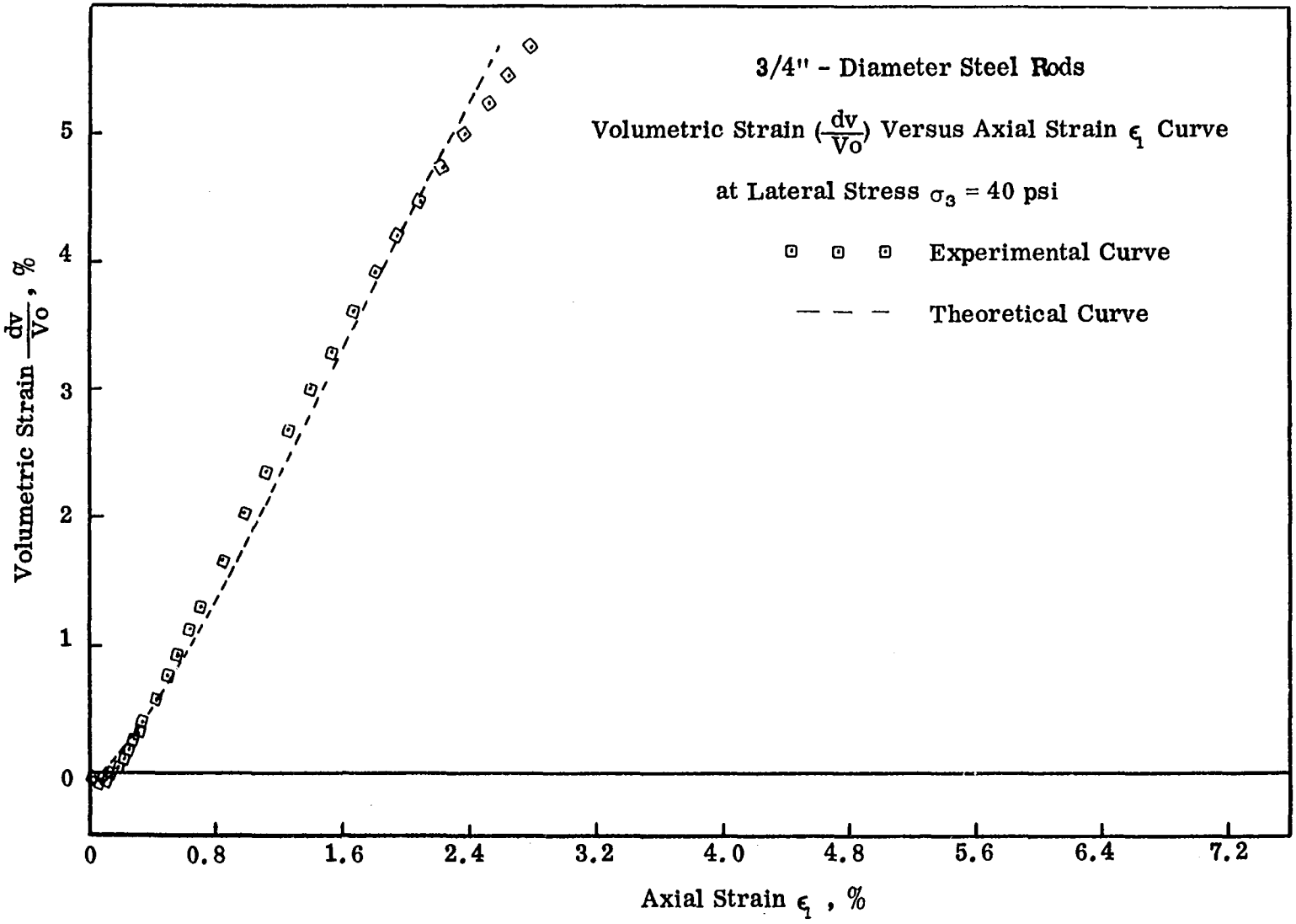

Figure 67. Volumetric strain curves

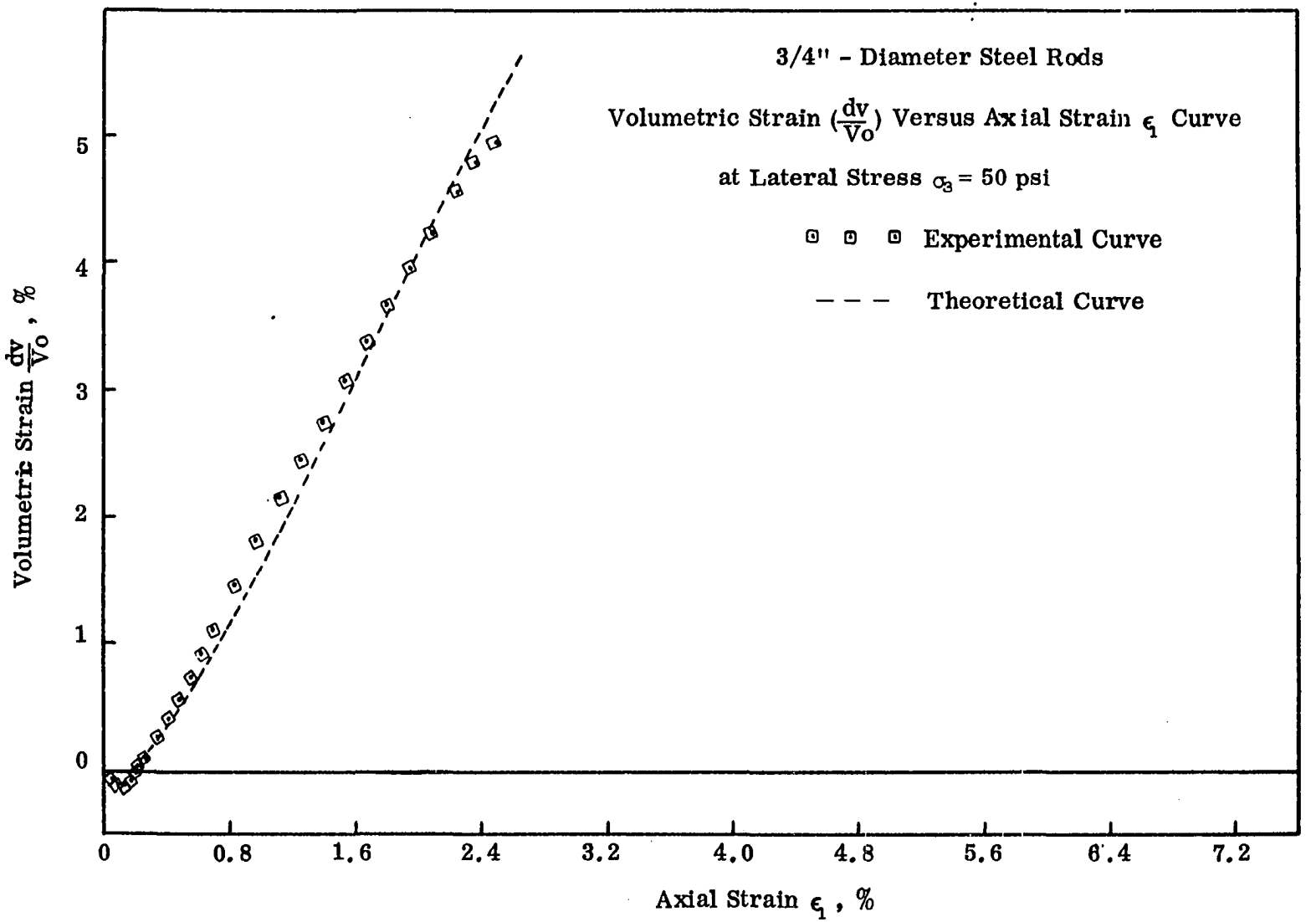

Figure 68. Volumetric strain curves

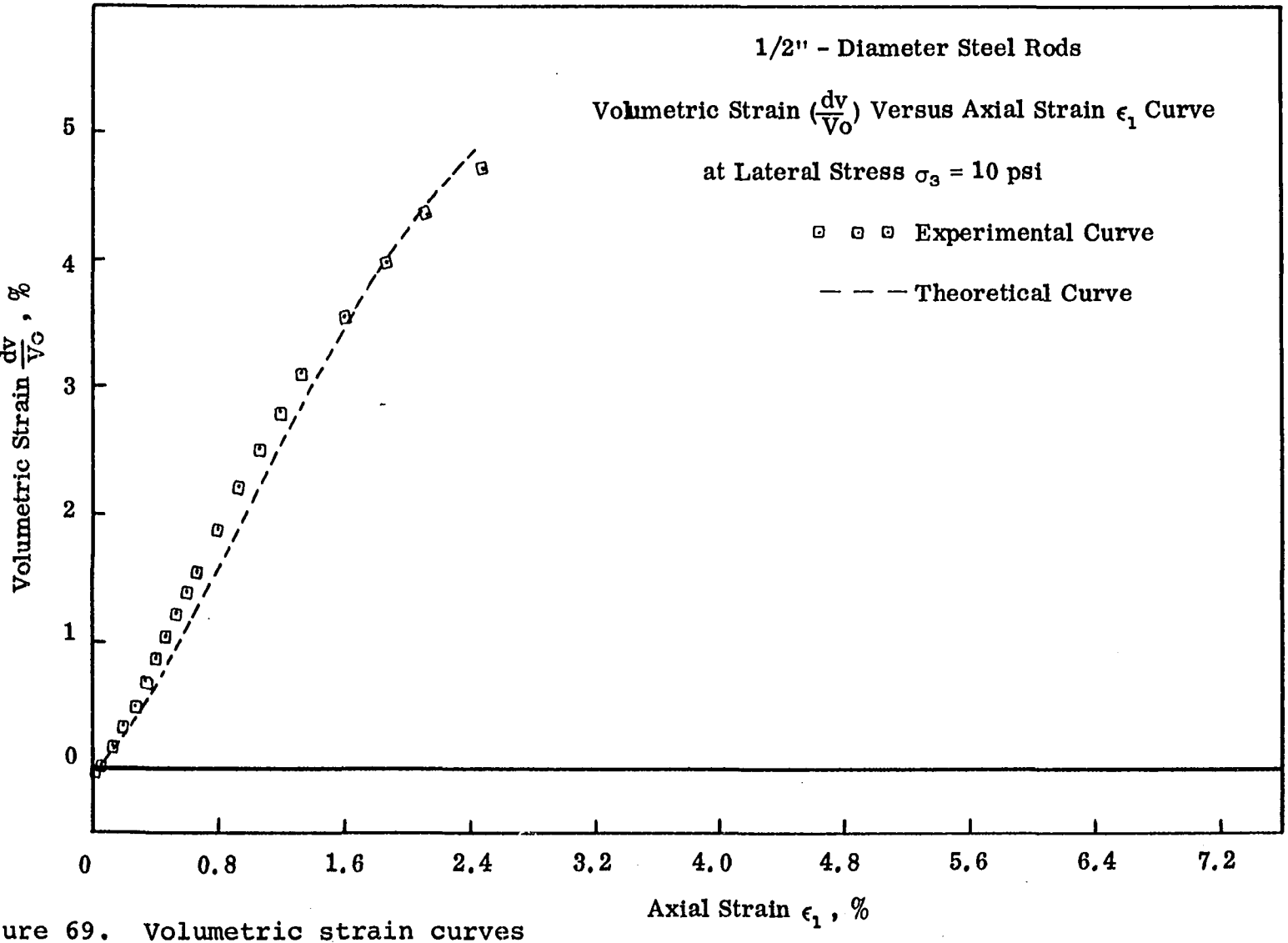

Figure 69. Volumetric strain curves

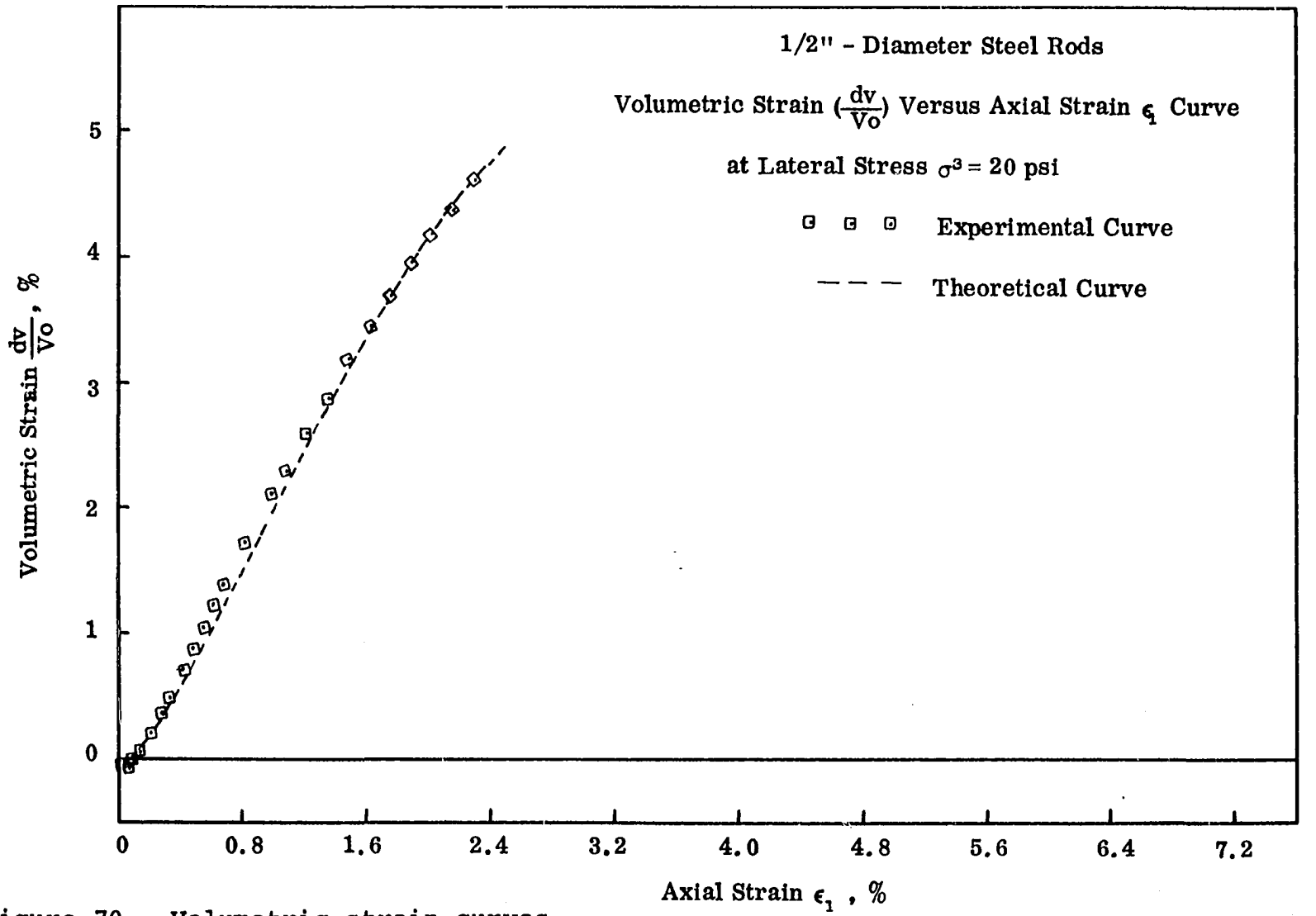

Figure 70. Volumetric strain curves

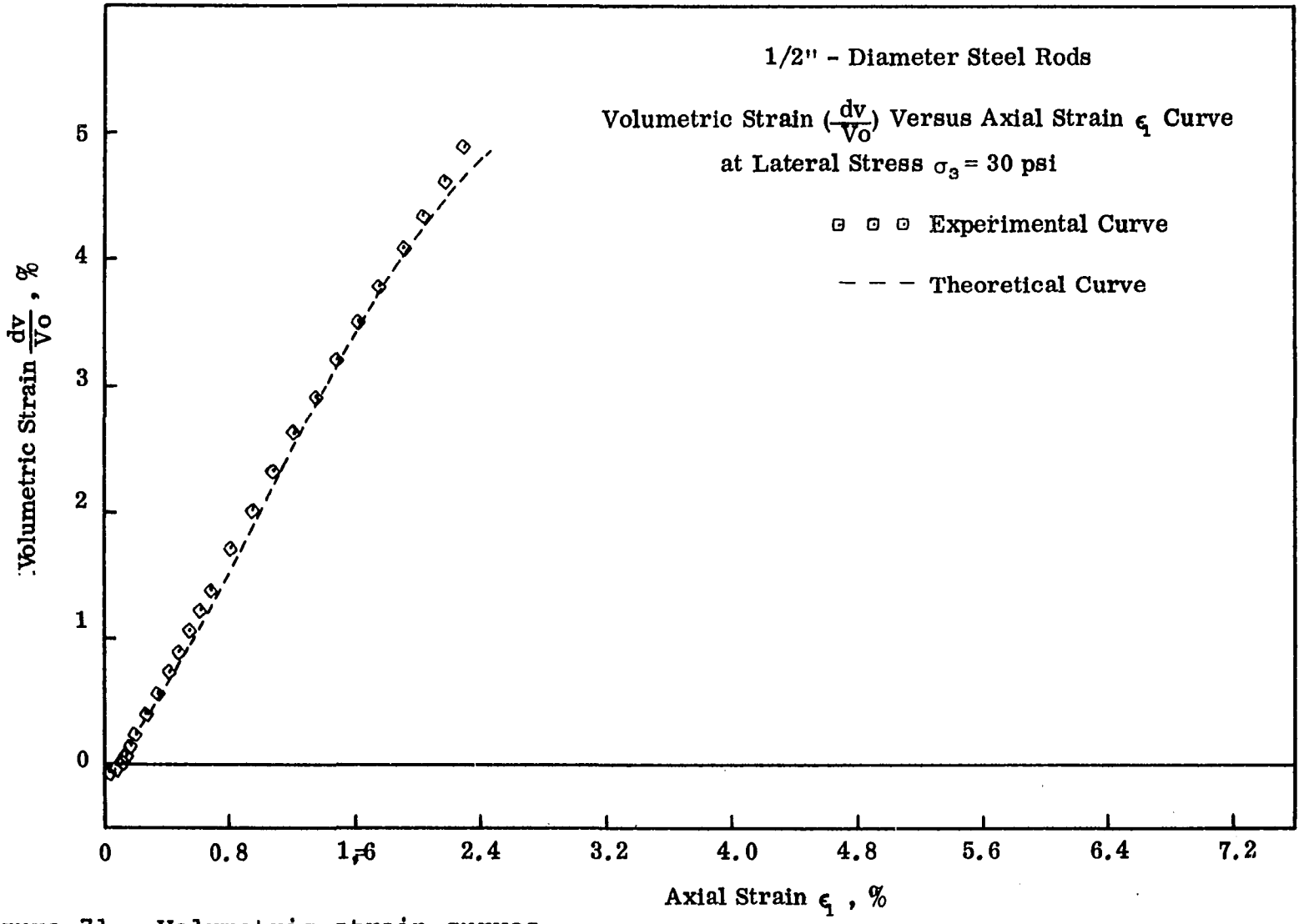

Figure 71. Volumetric strain curves

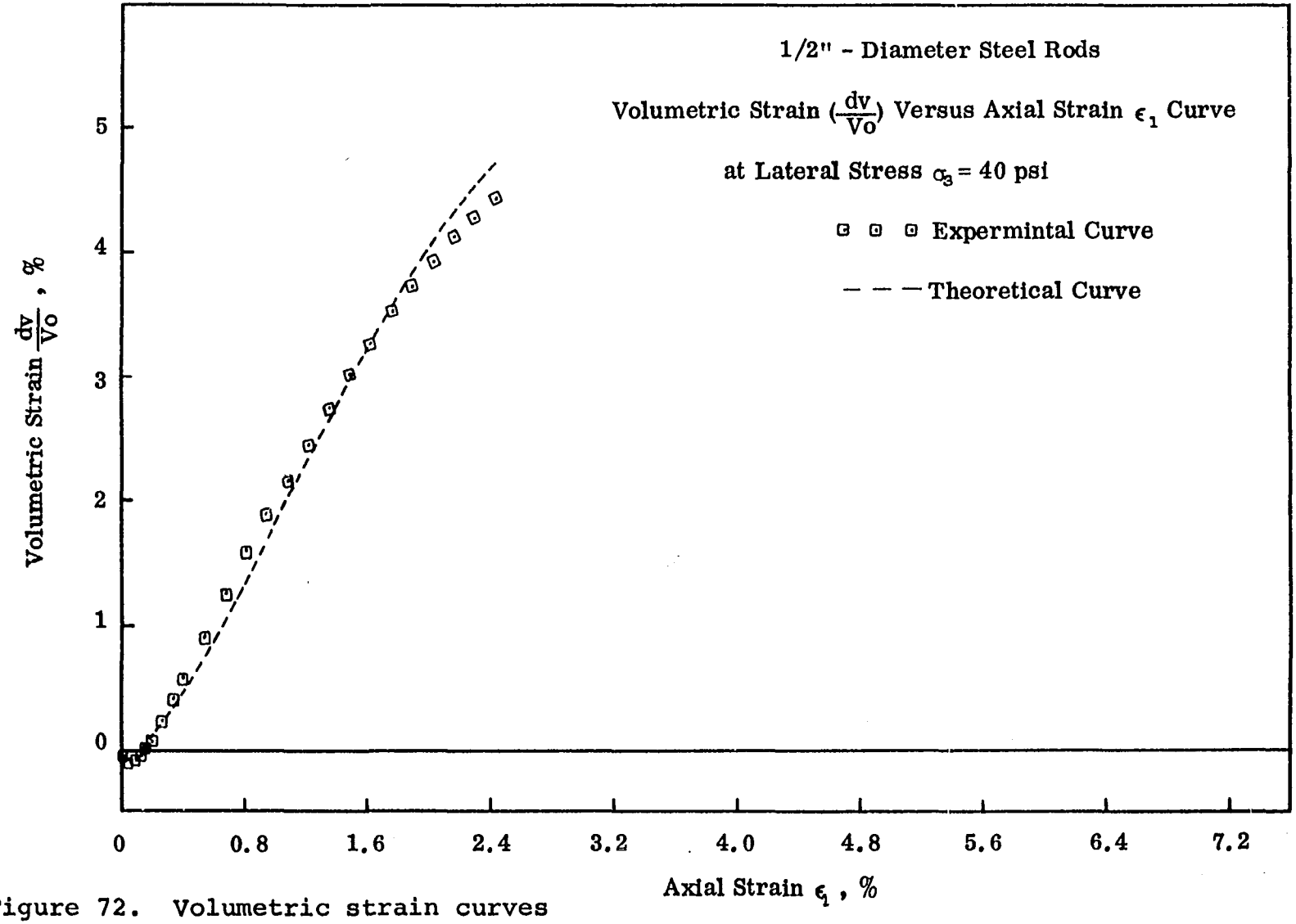

Figure 72. Volumetric strain curves

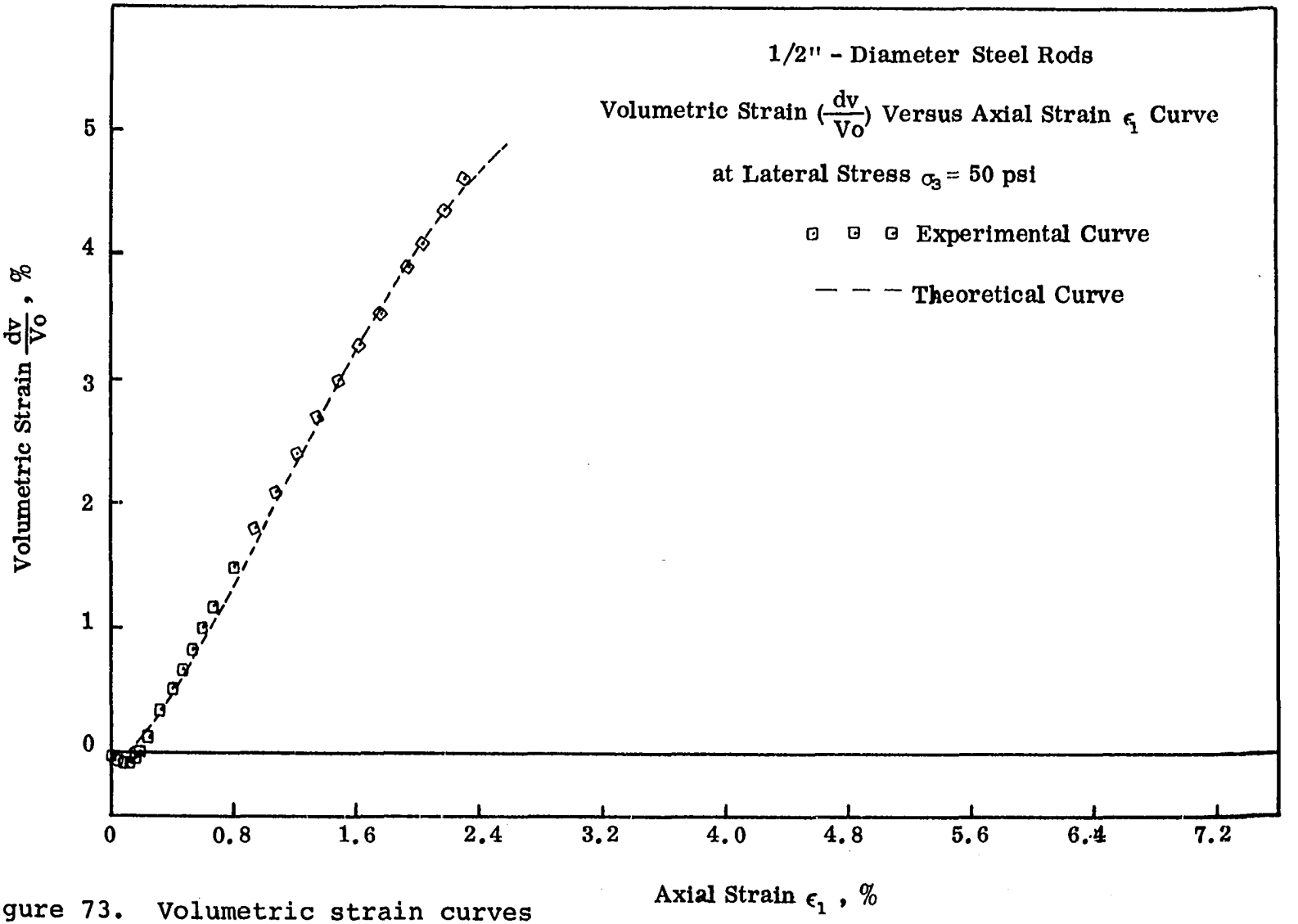

Figure 73. Volumetric strain curves

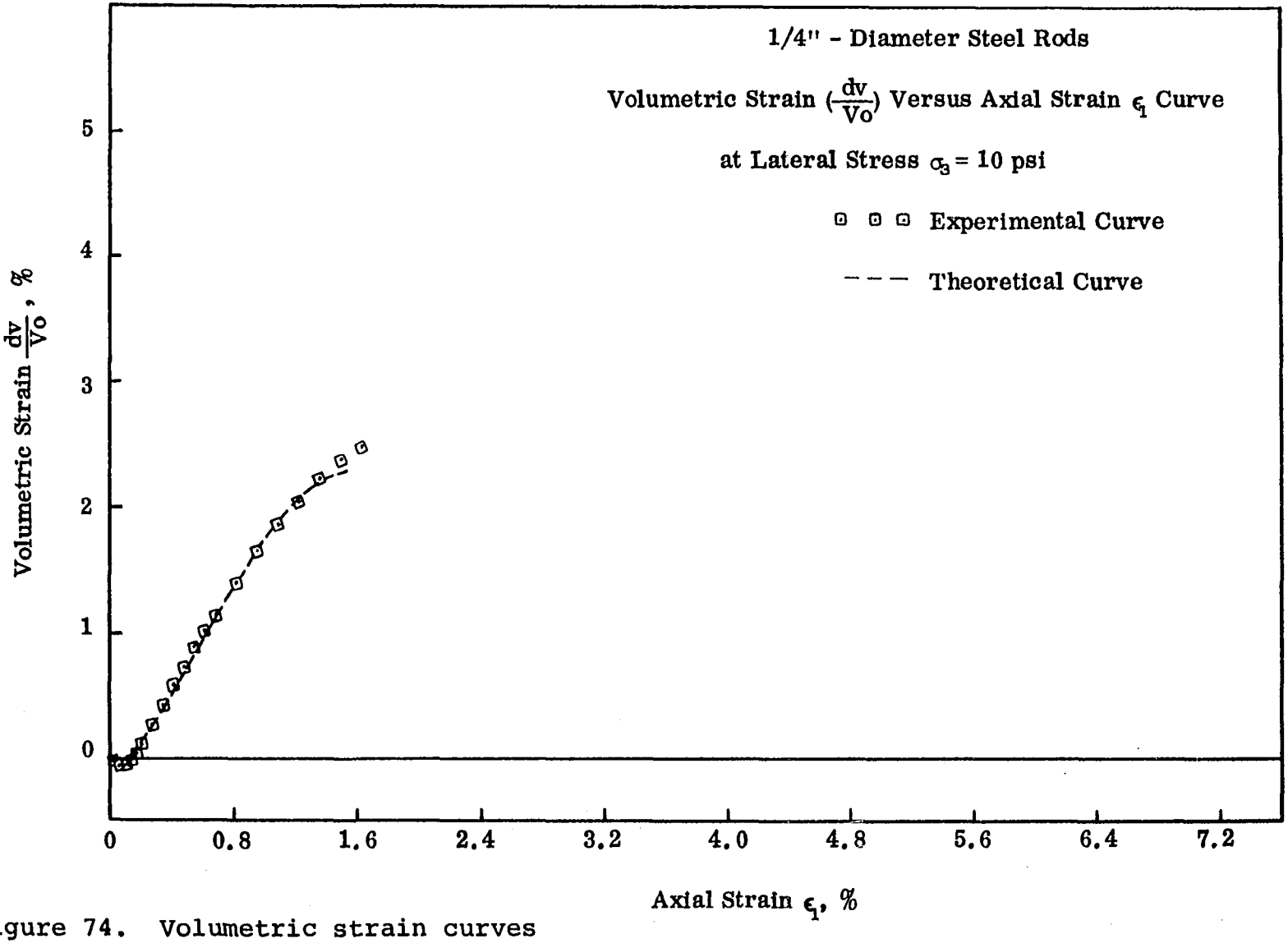

Figure 74. Volumetric strain curves

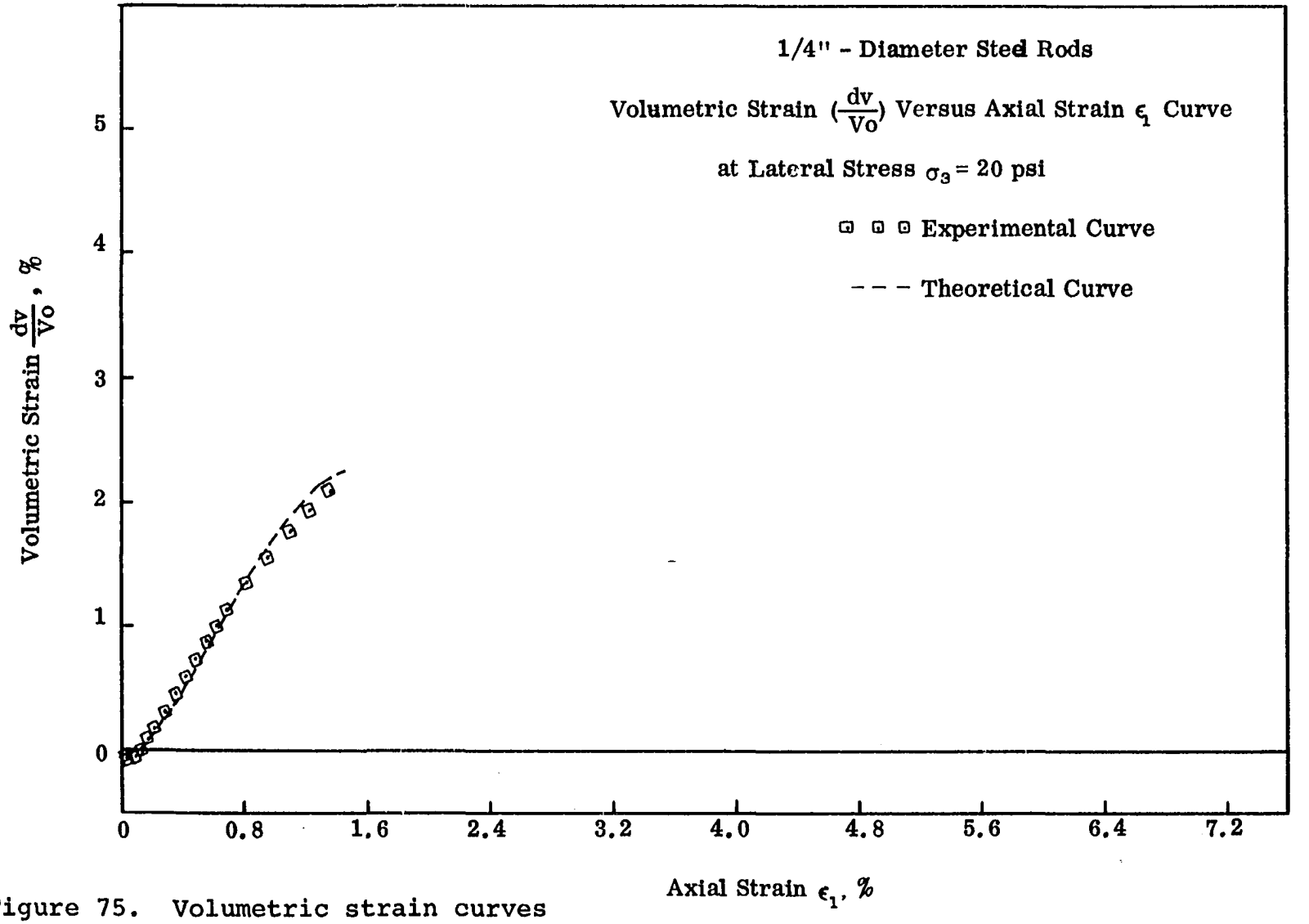

Figure 75. Volumetric strain curves

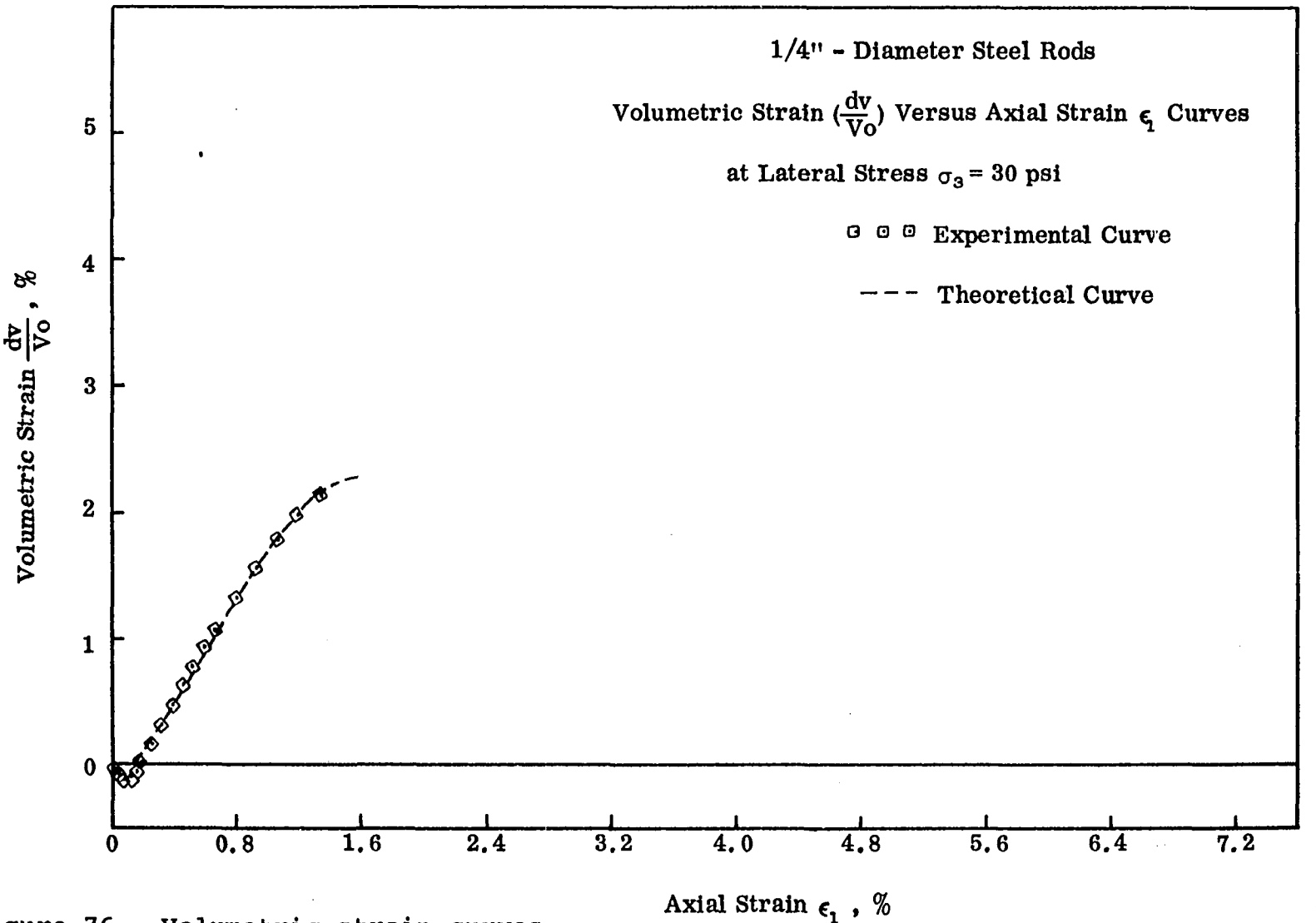

Figure 76. Volumetric strain curves

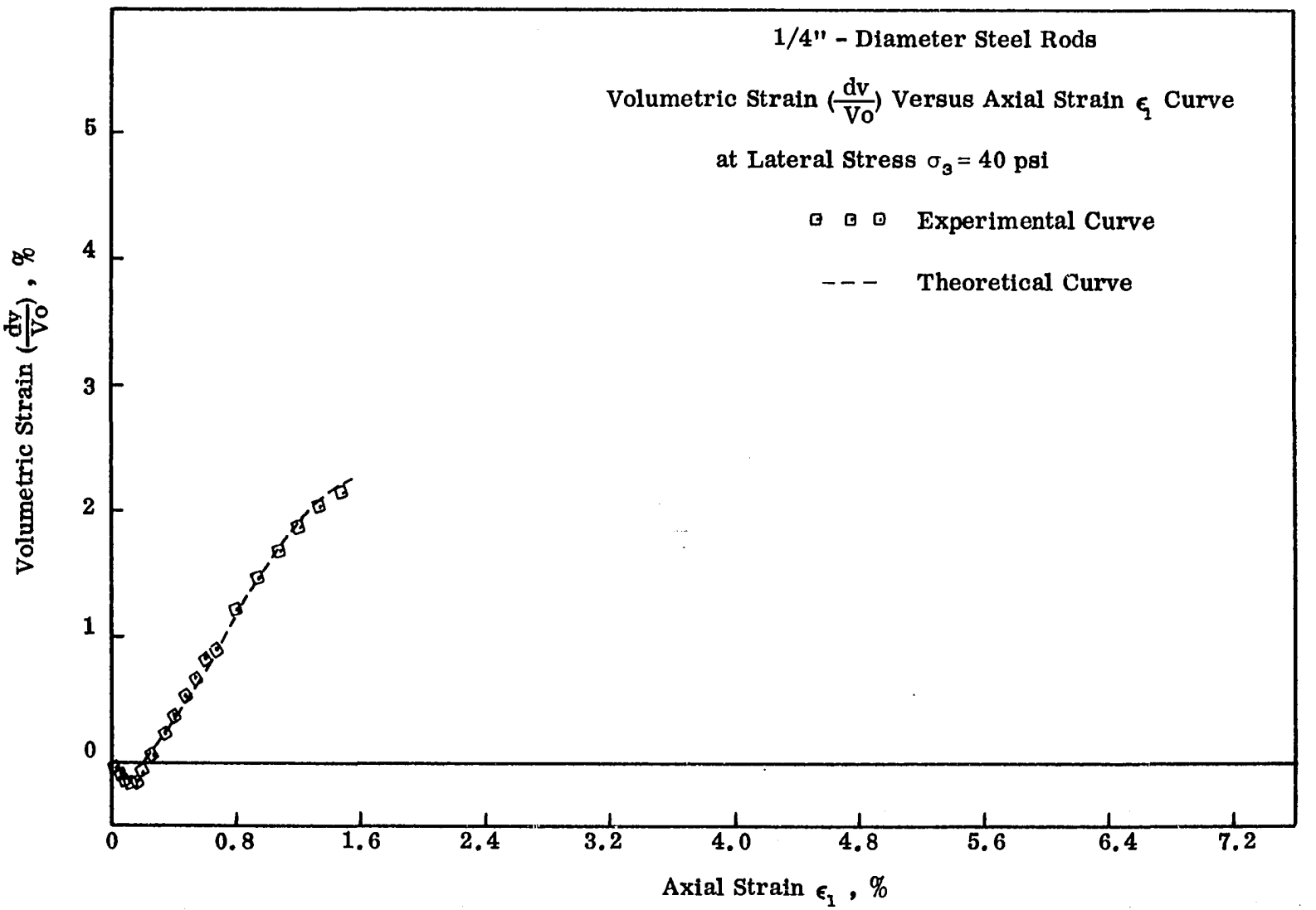

Figure 77. Volumetric strain curves

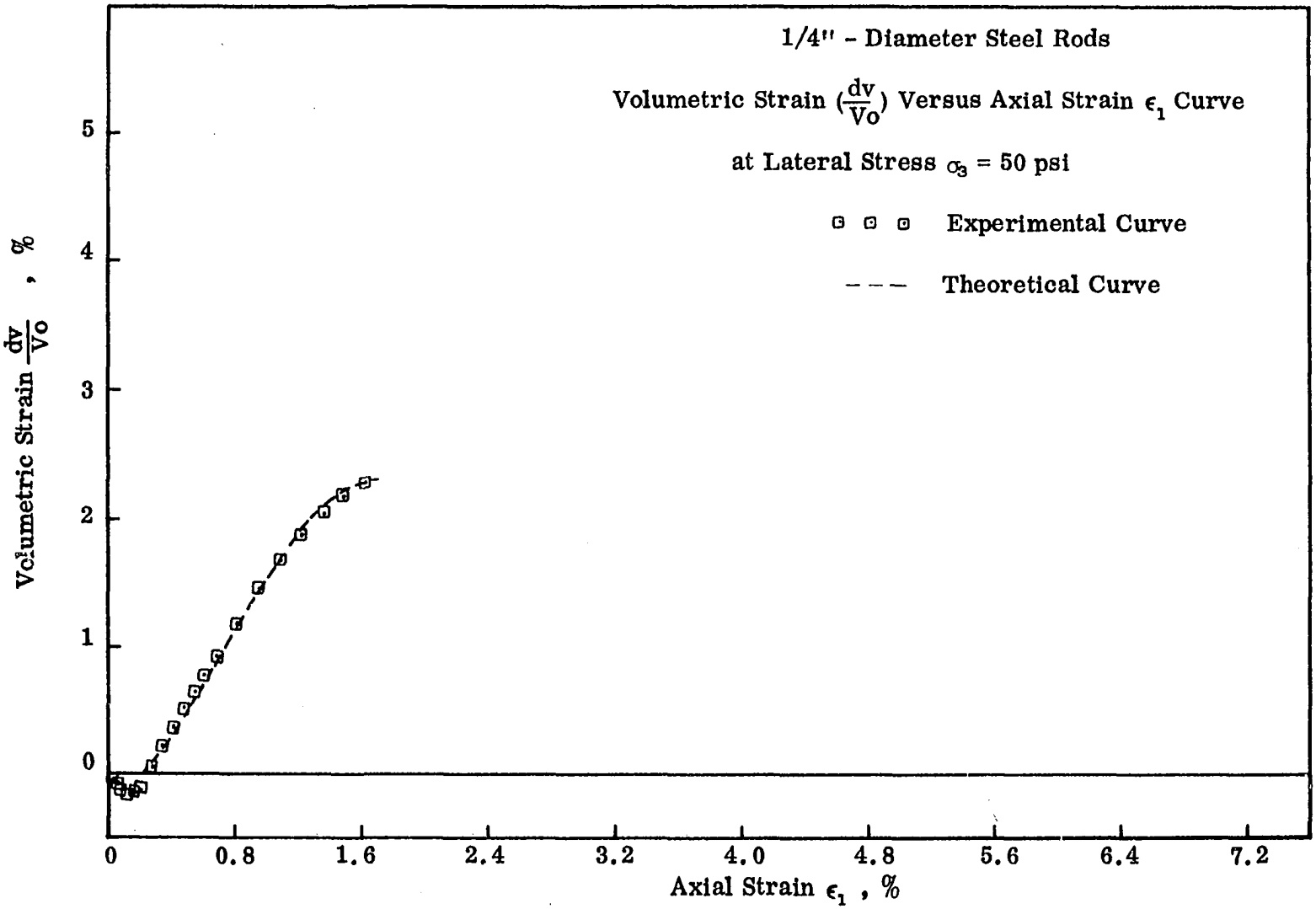

Figure 78. Volumetric strain curves

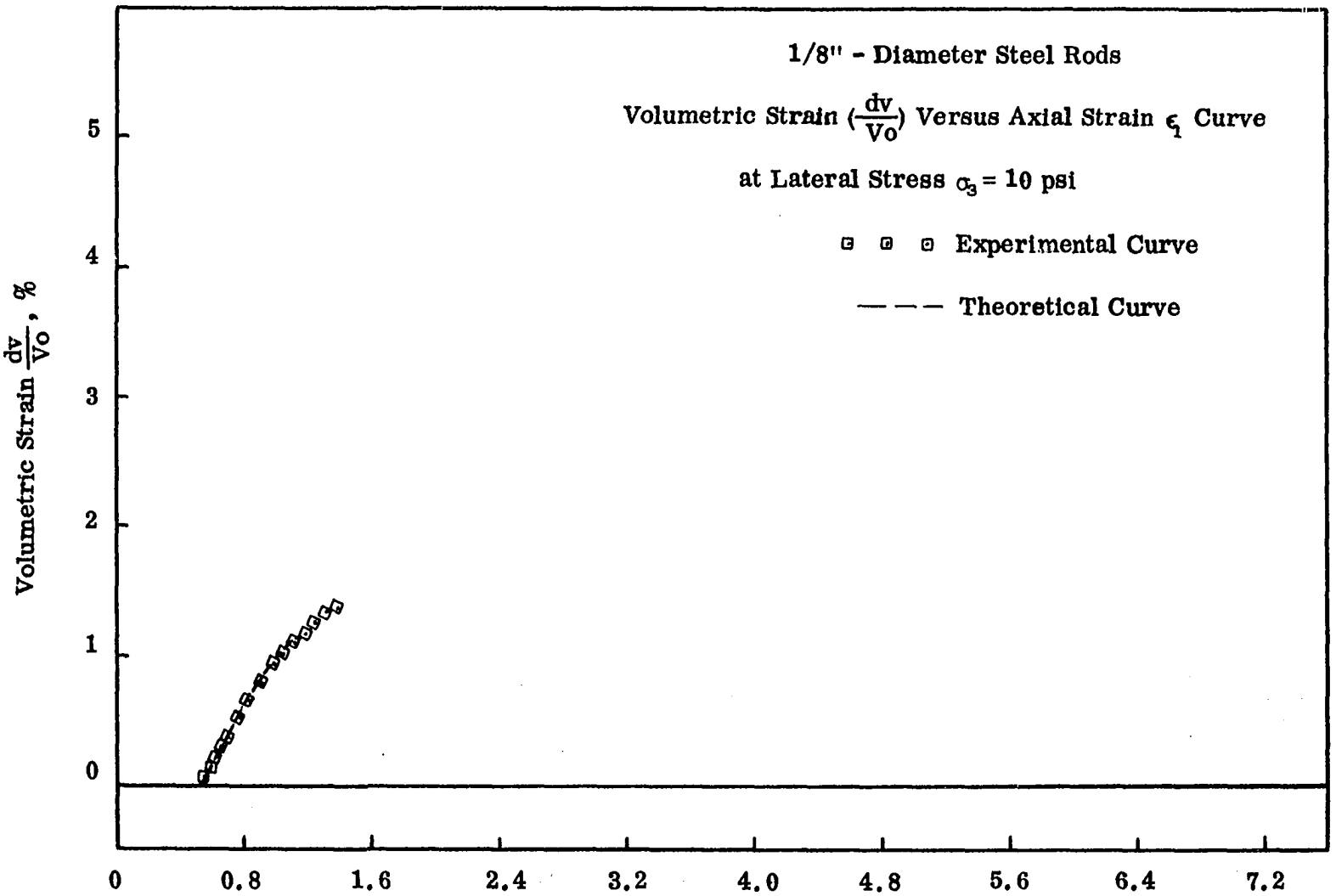

Figure 79. Volumetric strain curves

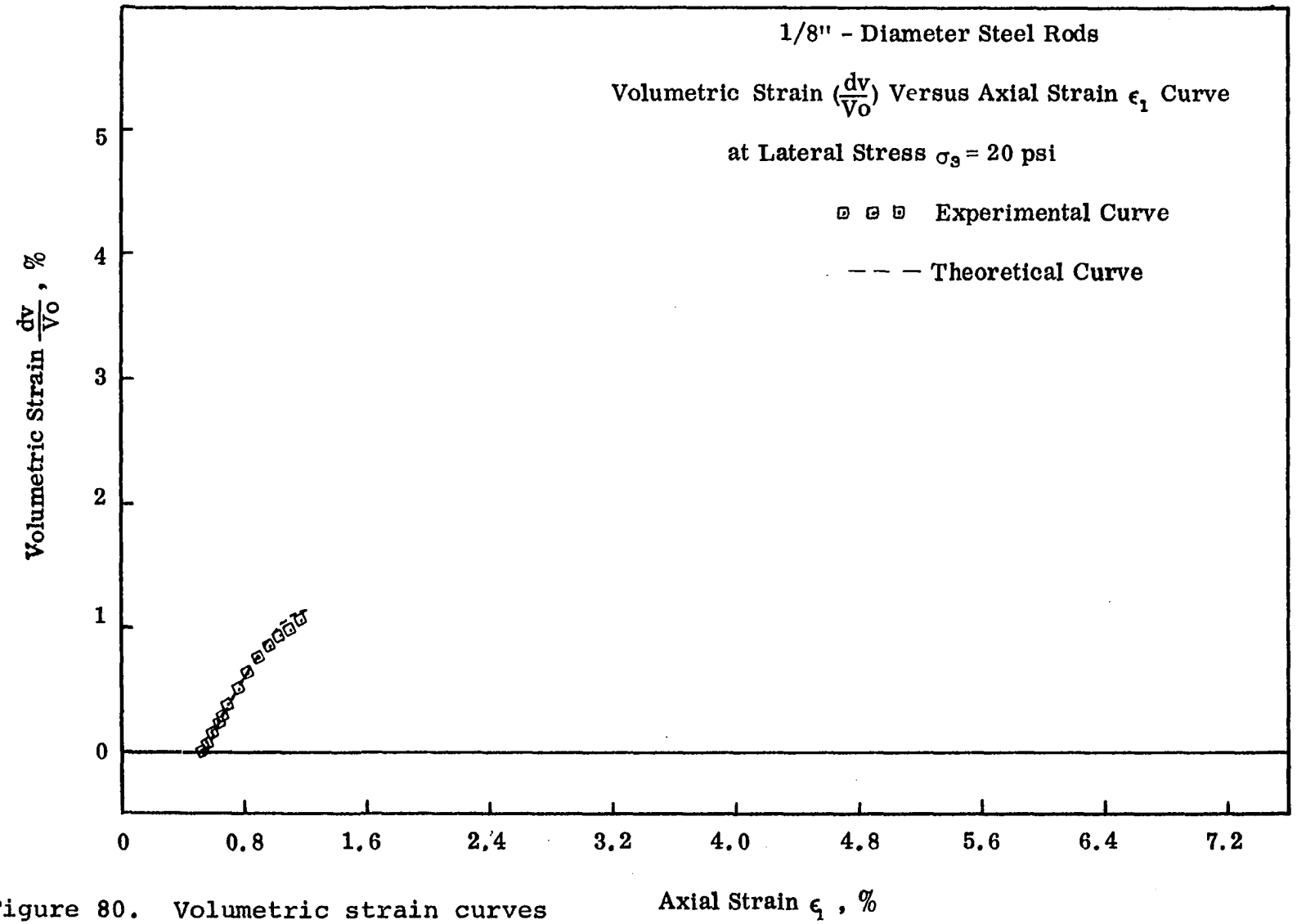

Figure 80. Volumetric strain curves

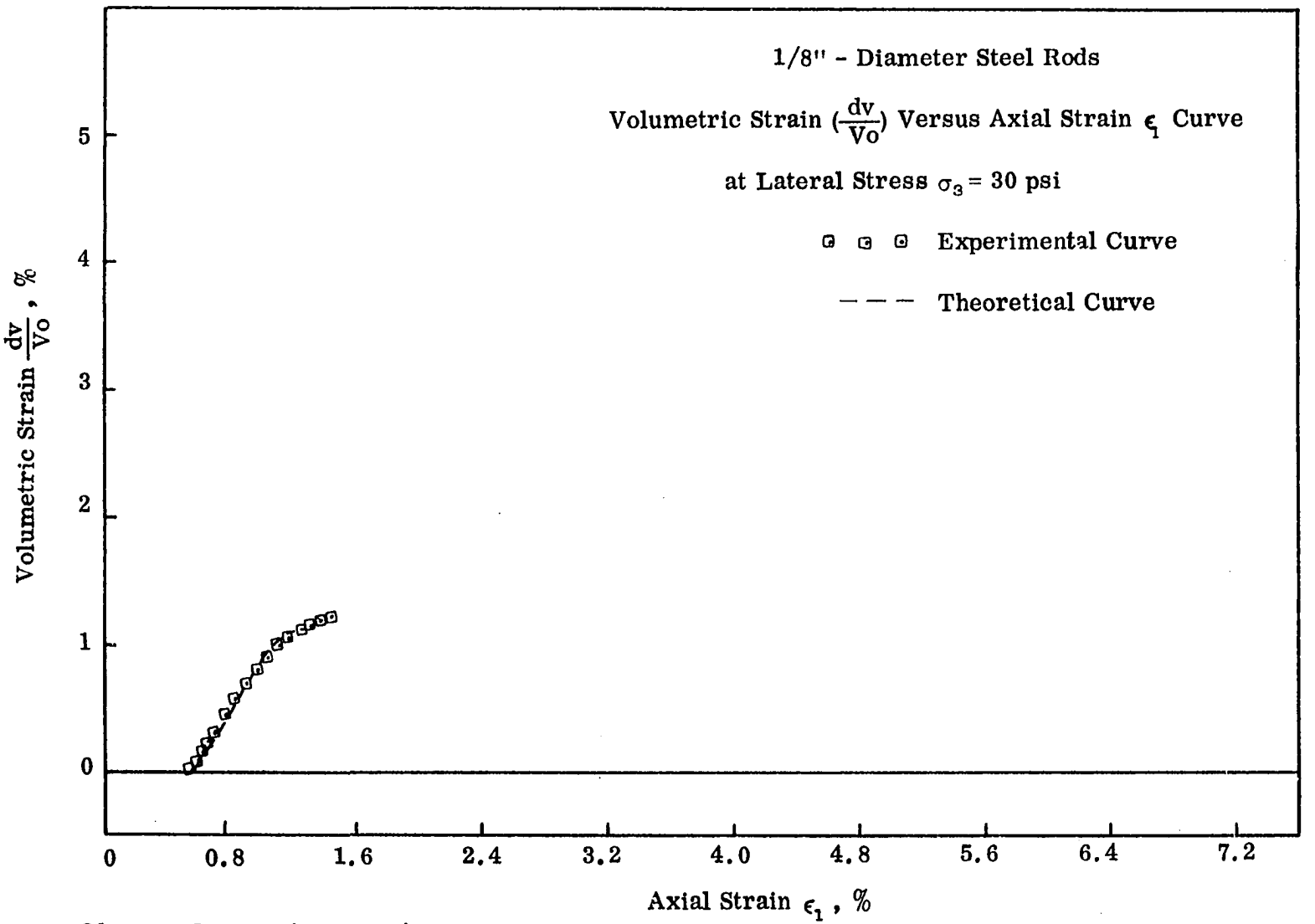

Figure 81. Volumetric strain curves

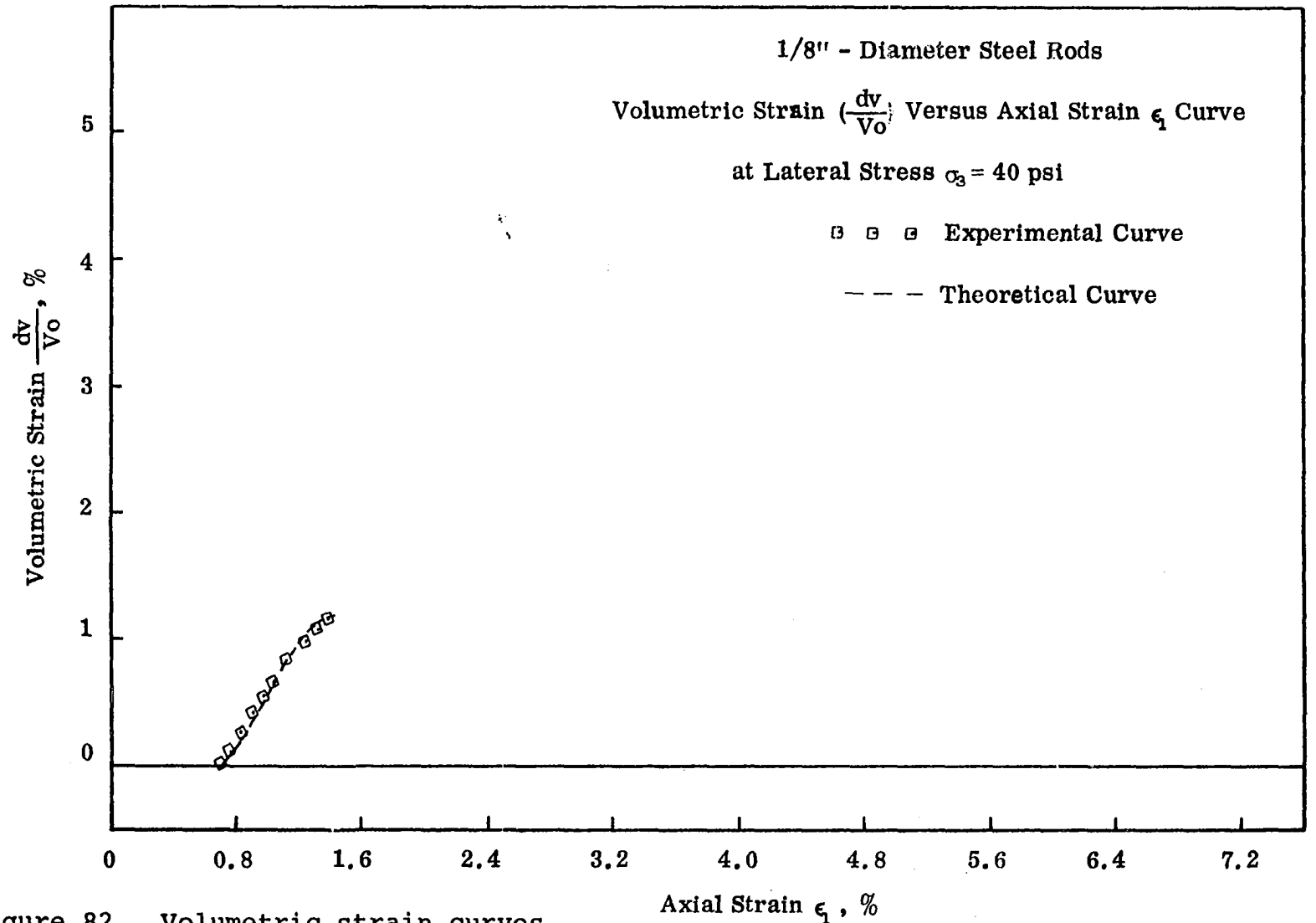

Figure 82. Volumetric strain curves

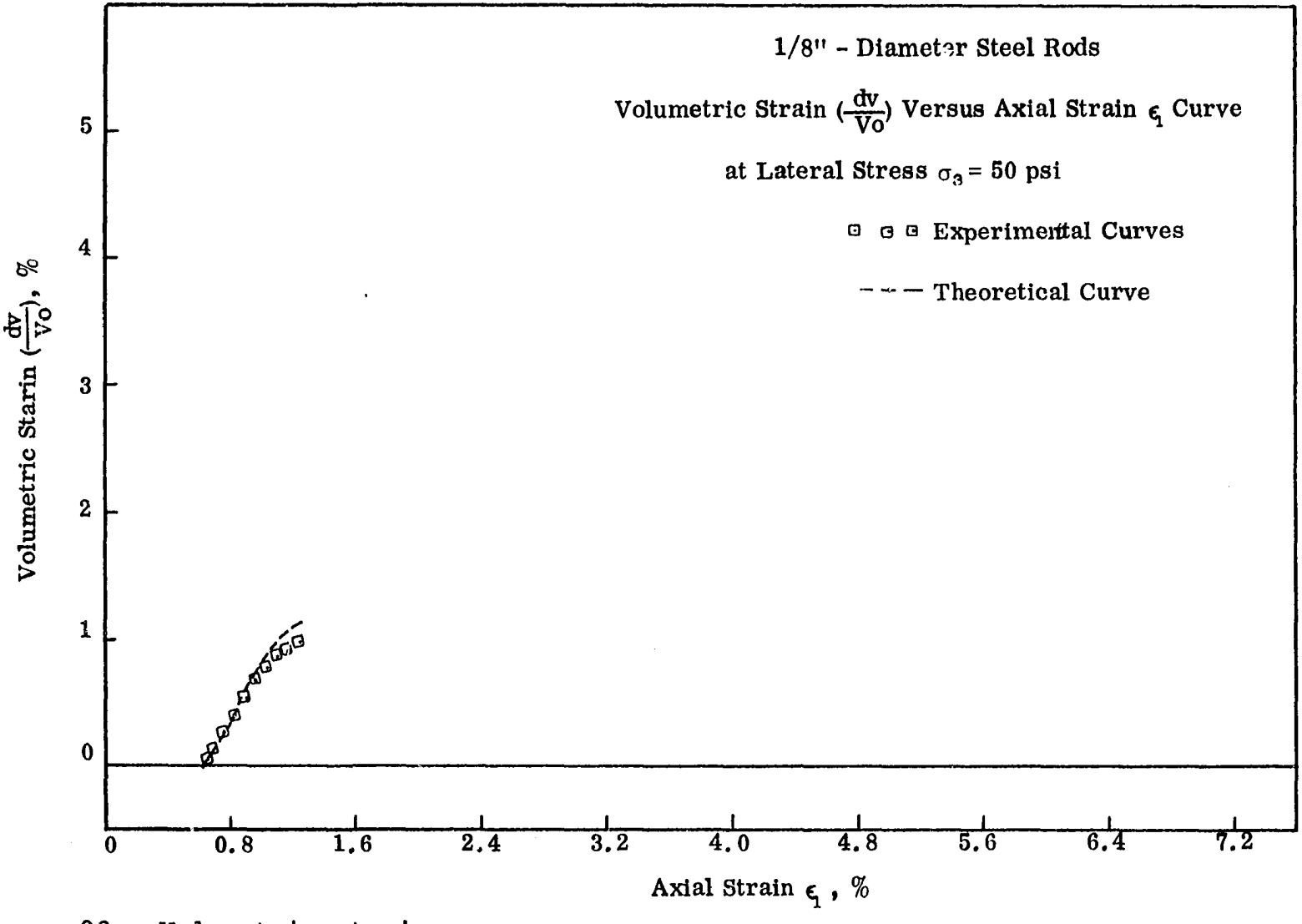

Figure 83. Volumetric strain curves

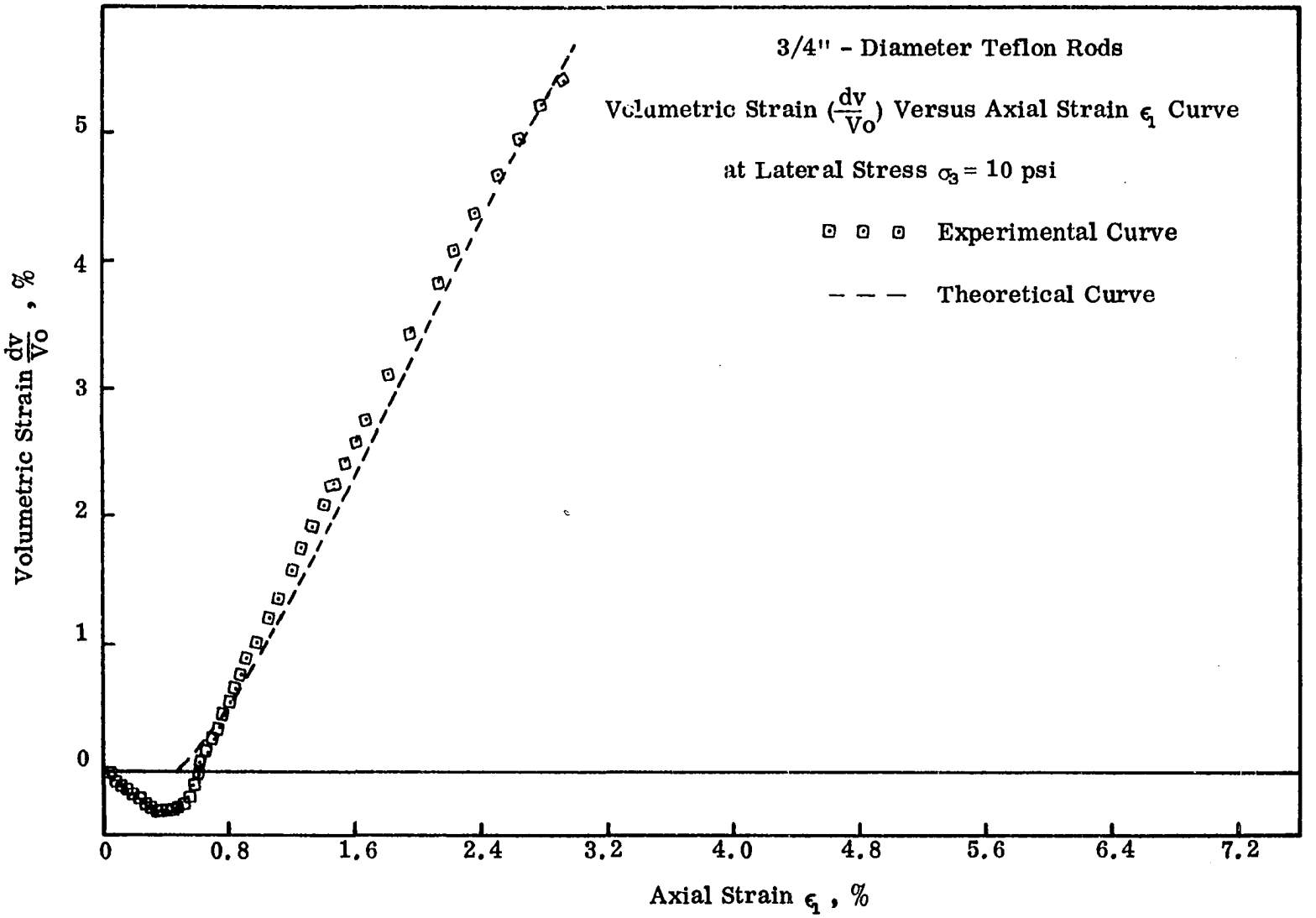

Figure 84. Volumetric strain curves

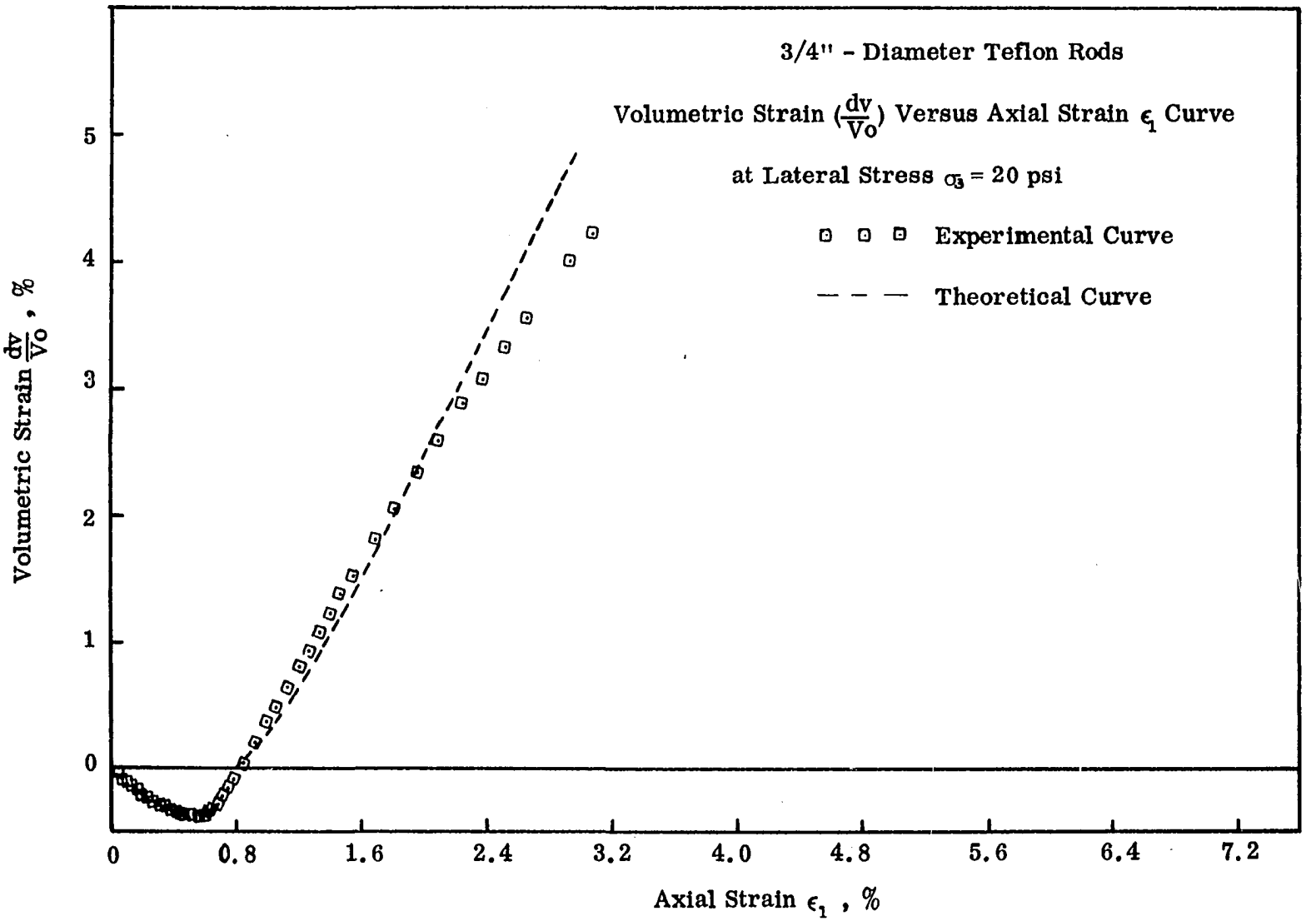

Figure 85. Volumetric strain curves

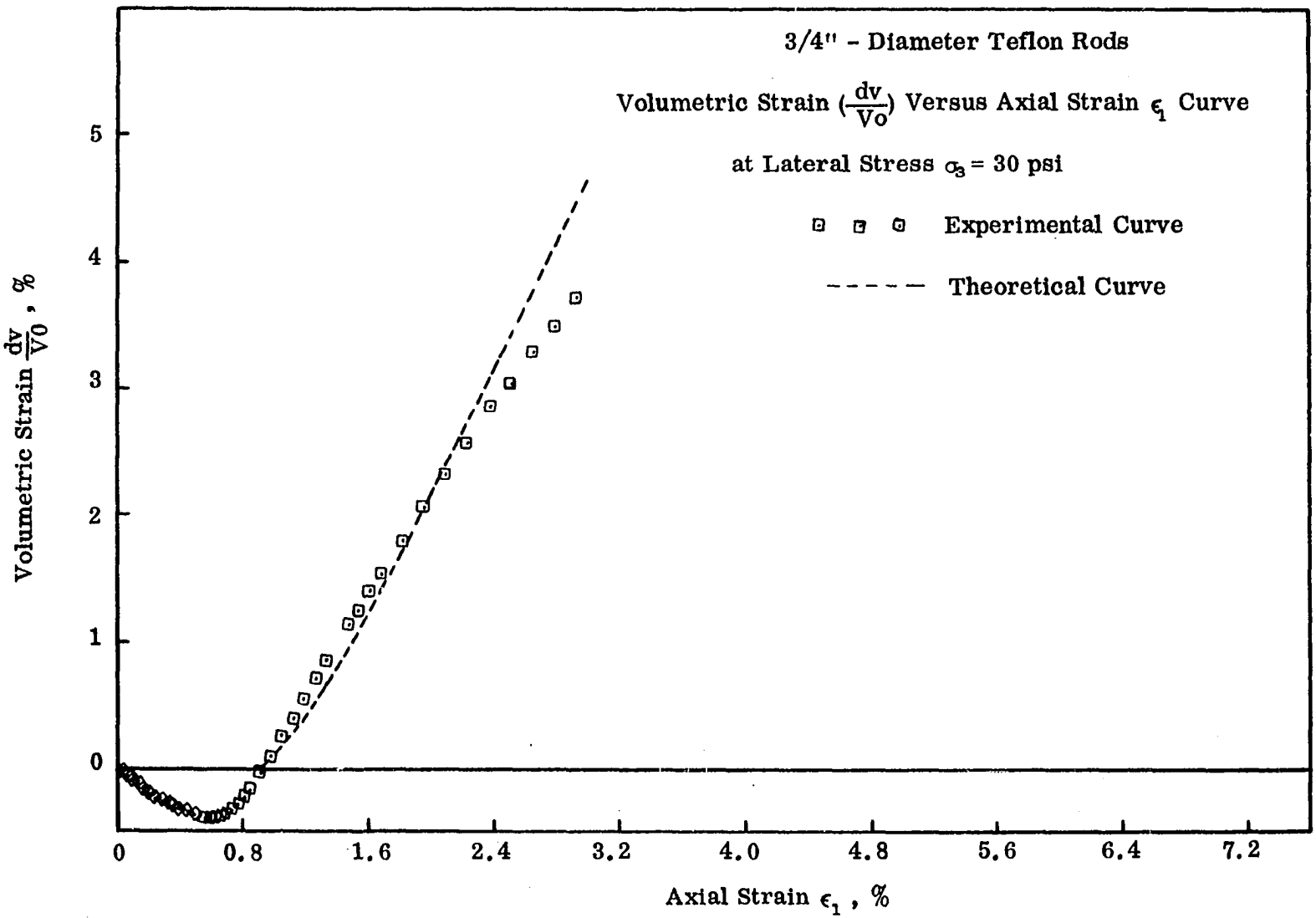

Figure 86. Volumetric strain curves

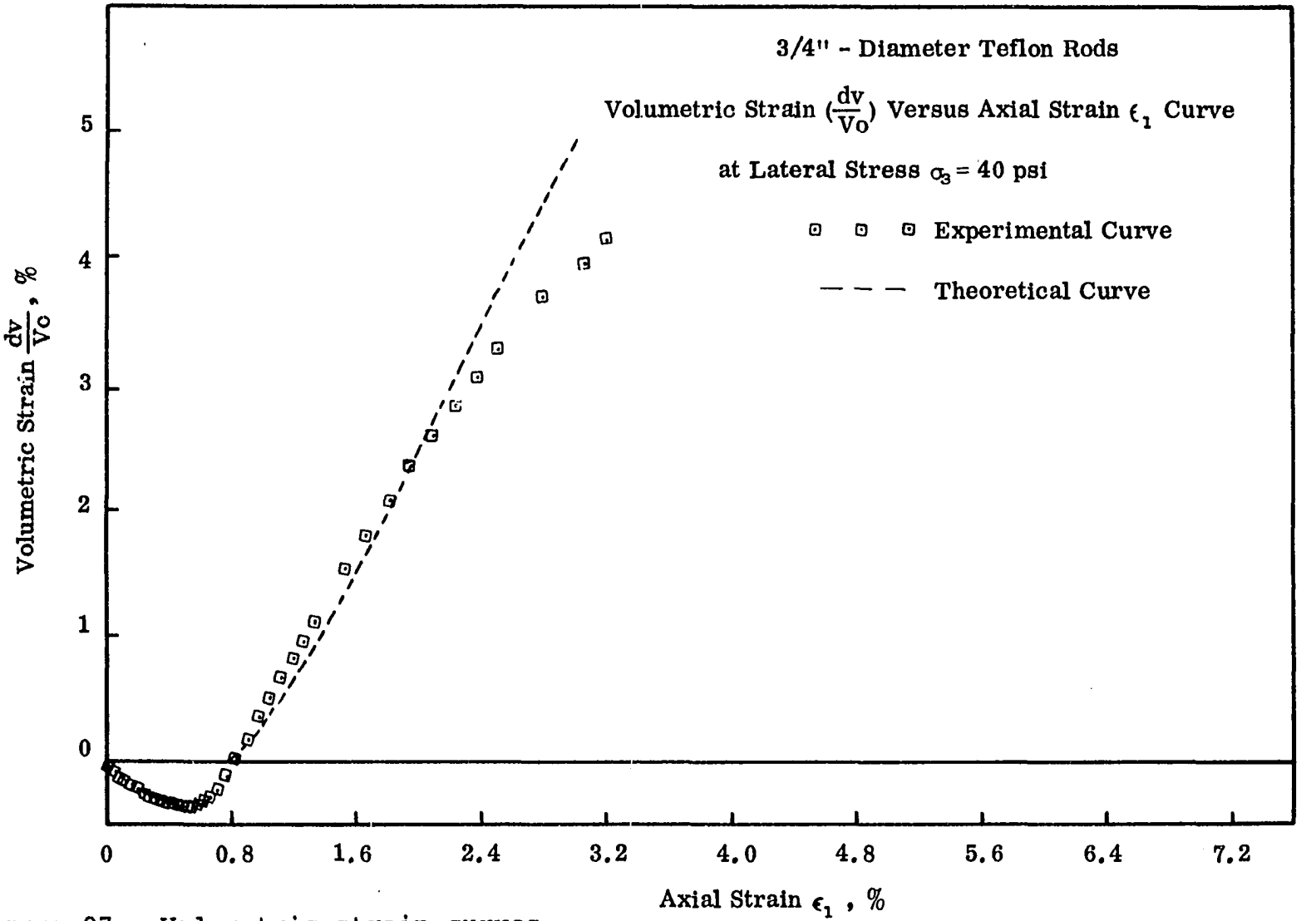

Figure 87. Volumetric strain curves

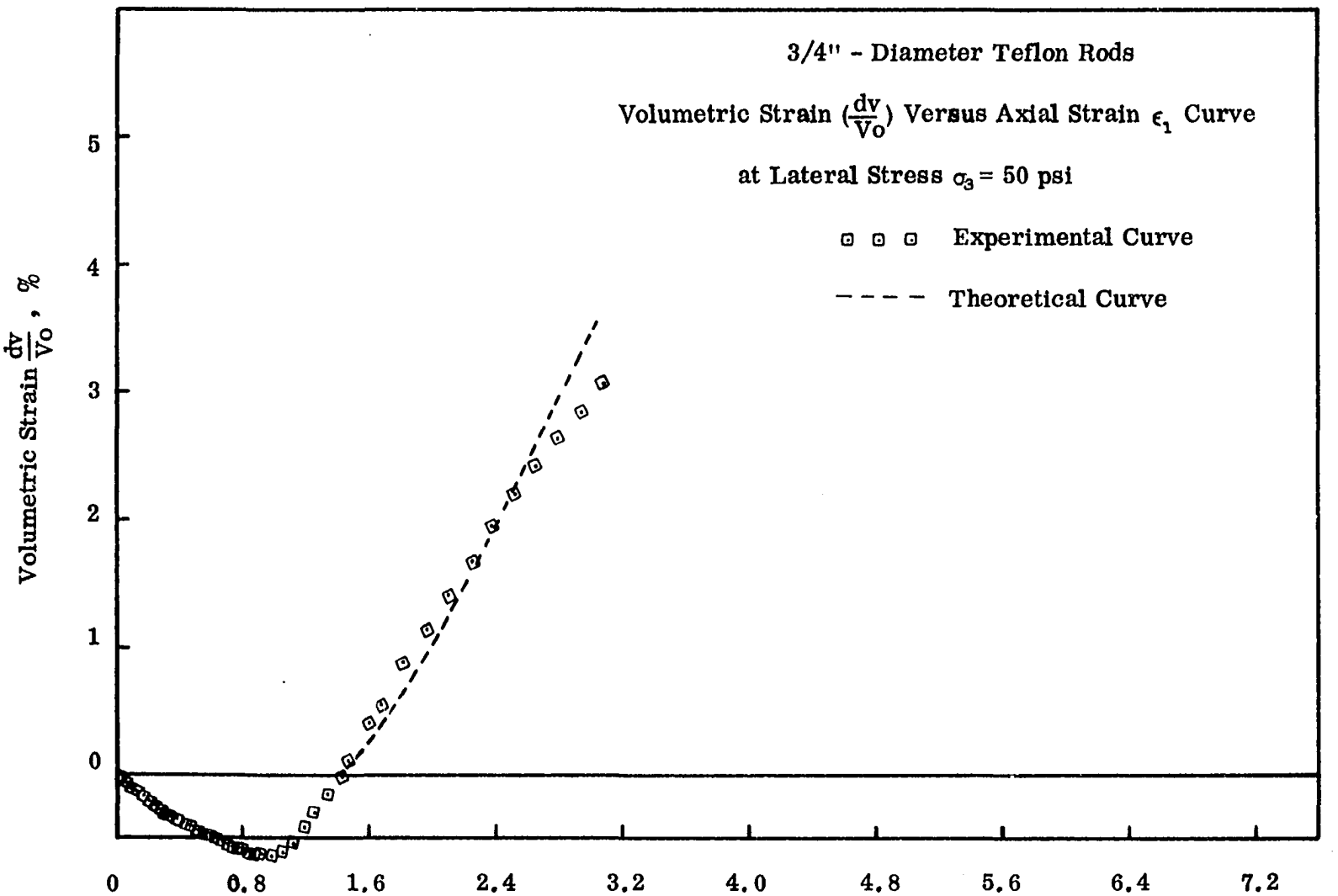

Figure 88. Volumetric strain curves

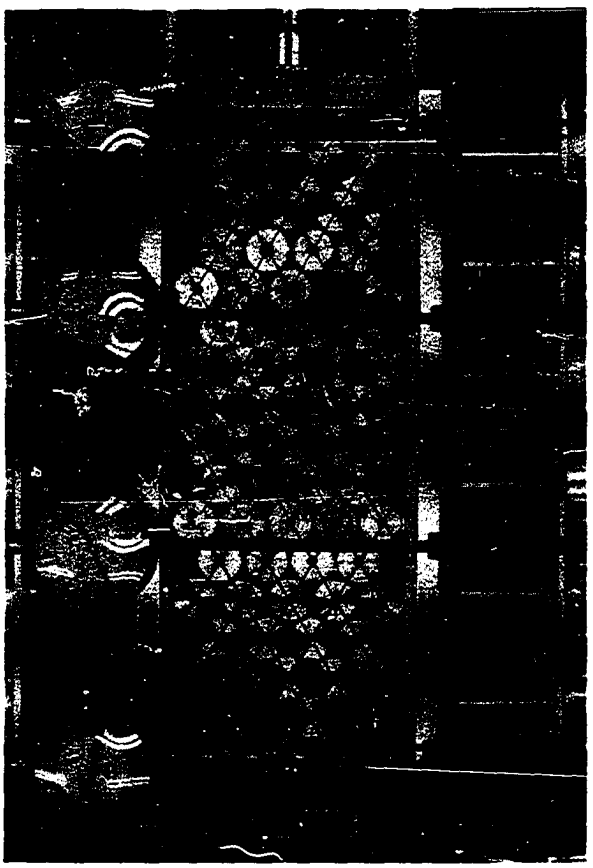

Figure 89. Single shear plane in the case of 1"-diameter rods

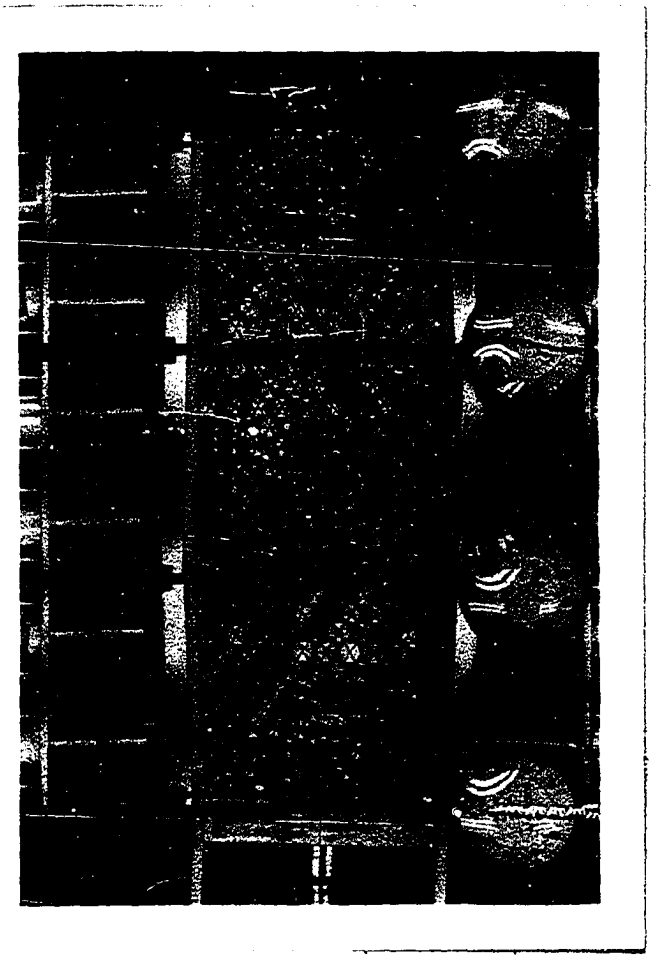

Figure 90. Multiple shear planes in the case of 1/2"-diameter rods

CONCLUSIONS

1. An assemblage of rods in initial maximum density packing and subjected to a biaxial stress field with an increasing stress ratio, always fails by fracture, i.e., by shear along a definite plane(s). This is explained by Reynolds' theory of dilatancy.
2. After the initial stage of elastic deformations, the granular mass (in this case, an assemblage of rods) has a tendency to split into semirigid groups. Outside of the shear zone of slip, no dilation was observed to take place within the semirigid groups themselves. At the surface of the rigid group, some interchange of particles between adjacent units was observed to be taking place.
3. Failure is facilitated by a layer of individual particles acting as rollers between the semirigid groups. This is explained by the fact that failure requires simultaneous rolling at some contacts and sliding on the others for each particle in the shear zone.
4. Dilatant volumetric strain $(\frac{dv}{v_0})$ does not depend on confining stresses, but is a pure geometric property of a particulate assemblage; it is a geometrical necessity if a densely packed granular

mass is to deform in an external stress or strain field.

5. Volumetric strain $(\frac{dv}{v_0})$ depends on the particle size of the granular mass or, in this case, the size of rods; the smaller the particle size, the smaller will be the volumetric deformation.
6. Starting with the maximum density packing, the volumetric deformation increases with induced axial deformation to a point where a minimum density condition exists in the shear zone. The volumetric deformation then levels off and may decrease somewhat, after which it will start increasing again. This is explained by geometrical regrouping of the granular mass during dilatant deformations.
7. Volumetric strain also depends on the number of shear planes along which slip takes place during failure. Slip occurs along a larger number of shear planes with smaller sized particles (rods). This is explained by the larger number of contacts and the statistical averaging of resolved friction along the possible shear planes.
8. Slippage along the shear zone could only be observed long after the maximum stress ratio $(\frac{\sigma_1}{\sigma_3})_{max}$ is reached. According to Mindlin (1953), at the maximum stress ratio $(\frac{\sigma_1}{\sigma_3})_{max}$, elastic movement may be expected to start at the edge of the elastic contact

surface and progress inwards with increasing axial deformations. With each increasing axial unit deformation, a new annulus of movement is created along the periphery of the surface of the remaining contact area. Thus, additional axial deformation is needed between initiation of movement at the edge of the surface of contact and the point when the movement annulus reaches the center of the contact surface. It is only after the elastic annulus has reached the center of the contact surface that shear slippage and dilatancy are initiated.

9. The maximum stress ratio $(\frac{\sigma_1}{\sigma_3})_{max}$ seems to be insensitive to confining stress σ_3, and depends only on the coefficient of sliding friction. This is explained by the theory presented.

10. There is a slight tendency for the maximum stress ratio to decrease with decreasing particle size. This is not explained by the theory presented.

11. The stress ratio in the post-maximum stress ratio $(\frac{\sigma_1}{\sigma_3})_{max}$ region is found to be dependent on the particle size of the granular mass, in this case on the size of rods. This is supported by the theory presented.

12. The stress ratio in the post-maximum stress ratio $(\frac{\sigma_1}{\sigma_3})_{max}$ is, to a great extent, controlled by slips on the shear planes. Slip can occur on one plane

throughout; it can also occur on one plane and then shift from plane to plane for the rest of the axial deformation. This may be termed as arrested slips. There can be several combinations of the above processes of slip.

13. The so-called residual stress, or the "constant volume" region, of stress-strain curves may relate to slips shifting continuously from plane to plane rather than a zero volume change condition. A continuous plateau of the stress-strain curve after the maximum stress ratio $(\frac{\sigma_1}{\sigma_3})_{max}$ is reached can also be explained by the process of shifting slip from plane to plane without confining itself to any plane for any appreciable duration.

SUGGESTION FOR FURTHER INVESTIGATIONS

This research has brought into light quite a few very interesting points. Two are:

1. Failure does not occur only due to sliding, but also due to a combination of sliding and rolling.
2. With decreasing size of the particles, the tendency of the failure slip to shift from plane to plane increases; in other words, more shear planes are developed than in the case of larger particles. This phenomenon of stopping and shifting slip keeps the stress ratio higher than if the slips were confined to one plane only.

To study in more detail and to confirm these aspects, it is suggested that experimentation should encompass:

1. Elliptical and hexagonal shaped rods.
2. Lateral stress level from 50 to 100 or 150 psi.
3. Mixture of different shapes.
4. Square rods arranged to simulate different angles of bedding planes.
5. Application of axial deformation from both sides.
6. Minimum density packing and other packings between minimum and maximum densities.

For improvement of the biaxial test apparatus, it is suggested that:

1. All the observations, load and deformation

measurement should be taken continuously and recorded electrically.

2. All the sides of the collapsible box should be coated with a thin film of frictionless coating.
3. An additional axial jack should be used to apply axial deformation from both the ends.

BIBLIOGRAPHY

Andrade, E. N. Dac., and Fox, J. W., "The mechanism of dilatancy," The Proceedings of the Physical Society, London, Section B, Vol. 62, Part 8, No. 356B, 1949, pp. 483-500.

Archard, J. F., "Elastic deformation and laws of friction," Proceedings of the Royal Society of London, Vol. 243, Series A, No. 1233, 1957, pp. 190-205.

Bahadur, Shyam, "The Correlation of Frictional and Visco-Elastic Properties of Polymers," Ph.D. thesis, University of Michigan, 1970.

Bishop, A. W., "On shear characteristics of a saturated silt, measured by triaxial compression, by Penman," Geotechnique, Vol. 4, No. 1, 1954, pp. 43-45.

Bowden, F. P., "The friction of non-metallic solids," J. Inst. Petrol., Vol. 40, 1954, pp. 89-103.

Bowden, F. P., and Tabor, D., The Friction and Lubrication of Solids, Part 1, Clarendon Press, Oxford, 1954.

Bowden, F. P., and Tabor, D., The Friction and Lubrication of Solids, Part 2, Clarendon Press, Oxford, 1964.

Brown, R. L., and Hawksley, P. G. W., "The internal flow of granular masses," Fuel, Vol. 26, No. 6, Nov.-Dec., 1947, pp. 159-173.

Byerlee, J. D., "Theory of friction based on brittle fracture," Journal of Applied Physics, Vol. 38, 1967, pp. 2928-2934.

Caquot, A., Equilibre des Massifs a Frottement Inteme, Stabilite des Terres Pulverent et Coherentes, Gauthier Villars, Paris, 1934.

Chang, Keng Liu, "Stresses and Deformation due to Tangential and Normal Loads on an Elastic Solid with Application to Contact Stresses," Ph.D. thesis, University of Illinois, 1950.

Coulson, J. H., The Effect of Surface Roughness on the Shear Strength of Joints in Rock, Corps of Engineers [Omaha] Missouri River Div. Tech. Rep. MRD-2-70, 1970.

Deresiewicz, H., "The half-space under pressure distributed over an elliptical portion of its plane boundary," Transactions of the A.S.M.E., Series E, Vol. 27, March, 1960, pp. 111-119.

Deresiewicz, H., "Stress-strain relations for a sample model of a granular medium," Transactions of the A.S.M.E., Vol. 80, 1958, pp. 402-406.

Drennon, C. B., and Handy, R. L., "Stick-Slip of Lightly Loaded Limestone," Iowa State Soil Research Lab. Contribution No. 72109, 1972.

Duffy, J., and Mindlin, R. D., "Stress-strain relations and vibrations of a granular medium," Transactions of the A.S.M.E., Vol. 79, 1957, pp. 585-593.

Finn, W. D. Liam, "Volume changes in triaxial and plane strain tests," Journal of the Soil Mechanics and Foundation Division, A.S.C.E., Vol. 93, SM6, 1967, pp. 297-308.

Haythornthwaite, R. M., "The role of friction in granular media," in International Union of Theoretical and Applied Mechanics, Rheology and Soil Mechanics Symposium, J. Kravtchenko and P. M. Sirieys, Eds., Springer-Verlag, New York, 1964, pp. 160-163.

Hetenyi, M., and McDonald, P. H., Jr., "Contact stresses under combined pressure and twist," Transactions of the A.S.M.E., Vol. 80, 1958, pp. 396-401.

Hills, E. Sherbon, Elements of Structural Geology, John Wiley and Sons Inc., New York, 1963.

Horn, H. M., and Deere, D. U., "Frictional characteristics of minerals," Geotechnique, Vol. 12, 1962, pp. 319-335.

Horne, M. R., "The behaviour of an assembly of rotund, rigid, cohesionless particles. I and II," Proceedings, Royal Society of London, Series A, Vol. 286, 1965, pp. 62-97.

Jaeger, J. C., "The friction properties of joints in rocks," Geofis. Pura Appl., Vol. 43, 1959, pp. 148-158.

Jaeger, J. C., and Cook, N. G. W., Fundamental of Rock Mechanics, Methuen and Co. Ltd., London, 1969.

Jenkin, C. F., "The pressure exerted by granular material: an application of the principles of dilatancy," Proceedings of the Royal Society of London, Series A, Vol. 131, June, 1931, pp. 53-89.

Kazdi, A., "Contributions to the investigation of granular systems," in International Union of Theoretical and Applied Mechanics, Rheology and Soil Mechanics, Symposium, J. Kravtchenko and P. M. Sirieys, Eds., Springer-Verlag, New York, 1964, pp. 164-178.

Lambe, T. William, and Whitman, Robert V., Soil Mechanics, John Wiley and Sons, New York, 1969.

Loo, Tsu-Tao, "Effect of curvature on the Hertz theory for two circular cylinders in contact," Transactions of the A.S.M.E., Vol. 80, 1958, pp. 122-124.

Love, A. E. H., A Treatise on the Mathematical Theory of Elasticity, Cambridge University Press, London, 1927.

Maurer, William C., "Shear failure of rock under compression," Journal, Society of Petroleum Engineers, Vol. 5, No. 2, 1965, pp. 167-175.

Mead, Warren J., "The geologic role of dilatancy," The Journal of Geology, Vol. 33, 1925, pp. 685-698.

Mindlin, R. D., "Compliance of elastic bodies in contact," Transactions of the A.S.M.E., Vol. 71, 1949, pp. 259-268.

Mindlin, R. D., and Deresiewicz, H., "Elastic spheres in contact under varying oblique forces," Transactions of the A.S.M.E., Vol. 75, 1953, pp. 327-344.

Murrell, S. A. F., "The effect of triaxial stress system on the strength of rocks at atmospheric temperature," Geophysics J., Vol. 10, 1965, pp. 231-281.

Newland, P. L., and Allely, B. H., "Volume changes in drained triaxial tests on granular materials," Geotechnique, Vol. 7, No. 1, 1957, pp. 17-34.

Patton, F. D., "Multiple modes of shear failure in rock," Proceedings of the First Congress of the International Society of Rock Mechanics, Lisbon, 1966, pp. 509-513.

Penman, A. D. M., "Shear characteristics of a saturated silt, measured in triaxial compression," Geotechnique, Vol. 3, No. 8, 1953, pp. 312-328.

Poritsky, H., "Stresses and deflection of cylindrical bodies in contact, with application to contact of gears and of locomotive wheels," Transactions of the A.S.M.E., Vol. 72, 1950, pp. 191-201.

Radzimovsky, Eugene I., "Stress Distribution and Strength Condition of Two Rolling Cylinders Pressed Together," Illinois University Engineering Experiment Station Bulletin No. 408, 1953.

Rennie, B. C., "On the strength of sand," Journal Australia Mathematical Society, Vol. 1, 1959, pp. 71-75.

Reynolds, Osborne, "On the dilatancy of media composed of rigid particles in contact with experimental illustrations," Philosophical Magazine and Journal of Science, Fifth Series 20, December, 1885, pp. 469-481.

Ripley, C. F., and Lee, K. L., "Sliding friction tests on sedimentry rock specimens," Communication 8, Seventh Congress on Large Dams, Vol. 4, 1961, pp. 657-671.

Rowe, P. W., "A stress-strain theory for cohesionless soil with applications to earth pressure at rest and moving walls," Geotechnique, Vol. 4, No. 2, 1954, pp. 70-88.

Rowe, P. W., "The stress-dilatancy relation for static equilibrium of an assembly of particles in contact," Proceedings, Royal Society of London, Series A, Vol. 269, 1962, pp. 500-527.

Rowe, P. W., "Stress-dilatancy, earth pressure, and slopes," Proceedings of the A.S.C.E., Vol. 89, No. SM3, 1963, pp. 37-61.

Rowe, P. W., "Stress-dilatancy, earth pressure, and slopes" [discussion: closure], Proceedings of the A.S.C.E., Vol. 90, No. SM4, 1964, pp. 145-180.

Rowe, P. W., Barden, L., and Lee, I. K., "Energy components during the triaxial cell and direct shear tests," Geotechnique, Vol. 14, 1964, pp. 247-261.

Scott, Ronald F., Principles of Soil Mechanics, Addison-Wesley Publishing Company, Reading, Mass., 1963.

Scott, R. F., Meyerhof, George G., Roscoe, K. H., Schofield, A. N., Pijushkanti, Som, and Das, S., "Stress-dilatancy, earth pressure, and slopes" [discussion], Proceedings of the A.S.C.E., Vol. 90, No. SM1, 1964, pp. 133-150.

Skempton, A. W., and Bishop, A. W., "Measurement of shear strength of soils," Geotechnique, Vol. 2, 1950, pp. 90-108.

Smith, J. O., and Liu, Chang Keng, "Stresses due to tangential and normal loads on an elastic solid with application to some contact stress problems," Transactions of the A.S.M.E., Vol. 75, 1953, pp. 157-166.

Sokolnikoff, I. S., Mathematical Theory of Elasticity, McGraw-Hill Book Company, New York, 1956.

Stagg, K. G., and Zienkiewicz, O. C., Rock Mechanics in Engineering Practice, John Wiley and Sons, New York, 1968.

Taylor, D. W., Fundamental of Soil Mechanics, John Wiley and Sons, Inc., New York, 1948.

Terzaghi, Karl, "Fundamental studies of shearing strength" [trans. by Arthur Casagrande], in From Theory to Practice in Soil Mechanics, Karl Terzaghi, Ed., John Wiley and Sons, New York, 1960, pp. 173-174.

Thomas, Howard R. and Hoersch, Victor A., "Stresses Due to the Pressure of One Elastic Solid upon Another," Illinois University Engineering Experiment Station Bulletin No. 212, 1930.

Thurston, C. W., and Deresiewicz, H., "Analysis of a compression test of a model of a granular medium," J. Appl. Mech., Vol. 26, 1959, pp. 251-258.

Timoshenko, S., Theory of Elasticity, McGraw-Hill Book Company, New York, 1951.

Tinoco, Fernando Heriberto, "Shear Strength of Granular Materials," Ph.D. thesis, Iowa State University, 1967.

Tinoco, F. H., and Handy, R. L., "Shear Strength of Granular Materials," Iowa State Soil Research Lab. Contribution No. 67-9, 1967.

Trollope, D. H., Parkin, A. K., Gibson, R. E., and Morgenstern, N. R., "Stress-dilatancy, earth pressure and slopes" [discussion], Proceedings A.S.C.E., Vol. 89, No. SM6, 1963, pp. 127-133.

Way, Steward, "Some observation on the theory of contact pressure," Transactions of the A.S.M.E., Vol. 62, 1940, A-147 - A-157.

ACKNOWLEDGEMENTS

The author would like to gratefully acknowledge the support given to the project by the Advanced Research Projects Agency and the Defense Nuclear Agency, Department of Defense, and by its predecessor, the Defense Atomic Support Agency.

The assistance of Dr. Elden Glen Ferguson throughout the research program, and especially in the initial stages of design and fabrication of the biaxial test apparatus, is most appreciated. The author wishes to express his thanks to Dr. Shyam Bahadur of the Mechanical Engineering Department who not only allowed the use of his friction apparatus, but also provided the assistance of one of his graduate students, Mr. M. Saleem. The assistance of Jerry Amenson with the use of the scanning electron microscope is greatly appreciated.

The author extends his special thanks to Professor William F. Riley who took special interest in this research and gave unfailing advice and help throughout the research program.

The author wishes to express his sincere appreciation to Dr. Richard L. Handy for his encouragement, leadership, guidance and continued personal interest, concern and recommendations. His ability to see meaningfully through nothingness is principally responsible for any success in this study.

A great deal of the credit is due my wife Suresh and my children Sanjay and Monica for their love, devotion and understanding, which provided incentive to complete this work. I also record with appreciation the blessing of my mother.